Stochastic modeling of catalytic processes in nanoporous materials: Beyond mean-field approach

by

Andrés García

A dissertation submitted to the graduate faculty
in partial fulfillment of the requirements for the degree of
DOCTOR OF PHILOSOPHY

Major: Condensed Matter Physics

Program of Study Committee:
James W. Evans, Major Professor
Ludovico Cademartiri
Beate Schmittmann
Sanjeevi Sivasankar
Alejandro Travesset-Casas

Iowa State University
Ames, Iowa
2017

DEDICATION

I would like to dedicate this thesis to my father Arturo, my mother María Eugenia and my brother Nicolás for their unconditional support and all the love they have given me through all this processes. I also want to thank Kaoru Ikuma for her patience and unconditional support in the past few months, without you everything would have been harder. I want to also thank Sandra Carrillo and Rodrígo López for their support and understanding the effort it takes to get a PhD. Finally, I would also like to dedicate this thesis to my dearest friends: Carlos and Catherine Infante, Natalia Acevedo, Leoncio Rodríguez, Juan David and Felipe Cortés, Arun and Sapna Madhavan, Natalia Londoño, Santiago Cortés, Miguel Ángel Martín and the "Colombian parche "(you know who you are); without you guys this adventure would have been unbearable. If you feel that I left you out, please do not hesitate to include yourself.

TABLE OF CONTENTS

LIST OF TABLES

LIST OF FIGURES

ACKNOWLEDGEMENTS

I would like to take this opportunity to express my thanks to those who helped me with various aspects of conducting research and the writing of this thesis. First and foremost, Dr. James W. Evans for his guidance, patience and support throughout this research and the writing of this thesis. His insights and words of encouragement have often inspired me and renewed my hopes for completing my graduate education. I would also like to thank my committee members for their efforts and contributions to this work: Dr. Ludovico Cademartiri, Dr. Beate Schmittmann, Dr. Sanjeevi Sivasankar and Dr. Alejandro Travesset-Casas; special thanks to Dr. Michael Tringides. I also acknowledge useful discussion with current and former members of the Evans research group: Dr. David Ackerman, Dr. Jing Wang, Dr. Chi-Jen Wang and Dr. Da-Jiang Liu. Also, other people who contributed to the projects: Dr. Igor Slowing and visiting scientist Dr. Tiago de Oliveira, from the Universidade Federal Fluminense in Brazil. I would additionally like to thank the Physics and Astronomy Department and The Ames Laboratory for their finalcial support during the time this work was conducted.

ABSTRACT

Transport and reaction in zeolites and other porous materials, such as mesoporous silica particles, has been a focus of interest in recent years. This is in part due to the possibility of anomalous transport effects (e.g. single-file diffusion) and its impact in the reaction yield in catalytic processes. Computational simulations are often used to study these complex non-equilibrium systems. Computer simulations using Molecular Dynamics (MD) techniques are prohibitive, so instead coarse grained one-dimensional models with the aid of Kinetic Monte Carlo (KMC) simulations are used. Both techniques can be computationally expensive, both time and resource wise. These coarse-grained systems can be exactly described by a set of coupled stochastic master equations, that describe the reaction-diffusion kinetics of the system. The equations can be written exactly, however, coupling between the equations and terms within the equations make it impossible to solve them exactly; approximations must be made. One of the most common methods to obtain approximate solutions is to use Mean Field (MF) theory. MF treatments yield reasonable results at high ratios of reaction rate k to hop rate h of the particles, but fail completely at low k/h due to the over-estimation of fluxes of particles within the pore. We develop a method to estimate fluxes and intrapore diffusivity in simple one- dimensional reaction-diffusion models at high and low k/h, where the pores are coupled to an equilibrated three-dimensional fluid. We thus successfully describe analytically these simple reaction-diffusion one-dimensional systems. Extensions to models considering behavior with long range steric interactions and wider pores require determination of multiple boundary conditions. We give a prescription to estimate the required parameters for these simulations. For one dimensional systems, if single-file diffusion is relaxed, additional parameters to describe particle exchange have to be introduced. We use Langevin Molecular Dynamics (MD) simulations to assess these parameters.

CHAPTER 1. INTRODUCTION

An excerpt from the paper published in *Chemical Reviews*: Kinetic Monte Carlo Simulation of Statistical Mechanical Models and Coarse-Grained Mesoscale Descriptions of Catalytic Reaction-Diffusion Processes: 1D Nanoporous and 2D Surface Systems.

Da-Jiang Liu[1], **Andrés García**[1,2], Jing Wang[1,3], David Ackerman[1], Chi-Jen Wang[1,3*],
and James W. Evans[1,2,3]

[1]*Ames Laboratory-USDOE, Iowa State University, Ames, Iowa 50011, USA*
[2]*Department of Physics and Astronomy, Iowa State University, Ames, Iowa 50011, USA*
[3]*Department of Mathematics, Iowa State University, Ames, Iowa 50011, USA*

(Received 22 August 2014; published 24 April 2015)

Traditionally mean-field rate equations of chemical kinetics for spatially uniform systems [1–3] and the corresponding reaction-diffusion equations describing spatial heterogeneity [4–6] have proved immensely useful in elucidating catalytic processes. However, it is well-recognized that standard mean-field rate expressions neglect spatial correlations in the reactant and/or product distribution. It is less well appreciated that the standard treatment of diffusion is generally applicable only at low concentrations and in unrestricted environments [7]. Generically, there are two sources of spatial correlations associated with either: (*i*) thermodynamics, where the reactant and product distribution is in some sense locally equilibrated and the distribution reflects interactions between molecules, (*ii*) kinetics for unequilibrated distributions, where correlations are induced by adsorption-desorption- reaction kinetics. For higher reactant concentrations, correlations of thermodynamic origin should be enhanced due to stronger interactions, and those of kinetic origin might also be amplified due to inhibited mobility.

---

[*] Current address: School of Mathematics, Georgia Institute of Technology, Atlanta, Georgia 30332, USA.

For catalysis in 1D nanoporous systems, such as zeolites [8–10] and functionalized mesoporous silica [11,12], severe transport limitations [13,14] (in the extreme case leading to single-file diffusion [15]) induce strong correlations of kinetic origin that invalidate standard mean-field treatments [16–19].

Spatial correlations of thermodynamic origin have been extensively characterized. Exact Ursell-Mayer cluster expansions, Kirkwood and quasimechanical approximations, and concepts such as Markovian spatial fields (which are often formulated in terms of conditional probabilities) can be utilized [20–22]. Kinetically induced correlations are less well characterized. Reactive non-equilibrium steady states (NESS) in open systems (reactants in, products out) are a natural analogue of equilibrium Gibbs states [23, 24]. One can make some general observations about their behavior. Clearly, a bimolecular reaction will deplete the population of associated nearby reactant pairs relative to a corresponding equilibrium state.

To effectively analyze these non-equilibrium processes, a molecular-level modeling strategy is required which can track evolution of system configurations on the appropriate time and length scales appropriately accounting for spatial correlations. To this end, one can implement spatially discrete stochastic (Markovian) reaction-diffusion models. For reactions in 1D nanoporous systems, one can divide the pore into cells comparable to reactant size and treat continuous diffusion by hopping and exchange between adjacent cells [16–19, 25–27]. The behavior of these models is in principle described exactly by master equations [23, 28]. However, given the difficulty of reliable analysis of the master equations, model behavior is usually instead determined precisely by Kinetic Monte Carlo (KMC) simulation [29–31], as described in recent reviews [7, 32, 33].

In these reaction-diffusion systems, nontrivial spatiotemporal behavior generally arises from the interplay between the typically nonlinear reaction kinetics and diffusive transport. In the 1D nanoporous catalytic systems, especially with inhibited transport within pores, net reactivity is often localized near pore openings either for catalytic conversion [25–27] or polymerization [34, 35] reactions. This feature induces strong concentration variations within the nanopores typically on a length scale of tens of nanometers.

For both more efficient modeling and a deeper understanding to spatiotemporal behavior in these systems, it is natural to coarse-grain the spatially discrete molecular-level models to obtain a spatially continuous reaction- diffusion equation (RDE) formulation. Typically, this type of analysis is generally associated with the deterministic "hydrodynamic regime" for large mobility and low concentration gradients, and the associated continuum RDE is often referred to as the hydrodynamic RDE [36, 37]. For these 1D nanoporous catalytic systems, there are particular challenges. Since the concentration gradients are large, significant net reactivity is restricted to near the pore openings, and it can be argued that the behavior is controlled by fluctuations in adsorption-desorption processes at the pore openings. This prompts consideration of a "generalized hydrodynamic" approach [38], and recently, such an approach has been successfully implemented for a simple conversion reaction [19].

For accurate description of basic behavior in 1D nanoporous system, an appropriate description of chemical diffusion in mixed multi-component system is key. This should be based on an appropriate Onsager formulation of transport theory that recognizes the coupling between concentration gradients and diffusion fluxes of different species and thus involves a diffusion tensor [37, 39]. Apart from fundamental statistical mechanical studies of diffusion in multi-component lattice-gas models [37, 40–42], there is a general appreciation of the complexity of diffusion for 1D nanoporous systems where additional anomalies appear in the single-file diffusion (SFD) regime [14, 43–45].

1.1 Thesis organization

This dissertation is based on three published papers, an excerpt of a published review and two additional parts.

Chapter 2 uses a modified excerpt from the published review "Kinetic Monte Carlo Simulation of Statistical Mechanical Models and Coarse-Grained Mesoscale Descriptions of Catalytic Reaction-Diffusion Processes: 1D Nanoporous and 2D Surface Systems" whose authors are Da-Jiang Liu, **Andres Garcia**, Jing Wang, David M. Ackerman, Chi-Jen Wang, and James W. Evans in the Chemical Reviews journal (*Chem. Rev.* 2015, 115, 5979-6050). In this article, I performed the simulations and numerical analysis for the presented information. The chapter describes the basic model, and defines the basic conventions and notation to be used throughout the document.

Chapter 3 is paper published in Physical Review E, in which I am the main author. A statistical mechanical model is presented for a coarse-grained lattice-gas reaction-diffusion system, where an isomeric stereoselective reaction is analyzed. The analysis is performed using KMC simulations and an analytic method is developed to treat correlations in the reaction terms.

Chapter 4 is a paper published in Journal of Chemical Physics, in which I am the main author. A statistical mechanical model is presented for a coarse-grained lattice-gas reaction-diffusion system, where a fluid-pore system in which there is nearest-neighbor exclusion is analyzed. The system is analyzed in two levels of coarse-graining, and an analytical theory is developed.

Chapter 5 is a paper published in Journal of Physical Chemistry C, in which I am the main author. The methodology to determine the KMC simulation parameters for a general family of coarse grained reaction-diffusion system is given, with a few applications. An analytic theory is developed for some of these models and are compared with the KMC simulation results.

Chapter 6 is a chapter that has not been published yet, in which I am the main author. In the chapter, a 3D reaction-diffusion process for molecules that are made out of spheres, and are confined to move in an infinitely long cylindrical channel of cross-section D_p, is mapped onto a 2D model, where molecules are made of circles and move in an infinitely long rectangular channel of width W. Using a Langevin MD approach, the results for the passing propensity of monomer-oligomer systems, where the oligomers are linear, are compared with the results obtained using the corresponding Fokker-Planck equation. The scaling exponent for the behavior of the passing propensity in small gaps is obtained for most of the systems. The motivation behind the study is that of polymerization reactions in narrow pores.

Chapter 7 is a chapter that has not been published yet, in which I am the main author. A real reaction-diffusion process using a coarse-grained model is analyzed. The reactant and product molecules are modeled using spheres as the building blocks. A Langevin MD technique is used to assess the diffusion of the molecules within a restricted cylinder. In particular, we assess the passing propensity of the molecules and map the results and parameters to a KMC model, where the results are compared to experimental results of the system under consideration.

Chapter 8 gives a brief summary of the thesis, along with the general conclusions.

Bibliography

[1] R. van Santen. *Chemical kinetics and catalysis.* Plenum, New York, 1995.

[2] P. Gray and S. K. Scott. *Chemical oscillations and instabilities: Non-linear kinetics.* Claredon, Oxford, UK, 1994.

[3] R. Imbihl. Oscillatory reactions on single crystal surfaces. *Prog. Surf. Sci.*, 44:pp. 185–343, 1993.

[4] G. Ertl. Reactions at surfaces: From atoms to complexity (Nobel Lecture). *Angew. Chem. Int. Ed.*, 47:pp. 3524–3535, 2008.

[5] R. Kapral and K. Showalter. *Chemical waves and patterns.* Kluwer, Dordrecht, 1995.

[6] R. Imbihl and G. Ertl. Oscillatory kinetics in heterogenous catalysis. *Chem. Rev.*, 95:pp. 697–773, 1995.

[7] D-J. Liu and J. W. Evans. Realistic multisite lattice-gas modeling and KMC simulation of catalytic surface reactions: Kinetics and multiscale spatial behavior for CO-oxidation on metal (100) surfaces. *Prog. Surf. Sci.*, 83:pp. 393–521, 2013.

[8] J. Kärger. *Handbook on heterogenous catalysis*, page p. 1714. Wiley-VCH, 2008.

[9] N. Y. Chen, J. T. F Degnan, and C. M. Smith. *Molecular transport and reaction in zeolites.* VCH, New York, 1994.

[10] G. Olhmann, H. P. Pfeifer, and G. Fricke, editors. *Catalysis and adsorption in zeolites.* Elsevier, Amsterdam, 1991.

[11] K. Tajima and T. Aida. *Nanostructured catalysis.* Plenum, New York, 2003.

[12] J. S. Beck, J. C. Vartulli, W. J. Roth, M. E. Leonowicz, C. T. Kresge, K. D. Schmitt, C. T. W. Chu, D.H. Olson, and E. W. Sheppard. A new family of mesoporous molecular sieves prepared with liquid crystal templates. *J. Am. Chem. Soc.*, 114:pp. 10834–10843, 1992.

[13] K. Malek, T. H. J. Vlugt, and B. Smit. *Catalysis and materials science*, chapter 14. Wiley-VCG, Weinheim, Germany, 2009.

[14] D. S. Sholl. Understanding macroscopic diffusion of adsorbed molecules in crystalline nanoporous materials via atomistic simulations. *Acc. Chem. Res.*, 39:pp. 403–411, 2006.

[15] K. Hahn, J. Kärger, and V. Kulka. Single-file diffusion observation. *Phys. Rev. Lett.*, 76:pp. 2762–2765, 1996.

[16] C. Rödenbeck, J. Kärger, and K. Hahn. Exact analytical description of tracer exchange and particle conversion in single-file systems. *Phys. Rev. E*, 55:pp. 5697–5712, 1997.

[17] M. S. Okino, R. Q. Snurr, H. H. Kung, J. E. Ochs, and M. L. Mavrovouniotis. A consistent correlation approach to single file diffusion with reaction. *J. Chem. Phys.*, 111:pp. 2210–2221, 1999.

[18] S. V. Nedea, A. P. J. Jansen, J. J. Lukkien, and P. A. J. Hilbers. Steady-state properties of single-file systems with conversion. *Phys. Rev. E*, 65:066701, 2002.

[19] D. M. Ackerman, J. Wang, and J. W. Evans. Generalized hydrodynamic treatment of the interplay between restricted transport and catalytic reactions in nanoporous materials. *Phys. Rev. Lett.*, 108:228301, 2012.

[20] D. A. McQuarrie. *Statistical mechanics.* Harper Collin, New York, 1976.

[21] R. H. Fowler and E. A. Guggenheim. *Statistical thermodynamics.* Cambridge University Press, Cambridge, UK, 1986.

[22] C. Preston. *Random fields.* Springer Lecture Notes in Mathematics, Springer, Berlin, 1976.

[23] G. Nicolis and I. Prigogine. *Self-organization in non-equilibrium systems.* Wiley, New York, 1977.

[24] A. Mikhailov. *Foundations of synergetics I.* Springer, Berlin, 1990.

[25] J. G. Tsikoyiannis and J. Wei. Diffusion and reaction in high-occupancy zeolite catalysts-I. A stochastic theory. *J. Chem. Eng. Sci.*, 46:pp. 233–253, 1991.

[26] J. Kärger, M. Petzold, H. Pfeifer, S. Ernst, and J. Weitkamp. Single-file diffusion and reaction in zeolites. *J. Catal.*, 136:pp. 283–299, 1992.

[27] C. Rödenbeck, J. Kärger, and K. Hahn. Tracer exchange and catalytic reaction in single-file systems. *J. Catal.*, 157:pp. 656–664, 1995.

[28] N. G. van Kampen. *Stochastic processes in physics and chemistry.* Elsevier, Amsterdam, 1981.

[29] A. Bortz, M. H. Kalos, and J. L. Lebowitz. A new algorithm for Monte Carlo simulation of Ising spin systems. *J. Comput. Phys.*, 17:pp. 10–18, 1975.

[30] A. F. Voter. Classically exact overlayer dynamics: Diffusion of Rhodium clusters on $Rh(100)$. *Phys. Rev. B*, 34:pp. 6819–6829, 1986.

[31] K. A. Fitchthorn and W. H. Weinberg. Theoretical foundations of dynamical Monte Carlo simulations. *J. Chem. Phys.*, 95:pp. 1090–1096, 1991.

[32] M. Stamatakis and D. G. Vlashos. Unraveling the complexity of catalytic reactions via kinetic Monte Carlo simulation: Current status and frontiers. *ACS Catal.*, 2:pp. 2648–2663, 2012.

[33] K. Reuter. *In modeling heterogenous catalytic reactions: From the molecular process to the technical system.* Wiley-VCH, Weinheim, Germany, 2011.

[34] D-J. Liu, H-T. Chen, V. S-Y. Lin, and J. W. Evans. Polymer length distributions for catalytic polymerization within mesoporous materials: Non-Markovian behavior associated with partial extrusion. *J. Chem. Phys.*, 132:154102, 2010.

[35] D-J. Liu, J. Wang, D. M. Ackerman, I. S. Slowing, M. Prusky, H-T. Chen, V. S-Y. Lin, and J. W. Evans. Interplay between anomalous transport and catalytic reaction kinetics in single-file nanoporous systems. *ACS Catal.*, 1:pp. 751–763, 2011.

[36] H. Spohn. *Large scale dynamics of interacting particles.* Springer, Berlin, 1991.

[37] A. Massi and E. Presutti. *Mathematical methods for hydrodynamic limits*, volume 1501. Springer Lectures in Mathematics, Berlin, 1991.

[38] B. J. Alder and W. E. Alley. Generalized hydrodynamics. *Phys. Today*, page p. 55, January 1984.

[39] E. L. Cussler. *Multicomponent diffusion.* Elsevier, Amsterdam, 1976.

[40] L. K. Moleko and A. R. Allnat. Exact linear relations between the phenomenological coefficients for matter transport in a random alloy. *Philos. Mag. A*, 58:pp. 677–682, 1988.

[41] K. W. Kerr, K. Binder, and S. M. Reulein. Mobility, interdiffusion, and tracer diffusion in lattice-gas models for two-component alloys. *Phys. Rev. B*, 39:pp. 4891–4910, 1989.

[42] J. Quastel. Diffusion of color in the simple exclusion process. *Commun. Pure Appl. Math.*, 45:pp. 623–679, 1992.

[43] J. Kärger and J. Freude. Mass transfer in micro- and mesoporous materials. *Chem. Eng. Technol.*, 25:pp. 769–778, 2002.

[44] R. Krishna, T. H. J. Vlugt, and B. Smit. Influence of isotherm inflection on diffusion in silicalite. *Chem. Eng. Sci.*, 54:pp. 1751–1757, 1999.

[45] D. Paschek and R. Krishna. Kinetic Monte Carlo simulations of transport diffusivities of binary mixtures in zeolites. *Phys. Chem. Chem. Phys.*, 3:pp. 3185–3191, 2001.

CHAPTER 2. THE BASIC MODEL: CONVENTIONS AND NOTATION

An excerpt from the paper published in *Chemical Reviews*: Kinetic Monte Carlo Simulation of Statistical Mechanical Models and Coarse-Grained Mesoscale Descriptions of Catalytic Reaction-Diffusion Processes: 1D Nanoporous and 2D Surface Systems.

Da-Jiang Liu[1], **Andrés García**[1,2], Jing Wang[1,3], David Ackerman[1], Chi-Jen Wang[1,3*],
and James W. Evans[1,2,3]

[1] *Ames Laboratory-USDOE, Iowa State University, Ames, Iowa 50011, USA*
[2] *Department of Physics and Astronomy, Iowa State University, Ames, Iowa 50011, USA*
[3] *Department of Mathematics, Iowa State University, Ames, Iowa 50011, USA*

(Received 22 August 2014; published 24 April 2015)

First-order conversion reactions in catalytically functionalized nanoporous materials incorporating arrays of linear nanopores with diameters of a few nanometers have been widely studied and modeled [1–4]. The basic ingredients are as follows. Reactant molecules from the medium surrounding the catalytic particles adsorb at the pore openings and diffuse into the pores. Upon reaching catalytic sites, they are converted to product that then diffuse out of the pores, possibly subject to significant interference from the reactant, which also shares the confined space within the pores. Catalytic reactions using zeolite materials are often performed using gas-phase flow reactors but where the reactants are with a carrier gas, which will also populate the pores within the zeolite. Catalysis using functionalized mesoporous silica nanoparticles (MSN) is usually performed in solution-phase batch reactors, so in this case often solvent molecules coexist with reactant and product species inside the pores. Thus, in either case, one might anticipate a stochastic description of reactant and product species dynamics within the pore

---

[*] Current address: School of Mathematics, Georgia Institute of Technology, Atlanta, Georgia 30332, USA.

implicitly accounting for the interaction with the carrier gas or solvent. For this reason, the discussion in Section 2.1 will start with the use of Langevin dynamics to describe reactant and product motion but then immediately transition to spatially discrete coarse-grained modeling, which allows more efficient simulation of the entire reaction-diffusion process.

We have already mentioned that typical catalytic nanoporous materials include zeolites and MSN, which can both consist of arrays parallel pores containing catalytic sites (although more complex pore morphologies are also possible). The reader is referred to extensive reviews of zeolite materials and their applications to catalysis [5–7]. Here, we just note that pore diameters (d_p) are typically in the range $d_p = 0.5 - 2\,\mathrm{nm}$. In contrast, for mesoporous silicas in the form of mesoporous silica nanoparticles (MSN), such as MCM-41 [8,9], and SBA-15 [10], nominal pore diameters are typically in the range $d_p = 2 - 10\,\mathrm{nm}$. However, it should be emphasized that effective pore diameters can be reduced below 2 nm by functionalization and also attachment of reactant species at the pore walls [11]. While mesoporous materials offer the advantage of large surface areas, restricted transport within the pores is potentially both a disadvantage (reducing reactivity or turnover frequencies), and an additional advantage (product selectivity) [12].

Given the importance of transport in these materials for application to catalysis, separations, and sequestration, there is naturally extensive experimental and theoretical literature on this topic. We refer reader to reviews [5,6,13,14] and selected recent papers [15,16]. There are extensive studies for species like CH_4, CF_4, and CCl_4, with diameters of $\sim 0.4\,\mathrm{nm}$ and above which are often described by a spherical united atom model [17]. Species such as ethane are described by the union of two spherical united atoms [18]. It is clear that these species should undergo SFD for narrower zeolite pores. Here, however, we emphasize that a relatively poor characterized aspect of transport is inhibited, passing of reactant and product molecules. This naturally has a strong impact on reactivity, as it limits extrusion of the product. Some MD studies have tagged molecules, from which changes in order (or otherwise) can be tracked [17,19]. One particularly instructive study focused on an effective two-molecule passing problem in an effort to more efficiently characterize passing propensity in narrow pores [18]. The strategy was to assess the free energy profile as a function of center-of-mass separation in the pore direction and to utilize a transition state theory (TST) formulation to assess passing. Most recently, the passing propensity in an effective two-particle problem with strongly damped Langevin dynamics was assessed, revealing deviations from TST predictions for this type of dissipative dynamics [20]. We discuss this analysis further in Chapter 6.

Our focus is not just on transport, but rather on diffusion-mediated catalytic conversion reactions in 1D nanoporous materials with strongly inhibited passing of reactant and product species within the pores. It is thus instructive to provide specific examples. The first example motivating earlier modeling studies [21] is the conversion of neopentane to isobutane catalyzed by Pd in L zeolites according to the mechanism [22]

$$(\mathrm{CH_3})_3-\mathrm{C}-\mathrm{CH_3}\ (\text{neopentane}) + \mathrm{H^+}-\mathrm{Pd} \quad\rightarrow\quad \mathrm{CH_4}\ (\text{methane}) + \mathrm{CH_3}-\mathrm{C^+}-\mathrm{Pd}$$

and

$$\mathrm{CH_4} + \mathrm{CH_3}-\mathrm{C^+}-\mathrm{Pd} + \mathrm{H_2} \quad\rightarrow\quad \mathrm{CH_3}-\mathrm{CH}\ (\text{isobutane}) + \mathrm{H^+}-\mathrm{Pd}.$$

The diameter of neopentane is about 0.62 nm and that of isobutane is similar (vs methane at ~ 0.4 nm). All these species might be effectively described by spherical united atom models. Experimental studies of reaction kinetics indicate SFD in zeolite L, a feature which should be expected since this material is composed of linear nanopores with small diameter $d_p \approx 0.73$ nm and no cross-connections [21,22] (see Figure 2.1). In contrast, reactivity is significantly higher in zeolite Y, which also has disconnected linear pores with similar narrow diameter, $d_p \approx 0.74$ nm. However, this difference in reactivity is explained by the feature that the zeolite Y pores include near-spherical supercages, which can act as mixing chambers. In contrast, the pores in zeolite L only have dislike bulges, which apparently cannot facilitate passing of reactant and product species [22].

The second example involves aldol condensation in MSN. Specifically, this reaction involves the conversion of $p-$nitrobenzaldehyde (PNB) to an aldol product by reaction with acetone in amine-functionalized MSN [11] (see Figure 2.2 and [23, 24] for related studies). Significantly, a range of pore-expanded, functionalized MSN were prepared to by including a pore-expander agent during synthesis [25], and reactivity was determined from a range of pore diameters. This potentially allows assessment of the transition to the SFD regime. To provide a more detailed description of this system, pore diameters after aminopropyl or methyl(aminopropyl) function-

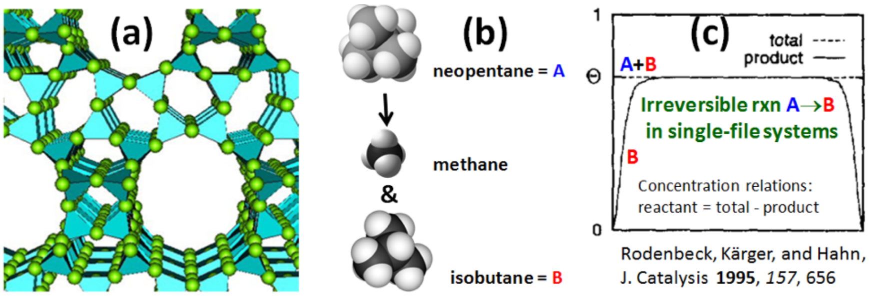

Figure 2.1: Neopentane (A) conversion to isobutane (B) in zeolite-supported Pd catalysis. (a) Image of zeolite structure adapted from http://www.personal.utulsa.edu/~geoffrey-price/zeolite/ (Beta-A Jpeg Image). (b) Schematic of reactant and product species. (c) Schematic of expected concentration profiles along the pore from the work of Rödenbeck et al. [21]

alization ranged from $d_p = 2.6\,\mathrm{nm}$ to $3.6\,\mathrm{nm}$. (Nominal diameters before functionalization, $d_p(\mathrm{pre})$, were larger as the amine groups with linear size $\sim 0.5\,\mathrm{nm}$ attached to the pore walls reduce the effective diameter by $\sim 1\,\mathrm{nm}$.) Reactivity measured from reaction yield was high for the largest pore diameters, but dropped dramatically for smaller diameters of $d_p = 2.6-2.8\,\mathrm{nm}$. However, the longest dimensions of the reactant and product species are $0.65\,\mathrm{nm}$ for PNB and $1.0\,\mathrm{nm}$ for the aldol product (and $0.4\,\mathrm{nm}$ for acetone). Thus, might one anticipate that, even in the narrowest pores, there is plenty of room for passing?

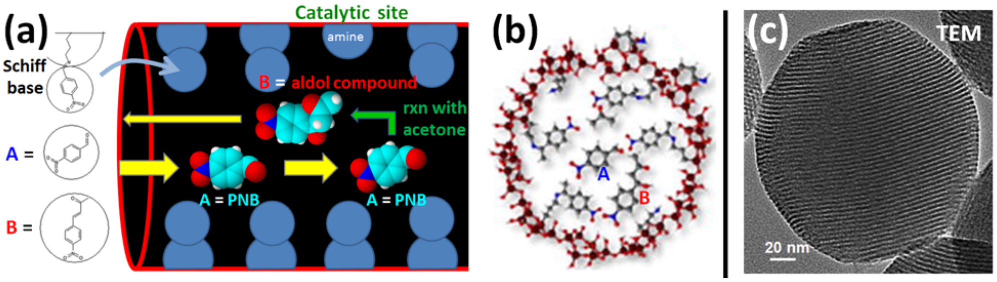

Figure 2.2: (a) Schematic of the conversion of PNB (A) to an aldol compound (B) by reaction with acetone in amine functionalized MSN. The attachment of PNB to the amine group to form a Schiff base, reducing the effective pore diameter. (b) Pore cross-sectional schematic. (c) TEM image of mesoporous silica nanoparticle (MSN) with visible pores oriented from left to right.

However, experimental analysis indicates that the diameter of the pore is significantly further reduced as a result of reaction. It was proposed, and confirmed by NMR studies, that the reactant PNB attaches to the functionalized pore walls in the sense that a Schiff base is formed between PNB and the aminopropyl group at the walls [11] (see Figure 2.2). One might anticipate that this would further reduce the pore diameter by twice the PNB size to a smaller effective value, $d_p(\text{eff})$. However, the size of the Schiff base of $d_{\text{sch}} \approx 1\,\text{nm}$ is somewhat smaller than the sum of the above listed PNB and amine dimensions. Thus, for $d_p(\text{pre}) \approx 3.8\,\text{nm}$ one estimates that $d_p(\text{eff}) \approx d_p(\text{pre}) - 2d_{\text{sch}} \approx 1.8\,\text{nm}$. With this reduced effective diameter, it is reasonable to expect that effects of inhibited passing of reactant and product species could significantly reduce reactivity. One caution is that formation of the Schiff base also inhibits access of PNB to amine catalytic sites, so this effect can also reduce reactivity.

In other type of reactions, such as bimolecular esterification (acid + alcohol $\leftrightarrow$ ester + water), there has been considerable interest in exploiting multifunctionalization of MSN to tune "reaction product-pore interior interactions" to enhance yield [26–28]. Specifically, multifunctionalizing the pore interior with hydrophobic groups can minimize interaction of the product water with the intrinsically hydrophilic MSN surface groups. potentially shifting the reaction equilibrium toward complete conversion. Multifunctionalization can also impact transport within the pores [29] (see Chapters 3 - 5). Finally, polymerization reactions in nanoporous materials will also naturally be impacted by the ability of monomers to pass oligomers that form in catalytically functionalized pores. One example is the oxidatively catalyzed formation of poly(phenylene butadinylene) polymer (PPB) in a Cu^{2+}-functionalized MCM-41 silica [30]. Modeling reveals unusual spatial kinetic features of polymerization in 1D nanoporous materials subject to SFD [31, 32].

2.1 From Spatially Continuous to Discrete Stochastic Models for Reactions in 1D Nanoporous Materials

Here, the focus will be on the case of catalytic conversion reactions for solution-phase batch reactors where the catalytic nano-particles are immersed in a well-stirred fluid initially containing the reactant species. As previously indicated, a comprehensive modeling description of these many-particle reaction-diffusion processes must include diffusion of reactant species into the nanopores from surrounding well-stirred fluid, reaction in the vicinity of catalytic sites on the interior pore surface, diffusion of both reactant and product species out of the pore, and product reentry when a significant fraction (F) of reactant is converted to product in the surrounding fluid. One might naturally start by considering comprehensive continuous-space description where the motion of reactant, product, and solvent molecules is described by classical molecular dynamics (MD) simulations [17, 18]. Alternatively and more efficiently, just the motion of reactants and products might be described by Langevin dynamics, implicitly accounting for the solvent [20] (see Figure 2.3). However, even the latter treatment is not computationally viable to describe either the entire reaction or even the attainment of a reactive quasi-steady state for a specific F.

As alluded to by the above reference to quasi-steady-state behavior, one significant aspect of these batch reactor processes is a time scale separation. The overall conversion of reactant to product occurs on the time scale of hours. Initially, there is typically only reactant in the surrounding fluid ($F = 0$), and one anticipates that, on the time scale of a few minutes, quasi-steady-state concentration profiles are established in the pore reflecting this $F = 0$ state of the fluid. As the reaction proceeds, an increasing fraction, F, of reactant outside the pores is converted to product. For each new F, quasi-steady-state concentration profiles are quickly re-established. Thus, by separately analyzing these quasi-steady states for a sequence of increasing F values, one can piece together the kinetics of the overall conversion reaction [29].

Since many-particle MD or Langevin simulations are prohibitive or impossible on the required time and length scales, there is motivation to apply "local coarse-graining" to map the above continuous-space picture onto a spatially discrete stochastic model. In the simplest scenario, one thus divides the linear pores into cells whose width, a, matches the typical reactant or product size of a $\sim 1\,\mathrm{nm}$ [1–4, 33, 34]. Sometimes, it is also convenient to extend this 1D array of cells to a 3D array outside the pores in the surrounding fluid [4] (see Figure 2.3). Thus, each cell can contain at most one reactant or product molecule. Diffusion within the pores is now described by hopping to adjacent empty cells and also by exchange of (distinct) species between adjacent cells. Adsorption-desorption processes at the pore openings correspond to hopping (or exchange) between the end cell of the linear array within the pore and the adjacent

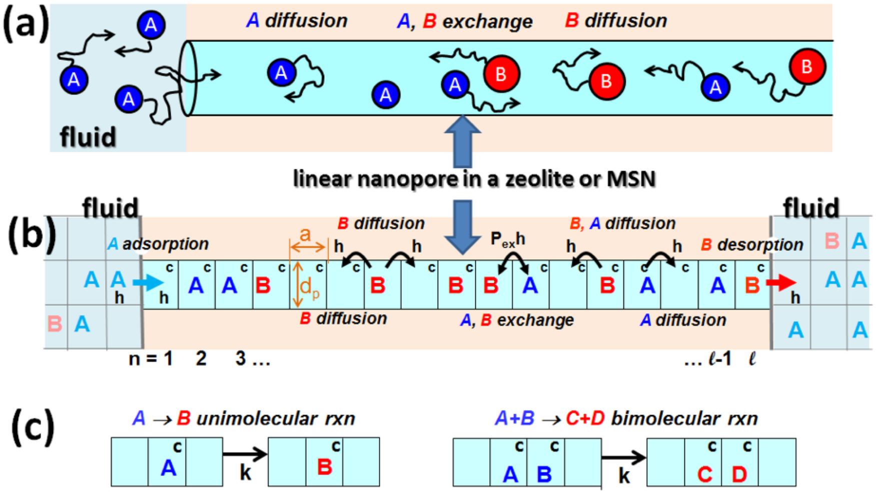

Figure 2.3: (a) Continuous-space Langevin representation of the many-particle reactant and product diffusive transport processes in a 1D linear nanopore. (b) Corresponding spatially discrete model formulation. (c) Treatment of unimolecular and bimolecular conversion reaction processes for the spatially discrete model.

cell in the surrounding fluid. Unimolecular reactions occur at cells within the pore designated as catalytic (c) and convert a reactant species to the appropriate product species within that cell. Bimolecular reactions might involve, for example, distinct reactant species in adjacent cells (see Figure 2.3). These stochastic models are described exactly by hierarchical master equations (see Section 2.2), although for precise analysis of behavior, it is typically most convenient to employ KMC simulations. Here, various processes are implemented stochastically with probabilities proportional to the physical rates. However, a non-trivial challenge is to obtain the basic rate parameters for this locally coarse-grained model that are consistent with the full continuous dynamics.

A few relevant observations on connecting spatially continuous to discrete descriptions of the reaction-diffusion process are as follows: (i) The rate, h, for hopping to adjacent cells would be chosen to match the prescribed continuous diffusion coefficient, D_0, in the regime of low reactant and product concentrations, so that $D_0 = a^2 h$ [35]. (ii) Clearly, exchange is absent for SFD. However, in general, it is not trivial to appropriately map the extent of inhibited passing, as assessed by MD or Langevin simulations in a narrow pore, onto a numerical value of the exchange probability (p_{ex}) in the spatially discrete model [20] (see Figure 2.3). Despite its significance in controlling reactivity, targeted quantitative analyses of the passing propensity of reactant and product species are rare [18,20]. Even here, many-particle MD or Langevin dynamics is not efficient, so an effective two-particle analysis is preferred [18,20] (see Chapter 3). (iii) Adsorption-desorption rates, and specifically their ratio, should reflect the possible different chemical potentials for various species in the surrounding fluid versus within the pore. This issue is particularly relevant in discussion of multifunctionalization to tune the pore interior to enhance reactivity (see Chapters 3 - 5). (iv) With regard to interactions between reactant and product species themselves and with the pore walls, the simplest treatment considers just steric (or geometric non-overlap) constraints. These constraints are incorporated into the feature that a cell can only be occupied by a single species. In the case of longer range interactions [36], the additional requirement that the neighboring cells to a non-empty cell, within the interaction range, are empty. However, a more sophisticated treatment would account for solvent-mediated interactions between reactants, products, and the pore walls [1,2,33], where these interactions would be suitably coarse- grained to fit our spatially discrete model. While significant recent developments exist in related coarse-graining approaches [37], these have not yet been applied to systems of interest here. (v) The microscopic reaction rate in the coarse-grained model would reflect not just the activation barrier but also local entropic factors and diffusion processes within the cell (or within adjacent cells for bimolecular reactions) related to achieving the necessary reaction configuration.

The above level coarse-grained modeling with one reactant or product species per cell has the simplifying feature that chemical diffusion in a system involving a single species is independent of concentration in the absence of interactions beyond steric blocking [38]. This feature, and its extension to multi-species models where distinct species have the same mobilities, is particularly useful in analysis of the more complex reaction-diffusion process [1–4]. However, a more realistic treatment bringing the above "very coarse" spatially discrete model and continuous-space Langevin descriptions would be to choose a finer discrete spatial grid within (and outside) the pores. Now particle centers reside at grid points, but the grid spacing is finer than the particle linear dimensions, so particles can only approach within a finite threshold distance (of multiple grid spacings) to avoid overlap (see Figure 2.4). In this case, the description of chemical diffusion is non-trivial even for a single-species problem (see Chapters 3 - 5).

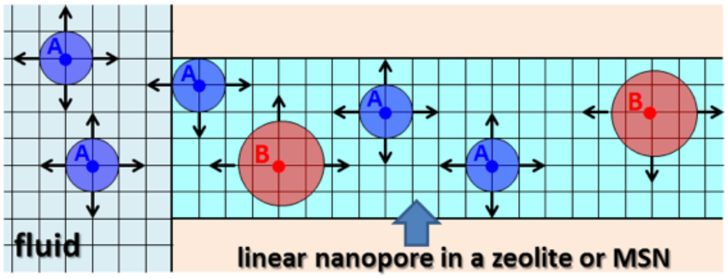

Figure 2.4: Finer-scale spatially discrete model that coarse-grains the continuous-space Langevin model for transport and reaction in a narrow nanopore.

2.2 Discrete Hierarchical Reaction-Diffusion Equations

For the above discrete reaction-diffusion models, the labeling of discrete cells or sites which form periodic arrays will be labeled by n, and the concentrations at those sites for species A, B, … by $\langle A_n \rangle$, $\langle B_n \rangle$, … . Again, at most one species can occupy a site or cell. Correspondingly, these concentrations are normalized so that their maximum value is unity, and they correspond to probabilities that a site is occupied by A, etc. Here, we leave implicit dependence on time (t), but explicitly account for possible spatial heterogeneity by allowing concentrations to depend on $\mathbf{n}$ (see Figure 2.5). In the following sections, it will be primarily described the case of systems with a single site type for each species. However, much of the formalism applies to the situation where there are distinct site types for each within the unit cell of the periodic system species, and brief comments are made in the text on this more general case. The site concentrations satisfy evolution equations of the form [39–45]

$$\frac{\mathrm{d}\langle A_{\mathbf{n}} \rangle}{\mathrm{d}t} = R_A(\mathbf{n}) - \nabla \cdot J_A(\mathbf{n}), \qquad \frac{\mathrm{d}\langle B_{\mathbf{n}} \rangle}{\mathrm{d}t} = R_B(\mathbf{n}) - \nabla \cdot J_B(\mathbf{n}), \quad \ldots \tag{2.1}$$

where the rate terms $R_c(\mathbf{n})$ include gain and loss terms for species C associated with reaction, and also with adsorption and desorption if operative. Also $\nabla \cdot J_C(\mathbf{n})$ is a suggestive notation representing discrete analogue of the divergence of the C diffusion flux. Specifically, if

$J_C\left(n \rightarrow \mathbf{n}+\mathbf{d}\right)$ denotes the net diffusive flux of C from $\mathbf{n}$ to $\mathbf{n}+\mathbf{d}$, then

$$\nabla \cdot J_C\left(\mathbf{n}\right) = \sum_{\mathbf{d}\in\Omega} \left[J_C\left(\mathbf{n} \rightarrow \mathbf{n}+\mathbf{d}\right) - J_C\left(\mathbf{n}-\mathbf{d} \rightarrow \mathbf{n}\right)\right], \tag{2.2}$$

where Ω denotes a half-space of $\mathbf{d}$ values [39]. For 1D systems and hopping between nearest neighbor sites (NN), $\mathbf{n} \rightarrow n$, $\nabla \cdot J_C\left(\mathbf{n}\right) \rightarrow \nabla \cdot J_C\left(n\right)$, where $J_C\left(n\right) = J_C\left(n \rightarrow n+1\right)$ and $\nabla K_n = K_n - K_{n-1}$ is the discrete gradient or divergence.

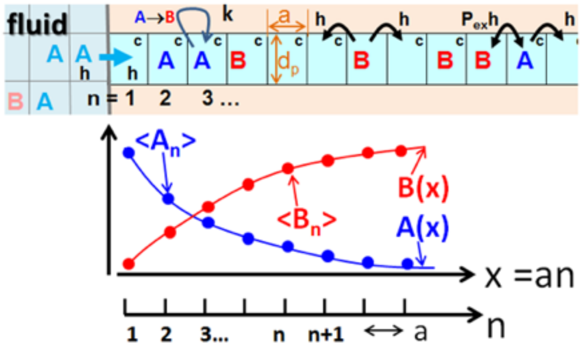

Figure 2.5: Schematic of concentration profile in a discrete reaction-diffusion $A \rightarrow B$ system in a 1D linear nanopore where $\langle A_n \rangle$ decreases and $\langle B_n \rangle$ increases into the pore.

For spatially uniform states with a single site type, $\langle A_n \rangle = \langle A \rangle$, etc., are independent of $\mathbf{n}$ and the diffusion terms vanish in equation (2.1) for these single site concentrations. For multiple site types, diffusive hopping flux terms remain as these describe mass transfer between sites of different types. If this mass transfer is rapid, then one expects local equilibration of concentrations for distinct sites.

The above apparently simple form of the discrete reaction-diffusion equations (RDE) hides much complexity, even for the spatially uniform case. Typically, neither the rate terms nor the diffusion terms are determined solely by single-site concentrations. Rather, they are generally dependent on the probabilities of multisite configurations, which cannot be simply expressed in terms of site concentrations due to the presence of spatial correlations. Thus, the above discrete RDE might be regarded as the lowest-order equations in an infinite coupled hierarchy [39,46–48]. Higher order equations describe the evolution of probabilities or correlations associated with configurations involving multiple sites. While diffusion terms are absent in the lowest-order equations for spatially uniform states in the case of a single site type, they persist in equations for probabilities of multisite configurations, thereby impacting the extent and nature of spatial correlations.

To illustrate the appearance of multisite probabilities, in the discrete RDE, consider a bimolecular reaction of A on site n with species B on a nearby site m. In the simplest case of an environment-dependent reaction rate k, the associated contribution to the reactive loss term in $K_A^{\mathrm{rxn}}(n)$ has the form

$$K_A^{\mathrm{rxn}}(\mathbf{n}|\mathbf{m}) = k\,\langle A_n B_m\rangle\,, \qquad \langle A_n B_m\rangle \equiv \text{probability of } A_n B_m \text{ pairs.} \tag{2.3}$$

This pair correlation can only be replaced by the product of site concentrations, $\langle A_n\rangle\langle B_m\rangle$, in the complete absence of correlations. In the simplest low-concentration quasi-equilibrated regime, one can write

$$\langle A_n B_m\rangle \approx \langle A_n\rangle\langle B_m\rangle \exp\left(-\beta\phi_{nm}\right) \tag{2.4}$$

for inverse temperature $\beta = 1/\left(k_B T\right)$ with interaction ϕ_{nm} between A and B, i.e., the first term in an Ursell-Mayer cluster expansion [49,50]. This expression immediately show that the effective barrier for reaction will be impacted by ϕ_{nm}. However, this is a crude approximation for higher concentrations or strong ordering, and a Kirkwood or quasi-chemical approximation might provide a more accurate expression [49,50]. There is no analogous simple formulation to account for correlations of kinetic origin.

In contrast to the above example with a single rate k, in general, rates and associated barriers are impacted by the local environment. The exact expression for the reactive loss contribution $K_A^{\mathrm{rxn}}(\mathbf{n}|\mathbf{m})$ to $R_A(\mathbf{n})$ generally involves a sum over various possible influencing environments of the reacting pair times the appropriate rates (as well as a sum over $\mathbf{m}$).

Similar complications arise in treating the net diffusive flux, $J_A(\mathbf{n}\to\mathbf{n}+\mathbf{d})$, of A, say, from $\mathbf{n}$ to $\mathbf{d}$. For diffusive hopping, one requires site $\mathbf{n}$ to be populated by A and site $\mathbf{n}+\mathbf{d}$ to be empty (E). In addition, the hop rate generally depends on the local environment of this pair of sites, with J_A involving a sum over associated configurations times the corresponding rates. It is instructive to consider the simplest case with an environment-independent hop rate, h, in both directions between pairs of sites where [39,51–53]

$$J_A(\mathbf{n}\to\mathbf{n}+\mathbf{d}) = h\left[\langle A_{\mathbf{n}} E_{\mathbf{n}+\mathbf{d}}\rangle - \langle E_{\mathbf{n}} A_{\mathbf{n}+\mathbf{d}}\rangle\right]. \tag{2.5}$$

Here $\langle A_{\mathbf{n}} E_{\mathbf{n+d}} \rangle$ is the probability that $\mathbf{n}$ is occupied by A and $\mathbf{n}+\mathbf{d}$ is empty, etc. Neglecting spatial correlations and factorizing these pair probabilities, one obtains

$$\begin{aligned} J_A(\mathbf{n} \to \mathbf{n}+\mathbf{d}) = -h\left(1 - \langle B_{\mathbf{n}} \rangle - \langle C_{\mathbf{n}} \rangle - \ldots\right)\left(\langle A_{\mathbf{n+d}} \rangle - \langle A_{\mathbf{n}} \rangle\right) - \\ h \langle A_{\mathbf{n}} \rangle \left[\left(\langle B_{\mathbf{n+d}} \rangle - \langle B_{\mathbf{n}} \rangle\right) + \langle C_{\mathbf{n+d}} \rangle - \langle C_{\mathbf{n}} \rangle + \ldots\right]. \end{aligned} \tag{2.6}$$

For 1D systems and hopping between NN sites, this reduces to [51–53]

$$J_A(n \to n+1) = -D_{AA} \nabla \langle A_{n+1} \rangle - D_{AB} \nabla \langle B_{n+1} \rangle - D_{AC} \nabla \langle C_{n+1} \rangle - \ldots; \tag{2.7}$$

where $D_{AA} = h\left(1 - \langle B_n \rangle - \langle C_n \rangle - \ldots\right)$ and $D_{AB} = D_{AC} = \ldots = h \langle A_n \rangle$, and again $\nabla K_n = K_n - K_{n-1}$. Coarse-graining to continuum formulation adds an extra factor of a^2 in these $D's$ (see Chapter 6 and Chapter 7). The form of equation (2.7) is qualitatively correct, i.e., consistent with Onsager transport theory. However, it does not provide the basis for a quantitative description of transport even for simple models without interactions [39]. This type of analysis can be extended to the case of multiple site types for each species, as indicated above, but the analysis of the diffusion coefficients is more complex.

2.2.1 Hierarchical truncation at the mean-field level

A fundamental observation from equation (2.1), or the simplified form for spatially uniform systems, do not constitute a closed set of equations in the presence of correlations but rather are just the lowest-order equations in an infinite coupled hierarchy. Higher-order equations in the hierarchy describe the evolution of various two-site, three-site, etc. configuration probabilities or correlations. Truncation of this hierarchy to obtain closed equations for a finite set of one-site, two-site, etc. probabilities generally implements a factorization approximation. The simplest mean-field (MF) site approximation neglects all spatial correlations [49, 50]. Extending this approach to a spatially heterogeneous state, one factorizes multisite probabilities as [39]

$$\langle A_{\mathbf{n}} B_{\mathbf{m}} \rangle \approx \langle A_{\mathbf{n}} \rangle \langle B_{\mathbf{m}} \rangle, \qquad \langle A_{\mathbf{n}} E_{\mathbf{n+d}} \rangle \approx \langle A_{\mathbf{n}} \rangle \langle E_{\mathbf{n+d}} \rangle, \tag{2.8}$$

and similarly for probabilities of configurations for larger number of sites. For homogeneous states, this yields the traditional mean-field rate equations of chemical kinetics.

For spatially heterogeneous states, this factorization yields a closed set of discrete RDE's for site concentrations. Spatial coupling in these $\frac{\mathrm{d}\langle C_n\rangle}{\mathrm{d}t}$ equations comes not just from the diffusion terms, since adsorption, and reaction rates, equations (2.6) and (2.7), but also from the rate terms, since adsorption, desorption, and reaction rates generally depend on concentrations at sites nearby $\mathbf{n}$. This contrasts the simpler coupling in the most commonly analyzed traditional discrete Nagumo-type RDE's [54, 55], which comes only through the diffusion terms, i.e.,

$$\frac{\mathrm{d}\left\langle A_{\mathbf{n}}\right\rangle}{\mathrm{d}t} = R_A\left(\left\langle A_{\mathbf{n}}\right\rangle, \left\langle B_{\mathbf{n}}\right\rangle, \ldots\right) + D_A \Delta \left\langle A_{\mathbf{n}}\right\rangle, \tag{2.9a}$$

$$\frac{\mathrm{d}\left\langle B_{\mathbf{n}}\right\rangle}{\mathrm{d}t} = R_B\left(\left\langle A_{\mathbf{n}}\right\rangle, \left\langle B_{\mathbf{n}}\right\rangle, \ldots\right) + D_B \Delta \left\langle A_{\mathbf{n}}\right\rangle, \ldots \tag{2.9b}$$

where Δ denotes a discrete Laplacian and D_A, D_B, etc. are constants. Indeed, even from the simple mean-field analysis of diffusion fluxes in multicomponent systems, it is clear that the diffusion flux of any species is more complicated than in the above Nagumo equations, as there is coupling to concentration gradients of other species, and also diffusion coefficients depend on concentrations. This complexity is consistent with Onsager's general theory of transport, a feature typically neglected in modeling.

2.2.2 Higher-order hierarchical truncation and conditional probabilities

Higher-order truncation approximations to the discrete hierarchical RDEs that retain some information on spatial correlations are generally needed to more accurately capture model behavior. However, the accuracy of these approaches is not guaranteed, even in simple reaction models, and they may be difficult to implement for complex realistic models. Examples of higher-order factorization schemes for 1D systems are

$$\left\langle A_n B_{n+1} C_{n+2}\right\rangle \approx \frac{\left\langle A_n B_{n+1}\right\rangle \left\langle B_{n+1} C_{n+2}\right\rangle}{\left\langle B_{n+1}\right\rangle}, \tag{2.10}$$

(pair approximation)

$$\left\langle A_n B_{n+1} C_{n+2} D_{n+3}\right\rangle \approx \frac{\left\langle A_n B_{n+1} C_{n+2}\right\rangle \left\langle B_{n+1} C_{n+2} D_{n+3}\right\rangle}{\left\langle B_{n+1} C_{n+2}\right\rangle}. \tag{2.11}$$

(triplet approximation)

Implementing the pair approximation, one factorizes the rate terms and diffusion terms in equation (2.1) in terms of single site and pair quantities. To obtain a closed set of equations, one must also add evolution equations for these pair quantities and suitably factorize the rate and diffusion terms. Similarly, implementing the triplet approximation, one must add evolution equations for both pair and triplet quantities. There are several examples where such higher-order truncation approximations have been implemented for simple spatially inhomogeneous models of reactions in 1D nanoporous systems [2–4, 33].

A useful observation is that another systematic way to formulate higher-order factorizations, and also a valuable tool to understand and quantify spatial correlations, is to introduce conditional probabilities [56, 57]. Recall the generic notation for the conditional probability of X given Y is $P\left(X|Y\right) = P\left(X \cup Y\right)/P\left(Y\right)$. Similarly, here we let the probability of A on site $\mathbf{n}$ given B on site $\mathbf{m}$ as $\langle A_{\mathbf{n}}|B_{\mathbf{m}}\rangle = \langle A_{\mathbf{n}}B_{\mathbf{m}}\rangle / \langle B_{\mathbf{m}}\rangle$, or given B on site $\mathbf{m}$ and given C on site $\mathbf{k}$ as $\langle A_{\mathbf{n}}|B_{\mathbf{m}}C_{\mathbf{k}}\rangle = \langle A_{\mathbf{n}}B_{\mathbf{m}}C_{\mathbf{k}}\rangle / \langle B_{\mathbf{m}}C_{\mathbf{k}}\rangle$, etc. Then, the above examples of higher-order factorization in 1D systems can be concisely recast as

$$\langle A_n|B_{n+1}C_{n+2}\rangle = \langle A_n|B_{n+1}\rangle \,(\text{pair}); \tag{2.12a}$$

$$\langle A_n|B_{n+1}C_{n+2}D_{n+3}\rangle = \langle A_n|B_{n+1}C_{n+2}\rangle \,(\text{triplet}), \textit{etc.} \tag{2.12b}$$

Pair or higher-order truncation can sometimes significantly improve accuracy over mean-field treatment of reaction kinetics, at least for simpler models [43–45]. However, in general these types of approximations fundamentally fail to describe diffusion fluxes. This is naturally a greater challenge since one must capture the small difference between similar quantities.

Bibliography

[1] C. Rödenbeck, J. Kärger, and K. Hahn. Exact analytical description of tracer exchange and particle conversion in single-file systems. *Phys. Rev. E*, 55:pp. 5697–5712, 1997.

[2] M. S. Okino, R. Q. Snurr, H. H. Kung, J. E. Ochs, and M. L. Mavrovouniotis. A consistent correlation approach to single file diffusion with reaction. *J. Chem. Phys.*, 111:pp. 2210–2221, 1999.

[3] S. V. Nedea, A. P. J. Jansen, J. J. Lukkien, and P. A. J. Hilbers. Steady-state properties of single-file systems with conversion. *Phys. Rev. E*, 65:066701, 2002.

[4] D. M. Ackerman, J. Wang, and J. W. Evans. Generalized hydrodynamic treatment of the interplay between restricted transport and catalytic reactions in nanoporous materials. *Phys. Rev. Lett.*, 108:228301, 2012.

[5] J. Kärger. *Handbook on heterogenous catalysis*, page p. 1714. Wiley-VCH, 2008.

[6] N. Y. Chen, J. T. F Degnan, and C. M. Smith. *Molecular transport and reaction in zeolites.* VCH, New York, 1994.

[7] G. Olhmann, H. P. Pfeifer, and G. Fricke, editors. *Catalysis and adsorption in zeolites.* Elsevier, Amsterdam, 1991.

[8] J. S. Beck, J. C. Vartulli, W. J. Roth, M. E. Leonowicz, C. T. Kresge, K. D. Schmitt, C. T. W. Chu, D.H. Olson, and E. W. Sheppard. A new family of mesoporous molecular sieves prepared with liquid crystal templates. *J. Am. Chem. Soc.*, 114:pp. 10834–10843, 1992.

[9] B. Trewin, I. I. Slowing, S. Giri, H-T. Chen, and V. S-Y. Lin. Synthesis and functionalization of a mesoporous silica nanoparticle based on the Sol-Gel process and applications in controlled release. *Acc. Chem. Res.*, 40:pp. 846–853, 2007.

[10] Z. Dongyuan, J. Feng, Q. Huo, N. Melosh, G. H. Frederickson, B. F. Chmelka, and G. D. Stucky. Triblock copolymer syntheses of mesoporous silica with periodic 50 to 30 angstrom pores. *Science*, 279:pp. 548–552, 1998.

[11] K. Kandel, S. M. Althaus, C. Peeraphatdit, T. Kobayashi, B. G. Trewyn, M. Prusky, and I. I. Slowing. Substrate inhibition in the heterogenous catalyzed aldol condensation: A mechanistic study of supported organo catalysis. *J. Catal.*, 291:pp. 63–68, 2012.

[12] B. Smit and T. L. M. Maesen. Towards a molecular understanding of shape selectivity. *Nature*, 452:pp. 671–678, 2008.

[13] K. Malek, T. H. J. Vlugt, and B. Smit. *Catalysis and materials science*, chapter 14. Wiley-VCG, Weinheim, Germany, 2009.

[14] D. S. Sholl. Understanding macroscopic diffusion of adsorbed molecules in crystalline nanoporous materials via atomistic simulations. *Acc. Chem. Res.*, 39:pp. 403–411, 2006.

[15] M. K. F. Abouelnasr and B. Smit. Diffusion in confinement: Kinetic simulations of self- and collective diffusion behavior of adsorbed gases. *Phys. Chem. Chem. Phys.*, 14:pp. 11600–11609, 2012.

[16] R. Awati, P. I. Ravikovitch, and D. S. Sholl. Efficient and accurate methods for characterizing effects of framework flexibility on molecular diffusion in zeolites: CH_4 diffusion in eight member ring zeolites. *J. Phys. Chem. C*, 117:pp. 13462–13473, 2013.

[17] D. S. Sholl and K. A. Fichthorn. Normal, single-file, and dual-mode diffusion of binary mixtures in AlPO4-5. *J. Chem. Phys.*, 107:pp. 4384–4389, 1997.

[18] D. S. Sholl. Characterizing adsorbate passage in molecular sieve pores. *Chem. Eng. J.*, 74:pp. 25–32, 1999.

[19] D. Keffer, A. V. McCormick, and H. T. Davis. Unidirectional and single-file diffusion in $AlPO4$-5: Molecular dynamics investigations. *Mol. Phys.*, 87:pp. 367–387, 1998.

[20] C-J. Wang, D. M. Ackerman, I. I. Slowing, and J. W. Evans. Langevin and Fokker-Planck analyses of inhibited molecular passing processes controlling transport and reactivity in nanoporous materials. *Phys. Rev. Lett.*, 113:038301, 2014.

[21] C. Rödenbeck, J. Kärger, and K. Hahn. Tracer exchange and catalytic reaction in single-file systems. *J. Catal.*, 157:pp. 656–664, 1995.

[22] Z. Karpinski, S. N. Gandhi, and W. M. H. Sachtler. Neopentane conversion catalyzed by Pd in L-zeolite: Effects of protons, ions and zeolite structure. *J. Catal.*, 141:pp. 337–346, 1993.

[23] R. K. Zeidan, S-J. Hwang, and M. E. Davis. Multifunctional heterogeneous catalysis: SBA-15-containing primary amines and sulfonic acids. *Angew. Chem. Int. Ed.*, 45:pp. 6332–6335, 2006.

[24] R. K. Zeidan and M. E. Davis. The effect of acid-base pairing on catalysis: An efficient acid-base functionalized catalyst for aldol condensation. *J. Catal.*, 247:pp. 379–382, 2007.

[25] I. I. Slowing, B. Trewin, and V. S-Y. Lin. Mesoporous silica nanoparticles for intracellular delivery of membrane-impermeable proteins. *J. Am. Chem. Soc.*, 129:pp. 8845–8849, 2007.

[26] I. K. Mbaraka and B. H. Shanks. Design of multifunctionalized mesoporous silica for esterification of fatty acid. *J. Catal.*, 229:pp. 365–373, 2005.

[27] J. P. Dacquin, H. E. Cross, D. B. Brown, T. Duren, J. J. Williams, A. F. Lee, and K. Wilson. Independent lateral interactions, hydrophobicity and acid strength and their influence on the catalytic activity of nanoporous sulfonic acid silicas. *Green. Chem.*, 12:pp. 1383–1391, 2010.

[28] C-H. Tsai, H-T. Chen, S. M. Althaus, K. Mao, T. Kobayashi, M. Prusky, and V. S-Y. Lin. Rational catalysis design: A multifunctional mesoporous silica catalyst for shifting the reaction equilibrium by removal of byproduct. *ACS Catal.*, 1:pp. 729–732, 2011.

[29] J. Wang, D. M. Ackerman, V. S-Y. Lin, M. Prusky, and J. W. Evans. Controlling reactivity of nanoporous catalyst materials by tuning reaction product-pore interior interactions: Statistical mechanical modeling. *J. Chem. Phys.*, 138:134705, 2013.

[30] V. S-Y. Lin, D. R. Radu, M-K. Han, W. Deng, S. Kuroki, B. H. Shanks, and M. Prusky. Oxidative polymerization of $1,4$-diethynylbenzene into highly conjugated poly(phenyle butadiynylene) within the channels of surface-functionalized mesoporous silica and alumina materials. *J. Am. Chem. Soc.*, 124:pp. 9040–9041, 2002.

[31] D-J. Liu, H-T. Chen, V. S-Y. Lin, and J. W. Evans. Polymer length distributions for catalytic polymerization within mesoporous materials: Non-Markovian behavior associated with partial extrusion. *J. Chem. Phys.*, 132:154102, 2010.

[32] D-J. Liu, J. Wang, D. M. Ackerman, I. S. Slowing, M. Prusky, H-T. Chen, V. S-Y. Lin, and J. W. Evans. Interplay between anomalous transport and catalytic reaction kinetics in single-file nanoporous systems. *ACS Catal.*, 1:pp. 751–763, 2011.

[33] J. G. Tsikoyiannis and J. Wei. Diffusion and reaction in high-occupancy zeolite catalysts-I. A stochastic theory. *J. Chem. Eng. Sci.*, 46:pp. 233–253, 1991.

[34] J. Kärger, M. Petzold, H. Pfeifer, S. Ernst, and J. Weitkamp. Single-file diffusion and reaction in zeolites. *J. Catal.*, 136:pp. 283–299, 1992.

[35] B. D. Hughes. *Random walks and random environments: Vol 1: Random walks.* Clarendon Press, Oxford, UK, 1995.

[36] A. García and J. W. Evans. Catalytic conversion in nanoporous materials: Concentration oscillations and spatial correlations due to inhibited transport and intermolecular interactions. *J. Chem. Phys.*, 45:174705, 2016.

[37] G. A. Voth, editor. *Coarse-graining of condensed phase and biomolecular systems.* CRC Press Taylor & Francis, Boca Raton, Florida, 2008.

[38] R. Kutner. Chemical diffusion in the lattice gas of non-interacting particles. *Phys. Lett. A*, 81:pp. 239–240, 1981.

[39] D-J. Liu and J. W. Evans. Realistic multisite lattice-gas modeling and KMC simulation of catalytic surface reactions: Kinetics and multiscale spatial behavior for CO-oxidation on metal (100) surfaces. *Prog. Surf. Sci.*, 83:pp. 393–521, 2013.

[40] P. Fischer and U. M. Titulaer. Kinetic phase transition in a model for surface catalysis. *Surf. Sci.*, 221:pp. 409–426, 1989.

[41] D. S. Sholl and R. T. Skodje. Kinetic phase transitions and bistability in a model surface reaction II. spatially inhomogenous theories. *Surf. Sci.*, 334:pp. 305–317, 1995.

[42] Y. De Decker, G. A. Tsekouras, A. Provata, Th. Erneux, and G. Nicolis. Propagating waves in one-dimensional discrete networks of coupled units. *Phys. Rev. E*, 69:036203, 2004.

[43] X. Guo, J. W. Evans, and D-J. Liu. Generic two-phase coexistence, relaxation kinetics, and interface propagation in the quadratic contact process: Analytic studies. *Physica A*, 387:pp. 177–201, 2008.

[44] X. Guo, Y. De Decker, and J. W. Evans. Metastability in Schloegl's second model for autocatalysis: Lattice-gas realization with particle diffusion. *Phys. Rev. E*, 82:021121, 2010.

[45] C-J. Wang, D-J. Liu, and J. W. Evans. Schloegl's second model for autocatalysis on hypercubic lattices: Dimension dependence of generic two-phase coexistence. *Phys. Rev. E*, 85:041109, 2012.

[46] J. W. Evans. Kinetic phase transitions in catalytic reaction models. *Langmuir*, 7:pp 2514–2519, 1991.

[47] N. G. van Kampen. *Stochastic processes in physics and chemistry.* Elsevier, Amsterdam, 1981.

[48] K. A. Fitchthorn and W. H. Weinberg. Theoretical foundations of dynamical Monte Carlo simulations. *J. Chem. Phys.*, 95:pp. 1090–1096, 1991.

[49] D. A. McQuarrie. *Statistical mechanics.* Harper Collin, New York, 1976.

[50] R. H. Fowler and E. A. Guggenheim. *Statistical thermodynamics.* Cambridge University Press, Cambridge, UK, 1986.

[51] M. Tammaro and J. W. Evans. Chemical diffusivity and wave propagation in surface reactions: Lattice-gas model mimicking $CO-$oxidation with high $CO-$mobility. *J. Chem. Phys.*, 108:pp. 762–764, 1998.

[52] M. Tammaro, M. Sabella, and J. W. Evans. Hybrid treatment of spatiotemporal behavior in surface reactions with coexisting immobile and highly mobile reactant. *J. Chem. Phys.*, 103:pp. 10277–10285, 1995.

[53] V. P. Zhdanov. General equations for description of surface diffusion in the framework of the lattice-gas model. *Surf. Sci. Lett.*, 149:pp. L13–L17, 1985.

[54] J. P. Keener. Propagation and its failure in coupled systems of discrete excitable cells. *SIAM J. Appl. Math*, 47:pp. 556–572, 1987.

[55] S-N. Chow, J. Mallet-Paret, and E. S. Van Vleck. Dynamics of lattice differential equations. *Int. J. Bifurcation Chaos*, 6:pp. 1605–1621, 1996.

[56] C. Preston. *Random fields.* Springer Lecture Notes in Mathematics, Springer, Berlin, 1976.

[57] J. W. Evans. Random and cooperative sequential adsorption. *Rev. Mod. Phys.*, 65:pp. 1281–1329, 1993.

CHAPTER 3. CATALYTIC CONVERSION REACTIONS IN NANOPOROUS SYSTEMS WITH CONCENTRATION-DEPENDENT SELECTIVITY: STATISTICAL MECHANICAL MODELING

A paper published in *Physical Review E*

Andrés García[1,2], Jing Wang[1,3,*], Theresa L. Windus[1,4], Aaron D. Sadow[1,4],
and James W. Evans[1,2,3]

[1]*Ames Laboratory-USDOE, Iowa State University, Ames, Iowa 50011, USA*
[2]*Department of Physics and Astronomy, Iowa State University, Ames, Iowa 50011, USA*
[3]*Department of Mathematics, Iowa State University, Ames, Iowa 50011, USA*
[4]*Department of Chemistry, Iowa State University, Ames, Iowa 50011, USA*

(Received 26 January 2016; published 20 May 2016)

Abstract

Statistical mechanical modeling is developed to describe a catalytic conversion reaction $A \rightarrow B_c$ or B_t with concentration-dependent selectivity of the products, B_c or B_t, where reaction occurs inside catalytic particles traversed by narrow linear nanopores. The associated restricted diffusive transport, which in the extreme case is described by single-file diffusion, naturally induces strong concentration gradients. Furthermore, by comparing kinetic Monte Carlo simulation results with analytic treatments, selectivity is shown to be impacted by strong spatial correlations induced by restricted diffusivity in the presence of reaction and also by a subtle clustering of reactants, A. DOI: 10.1103/PhysRevE.93.052137

---

[*] Current address: American Institute for Research, 1000 Thomas Jefferson St. NW, Washington, DC 20007, USA.

3.1 Introduction

Molecular-level non-equilibrium statistical mechanical modeling has the potential to provide a reliable description of cooperative catalytic reaction-diffusion phenomena where traditional mean-field (MF) treatments of chemical kinetics are inadequate [1, 2]. The focus of this paper is on providing such a treatment of catalytic systems with two distinctive features. The *first* involves solution-phase first-order $A \to B$ conversion reactions occurring in catalytically functionalized particles traversed by narrow linear nanopores which result in restricted diffusive transport [3–11]. The extreme case of restricted transport, on which we place some emphasis here, is single-file diffusion (SFD) [12–14] wherein reactant and product species cannot pass each other within the linear nanopores. Then the interplay between reaction and SFD produces rapidly varying concentration profiles near the pore openings (where the reactant is supplied from the surrounding fluid), and strong spatial correlations in reactant locations. The latter are neglected in MF treatments. The *second* phenomenon involves reactions with concentration-dependent selectivity, and specifically stereoselectivity where the product B can have distinct cis (B^c) and trans (B^t) forms [15]. Here, the selection of the B^c or B^t product is controlled by the concentration of the reactant, A. More precisely, in a molecular-level picture, the rate for conversion of A to B^c or B^t depends on the number and local arrangement of other nearby A species. This, in turn, means that the selectivity, i.e., the relative yield of each of these products, depends on spatial correlations in the reactant distribution.

Characteristic indicators of SFD in catalytic mesoporous systems were observed long ago for certain classes of zeolites with uncoupled narrow linear pores [16, 17]. It should, however, also be noted that in samples with linear dimensions of tens of microns, these uncoupled pores may not traverse the entire sample [18]. A primary motivation for our study is a catalytic processes in functionalized mesoporous silica nanoparticles (MSNs) with diameters of around $100-200\,\mathrm{nm}$ where hexagonal arrays of parallel uncoupled linear nanopores do traverse the entire nanoparticle [19]. While synthesis with a range of pore diameters is possible, the broadest of which certainly allows uninhibited transport, recent studies for narrow pores did reveal behavior indicative of SFD [2, 20].

There has been extensive characterization of spatial correlations of thermodynamic origin associated with intermolecular interactions in equilibrium systems. However, understanding of spatial correlations of kinetic origin in the non-equilibrium steady states of reaction-diffusion systems is limited [1,2]. Nonetheless, it is precisely the characterization of such non-equilibrium correlations which is required for reliable prediction of selectivity and other features of concentration dependent stereoselective reactions in nanoporous systems. Given the fundamental nature of this challenge, it is addressed here with somewhat simplified statistical mechanical models, as described in detail below. We note that over the last two decades a substantial body of analysis based on such models has been performed for conversion reactions in nanoporous systems (usually zeolites) with simple concentration-independent first-order kinetics [3–11]. One can straightforwardly extend this type of modeling to incorporate cooperative concentration-dependent kinetics, but it will prove a significant challenge to provide a reliable analytic treatment.

Our focus is on such simplified and generic modeling. However, here we first provide some brief comments for broader background and motivation regarding the type of systems falling into the above class and also on theoretical methodologies with the potential to provide a first principles characterization of reaction kinetics. With regard to concentration-dependent selectivity, homogeneous catalytic desymmetrization of diallylamines to give diastereomers (using a Zr-centered catalyst) exhibits a quite strong variation with reactant concentration of cis to trans selectivity [15]. Specifically, the yield of trans relative to cis product increases with reactant concentration. These studies are part of a broader analysis of stereoselectivity in Zr catalyzed reactions [15, 21]. To develop a heterogeneous version of this process, one might anticipate functionalizing the interior pore surfaces of MSN with an appropriate Zr-centered catalytic group. The effective diameter of the pores after functionalization can be reduced to the range of $d \sim 1 - 2\,\mathrm{nm}$ where passing of molecular species within the pore can be strongly inhibited. While such functionalization remains a significant challenge, substantial progress has been made recently [22].

Next, we remark that electronic structure analysis could provide a detailed theoretical assessment of the origin and nature of concentration-dependent selectivity. More specifically, such analysis should ideally elucidate variations in reaction barriers and possibly also pathways with the local environment of the reacting "substrate" molecule A. This is a significant challenge even for homogeneous catalytic systems, but one might anticipate that the basic features are preserved for heterogeneous catalytic analogues. Given the typical complexity and size of the catalytic group, and the requirement to incorporate multiple reactant molecules, it is natural to utilize computationally less expensive density functional theory (DFT) to facilitate such an analysis rather than higher-level quantum chemistry approaches. Indeed, this type of analysis has been performed for systems similar to that described above and has demonstrated that certain barriers can indeed be lowered by increasing the number of reactant molecules [23]. Current analysis has not included solvent effects, but this could be done explicitly or using implicit solvent approaches such as COSMO [24] or PCM [25]. It is also appropriate to note that once geometries along the reaction path have been determined by DFT, higher-level analyses such as MP2 and CCSD can be implemented utilizing those geometries to assess corrections to the energetics. In one case, the MP2 calculations yielded similar energetics to the DFT analysis [23].

Returning to statistical mechanical modeling, we briefly review an effective strategy utilized in previous studies to describe solution-phase catalytic conversion reactions with restricted transport within catalytically functionalized linear nanopores. Direct molecular or Langevin dynamics simulation [26–28] is not viable to describe the overall reaction-diffusion process on the appropriate time scale (i.e., reactants entering, diffusing within, reacting, and products diffusing within and being extruded from the pore, with dynamics generally mediated by the presence of a solvent). Thus, instead spatially discrete coarse-grained stochastic modeling is typically implemented [3–11]. In this approach, each pore is divided into a linear array of cells each with width $a \sim 1\,\mathrm{nm}$ comparable to that of the reactant and product species. Then solvent-mediated diffusion is described by hopping to adjacent empty cells. Refinements can be made to relax the SFD constraint. Adsorption and desorption from the pore are reflected in appropriate boundary conditions at the pore openings. A conversion reaction will be analyzed here with rates which reflect the local environment of the cell where reaction is occurring. The behavior of the stochastic one-dimensional lattice-gas model is precisely assessed by kinetic

Monte Carlo (KMC) simulation [2]. However, for a deeper understanding, one can develop exact master equations for the model. Although these cannot be solved exactly, and standard mean- field type treatments are inadequate, effective analytic treatments such as a generalized hydrodynamic (GH) approximation [10] might be developed to elucidate behavior.

In Section 3.2 we develop a spatially discrete stochastic model for catalytic conversion $A \rightarrow B^c$ or B^t in nanopores with restricted transport, present the exact evolution equations, and comment on an effective analytic treatment of diffusion. Section 3.3 provides a characterization of the key spatial correlations in the steady state of the non-equilibrium reaction-diffusion system, focusing on the reactant distribution and elucidating the strong correlations which impact the diffusion fluxes. In Section 3.4, we present an analysis of model behavior, specifically describing nontrivial concentration profiles in the steady state and elucidating the key features impacting the selectivity. Conclusions are provided in Section 3.5.

3.2 Model Specification and Evolution Equations

3.2.1 Specification of the spatially discrete stochastic model

Spatially discrete modeling describes catalytically functionalized nanoporous particles, such as MSN, by an ensemble of linear pores each consisting of a 1D array of L cells, labeled $n = 1{-}L$, each of width $a \sim 1\,\mathrm{nm}$ [3–11]. In our treatment, all cells are regarded as catalytically active. It is convenient to consider these 1D arrays as being extended to a 3D array of cells in the exterior fluid surrounding the catalytic particles as this facilitates specification of adsorption and desorption processes at the pore ends. The exterior fluid supplies reactant, A, to the pores, and we consider here only the initial stage of the reaction where a negligible fraction of the reactant in the external fluid has been converted to product. We consider the conversion reaction $A \rightarrow B^c$ or B^t occurring exclusively inside the pores, as indicated above, and let E denote empty cells. It will also be useful to let $B = B^c + B^t$ denote either product, $X = A + B$ denote any type of species, and $Z = B + E$ denote cells not populated by A. Also if $C = A$, B^c, or B^t , then we will let C' denote other molecular species, e.g., if $C = A$ then $C' = B$.

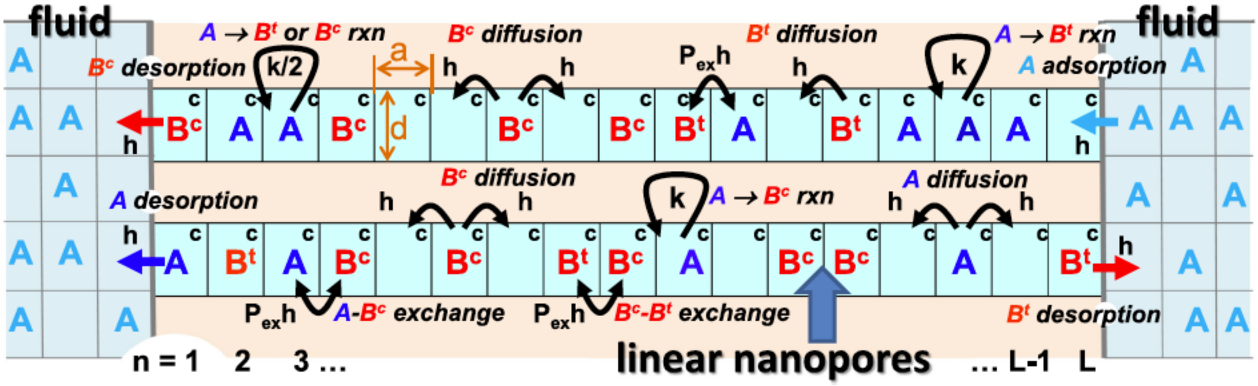

Figure 3.1: Schematic of spatially discrete stochastic reaction model for concentration-dependent conversion reaction $A \rightarrow B^c$ or B^t in catalytically functionalized linear nanopores described by a 1D array of cells.

The probability that site n is occupied by some species C, corresponding to a concentration at site n, is denoted by $\langle C_n \rangle$, where $0 \leq \langle C_n \rangle \leq 1$. Similarly, the pair probability that site n is occupied by C and $n+1$ by D is denoted by $\langle C_n D_{n+1} \rangle$, etc. The "well-stirred" exterior fluid has a large volume compared to the intrapore region. For the initial stages of the reaction under consideration, we specify that a fixed fraction, $\langle A_0 \rangle = \langle X_0 \rangle$ of cells in the exterior fluid are randomly populated by reactant A. Thus, the fraction of exterior empty cells is given by $\langle E_0 \rangle = 1 - \langle X_0 \rangle$. As an aside, one can regard efficient stirring of the exterior fluid as corresponding to very rapid hopping of A between adjacent exterior cells.

The key ingredients of our stochastic model for the catalytic reaction-diffusion process, shown schematically in Figure 3.1, are as follows:

(i) Reactants A "adsorb" at rate h from the fluid cell just outside the pore to empty end cells $n = 1$ and $n = L$. Thus, the overall rate to adsorb, e.g., at the left end of the pore is $h \langle A_0 \rangle \langle E_1 \rangle$ accounting for the feature there is no correlation between the occupancy of the exterior and interior cells.

(ii) Reactants A hop at rate h to nearest-neighbor (NN) empty cells within the pore.

(iii) Reactants A convert to products B^c or B^t with rates depending on the local environment, specifically the state of the neighboring cells, as prescribed below.

(iv) Both types of product also hop at rate h to NN empty sites within the pore.

(v) Reactants and products "desorb" by hopping from end cells at rate h to NN empty cells in the surrounding fluid. Thus, e.g., the overall rate for A to desorb from the left end of the pore is $h \langle A_1 \rangle \langle E_0 \rangle$.

(vi) One can relax the SFD constraint implicit in the above prescription of hopping by simply allowing exchange of adjacent (NN) species within the pore with rate $P_{\text{ex}}h$. Of key impact is exchange of reactants and products. Selecting $P_{\text{ex}} = 0$ recovers SFD (for narrow pores), and setting $P_{\text{ex}} = 1$ corresponds to uninhibited passing (for wide pores).

It is appropriate to note that since we focus on the initial stage of the reaction, the extruded product is extremely diluted in the well-stirred fluid and does not readsorb. Also, we remark that the assignment of equal hop rates is natural for cis and trans products, and this is also reasonable for reactants for the type of reaction mentioned in Section 3.1 which motivates this study.

Our primary aim of incorporating concentration-dependent selectivity, or more precisely environment-dependent selectivity, is achieved by specifying that the rate for conversion of A at cell n depends on the state of neighboring cells as follows:

$$A_{n-1}A_nA_{n+1} \rightarrow A_{n-1}B_n^tA_{n+1} \quad \text{at rate } k, \tag{3.1a}$$

$$A_{n-1}A_nZ_{n+1} \rightarrow A_{n-1}B_n^cZ_{n+1} \quad \text{or} \quad A_{n-1}B_n^tZ_{n+1} \quad \text{each at rate } k/2, \tag{3.1b}$$

$$Z_{n-1}A_nA_{n+1} \rightarrow Z_{n-1}B_n^cA_{n+1} \quad \text{or} \quad Z_{n-1}B_n^tA_{n+1} \quad \text{each at rate } k/2, \tag{3.1c}$$

$$\text{and } Z_{n-1}A_nZ_{n+1} \rightarrow Z_{n-1}B_n^cZ_{n+1} \quad \text{at rate } k, \tag{3.1d}$$

where again Z means *not* A. Using exact "conservation of probability" relations, the above prescription implies that the rate of loss by reaction of A at site n equals $R_n(A) = -k\langle A_n \rangle$. Likewise, the rates of gain by reaction of specific products at site n are given by:

$$R_n\left(B^t\right) = \frac{1}{2}k\left(\langle A_nA_{n+1}\rangle + \langle A_{n-1}A_n\rangle\right) \quad \text{and} \quad R_n\left(B^c\right) = \frac{1}{2}k\left(\langle A_nZ_{n+1}\rangle + \langle Z_{n-1}A_n\rangle\right), \tag{3.2}$$

where $R_n(B^c)$ can be rewritten using $\langle A_nZ_{n+1}\rangle = \langle A_n\rangle - \langle A_nA_{n+1}\rangle$, etc. Clearly, the overall gain products satisfies $R_n(B) = R_n(B^c) + R_n\left(B^t\right) = -R_n(A)$.

This model has the following special features. Ignoring the distinction between B^c and B^t, the model reduces exactly to a simple concentration-independent conversion model $A \to B$ with rate k for all cells. Thus, the concentration profile for A (which decays quickly into the pore), and all spatial correlations in the location of A species in the full $A \to B^c$ or B^t model, are determined by this simpler $A \to B$ model. If one does not distinguish A and B, then the model reduces to a simple nonreactive diffusion model for a single species X. Thus, the steady state corresponds to a random distribution of X in cells within the pore with uniform concentration, $\langle X_n \rangle = \langle X_0 \rangle$. A corollary of this observation is that empty cells are also distributed randomly in the steady state with uniform concentration $\langle E_n \rangle = 1 - \langle X_0 \rangle = \langle E_0 \rangle$.

Finally, we note that the above modeling can be refined or extended in various ways. For example, the SFD constraint could instead be relaxed by modeling pores as consisting of multiple parallel rows of cells [2] (rather than by including place exchange for pores with a single row of cells). Also, rather than just considering the initial stages of reaction where a negligible fraction of reactant in the fluid is converted to product, one can also assess reactivity for various degrees, f, of conversion of reactant to products. Here one exploits an assumed separation-of-time-scales feature that a quasi-steady state within pores will be quickly achieved for each f relative to the time scale for conversion of most reactant to product in the fluid. Thus, from an analysis of reactivity for a series of f values, one can piece together overall reaction kinetics [11].

3.2.2 KMC simulation and master equation analysis

Precise analysis of model behavior will be achieved by kinetic Monte Carlo (KMC) simulations, some details of which are described in Section 3.7. However, potentially deeper insight comes from an analytic treatment based on exact evolution equations for the $A \to B^c$ or B^t model, which can be written in compact form:

$$\mathrm{d}/\mathrm{d}t \, \langle C_n \rangle = R_n(C) - \nabla_n J_C(n > n+1), \quad \text{for } 1 < n < L \text{ with } C = A, B^c, \text{ or } B^t. \tag{3.3}$$

Here $\nabla_n K_n = K_n - K_{n-1}$ denotes a discrete gradient, and the net diffusion flux, $J_C\left(n > n+1\right)$, of C from cell n to cell $n+1$ satisfies [10]

$$J_C\left(n > n+1\right) = h\left(\langle C_n E_{n+1}\rangle - \langle E_n C_{n+1}\rangle\right) + P_{\mathrm{ex}} h\left(\left\langle C_n C'_{n+1}\right\rangle - \left\langle C'_n C_{n+1}\right\rangle\right). \tag{3.4}$$

Separate equations are needed for end cells which reflect the feature that the cell just outside the pore is randomly populated by A with probability $\langle X_0\rangle$. Thus, pair probabilities involving the end cell and the adjacent exterior cell factorize as a product of single-cell probabilities, e.g., $\mathrm{d}/\mathrm{d}t\,\langle A_1\rangle = R_1\left(A\right) - J_A\left(1 > 2\right) + h\left(\langle A_0\rangle\langle E_1\rangle - \langle E_0\rangle\langle A_1\rangle\right)$.

All these equations couple single-cell probabilities to pair probabilities. One can develop separate equations for pair probabilities [2], e.g.,

$$\begin{aligned}\mathrm{d}/\mathrm{d}t\,\langle A_n A_{n+1}\rangle = &-2k\,\langle A_n A_{n+1}\rangle - h\left(\langle A_n A_{n+1} E_{n+2}\rangle - \langle A_n E_{n+1} A_{n+2}\rangle\right)\\ &+ h\left(\langle A_{n-1} E_n A_{n+1}\rangle - \langle E_{n-1} A_n A_{n+1}\rangle\right)\\ &- P_{\mathrm{ex}} h\left(\left\langle A_n A_{n+1} A'_{n+2}\right\rangle - \left\langle A_n A'_{n+1} A_{n+2}\right\rangle\right)\\ &+ P_{\mathrm{ex}} h\left(\left\langle A_{n-1} A'_n A_{n+1}\right\rangle - \left\langle A'_{n-1} A_n A_{n+1}\right\rangle\right),\end{aligned} \tag{3.5}$$

for $1 < n < L-1$ which couple to triplet probabilities. Continuing to develop equations for triplets, etc., generates a hierarchy of evolution equations.

The simplest mean-field (MF) treatment completely neglects spatial correlations by factorizing all multicell probabilities as products of single-cell quantities. However, for the $A \to B$ conversion reaction, this MF treatment has been shown to greatly overestimate the magnitude of the diffusion flux terms, $J_C\left(n > n+1\right)$, for SFD, and thus overestimates reactant penetration into the pore and reactivity in the steady state for $k << h$ [9, 10]. This is perhaps not surprising as it is well recognized that there are strong back correlations in hop sequences associated with SFD [14]. Of course, the MF treatment also neglects correlations determining $\langle A_n A_{n+1}\rangle$ pair probabilities which will be important for accurate description of reaction kinetics. The pair approximation sets $\langle C_n D_{n+1} F_{n+2}\rangle \approx \langle C_n D_{n+1}\rangle\langle D_{n+1} F_{n+2}\rangle / \langle D_{n+1}\rangle$ attempting to account for spatial correlations, and requires simultaneous analysis of equations for both single-cell and pair probabilities. This yields somewhat improved results, but still significantly overestimates fluxes for $k << h$, as do higher-order triplet, etc., approximations [10].

The deficiency of MF-type approximations in describing diffusion fluxes has been remedied by implementing a generalized hydrodynamic (GH) treatment [10] of diffusion for the relevant counter-diffusion modes [29] where the total concentration $\langle X_n \rangle = \langle X_0 \rangle$ is constant. Here we start with a hydrodynamic expression for diffusion fluxes $J_C\,(n > n+1) = -D_{tr} \nabla_n \langle C_{n+1} \rangle$ which is applicable for counter diffusion and involves a tracer diffusion coefficient, D_{tr} [2, 10, 29–31]. Then, we replace the hydrodynamic D_{tr}, which equals zero for SFD in an infinite pore, by a GH form $D_{tr}\,(n, n+1) = h\, F_{tr}\,(n, n+1)$. This GH form has a finite value $O\,(1/L)$ in the pore center and is enhanced near the pore openings [10]. Then the diffusion flux is given in this GH formulation by

$$J_C\,(n > n+1) \approx -hF_{tr}\,(n, n+1)\, \nabla_n \langle C_{n+1} \rangle\,. \tag{3.6}$$

As described in detail elsewhere [2, 10, 29], $F_{\mathrm{tr}}\,(n, n+1)$ are determined either from the form of concentration profiles for a counter-permeation setup, or by suitable analysis of tagged particle diffusion with various starting locations. Illustrative values for $F_{\mathrm{tr}}\,(n, n+1)$ will be given below. This analysis produces a diffusion flux which is far smaller in magnitude than the MF prediction for SFD. Additional perspective on this feature comes from the observation that the MF value of F_{tr} is given by

$$F_{tr}\,(\mathrm{MF}) = \langle E_0 \rangle + P_{\mathrm{ex}} \langle X_0 \rangle\,. \tag{3.7}$$

See Section 3.8. For SFD with $P_{\mathrm{ex}} = 0$, we will find that $F_{tr}\,(n, n+1)$ is well below $F_{tr}\,(\mathrm{MF}) = \langle E_0 \rangle$. We discuss further the implications of the success of the GH treatment in Section 3.3.

The regime where spatial correlations are strongest and where analytic treatment most challenging is for $P_{\mathrm{ex}} = 0$ (SFD) with higher values of $\langle X_0 \rangle$ and $k << h$. Higher $\langle X_0 \rangle$ amplifies the constraints of SFD, and $k << h$ produces substantial reactant penetration to the pore so the form of the concentration profile impacted strongly by SFD. Thus, our discussion will particularly emphasize the case $P_{\mathrm{ex}} = 0$, $\langle X_0 \rangle = 0.8$, and $k/h = 0.001$, choosing a pore length $L = 100$. Spatial correlations are reduced upon allowing exchange or reducing $\langle X_0 \rangle$, so any treatment which is effective for $P_{\mathrm{ex}} = 0$ and high $\langle X_0 \rangle$ will be even more accurate for $P_{\mathrm{ex}} > 0$ and lower $\langle X_0 \rangle$. We will also consider behavior for $\langle X_0 \rangle = 0.2$ and $P_{\mathrm{ex}} = 0.25$ confirming this

Table 3.1: $F_{tr}(n, n+1)$ versus n near the end of a pore with $L = 100$ for different values of total concentration $\langle X_0 \rangle$ and for SFD ($P_{\text{ex}} = 0$) as well as with exchange ($P_{\text{ex}} = 0.25$). Decay into the pore (increasing n) is strong for SFD and weak with exchange. MF values, $F_{tr}(\text{MF}) = 1 - (1 - P_{\text{ex}}) \langle X_0 \rangle$ are shown in the bottom row. $F_{tr}(n, n+1)$ is closest to $F_{tr}(\text{MF})$ for low $\langle X_0 \rangle$ and $P_{\text{ex}} > 0$, and furthest below $F_{tr}(\text{MF})$ for high $\langle X_0 \rangle$ and $P_{\text{ex}} = 0$.

$F_{tr}(n, n+1)$	$\langle X_0 \rangle = 0.20, P_{\text{ex}} = 0.00$	$\langle X_0 \rangle = 0.20, P_{\text{ex}} = 0.25$	$\langle X_0 \rangle = 0.80, P_{\text{ex}} = 0.00$	$\langle X_0 \rangle = 0.80, P_{\text{ex}} = 0.25$
$n = 1$	0.59353	0.76127	0.05463	0.32147
$n = 2$	0.43812	0.71861	0.02302	0.31004
$n = 3$	0.35470	0.69915	0.01295	0.30757
$n = 4$	0.27708	0.68507	0.00865	0.30522
$n = 5$	0.23021	0.69082	0.00627	0.30112
$n = 6$	0.19527	0.66456	0.00494	0.30126
$n = 7$	0.16801	0.66701	0.00411	0.29957
$n = 8$	0.15003	0.66144	0.00358	0.29984
$n = 9$	0.13627	0.66434	0.00327	0.29802
$n = 10$	0.12136	0.65699	0.00304	0.29793
$n = 11$	0.10895	0.65478	0.00286	0.29734
$n = 12$	0.09805	0.64189	0.00274	0.29869
$n = 13$	0.09060	0.64692	0.00265	0.29780
$n = 14$	0.08285	0.64900	0.00260	0.29823
$n = 15$	0.07682	0.64390	0.00255	0.29618
$F_{tr}(\text{MF})$	0.80	0.85	0.20	0.40

feature. Likewise, for larger k, significant reactant concentration is limited to near pore openings where correlations are weaker, and thus lower-level approximations are more effective [2].

Our most successful analytic treatment, described as an "extended GH" or eGH approach, will incorporate a GH treatment of diffusion fluxes with a tailored treatment of spatial correlations in the pair quantities $\langle A_n A_{n+1} \rangle$, which control the reaction kinetics $R_n(C)$. See Section 3.3 for details of the latter.

3.3 Spatial Correlations in the Reactive Steady State

3.3.1 Correlations related to diffusion fluxes

The dramatic failure of the MF treatment of diffusion fluxes for SFD, which is reflected in the inequality $F_{tr}(n, n+1) << F_{tr}(\text{MF}) = \langle E_0 \rangle$, implies strong spatial correlations between the location of cells which are empty and those which are populated by reactants, A, within

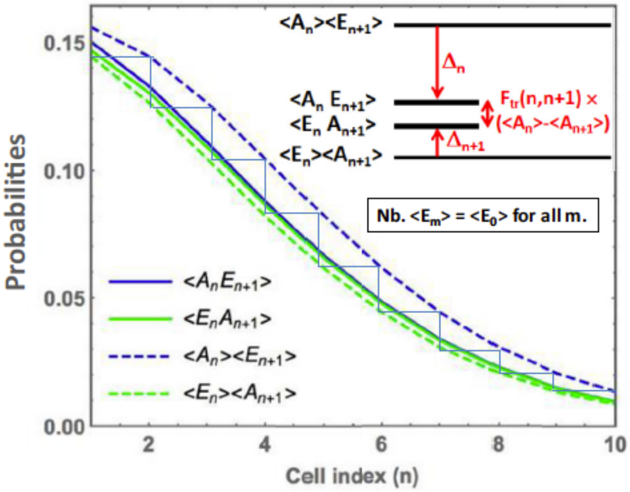

Figure 3.2: KMC results for behavior of $\langle A_n E_{n+1}\rangle$ and $\langle E_n A_{n+1}\rangle$ (solid curves) relative to their MF approximations (dashed curves) versus n near the left end of a pore with $L = 100$, $\langle X_0\rangle = 0.8$ (so $\langle E_0\rangle = 0.2$), $k/h = 0.001$, and $P_{\text{ex}} = 0$ (SFD). Since $\langle E_n\rangle = \langle E_0\rangle$, both MF approximations are determined solely by the variation of $\langle A_n\rangle$ with n (as reflected in the "staircase" construction connecting dashed curves).

the pore. This behavior is quantified by the GH formulation (3.6) which shows that

$$\langle A_n E_{n+1}\rangle - \langle E_n A_{n+1}\rangle \approx F_{tr}\left(n, n+1\right)\left(\langle A_n\rangle - \langle A_{n+1}\rangle\right) << \langle E_0\rangle\left(\langle A_n\rangle - \langle A_{n+1}\rangle\right), \tag{3.8}$$

where these quantities are positive near the left end of the pore, and where illustrative values for $F_{tr}\left(n, n+1\right)$ are given in Table 3.1. Thus, as is shown in Figure 3.2 for SFD with $\langle X_0\rangle = 0.8$ and $k/h = 0.001$, $\langle A_n E_{n+1}\rangle$ and $\langle E_n A_{n+1}\rangle$ are much closer to each other than the MF predictions. (The large difference between the MF estimates reflects a strong variation in $\langle A_n\rangle$ near the pore opening, noting that $\langle E_n\rangle = E_0$ is constant.) The similarity of $\langle A_n E_{n+1}\rangle$ and $\langle E_n A_{n+1}\rangle$ is readily understood as a consequence of the restricted dynamics associated with SFD. Consider the pair probability $\langle A_n E_{n+1}\rangle$. Since cell $n + 1$ is empty, A on cell n can readily hop to cell $n + 1$ and will then quite likely hop back to cell n (which is guaranteed to be empty immediately after A hopping). This results in a "near-equalization" of the probabilities $\langle A_n E_{n+1}\rangle$ and $\langle E_n A_{n+1}\rangle$. This idea naturally extends to triplets $\langle A_n E_{n+1} E_{n+2}\rangle$, $\langle E_n A_{n+1} E_{n+2}\rangle$ and $\langle E_n E_{n+1} A_{n+2}\rangle$ which are much closer to each other than the MF values, and also extends to associated quartets, quintets, etc.

The GH formulation only quantifies the difference between the pair probabilities as indicated in (3.8). However, it will be useful to also have reliable estimates of the individual probabilities $\langle A_n E_{n+1} \rangle$ and $\langle E_n A_{n+1} \rangle$. To this end, we introduce an extended GH or eGH approximation as follows. First, we note the anticipated inequality

$$\langle A_n \rangle \langle E_0 \rangle = \langle A_n \rangle \langle E_{n+1} \rangle > \langle A_n E_{n+1} \rangle > \langle E_n A_{n+1} \rangle > \langle E_n \rangle \langle A_{n+1} \rangle = \langle E_0 \rangle \langle A_{n+1} \rangle , \tag{3.9}$$

for the left end of the pore (smaller n) which is confirmed by the results in Figure 3.2. One approach to assess $\langle A_n E_{n+1} \rangle$ and $\langle E_n A_{n+1} \rangle$ accounts for a "strong asymmetry" in the behavior of these quantities relative to MF predictions in that both are much closer to $\langle E_n \rangle \langle A_{n+1} \rangle$ than to $\langle A_n \rangle \langle E_{n+1} \rangle$ for SFD with high $\langle X_0 \rangle$ (or low $\langle E_0 \rangle$) [32]. In the notation of the inset to Figure 3.2, this suggests setting $\Delta_{n+1} = 0$ which immediately yields a fully asymmetric eGH formulation eGH(f):

$$\langle A_n E_{n+1} \rangle_{\text{eGH}(f)} = \langle E_0 \rangle \langle A_{n+1} \rangle + F_{tr} (n, n+1) \left(\langle A_n \rangle - \langle A_{n+1} \rangle \right) \quad \text{and} \tag{3.10a}$$

$$\langle E_n A_{n+1} \rangle_{\text{eGH}(f)} = \langle E_0 \rangle \langle A_{n+1} \rangle \tag{3.10b}$$

A less extreme but still asymmetric eGH formulation, eGH(a), anticipates weaker asymmetry upon relaxing the SFD constraint or for lower $\langle X_0 \rangle$. We have confirmed this trend (not shown). In this case, we assume that deviations of pair probabilities from the MF results are proportional to the relevant A concentration, i.e., one assumes that $\Delta_n \propto \langle A_n \rangle$ and $\Delta_{n+1} \propto \langle A_{n+1} \rangle$ Figure 3.2. This formulation yields

$$\langle A_n E_{n+1} \rangle_{\text{eGH}(a)} = \frac{2 \langle A_n \rangle \langle A_{n+1} \rangle \langle E_0 \rangle}{\left(\langle A_n \rangle + \langle A_{n+1} \rangle \right)} + \frac{F_{tr} (n, n+1) \langle A_n \rangle \left(\langle A_n \rangle - \langle A_{n+1} \rangle \right)}{\left(\langle A_n \rangle + \langle A_{n+1} \rangle \right)} \quad \text{and} \tag{3.11a}$$

$$\langle E_n A_{n+1} \rangle_{\text{eGH}(a)} = \frac{2 \langle A_n \rangle \langle A_{n+1} \rangle \langle E_0 \rangle}{\left(\langle A_n \rangle + \langle A_{n+1} \rangle \right)} - \frac{F_{tr} (n, n+1) \langle A_{n+1} \rangle \left(\langle A_n \rangle - \langle A_{n+1} \rangle \right)}{\left(\langle A_n \rangle + \langle A_{n+1} \rangle \right)} \tag{3.11b}$$

We note that for our application, results using (3.10) or (3.11), or even an alternative symmetric eGH formulation, eGH(s), where $\Delta_n = \Delta_{n+1}$ [33], are all much closer to precise model behavior determined by KMC simulation than the MF approximation.

3.3.2 Correlations impacting reaction kinetics

Next, we discuss analysis of the pair probabilities, $\langle A_n A_{n+1} \rangle$, which is necessary to describe the reaction kinetics, $R_n (C)$, in the evolution equations (3.3). The simplest treatment of

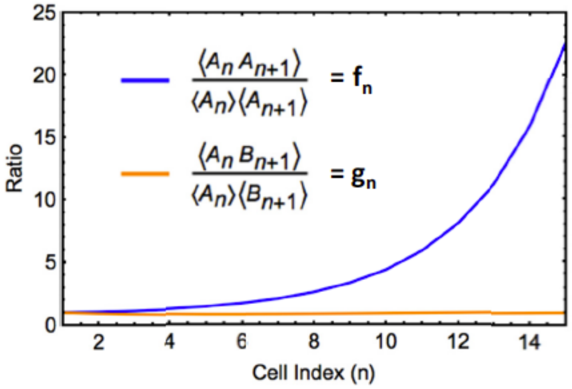

Figure 3.3: KMC results for $f_n = \langle A_n A_{n+1}\rangle / (\langle A_n\rangle \langle A_{n+1}\rangle)$, $g_n = \langle A_n B_{n+1}\rangle / (\langle A_n\rangle \langle B_{n+1}\rangle)$, versus n near the left end of a pore with $L = 100$, $\langle X_0\rangle = 0.8$, $k/h = 0.001$, and $P_{\text{ex}} = 0$ (SFD). Deviations from unity reflect the strength of the associated NN spatial correlations.

reaction kinetics would simply apply a MF approximation $\langle A_n A_{n+1}\rangle \approx \langle A_n\rangle \langle A_{n+1}\rangle$. A simple hybrid approach might combine this MF treatment of reaction kinetics with a GH treatment of diffusion fluxes. A more refined approach would involve analysis of the evolution Eqs. (3.5) for $\langle A_n A_{n+1}\rangle$. This, in turn, requires analysis of the associated pair diffusion terms which involve quantities like $\langle A_n A_{n+1} E_{n+2}\rangle$, $\langle A_n E_{n+1} A_{n+2}\rangle$ and $\langle E_n A_{n+1} A_{n+2}\rangle$. The same argument as used above for pair probabilities and, as quantified in (3.8), suggests that these quantities will be much closer to each other than their MF estimates. Not only is this correct, but more sophisticated factorization approximations also fail to capture the key differences in these quantities. The reason for failure of such higher-order approximations is briefly discussed in Section 3.9. Another relevant observation is that unlike the conventional diffusion flux terms appearing in the evolution equation for $\langle A_n\rangle$, one cannot readily adapt a hydrodynamic transport theory to reliably treat the unconventional pair diffusion flux terms appearing in the evolution equation for $\langle A_n A_{n+1}\rangle$. We will find that various treatments of the reaction kinetics of the above type produce qualitatively reasonable, but not quantitatively predictive results. Thus, we are motivated find an alternative strategy to assess $\langle A_n A_{n+1}\rangle$.

In fact, we resort to direct estimation of correlations associated with $\langle A_n A_{n+1}\rangle$ allowing treatment of reaction kinetics without analysis of the additional evolution equations for this quantity. To motivate our treatment, first we show KMC simulation results in Fig 3.3 for SFD with $L = 100$, $\langle X_0 \rangle = 0.8$ and $k/h = 0.001$ for $f_n = \langle A_n A_{n+1} \rangle / (\langle A_n \rangle \langle A_{n+1} \rangle)$, and also for $\mathrm{g}_n = \langle A_n B_{n+1} \rangle / (\langle A_n \rangle \langle B_{n+1} \rangle)$, versus n, where deviations from unity reflect the strength of the spatial correlations. It is clear that values of $f_n > 1$ reflect clustering of A's which becomes particularly strong for increasing n. We emphasize that this clustering feature will significantly impact selectivity in reaction kinetics. In contrast, $\mathrm{g}_n < 1$ values reflect anti-clustering which is rather weak for intermediate n and becomes negligible for both large and small n [34].

The origin of the strong clustering of the A's deeper in the pore is somewhat subtle, so further discussion of this feature is appropriate (as well as of the weaker correlations between A's and B's). The rare event where A penetrates deep into the pore without reaction might be associated with density fluctuations near the pore openings, lower densities facilitating such transport. Clearly, if such a fluctuation facilitates transport of one A deep into the pore, it also facilitates transport of nearby pairs or larger groups of A. This feature explains the observed clustering of A's. However, this clustering is even more subtle in the sense the probability for a site n to be populated by A is enhanced not just by knowledge that site $n+1$ is populated by A (and more so if both $n+1$ and $n+2$ are populated by A), but it is also enhanced if it is known that site $n+2$ is populated by A and $n+1$ by B. For further discussion, see Section 3.9. With regard to $A - B$ correlations, most A deep in the pore will be isolated from each other and surrounded by a significant population of B's. There is no mechanism to induce significant positional correlations between these A and B species.

The above observations suggest the possibility of estimation of $\langle A_n A_{n+1} \rangle$ in the left half of the pore by using the exact relation $\langle A_n \rangle = \langle A_n A_{n+1} \rangle + \langle A_n B_{n+1} \rangle + \langle A_n E_{n+1} \rangle$, and then neglecting correlations in $\langle A_n B_{n+1} \rangle$, and also using (3.10a) or (3.11a) or alternatively eGH expressions for $\langle A_n E_{n+1} \rangle$. Specifically, we set:

$$\langle A_n A_{n+1} \rangle \approx \langle A_n \rangle - \langle A_n \rangle \langle B_{n+1} \rangle - \langle A_n E_{n+1} \rangle_{\mathrm{eGH}} . \tag{3.12}$$

Then $\langle A_n A_{n+1} \rangle$ in the right half of the pore is determined from the above results using symmetry about the pore center. In Table 3.2, we show corresponding results for $f_n = \langle A_n A_{n+1} \rangle / (\langle A_n \rangle \langle A_{n+1} \rangle)$ for high concentration $\langle X_0 \rangle = 0.8$ obtained from various eGH formulations. For SFD ($P_{\mathrm{ex}} = 0$), all eGH formulations capture the strong increase in f_n with increasing n, as determined precisely from KMC simulation. The fully asymmetric eGH formulation eGH(f), is most successful in capturing behavior up to $n = 10$. All formulations eventually increase more quickly than precise behavior, actually with eGH(f) deviating most. However, we find that it is primarily behavior for $n \leq 10$ which controls the reactive steady state, i.e., behavior deeper in the pore is not so relevant. From this perspective, eGH(f) is the most successful formulation as anticipated for SFD with high $\langle X_0 \rangle$. For $P_{\text{ex}} = 0.25$, correlations are far weaker, so any formulation gives reasonable results. As anticipated, eGH(a) performs slightly better than eGH(f). In Section 3.4, we shall see that (3.12) allows successful analytic treatment of behavior in the reactive steady state.

Finally, we have also analyzed behavior of f_n for $\langle X_0 \rangle = 0.2$ (not shown). For SFD ($P_{\text{ex}} = 0$), again f_n increases smoothly now from $f_1 = 1.003$ for $n = 1$ to $f_{15} = 1.421$ for $n = 15$ as determined from KMC simulation (a much slower increase than for $\langle X_0 \rangle = 0.8$). In this case the eGH($a$) predictions varying from $f_0 = 1.012$ to $f_{15} = 1.498$ match better precise KMC results than eGH(f) predictions varying from $f_0 = 1.024$ to $f_{15} = 1.948$. For $P_{\text{ex}} = 0.25$, spatial correlations are very weak and again eGH(a) is very effective.

3.4 Results for Concentration-Dependent Selectivity: $A \rightarrow B^c$ or B^t

First, we present results for the steady-state concentration profiles for single-file diffusion (SFD with $P_{\text{ex}} = 0$) where spatial correlations are strongest, and effective analytic treatment is most difficult. Precise KMC simulation results in Figure 3.4 for $L = 100$ and $\langle X_0 \rangle = 0.8$ show that $\langle A_n \rangle \approx 0$ in the center of the pore, and that the $\langle B_n^c \rangle$ and $\langle B_n^t \rangle$ profiles exhibit plateaus with nontrivial values subject to the constraint $\langle B_n^c \rangle + \langle B_n^t \rangle \approx \langle X_0 \rangle$. This plateau behavior is somewhat less clear for $L = 100$ with significantly lower $\langle X_0 \rangle = 0.2$, but would become quite clear for this $\langle X_0 \rangle$ in longer pores.

Since B^t is is preferentially created in regions with higher A concentration, one might have expected a bimodal profile for $\langle B_n^t \rangle$ (rather than a plateau) with peaks near the pore openings. Correspondingly, the profile for $\langle B_n^c \rangle$ would then be peaked in the pore center (since $\langle B_n^c \rangle + \langle B_n^t \rangle \approx \langle X_0 \rangle$). While such transient behavior is found if starting with an initially empty pore (see Section 3.11), it cannot be sustained in the steady state. The reason is

Table 3.2: f_n values for $\langle X_0 \rangle = 0.8$ for three different eGH formulations: fully asymmetric choice (f) expected to be most appropriate for SFD and high $\langle X_0 \rangle$, asymmetric choice (a), and simple symmetric choice (s). Results are shown for SFD ($P_{\text{ex}} = 0$) and $P_{\text{ex}} = 0.25$.

	$P_{\text{ex}} = 0.00$	$P_{\text{ex}} = 0.00$	$P_{\text{ex}} = 0.00$	$P_{\text{ex}} = 0.00$	$P_{\text{ex}} = 0.25$	$P_{\text{ex}} = 0.25$	$P_{\text{ex}} = 0.25$	$P_{\text{ex}} = 0.25$
f_n values	eGH(s)	eGH(a)	eGH(f)	KMC	eGH(s)	eGH(a)	eGH(f)	KMC
$n = 1$	1.00693	1.00717	1.01385	1.01081	0.99563	0.99551	0.99125	1.00029
$n = 2$	1.01870	1.02004	1.03741	1.04782	0.99568	0.99556	0.99135	1.00037
$n = 3$	1.03618	1.04011	1.07235	1.12252	0.99551	0.99538	0.99101	1.00031
$n = 4$	1.06268	1.07160	1.12535	1.24534	0.99533	0.99520	0.99065	1.00015
$n = 5$	1.10838	1.12740	1.21676	1.42971	0.99519	0.99506	0.99039	1.00029
$n = 6$	1.18651	1.22442	1.37301	1.69431	0.99492	0.99478	0.98984	1.00010
$n = 7$	1.32613	1.40026	1.65225	2.06707	0.99469	0.99454	0.98939	0.99976
$n = 8$	1.57841	1.72113	2.15682	2.59594	0.99439	0.99423	0.98877	1.00000
$n = 9$	2.02822	2.29550	3.05643	3.34233	0.99414	0.99398	0.98829	0.99964
$n = 10$	2.84333	3.34063	4.68666	4.39688	0.99382	0.99364	0.98764	0.99930
$n = 11$	4.36949	5.31141	7.73897	5.89006	0.99350	0.99332	0.98700	0.99925
$n = 12$	7.18499	8.95460	13.36998	8.04207	0.99308	0.99288	0.98616	0.99892
$n = 13$	12.46148	15.80610	23.92296	11.10158	0.99275	0.99254	0.98549	0.99885
$n = 14$	22.13462	28.34838	43.26924	15.62479	0.99233	0.99212	0.98467	0.99938
$n = 15$	40.48814	52.25351	79.97628	22.42215	0.99204	0.99181	0.98407	0.99845

simply that in the pore interior with no significant A population, concentration gradients in B^c and B^t are eventually eliminated by small but nonzero diffusion fluxes, $J_C\left(n > n+1\right) \approx -hF_{tr}\left(n, n+1\right) \nabla_n \left\langle C_{n+1} \right\rangle$ with $C = B^t$ and B^c.

We also show the predictions of the standard MF approximation and of our eGH formulations [using the GH approximation for diffusion fluxes, and (3.10a) or (3.11a) for $\langle A_n A_{n+1} \rangle$]. The standard MF approximation fails completely to capture concentration profile behavior. In contrast, the eGH formulations are particularly effective in capturing behavior even including the heights of the plateaus for individual B^c and B^t concentrations. More specifically, the eGH(f) formulation works especially well for higher $\langle X_0 \rangle$ and the eGH(a) formulation for lower $\langle X_0 \rangle$, as anticipated previously. To highlight the success of the eGH formulations, we emphasize that prediction of the values of the individual plateau concentrations is particularly delicate. We have explored various other "hybrid" treatments which use the GH approximation for diffusion fluxes, but either a MF treatment of reaction kinetics, or using other factorization approximations to treat pair diffusion fluxes. These produce qualitatively reasonable forms for

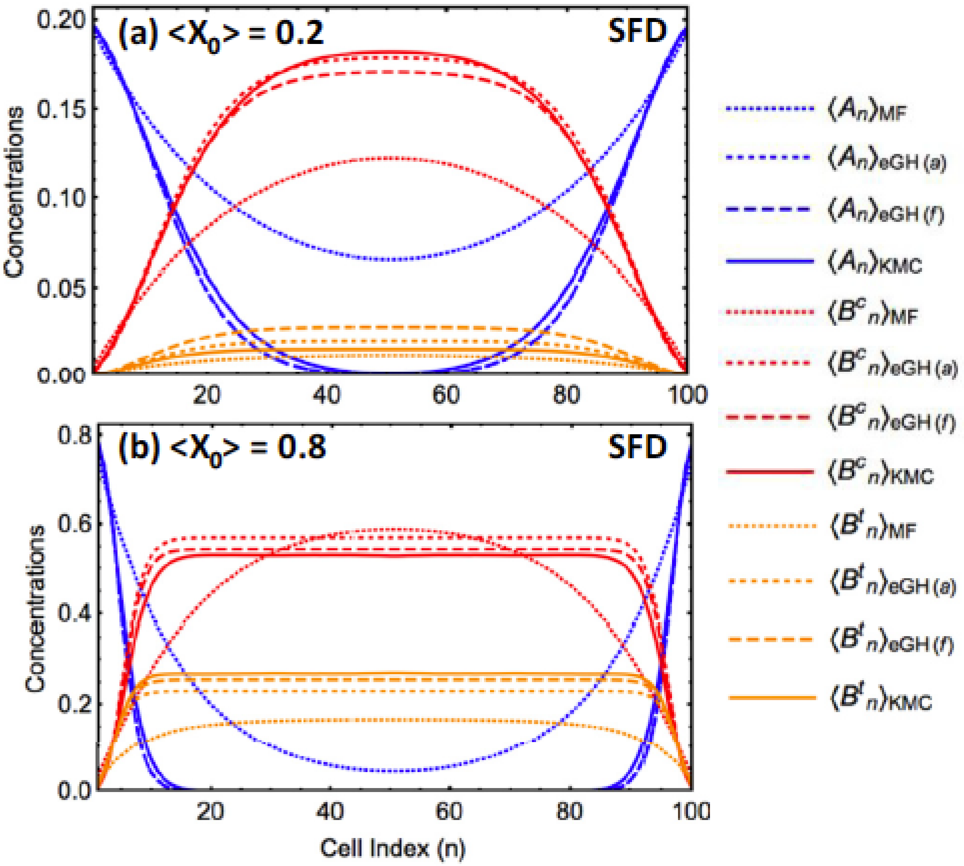

Figure 3.4: Steady-state concentration profiles for SFD with $L = 100$ and $k/h = 0.001$: (a) $\langle X_0 \rangle = 0.2$; (b) $\langle X_0 \rangle = 0.8$. Comparison of precise behavior obtained from KMC simulation (solid curves) with poor MF predictions (dotted curves) and two successful eGH formulations (dashed curves).

concentration profiles, but do not have the quantitative predictivity of our eGH formulations. See Section 3.10.

Next, we more briefly describe behavior when the SFD constraint is relaxed by selecting $P_{\text{ex}} = 0.25$. Here enhanced diffusion means greater reactant penetration into the pore, so longer pore lengths than $L = 100$ are needed to display a clear plateau in the pore center. Results for concentrations when $L = 100$ shown in Figure 3.5 reveal that MF predictions (dotted curves) are significantly closer to precise behavior determined from KMC simulations (solid curves) than for SFD, although still not quantitatively precise. In contrast, predictions of our eGH formulations are effectively indistinguishable on these plots from the precise behavior.

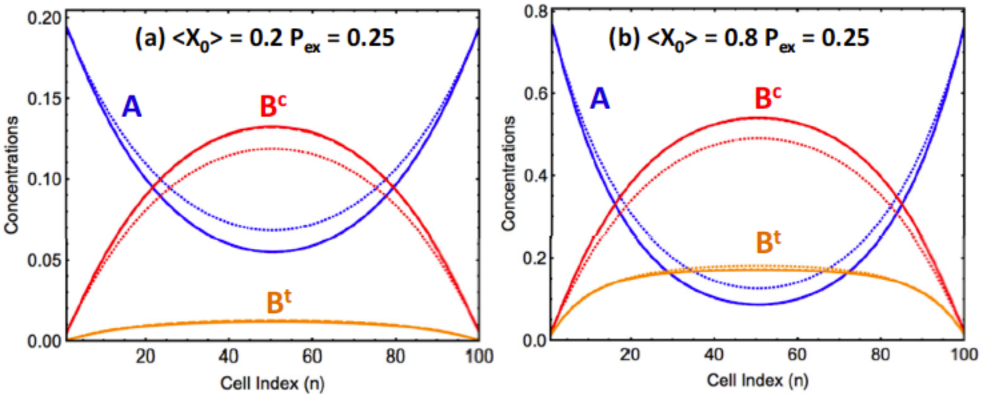

Figure 3.5: Steady-state concentration profiles with exchange, $P_{\text{ex}} = 0.25$, for $L = 100$ and $k/h = 0.001$: (a) $\langle X_0 \rangle = 0.2$; (b)$\langle X_0 \rangle = 0.8$. Comparison of precise behavior obtained from KMC simulation (solid curves) with poor MF predictions (dotted curves). eGH formulations are effectively indistinguishable from precise behavior.

Perhaps more significant than prediction of concentration profiles is the assessment of selectivity, i.e., determination of the relative yields of products B^c versus B^t. KMC simulation allows precise determination of the entire conversion rate profiles, $R_n\left(B^c\right)$ and $R_n\left(B^t\right)$, versus n. See Figure 3.6 for results for SFD with $L = 100$, $k/h = 0.001$, and $\langle X_0 \rangle = 0.8$. Also shown are the results from a MF treatment, and from our analytic eGH(a) and eGH(f) treatments. The total conversion rates, $R_{\text{tot}}\left(B^{c,t}\right) = \sum_n R_n\left(B^{c,t}\right)$, determine the selectivity through the ratio $\Re = R_{\text{tot}}\left(B^t\right)/R_{\text{tot}}\left(B^c\right)$. Analysis of behavior in Figure 3.6 for SFD reveals that for $\langle X_0 \rangle = 0.8$, one has $\Re = 1.56$ from precise KMC analysis versus our best analytic eGH(f) estimate of $\Re = 1.40$, and the poor MF estimate of $\Re = 0.64$. For SFD with $\langle X_0 \rangle = 0.2$, one has $\Re = 0.171$ from KMC analysis versus our best eGH(a) estimate of $\Re = 0.181$, and the poorer MF estimate of $\Re = 0.135$. A more comprehensive comparison of KMC results with various analytic treatments are provided in Table 3.3. As might be anticipated, eGH formulations reasonably recover precise behavior, but the MF treatment is inadequate particularly for higher $\langle X_0 \rangle$. Results are also given in Table 3.3 including exchange ($P_{\text{ex}} = 0.25$), where even the MF estimate is reasonable.

It is appropriate to provide further insight into the influence on selectivity of restricted diffusion (and particularly SFD), which impacts reactant concentration profiles, and of spatial correlations in the form of reactant clustering which impacts reaction kinetics. To this end, it is

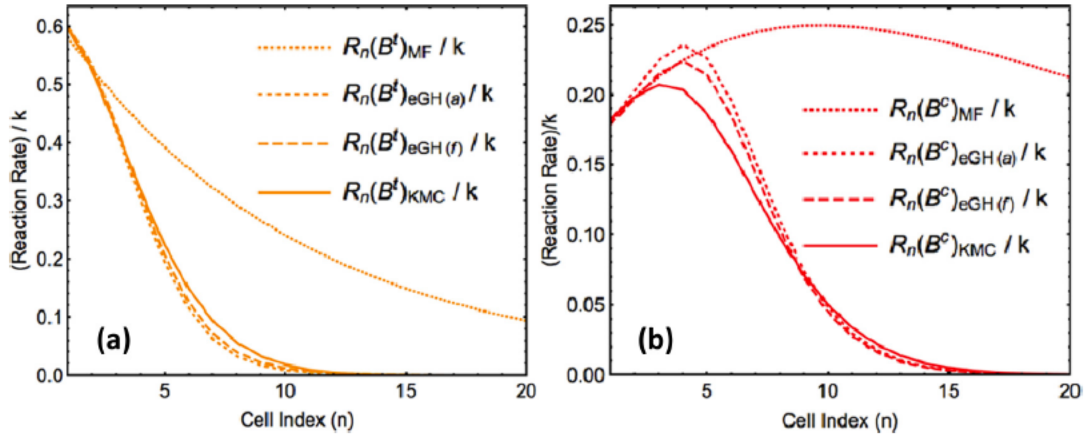

Figure 3.6: Steady-state concentration profiles with exchange, $P_{\text{ex}} = 0.25$, for $L = 100$ and $k/h = 0.001$: (a) $\langle X_0 \rangle = 0.2$; (b)$\langle X_0 \rangle = 0.8$. Comparison of precise behavior obtained from KMC simulation (solid curves) with poor MF predictions (dotted curves). eGH formulations are effectively indistinguishable from precise behavior.

Table 3.3: f_n values for $\langle X_0 \rangle = 0.8$ for three different eGH formulations: fully asymmetric choice (f) expected to be most appropriate for SFD and high $\langle X_0 \rangle$, asymmetric choice (a), and simple symmetric choice (s). Results are shown for SFD $(P_{\text{ex}} = 0)$ and $P_{\text{ex}} = 0.25$.

Analysis of $\Re$	$\langle X_0 \rangle = 0.2, P_{\text{ex}} = 0.00$	$\langle X_0 \rangle = 0.8, P_{\text{ex}} = 0.00$	$\langle X_0 \rangle = 0.2, P_{\text{ex}} = 0.25$	$\langle X_0 \rangle = 0.8, P_{\text{ex}} = 0.25$
$n = 1$	1.00693	1.00717	1.01385	1.01081
$n = 2$	1.01870	1.02004	1.03741	1.04782
$n = 3$	1.03618	1.04011	1.07235	1.12252
$n = 4$	1.06268	1.07160	1.12535	1.24534
$n = 5$	1.10838	1.12740	1.21676	1.42971

instructive to examine the value of $\Re$ determined by other simple treatments. In an alternative spatially coarse-grained description, one regards position in the pore as described by a continuous variable $x = na$ and the reactant concentration profile as a function of this continuous variable $\langle A(x) \rangle = \langle A_n \rangle$. In a MF treatment of reaction kinetics [factorizing expressions (3.2) for rates and coarse-graining], one has that

$$R_{\text{tot}}\left(B^t\right) \approx k \int \mathrm{d}x \; \langle A(x) \rangle^2 , \quad \text{and} \quad R_{\text{tot}}\left(B^t\right) \approx k \int \mathrm{d}x \; \langle A(x) \rangle \left[1 - \langle A(x) \rangle\right] . \tag{3.13}$$

One can further show that for a MF treatment of diffusion, concentration profiles have exponential variation near the ends of a long pore so that $\langle A(x) \rangle \approx \langle X_0 \rangle \exp\left[-\left(x/L_p\right)\right]$ near the left end of the pore where L_p denotes a penetration depth [7–9]. Then evaluation of the integrals in (3.13) yields

$$\Re\left(\mathrm{MF}\right) \approx \langle X_0\rangle \,/\, \left(2 - \langle X_0\rangle\right), \tag{3.14}$$

so the maximum $\Re\left(\mathrm{MF}\right) \approx 1$ occurs for $\langle X_0\rangle = 1$. For SFD with high $\langle X_0\rangle = 0.8$, this yields $\Re\left(\mathrm{MF}\right) = 2/3 \approx 0.67$, far below the value above precise value of 1.56. (For SFD with $\langle X_0\rangle = 0.2$, one finds $\Re\left(\mathrm{MF}\right) = 1/9 \approx 0.11$ also well below the precise value of 0.17.)

Next, we consider a hybrid treatment retaining MF reaction kinetics, but utilizing a GH formulation to account for the effect of SFD on the reactant concentration profile. If the GH tracer diffusion coefficient decays like $F_{tr} \sim x^{-p}$ into the pore, then it has been shown that $\langle A\left(x\right)\rangle \approx \langle X_0\rangle \exp\left[-\left(x/L_p\right)^q\right]$ where $q = \left(2+p\right)/2$ where we discuss the appropriate values of $p > 0$ and $q > 1$ below [2, 10]. Note that MF behavior corresponds to $p = 0$ and $q = 1$. Evaluation of integrals in (3.13) now yields

$$\Re\left(\text{hybrid MF}\right) = \langle X_0\rangle \,/ (2^{1/q} - \langle X_0\rangle). \tag{3.15}$$

For SFD with high $\langle X_0\rangle = 0.8$, behavior is well described by the choice $p = 2$ and thus $q = 2$ [2, 10], which yields $\Re\left(\text{hybrid MF}\right) \approx 1.30$ much closer to the precise value of 1.56 than the pure MF estimate for $q = 1$. However, a more appropriate hybrid MF treatment (see Section 3.10), based on discrete evolution equations using a GH formulation for diffusion fluxes and MF treatment of reaction kinetics, obtains $\Re \approx 1.19$ not so close to the precise value. [For SFD with $\langle X_0\rangle = 0.2$, one finds an effective $p \approx 1$ corresponding to $q \approx 3/2$ [2, 10]. This yields $\Re\left(\text{hybrid MF}\right) \approx 0.14$ improving over the simple MF estimate, but still below the precise value of 0.17.]

We conclude that deviations from a MF exponential reactant concentration profile are important in determining selectivity, but also clustering of reactants has a significant impact, particularly in producing higher values for SFD with high $\langle X_0\rangle$.

3.5 Conclusions

There is extensive interest within the statistical physics community in cooperative reaction-diffusion phenomena where traditional MF treatments of chemical kinetics and transport are inadequate [1, 2]. Catalytic reactions in nanoporous materials with restrictive diffusive transport provide such an example where spatial correlations of kinetic origin invalidate MF assumptions. The additional feature of cooperative reaction kinetics, such as concentration- or environment-dependent selectivity considered here, constitutes an additional complication in the understanding and prediction of behavior. While KMC simulation of such reaction-diffusion models can reliably characterize such behavior, we show that for the system of interest here, an analytic formulation can be developed which provides deeper insight into the nature and role of subtle non-equilibrium spatial correlations in determining reaction behavior.

3.6 Acknowledgements

We thank Sanjeevi Sivasankar for instructive comments on the form of concentration profiles inside the pore. This work was supported by the U.S. Department of Energy (USDOE), Office of Basic Energy Sciences, Division of Chemical Sciences, Geosciences, and Biosciences through the Ames Laboratory Chemical Physics program for the theory and modeling studies. The work was performed at Ames Laboratory which is operated for the USDOE by Iowa State University under Contract No. DE-AC02-07CH11358.

3.7 Appendix A: KMC Simulation Algorithms

The basic principle of KMC simulation is to implement various processes (adsorption, desorption, diffusion, reaction) in the stochastic reaction-diffusion model with probabilities proportional to their physical rates.We first describe a rejection (rej) algorithm which is simpler to implement, but includes a fraction of failed attempts thus its reducing efficiency. One assigns a total rate $r_t = k + 6h$ for all types of processes at each cell in the pore (reaction plus hopping left or right of each of three types of species). The total rate, R_t (rej), for the system is r_t times the number of sites (taken as $L + 2$ since we must consider sites just outside the pore to treat adsorption). At each KMC step, simulation randomly picks sites and processes and attempts to implement (reaction is only implemented with probability k/r_t if the selected cell has an A; hopping right of B^c is only implemented with probability h/r_t if the selected cell has a B^c and the cell to the right is empty; etc.). The simulation is run for $\sim 10^{11}$ KMC steps to be certain the steady state is reached, and then simulation data are collected for an additional $\sim 2\times 10^{11}$ KMC steps.

A Bortz-type rejection-free (rf) algorithm maintains lists of the sets of particles which can be involved in each type of process (all n_A A's in the pore can react; the set of n_{Ar} A's with empty right NN cells which can hop right; etc.) The list must be updated after each simulation step, which requires extensive bookkeeping. Then the total rate of processes for the system is $R_t\,(\mathrm{rf}) = n_A k + n_{Ar} h + \ldots$. Now one picks a type of process with probability proportional to its rate, i.e., $n_A k / R_t\,(\mathrm{rf})$ for reaction of A, picks a particle from the relevant list and implements the process for that particle. (For reaction, one would also have to select the product based on the local environment.) The simulation is run for $\sim 10^9$ KMC steps to equilibrate, and then data are collected for an additional $\sim 10^{10}$ KMC steps.

For our primarily focus on steady-state behavior, tracking of physical time in the simulation is not relevant. However, for studies of transient behavior, see D, time is incremented by $\Delta t = -\ln(w)/R_t$ at each Monte Carlo step where w is a random number uniformly distributed on $[0,1]$.

3.8 Appendix B: MF Analysis of Tracer Diffusivity

It is possible to somewhat unconventionally assess tracer diffusivity, either at the MF-level or for higher-level approximations, from behavior of the concentration profiles in the steady state of our reaction-diffusion model [2,9]. This strategy exploits the feature noted in Section 3.2 that the steady state corresponds to a counter diffusion mode where diffusion fluxes are proportional to the tracer diffusion coefficient in a hydrodynamic formulation. Here it suffices to take Eqs. (3.3) and (3.4) for $C = A$ and apply MF factorization. After substantial simplification, this equation reduces to

$$0 = \mathrm{d}/\mathrm{d}t \left\langle A_n \right\rangle = -k \left\langle A_n \right\rangle + \left(\left\langle E_0 \right\rangle + P_{\mathrm{ex}} \left\langle X_0 \right\rangle \right) h \nabla^2 \left\langle A_n \right\rangle, \tag{3.16}$$

where $\nabla^2 \langle A_n \rangle = \langle A_{n+1} \rangle - 2\langle A_n \rangle + \langle A_{n-1} \rangle$ represents a discrete Laplacian. Since the coefficient in front of $\nabla^2 \langle A_n \rangle$ corresponds to D_{tr}, we obtain $F_{tr}\,(\mathrm{MF}) = \langle E_0 \rangle + P_{\mathrm{ex}} \langle X_0 \rangle$.

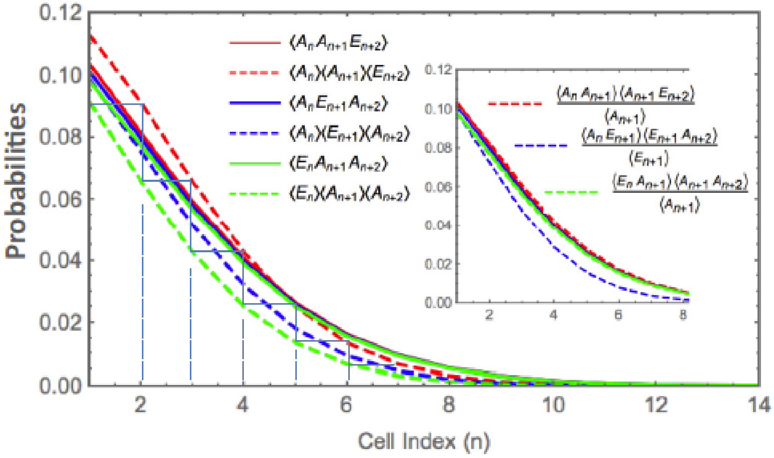

Figure 3.7: Comparison of $\langle A_n A_{n+1} E_{n+2}\rangle$, $\langle A_n E_{n+1} A_{n+2}\rangle$, and $\langle E_n A_{n+1} A_{n+2}\rangle$ versus n determined precisely from KMC simulation and MF approximations near the left end of a pore for $L = 100$, $\langle X_0\rangle = 0.8$, $k/h = 0.001$, and $P_{\text{ex}} = 0$ (SFD).

3.9 Appendix C: Analysis of Multisite Configurational Probabilities

The form of the "pair diffusion terms" in (3.5) motivates consideration and comparison of $\langle A_n A_{n+1} E_{n+2}\rangle$, $\langle A_n E_{n+1} A_{n+2}\rangle$, and $\langle E_n A_{n+1} A_{n+2}\rangle$. The same argument as used for $\langle A_n E_{n+1}\rangle$ and $\langle E_n A_{n+1}\rangle$ in Section 3.3 suggests that these triplet probabilities will be much closer than their MF values for SFD especially with high $\langle X_0\rangle$. This feature, which is confirmed in Figure 3.7 for SFD with $\langle X_0\rangle = 0.8$ and $k/h = 0.001$, complicates the requirement of accurately describing differences in these quantities which constitute pair diffusion terms. Setting $\langle A_n A_{n+1} E_{n+2}\rangle - \langle A_n E_{n+1} A_{n+2}\rangle \approx \langle A_n\rangle (\langle A_{n+1} E_{n+2}\rangle - \langle E_{n+1}\rangle \langle A_{n+2}\rangle)$ would enable use of the GH approximation for the difference of pair probabilities. However, this crude factorization, denoted by (c) below, is not reliable. Also, as shown in the inset to Fig 3.7, a standard pair approximation, denoted (pa) below, reliably describes $\langle A_n A_{n+1} E_{n+2}\rangle$ and $\langle E_n A_{n+1} A_{n+2}\rangle$ in terms of pair quantities, but not $\langle A_n E_{n+1} A_{n+2}\rangle$. Thus, the pair approximation will fail to describe key differences in these quantities. The failure of the pair approximation for the quantity $\langle A_n E_{n+1} A_{n+2}\rangle$, and the failure of higher-order approximations for analogous probabilities involving four or more cells, is further elucidated by the conditional concentration analysis below.

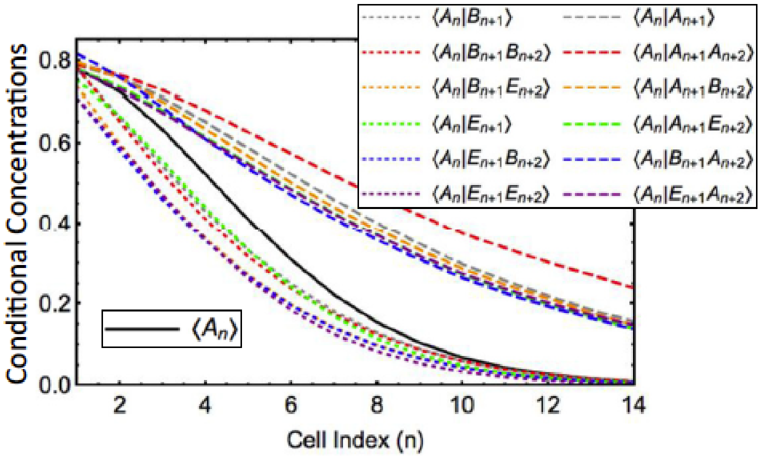

Figure 3.8: Comparison of various conditional reactant concentrations versus n determined precisely from KMC simulation for $L = 100$, $\langle X_0 \rangle = 0.8$, $k/h = 0.001$, and $P_{\text{ex}} = 0$ (SFD).

Spatial correlations in the reactant distribution can be further elucidated by considering conditional reactant probabilities or concentrations $\langle A_n | C_{n+1} D_{n+2} \ldots \rangle = \langle A_n C_{n+1} D_{n+2} \ldots \rangle \,/\, \langle C_{n+1} D_{n+2} \ldots \rangle$ describing the probability that site n is occupied by A given that site $n+1$ is occupied by C, site $n+2$ is occupied by D, etc. In the absence of spatial correlations, one has that $\langle A_n | C_{n+1} D_{n+2} \ldots \rangle = \langle A_n \rangle$. Results are shown in Figure 3.8 for SFD with $\langle X_0 \rangle = 0.8$ and $k/h = 0.001$ for a substantial set of conditional reactant concentrations with one or two conditioning sites. These fall into distinct groups with values either above or below $\langle A_n \rangle$.

All of $\langle A_n | A_{n+1} \rangle$, $\langle A_n | A_{n+1} A_{n+2} \rangle$, $\langle A_n | A_{n+1} E_{n+2} \rangle$, $\langle A_n | E_{n+1} A_{n+2} \rangle$, $\langle A_n | A_{n+1} B_{n+2} \rangle$ and $\langle A_n | B_{n+1} A_{n+2} \rangle$ exceed $\langle A_n \rangle$, i.e., conditional reactant concentrations given one or more nearby A exceed $\langle A_n \rangle$. We also expect this feature to apply for conditional concentrations with more than two specified cells. This feature indicates a subtle type of clustering corresponding to enhanced probabilities (relative to MF values) for configurations with an A on site n and one or more other A's on sites $n+1$ and $n+2$. The explanation of this behavior extends that used to rationalize the inequality $\langle A_n | A_{n+1} \rangle > \langle A_n \rangle$ in Section 3.3. A density fluctuation near the pore opening reducing the density could facilitate diffusion of A and of clusters of A deeper into the pore. Then it follows that $\langle A_n | A_{n+1} \rangle$, $\langle A_n | A_{n+1} B_{n+2} \rangle$, $\langle A_n | E_{n+1} A_{n+2} \rangle$, etc., exceed $\langle A_n \rangle$. It is perhaps less clear why $\langle A_n | B_{n+1} A_{n+2} \rangle > \langle A_n \rangle$, but consider a triple of A's diffusing deep into the pore (aided by a density fluctuation) where the central A reacts to convert to B.

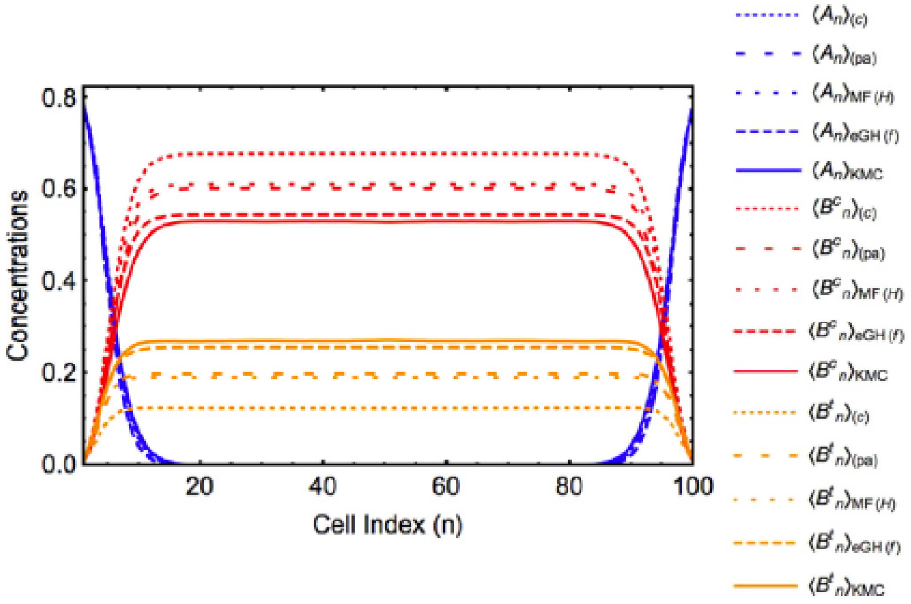

Figure 3.9: Comparison of various hybrid approximations, including MF(H) and a crude factorization of pair diffusion terms (c) and a pair factorization (pa) with precise behavior (KMC) and our eGH(f) treatment for $L = 100$, $\langle X_0 \rangle = 0.8$, $k/h = 0.001$, and $P_{\mathrm{ex}} = 0$ (SFD).

This scenario can lead to formation of $A_n B_{n+1} A_{n+2}$ configurations.

Next, we note that both $\langle A_n | E_{n+1} \rangle$ and $\langle A_n | E_{n+1} E_{n+2} \rangle$ are below $\langle A_n \rangle$. These results are equivalent to the inequalities $\langle A_n E_{n+1} \rangle < \langle A_n \rangle \langle E_{n+1} \rangle$ and $\langle A_n E_{n+1} E_{n+2} \rangle < \langle A_n \rangle \langle E_{n+1} E_{n+2} \rangle = \langle A_n \rangle \langle E_{n+1} \rangle \langle E_{n+2} \rangle$ (the latter equality following since empty cells are randomly distributed). These inequalities have been explained at the beginning of Section 3.3, where we note that values of $\langle A_n E_{n+1} \rangle$ and $\langle E_n A_{n+1} \rangle$ are close, as are those of $\langle A_n E_{n+1} E_{n+2} \rangle$, $\langle E_n A_{n+1} E_{n+2} \rangle$, and $\langle E_n E_{n+1} A_{n+2} \rangle$ (due to the facile diffusion of A between the indicated pair or triple of sites). Our resulting understanding of the contrasting behavior of $\langle A_n | E_{n+1} \rangle < \langle A_n \rangle$ and of $\langle A_n | E_{n+1} A_{n+2} \rangle > \langle A_n \rangle$ explains the failure of the standard pair approximation to treat $\langle A_n E_{n+1} A_{n+2} \rangle$ and thus to treat pair diffusion fluxes in the evolution equation for $\langle A_n A_{n+1} \rangle$, see Section 3.3.

Finally, we note that all of $\langle A_n | B_{n+1} \rangle$, $\langle A_n | B_{n+1} B_{n+2} \rangle$, $\langle A_n | B_{n+1} E_{n+2} \rangle$, and $\langle A_n | E_{n+1} B_{n+2} \rangle$ are also below $\langle A_n \rangle$, but also that these quantities approach $\langle A_n \rangle$ for large n where the associated correlations are diminished deeper in the pore.

3.10 Appendix D: Hybrid Approximations

We have seen that a standard MF approximation applied to treat both diffusion fluxes and reaction kinetics fails dramatically to describe reactant penetration into the pore for small P_{ex} and small k [10]. However, a GH formulation of diffusion fluxes yields reliable description of the reactant concentration profile. Thus, it remains only to treat the reaction kinetics in order to describe behavior of the $A \to B^c$ or B^t conversion reaction. Here we first consider the simplest hybrid formulation, MF(H), using a GH treatment of diffusion fluxes and a MF treatment of of reaction kinetics (i.e. ignoring spatial correlations in the reactant distribution). MF(H) results for steady-state concentration profiles shown in Figure 3.9 for SDF with $\langle X_0 \rangle = 0.8$ qualitatively reproduce KMC simulation behavior. However, predictions for plateau concentrations of B^c and B^t differ significantly from the precise values, in contrast our eGH formulation accounting for reactant clustering. As noted in Table 3.3, one obtains $\Re = 1.19$ for MF(H) versus $\Re = 1.40$ for eGH(f) versus the precise value of $\Re = 1.56$ from KMC simulation.

We have implemented other hybrid formulations which retain the GH treatment of diffusion flux in the equations for single-cell concentrations, but apply various factorization approximations to the pair diffusion fluxes in the evolution equations for $\langle A_n A_{n+1} \rangle$. We have applied a crude factorization (c), e.g., $\langle A_n A_{n+1} E_{n+2} \rangle - \langle A_n E_{n+1} A_{n+2} \rangle \approx \langle A_n \rangle \left(\langle A_{n+1} E_{n+2} \rangle - \langle E_{n+1} \rangle \langle A_{n+2} \rangle \right)$, and then used the GH treatment of the second factor. Figure 3.9 also reveals that for SFD with $\langle X_0 \rangle = 0.8$, predictions of this approach (c) while qualitatively reasonable actually give a poorer estimate of plateau concentrations even than the hybrid MF approach. As another alternative denoted (pa), we have implemented a standard pair factorization for the pair diffusion terms and then used the eGH approximation to describe $\langle A_n E_{n+1} \rangle$ and $\langle E_{n+1} A_n \rangle$ terms. Recall that we know from Section 3.8 that the pair approximation is inadequate for $\langle A_n E_{n+1} A_{n+2} \rangle$. This approach predicts concentration profiles very similar to the MF(H) prediction for SFD with $\langle X_0 \rangle = 0.8$, and thus again deviating significantly from precise results in contrast to our eGH approach. See Figure 3.9.

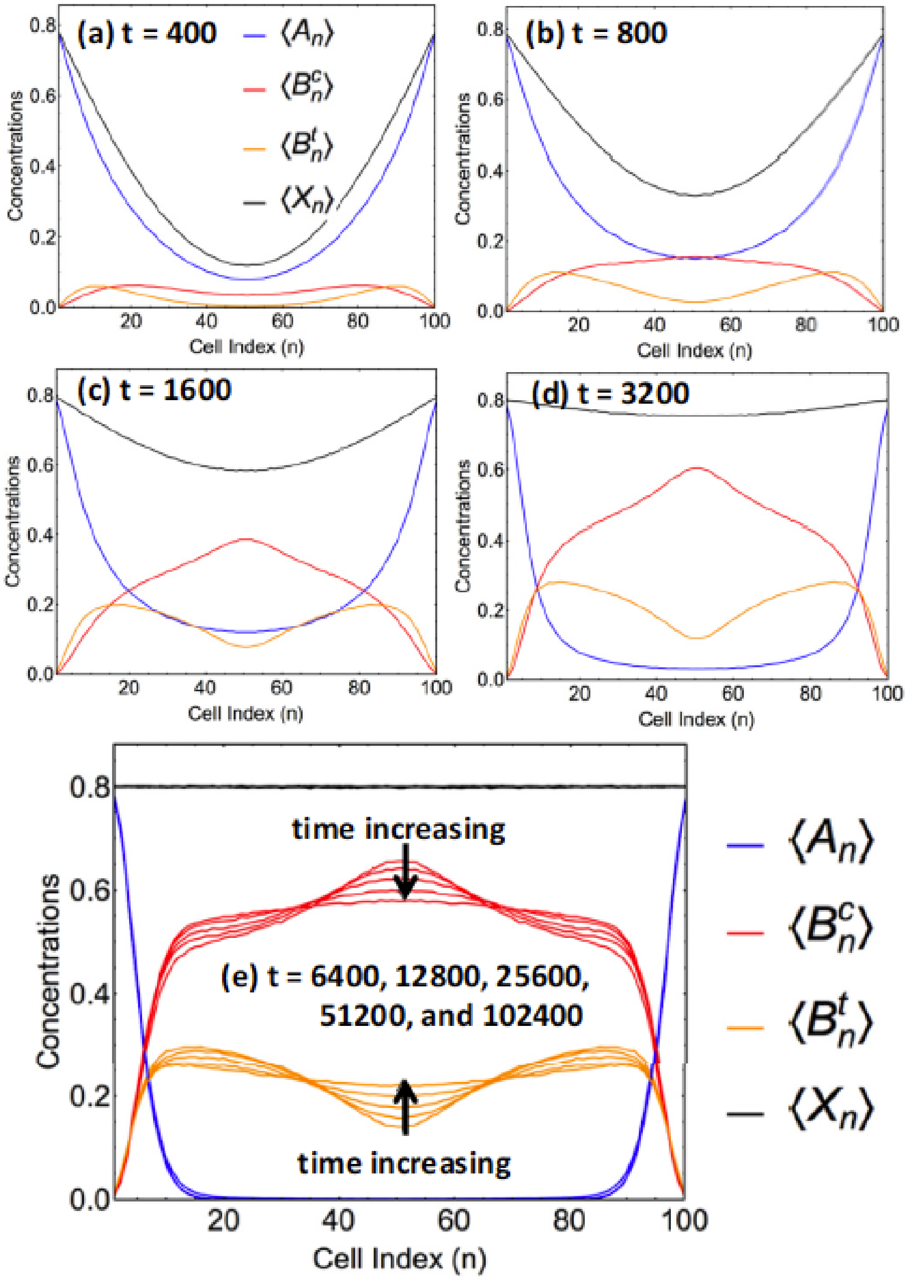

Figure 3.10: KMC simulation results for the evolution of concentration profiles starting from an empty pore for $L = 100$, $\langle X_0 \rangle = 0.8$, and $k/h = 0.001$. Times are indicated (in units where $h = 1$) and increase from panels (a) to (e).

3.11 Appendix E: Transient Behavior With an Initially Empty Pore

We have performed simulations to characterize evolution of concentration profiles starting with an initially empty pore for $L = 100$, $\langle X_0 \rangle = 0.8$, and $k/h = 0.001$. See Figure 3.10. The key features are as follows. The quasi-steady-state reactant profile develops relatively quickly on the times scale of pore filling, where the filling process takes a time $t_f \sim 2000$ (in units of $1/h$) to achieve a roughly constant total concentration of $\langle X_n \rangle \approx 0.8$. This time scale follows from Einstein's relation $(L/2)^2 \sim h\, t_f$ since particles must diffuse a length $\sim L/2$ to fill the pore. At the end of this filling stage, B^t has a bimodal profile peaked towards the pore openings, and the B^c profile is peaked in the pore center. The second stage of evolution to achieve the true steady state, where both B^c and B^t profiles exhibit plateaus in the pore center, takes much longer around $t_{ss} \sim 10^5$. This much slower time scale is understood since such evolution is controlled by the magnitude of the tracer diffusion coefficient $F_{tr}\,(n, n+1) \approx (1 - \langle X_0 \rangle)\,(\langle X_0 \rangle)^{-1}/L \approx 0.0025$ in the pore center [35]. Diffusion over a length scale of ~ 20 cells would only occur on a time scale of $\sim t_{ss}$ given such a low diffusion coefficient.

Bibliography

[1] K. Lindenberg, G. Oshanin, and M. Tachiya. Chemical kinetics beyond the textbook: Fluctuations, many-particle effects and anomalous dynamics. *J. Phys.: Condens. Matter*, 19(6), 2007.

[2] D-J. Liu, A. García, J. Wang, D. M. Ackerman, C-J. Wang, and J. W. Evans. Kinetic Monte Carlo simulation of statistical mechanical models and coarse-grained mesoscale descriptions of catalytic reaction–diffusion processes: 1D nanoporous and 2D surface systems. *Chem. Rev.*, 115:pp. 5979–6050, 2015.

[3] J. G. Tsikoyiannis and J. E. Wei. Diffusion and reaction in high-occupancy zeolite catalysts−I. A stochastic theory. *Chem. Eng. Sci.*, pages pp. 233–253, 1991.

[4] C. Rödenbeck, J. Kärger, and K. Hahn. Tracer exchange and catalytic reaction in single-file systems. *J. Catal*, 157:pp. 656–664, 1995.

[5] C. Rödenbeck, J. Kärger, and K. Hahn. Exact analytical description of tracer exchange and particle conversion in single-file systems. *Phys. Rev. E*, 55:pp. 5697–5712, 1997.

[6] M. S. Okino, Q. Snurr, H. H. Kung, J. E. Ochs, and M. L. Mavrovouniotis. A consistent correlation approach to single file diffusion with reaction. *J. Chem. Phys.*, 111:pp. 2210–2221, 1999.

[7] S. V. Nedea, A. P. J. Jansen, J. J. Lukkien, and P. A. J. Hilbers. Steady-state properties of single-file systems with conversion. *Phys. Rev. E*, 65:066701, 2002.

[8] S. V. Nedea, A. P. J. Jansen, J. J. Lukkien, and P. A. J. Hilbers. Transient behavior in single-file systems. *Phys. Rev. E*, 66:066705, 2002.

[9] D. M. Ackerman, J. Wang, J. H. Wendel, D-J. Liu, M. Prusky, and J. W. Evans. Catalytic conversion mediated by single-file diffusion in linear nanopores: Hydrodynamic versus stochastic behavior. *J. Chem. Phys.*, 134:114107, 2011.

[10] D. M. Ackerman, J. Wang, and J. W. Evans. Generalized hydrodynamic treatment of the interplay between restricted transport and catalytic reactions in nanoporous materials. *Phys. Rev. Lett.*, 108:228301, 2012.

[11] J. Wang, D. M. Ackerman, V. S-Y. Lin, M. Prusky, and J. W. Evans. Controlling reactivity of nanoporous catalyst materials by tuning reaction product-pore interior interactions: Statistical mechanical modeling. *J. Chem. Phys.*, 138:134705, 2013.

[12] T. E. Harris. Diffusion with "collisions" between particles. *J. Appl. Prob.*, 2:pp. 323–338, 1965.

[13] M. Kollmann. Single-file diffusion of atomic and colloidal systems: Asymptotic laws. *Phys. Rev. Lett.*, 90:180602, 2003.

[14] F. Marchesoni and A. Taloni. Subdiffusion and long-time anticorrelations in a stochastic single file. *Phys. Rev. Lett.*, 97:106101, 2006.

[15] K. Manna, N. Eedugurala, and A. D. Sadow. Zirconium-catalyzed desymmetrization of aminodialkenes and aminodialkynes through enantioselective hydroamination. *J. Am. Chem. Soc.*, 137:pp. 425–435, 2015.

[16] F. J. M. M. de Gauw, J. van Grondelle, and R. A. van Santen. Effects of single-file diffusion on the kinetics of hydroisomerization catalyzed by Pt/H–mordenite. *J. Catal.*, 204:pp. 53–63, 2001.

[17] Z. Karpinski, S. N. Gandhi, and W. M. H. Sachtler. Neopentane conversion catalyzed by Pd in L-zeolite: Effects of protons, ions, and zeolite structure. *J. Catal.*, 141:pp. 337–346, 1993.

[18] L. Heinke and J. Kärger. Correlating surface permeability with intracrystalline diffusivity in nanoporous solids. *Phys. Rev. Lett.*, 106:074501, 2011.

[19] B. G. Trewyn, I. I. Slowing, S. Giri, H. T. Chen, and V. S-Y. Lin. Synthesis and functionalization of a mesoporous silica nanoparticle based on the Sol–Gel process and applications in controlled release. *Accounts Chem. Res.*, 40:pp. 846–853, 2007.

[20] K. Kandel, S. M. Althaus, C. Peraphadit, B. G. Trewyn, M. Prusky, and I. I. Slowing. Substrate inhibition in the heterogeneous catalyzed aldol condensation: A mechanistic study of supported organocatalysts. *J. Catal.*, 291:pp. 63–68, 2012.

[21] K. Manna, W. S. Everett, G. Schoendorff, A. Ellern, T. L. Windus, and A. D. Sadow. Highly enantioselective zirconium-catalyzed cyclization of aminoalkenes. *J. Am. Chem. Soc.* ***135**, 7235 (2013).*, 135:pp. 7235–7250, 2013.

[22] N. Eedugurala, Z. R. Wang, U. Chaudhary, N. Nelson, K. Kandel, T. Kobayashi, I. I. Slowing, M. Prusky, and A. D. Sadow. Mesoporous silica-supported amidozirconium-catalyzed carbonyl hydroboration. *ACS Catal.* ***5**, 7399 (2015).*, 5:pp. 7399–7414, 2015.

[23] W. C. Everett, J. W. Evans, A. D. Sadow, and T. L. Windus. Unpublished.

[24] A. Klamt and G. Schuurmann. Cosmo: A new approach to dielectric screening in solvents with explicit expressions for the screening energy and its gradient. *J. Chem. Soc., Perkin Trans.*, 2:pp. 799–805, 1993.

[25] M. Cossi, N. Rega, G. Scalmani, and V. Barone. Energies, structures, and electronic properties of molecules in solution with the C−PCM solvation model. *J. Comput. Chem.*, 24:pp. 669–681, 2003.

[26] D. S. Sholl. Understanding macroscopic diffusion of adsorbed molecules in crystalline nanoporous materials via atomistic simulations. *Acc. Chem. Res.*, 39:pp. 403–411, 2006.

[27] K. Malek, T. J. H. Vlugt, and B. Smit. *Catalysis and materials science*, chapter 14. Wiley-VCH, Weinheim, 2009.

[28] C-J. Wang, D. M. Ackerman, I. I. Slowing, and J. W. Evans. Langevin and Fokker-Planck analyses of inhibited molecular passing processes controlling transport and reactivity in nanoporous materials. *Phys. Rev. Lett.*, 113:038301, 2014.

[29] P. H. Nelson and S. M. Auerbach. Modeling tracer counter-permeation through anisotropic zeolite membranes: from mean field theory to single-file diffusion. *Chem. Eng. J.*, 74:pp. 43–56, 1999.

[30] H. Spohn. *Large scale dynamics of interacting particles.* Springer, Berlin, 1991.

[31] J. Quastel. Diffusion of color in the simple exclusion process. *Commun. Pure Appl. Math.*, 45:pp. 623–679, 1992.

[32] The mean residence time of an A in the pore at site $n+1$, and such an A given site n is E, are expected to be similar. The mean residence time of A at n is likely below that of A at n given site $n+1$ is E. In the latter case, the A at n could have likely explored site $n+1$ previously indicating that it has been in the pore longer. The probability for conversion of A to B naturally increases with residence time [5].

[33] The symmetric version of the eGH approximation, eGH(s), yields $\langle A_n E_{n+1}\rangle$eGH($s$)$\approx$ $1/2\left(\langle A_n\rangle+\langle A_{n+1}\rangle\right)\langle E_0\rangle + 1/2F_{tr}\left(n,n+1\right)\left(\langle A_n\rangle-\langle A_{n+1}\rangle\right)$ and $\langle E_n A_{n+1}\rangle$eGH($s$)$\approx$ $1/2\left(\langle A_n\rangle+\langle A_{n+1}\rangle\right)\langle E_0\rangle - 1/2F_{tr}\left(n,n+1\right)\left(\langle A_n\rangle-\langle A_{n+1}\rangle\right)$.

[34] We find similar strength of weak AA-clustering and weak AB-anticlustering near the pore opening. Setting $\mathrm{g}_n = 1/f_n$ leads to some improvement in estimates of f_n for $n \approx 1-4$, but fails completely for larger n.

[35] D-J. Liu, J. Wang, D. M. Ackerman, I. I. Slowing, M. Pruski, H-T. Chen, V. S-Y. Lin, and J. W. Evans. Interplay between anomalous transport and catalytic reaction kinetics in single-file nanoporous systems. *ACS Catal.*, 1:pp. 751–763, 2011.

CHAPTER 4. CATALYTIC CONVERSION IN NANOPOROUS MATERIALS: CONCENTRATION OSCILLATIONS AND SPATIAL CORRELATIONS DUE TO INHIBITED TRANSPORT AND INTERMOLECULAR INTERACTIONS

A paper published in the *Journal of Chemical Physics*

Andrés García and James W. Evans*

Division of Chemical & Biological Sciences, Ames Laboratory– U.S. Department of Energy and Department of Physics & Astronomy, Iowa State University, Ames, Iowa 50011, USA

(Received 4 August 2016; accepted 17 October 2016; published online 3 November 2016)

Abstract

We show that steady-state catalytic conversion in nanoporous materials can occur in a quasi-counter-diffusion mode with the reactant (product) concentration strongly decaying (growing) into the pore, but also with oscillations in the total concentration. These oscillations reflect the response of the fluid to the transition from an extended to a confined environment near the pore opening. We focus on the regime of strongly inhibited transport in narrow pores corresponding to single-file-diffusion. Here, limited penetration of the reactant into the pores and the associated low reaction yield is impacted by strong spatial correlations induced by both reaction (non-equilibrium correlations) and also by intermolecular interactions (thermodynamic correlations). We develop a generalized hydrodynamic formulation to effectively describe inhibited transport accounting for the effect of these correlations, and incorporate this

---

[*] Author to whom correspondence should be addressed. Electronic mail: evans@ameslab.gov

description of transport into appropriate reaction-diffusion equations. These equations accurately describe both shorter-range concentration oscillations near the pore opening and the longer-range mesoscale variation of concentration profiles in the pore (and thus also describe reaction yield). Success of the analytic theory is validated by comparison with a precise kinetic Monte Carlo simulation of an appropriate molecular-level stochastic reaction-diffusion model. This work elucidates unconventional chemical kinetics in interacting confined systems. *Published by AIP Publishing.* [http://dx.doi.org/10.1063/1.4966543]

4.1 Introduction

Traditional mean-field (MF) rate and reaction-diffusion equations of chemical kinetics apply in weakly interacting systems with locally well-stirred and randomized distributions of reactants and products. These formulations do not account for spatial correlations or the impact of such correlations on particle-number fluctuations [1,2]. In fact, intermolecular interactions generally induce non-trivial short-range ordering in fluids. However, extensive analysis of equilibrium systems has provided substantial insight into the associated thermodynamic pair correlations which aids assessment of their effect on reaction kinetics. Coincidentally, this type of short-range ordering is also reflected in the presence of concentration oscillations for fluids near walls and in confined environments [3]. There is less appreciation of the feature that for systems with limited mobility, such as occurs in crowded reaction environments, distinct and sometimes strong non-equilibrium correlations can be induced by the presence of reaction [1,2]. Examples include catalytic surface reactions under high-pressure conditions [4,5], and catalytic conversion in nanoporous materials with inhibited transport due to narrow pores [2,6]. The most extreme case for the latter where such non-equilibrium correlations should be strongest is where narrow pores impose a single-file diffusion (SFD) constraint, i.e., no passing of reactant and product molecules [2,6]. The lack of a general theoretical framework to precisely determine non- equilibrium correlations and their effect on reaction kinetics poses a major challenge for reliable beyond-MF assessment of the reaction yield.

In this contribution, we develop stochastic models for first-order catalytic conversion reactions $A \to B$, where reactants A in a well-stirred external fluid diffuse into a decoupled array of narrow linear pores in a nanoporous material [2, 7–13]. Conversion of A to product B can occur anywhere inside the pores, but significant yield relies on efficient removal of product from the pores to facilitate further entry of the reactant. We focus on the SFD regime where product removal is most inhibited. However, we emphasize that our model and theoretical formulation, as well as our basic observations, extend to the regime where passing within the pore is possible [2].

Investigation of such reaction systems from the early 1990s was initially motivated by extensive studies of catalysis in zeolites, noting that a large subset of these materials do indeed consist of very narrow (∼ 1 nm) decoupled linear pores [6]. Furthermore, experimental analysis for selected zeolite systems revealed clear indication of the presence of SFD and its influence on the reaction kinetics [8, 14, 15]. Subsequent studies have exploited new experimental techniques to characterize SFD in these systems [16]. Additional interest in reaction systems subject to SFD was motivated by more recent studies of liquid-phase reactions utilizing catalytically functionalized mesoporous silica nanoparticles (MSN) [2, 17, 18]. In general MSN particles can have coupling between pores. However, our particular interest relates to studies for MSN synthesized with hexagonal arrays of decoupled parallel linear pores with length ∼ 100 nm which traverse the entire nanoparticle, and where pores are not connected and are narrow [17]. We should further emphasize that this synthesis procedure readily produces pores with nominal diameters of ∼ 2 nm, and adsorption of species on the pore walls under reaction conditions can lead to even narrower effective pore diameters. Significantly, such MSN systems have been shown to induce SFD [18].

Coarse-grained spatially discrete stochastic modeling (described in more detail below) of catalytic conversion subject to SFD has typically been applied in order to efficiently treat the entire reaction-diffusion process [2, 7–13]. Behavior of such models was precisely characterized by kinetic Monte Carlo (KMC) simulation. For previous simpler models, which did not incorporate non-trivial intermolecular interactions, it was recognized that a steady-state reaction occurs with reactant (product) concentration strongly decreasing (increasing) into the pore [7–13]. Furthermore, the total concentration was constant for these simple models, and thus the reaction-diffusion system was characterized by exactly counter- balancing gradients. This corresponds to a classic counter-diffusion mode [2, 13, 19].

With regard to analytic approaches to complement and provide further insight beyond KMC analysis, the limitations of MF-type treatments for even these simple systems have been recognized. In particular, such treatments were found to greatly overestimate diffusion fluxes in the presence of inhibited diffusion [2, 12, 13]. Such treatments do account for the non-trivial collective many-particle aspects of inhibited transport and its interplay with reaction. On the other hand, the so-called hydrodynamic treatments also fail in that they underestimate diffusion fluxes near pore openings [12]. Such treatments apply strictly only in the regime of small concentration gradients. As an aside, here the term "hydrodynamic" is used in a broad context of interacting particle systems [20, 21], and in particular diffusive systems, rather than just for convective fluid flow. Recent work on analytic treatments has shown the effectiveness of generalized hydrodynamic (GH) treatments of transport in the presence of strong mesoscale concentration gradients [13]. This GH terminology is borrowed from early studies of convective fluid dynamics going beyond hydrodynamic treatments to describe transport on shorter time- and length-scales [22]. Again our use is in a broader sense considering diffusive interacting particle systems.

Our goal here is to extend previous simple reaction models to include steric intermolecular interactions which are present in real systems. These interactions induce concentration oscillations in an external fluid approaching the catalytic nanoparticle, and would induce radial concentration oscillations in wider pores (although this feature is not included in or relevant for our modeling of narrow pores). Perhaps unexpectedly, we show that these interactions do induce oscillations along the pore axes near the pore openings, a key feature which must be incorporated in our modeling. This feature implies that it is necessary to extend the standard concept of counter-diffusion modes (applying just for constant total concentration), and also to adapt the previous GH formulation to this more complex scenario. In Section 4.2, we present our model for catalytic conversion in nanopores with SFD which incorporates intermolecular interactions. Of particular significance is development of a strategy enabling explicit simulation of processes just inside the pore, avoiding computationally expensive simulation of the surrounding well-stirred equilibrated fluid. Section 4.2 also presents basic KMC simulation results for concentration profiles inside the pore. In Section 4.3, we develop our analytic GH formulation, and demonstrate that it can accurately capture behavior seen in KMC simulation analysis. Thus, the GH formulations provide insight into the failure of simple MF-type formulations. Conclusions are provided in Section 4.4.

4.2 Model Specification and KMC Simulation Analysis

4.2.1 Specification of the stochastic reaction model

We first provide a detailed description of our model which is illustrated schematically in Figure 4.1. In the spirit of classic lattice-gas descriptions of liquids [23], each pore is divided into a linear array of cells labeled $n = 1-L$ whose centers correspond to discrete molecular positions. For prescription of adsorption and desorption at pore openings, it is actually convenient to extend this linear array within the pore to a three-dimensional simple-cubic array of cells in the surrounding fluid. The cell spacing, $a \sim 1\,\text{nm}$, is regarded as being slightly smaller than molecular dimensions, so that nearest-neighbor (NN) cells *cannot* be occupied. For convenience, we often set $a = 1$ below. This steric exclusion constraint suffices to induce all of the features (equilibrium spatial correlations, concentration oscillations, etc.) associated with more general molecular interactions [23]. The key ingredients of our model are as follows:

(i) Reactants A adsorb into the pore from the surrounding external fluid. This process is described by hopping at rate h from cells just outside the pore to an end cell $n = 1$ or L, provided the end cell and its NN cell within the pore are empty.

(ii) Reactants A diffuse within the pore by hopping to NN empty cells at rate h (in either direction) provided that this creates no NN pairs of species.

(iii) Reactants A convert to products B at rate k at any cell inside the pore.

(iv) Products B diffuse within the pore by the same mechanism as for A. This prescription automatically imposes SFD, i.e., no passing of A and B in the pore.

(v) Reactants A and products B desorb from the pore to the surrounding external fluid, a process which is described by hopping from end sites of the pore at rate h to cells just outside the pore provided that such cells are empty, and also that all of the five NN cells of that target cell are also empty.

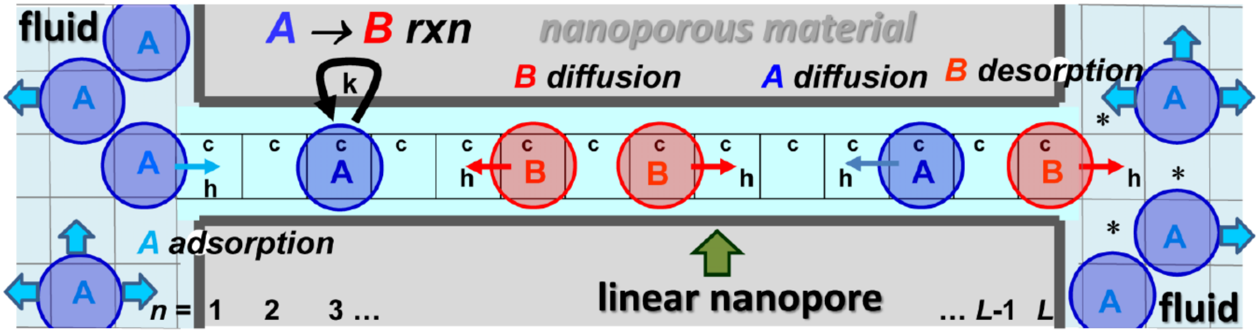

Figure 4.1: The spatially discrete stochastic model for catalytic conversion in linear nanopores. Reactant (A) and product (B) cannot occupy adjacent cells which constrains diffusive hops. c denotes catalytic sites. For desorption, in addition to the target site just outside the pore, multiple additional cells (*) must be empty. A desorption (not shown) at rate h as well as B desorption is active. The exterior fluid is represented by a 3D array of cells (appearing as 2D in the schematic).

Thus, local diffusion within the pore in the direction along the pore axis is described by a single hop rate, h (and a corresponding low-concentration diffusion coefficient of $D_0 = a^2h$). A central component of the analysis in Section 4.3 is to appropriately describe the corresponding chemical diffusion for finite concentrations in this multi-component system. Diffusion in the radial direction within pores is not relevant for the model. The exterior fluid is regarded as being in a well-stirred equilibrated state (corresponding to a lattice-gas with NN exclusion). We emphasize that this equilibrium assumption means that the associated diffusive or convective dynamics in the external fluid is not relevant for modeling. (As an aside, we note that one could regard this equilibrium state as being achieved by rapid effective hopping between neighboring cells subject to NN exclusion.) Another key feature of our model is that the exterior fluid has a large volume compared with the pores, so the desorbing product is quickly diluted and does not re-enter the pore. Thus, the external bulk reactant concentration, $\langle A_b \rangle$, matches the total external concentration, $\langle X_b \rangle$, and is a fixed constant. Finally, we emphasize that the equilibrium state of the external fluid is non-trivial with long-range ordering or crystallinity developing above a critical concentration $\langle X_c \rangle \approx 0.209$ [23]. Consequently, we consider only the regime with short-range order for bulk concentrations $\langle A_b \rangle = \langle X_b \rangle$ below $\langle X_c \rangle$.

Since in this model, reactants and products are "identical" in terms of interactions and diffusional dynamics, evolution of the total concentration corresponds to a pure diffusion problem for a single-component lattice-gas model with NN exclusion. The current study just focuses on steady-state behavior, so such evolution is not directly relevant. Nonetheless, we note that evolution is non-trivial even in the hydrodynamic regime of small concentration gradients given a non-trivial concentration-dependence of chemical diffusion in this model [24]. In the reactive steady-state of interest here, the total concentration matches that of an equilibrium model with NN exclusion. However, even this concentration distribution is non-trivial. The fluid + pore geometry induces concentration oscillations in the external fluid approaching the interface with the nanoporous material, and also a particularly complicated three-dimensional variation of the concentration near the pore opening. Furthermore, we shall see that there are also concentration oscillations within the pore along its axis within, but restricted to near the pore openings. All of these complex concentration variations will impact key adsorption and desorption rates at the pore openings, as discussed below.

4.2.2 Optimal KMC simulation procedure treating explicitly just the pore

Behavior of the above stochastic model can be assessed precisely by KMC simulation. The default treatment would simultaneously simulate behavior in both the pore interior and the external fluid. However, this approach is inefficient due to the large external fluid volume. Furthermore, it is unnecessary due to the assumed rapid equilibration of the external fluid. Thus, we are motivated to develop a strategy to enable explicit simulation of just the pore region while exactly accounting for the non-trivial coupling to the equilibrated external fluid. To this end, we first perform *tailored simulations* of the exterior fluid region to extract key adsorption and desorption parameters which will constitute the appropriate boundary conditions at pore openings for these stand-alone simulations of the pore region.

For *adsorption*, we first note that the concentration, $\langle A_0 \rangle$, at cells just outside the pore, *given* that the end pore cell is empty, corresponds to the concentration of a fluid against the wall in a semi-infinite fluid system. Thus, we perform a simulation analysis of our lattice-gas model of the fluid with NN exclusion for a semi-infinite system, where the concentration only depends on the distance from the wall and exhibits strongly decaying oscillations away from the wall. Of most relevance, we find that the concentration, $\langle A_0 \rangle$, is enhanced relative to the bulk concentration, $\langle A_b \rangle$. This enhancement is a natural consequence of the lower coordination of cells against the wall (with 5 neighbors which could possibly be occupied) relative to the coordination of cells in the bulk of the fluid (with 6 neighbors). See Section 4.7 for further discussion and results for these concentration oscillations and enhancement at the wall, including a simple analytic estimate. This enhancement is quantified in Table 4.1 for a range of $\langle A_b \rangle$. Finally, we note that the adsorption rate at empty end cells of the pore (which also have empty NN cells within the pore) is given by $R_{\text{ads}} = h \langle A_0 \rangle$, and thus is not determined simply by the bulk concentration $\langle A_b \rangle$, but rather by $\langle A_0 \rangle$.

For *desorption*, the presence of a particle at the end cell within the pore implies that the cell just outside the pore is empty. However, desorption requires that in addition all five cells adjacent to this cell are also empty. (The 2D analogue of these sites is denoted by * in Figure 4.1.) Based on these observations, we perform additional tailored simulations of a semi-infinite fluid with one cell against a wall specified empty. These reveal a complicated three-dimensional variation of the concentration near the cell specified empty (in addition to the type of concentration oscillations approaching the wall away from this cell described above). See Section 4.8 for further discussion. These tailored simulations allow determination of the

Table 4.1: Adsorption and desorption parameters as a function of bulk fluid concentration. Note that Q_5 values differ from the simple MF estimate, $Q_5 \approx (1 - \langle A_b \rangle)^5$, or from MF-type refinements accounting for concentration variations.

Fluid conc. $\langle A_b \rangle$	$\langle A_0 \rangle$ **(adsorption)**	Q_5 **(desorption)**
0.20	0.211	0.279
0.15	0.158	0.385
0.10	0.106	0.546
0.05	0.052	0.758

conditional probability, Q_5, that these five additional cells are empty. Results for Q_5 are given in Table 4.1. Then, it follows that the desorption rate from the filled end cell of the pore equals $R_{\text{des}} = hQ_5$.

As an aside, above we have described above the nontrivial and distinct concentration variations in the external fluid associated with both of our tailored simulations to extract adsorption and desorption parameters. Neither of these corresponds to the concentration variation in the external fluid under steady-state reaction conditions (which is just the equilibrium concentration of a lattice-gas with NN exclusion in a geometry corresponding to the fluid + pore system). However, we describe in Section 4.8 how this latter concentration distribution can be reconstructed from the two distinct distributions extracted from our tailored simulations.

4.2.3 KMC results for basic steady-state behavior

Below, we present KMC results of basic steady-state behavior. These and subsequent results are obtained from simulations just of the pore region with the appropriate nontrivial adsorption-desorption boundary conditions described in Section 4.2.2. However, we have confirmed in selected cases that results are consistent with large-scale simulations of the entire fluid + pore system. Figure 4.2 shows typical steady-state concentration profiles in the pore for $L = 30$ with $k/h = 0.001$ and $\langle A_b \rangle = 0.2$. Oscillations are apparent in both the total concentration and the reactant concentration near the pore openings. Thus, the steady-state does not correspond to a conventional counter-diffusion mode with constant total concentration and exactly counter-opposing gradients of A and B [19]. However, we describe it as a quasi-counter diffusion mode since these conditions still apply away from the pore openings. See the supplementary material FigureS1 for behavior with larger L where $\langle A_n \rangle \approx 0$ in the pore center.

With regard to total concentrations within the pore for $L = 30$ with $k/h = 0.001$ and $\langle A_b \rangle = 0.2$ we specifically find that $\langle X_1 \rangle = 0.321$, $\langle X_2 \rangle = 0.254$, $\langle X_3 \rangle = 0.279$, $\langle X_4 \rangle = 0.270$, $\langle X_5 \rangle = 0.273$, etc., and a total concentration near the pore center of around $\langle X_{\text{int}} \rangle = 0.272$. Clearly all of these values are substantially higher than in the bulk of the external fluid at $\langle X_b \rangle = 0.200$, and also higher than the enhanced value of $\langle X_0 \rangle \approx 0.211$ just outside the pore opening. This strong enhancement of concentration within the pore reflects the much lower

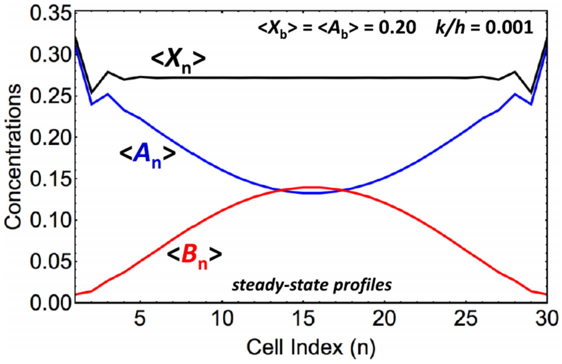

Figure 4.2: Steady-state concentration profiles for $L = 30$ with $k/h = 0.001$ and $\langle A_b \rangle = 0.2$.

coordination of cells within the pore (with 2 neighbors which could possibly be occupied) relative to the coordination of cells in the bulk of the fluid (with 6 neighbors which could be occupied). See Section 4.9 for further discussion including a simple analytic estimate of this strong enhancement. The sudden transition from high-coordinated sites just outside the pore to lower coordinated sites within produces the concentration oscillations near pore openings as is evident in Figure 4.1. We show in Section 4.3 that an accurate analytic description of this complicated behavior is possible within our GH formulation.

4.3 Development of Analytic Theory and Comparison With KMC

4.3.1 Development of analytic GH theory

Deeper insight into reaction model behavior comes from an analytic formulation based on exact master equations for the stochastic process. Let $\langle C_n \rangle$ denote the probability that cell n in the pore is occupied by species $C = A, B$, or is empty E. It is also convenient to introduce the notation $X = A$ or B for either type of species, so that $\langle X_n \rangle = \langle A_n \rangle + \langle B_n \rangle$ denotes the total concentration at cell n. Let $\langle A_n E_{n+1} E_{n+2} \rangle$ denote the probability that cell n is occupied by A and cells $n+1$ and $n+2$ are empty, etc. The NN exclusion constraint and conservation of probability impose various relations on these multisite probabilities [2]. The lowest-order evolution equations have the form

$$\mathrm{d}/\mathrm{d}t \, \langle A_n \rangle = -k \, \langle A_n \rangle - \nabla J_A^{n>n+1}$$

and

$$\mathrm{d}/\mathrm{d}t \left\langle B_n \right\rangle = +k \left\langle A_n \right\rangle - \nabla J_B^{n>n+1}, \quad \text{for } 3 \leq n \leq L-2, \tag{4.1}$$

where

$$J_C^{n>n+1} = h \left[\left\langle C_n E_{n+1} E_{n+2} \right\rangle - \left\langle E_{n-1} E_n C_{n+1} \right\rangle \right] \tag{4.2}$$

is the net diffusion flux of $C = A$ or B from cell n to cell $n+1$. Also $\nabla K_n = K_n - K_{n-1}$ denotes a discrete derivative. Separate equations apply for the end cells, $n = 1, 2$ and $L-1, L$, reflecting the non-trivial adsorption-desorption boundary conditions described above. See Section 4.10. The overall conversion rate of A to B is given by $R_{\text{tot}} = k \sum_n \left\langle A_n \right\rangle$ simply reflecting the total amount of reactant inside the pore. Equation (4.1) is not closed due to the appearance of triplet probabilities in $J_C^{n>n+1}$, but equations can be developed for such multisite probabilities generating a coupled hierarchy. See again Section 4.10.

Adding (4.1) for $\left\langle A_n \right\rangle$ and (4.1) for $\left\langle B_n \right\rangle$ leads to the pure diffusion equations

$$\mathrm{d}/\mathrm{d}t \left\langle X_n \right\rangle = -\nabla J_X^{n>n+1}, \quad \text{for } 3 \leq n \leq L-2, \tag{4.3}$$

for the total concentration $\left\langle X_n \right\rangle = \left\langle A_n \right\rangle + \left\langle B_n \right\rangle$, for diffusion flux $J_X^{n>n+1} = h \left[\left\langle X_n E_{n+1} E_{n+2} \right\rangle - \left\langle E_{n-1} E_n X_{n+1} \right\rangle \right]$. Again, separate equations are needed for end cells, $n = 1, 2$ and $L-1, L$. In the steady-state, the spatial Markov property of 1D lattice models with NN interactions ensures the pair approximation factorization becomes exact, e.g.,

$$\begin{aligned} \left\langle X_n E_{n+1} E_{n+2} \right\rangle &= \left\langle X_n E_{n+1} \right\rangle \left\langle E_{n+1} E_{n+2} \right\rangle / \left\langle E_{n+1} \right\rangle \\ &= \left\langle X_n \right\rangle \left(1 - \left\langle X_n \right\rangle - \left\langle X_{n+1} \right\rangle\right) / \left(1 - \left\langle X_n \right\rangle\right). \end{aligned} \tag{4.4}$$

In obtaining the reduced expression after the last equality, we have also exploited NN exclusion. Using a similar relation for $\left\langle E_{n-1} E_n X_{n+1} \right\rangle$ together with the adsorption-desorption boundary conditions, one can solve exactly a coupled set of equations for $\left\langle X_n \right\rangle$ to recover the oscillations in the total concentration shown in Figure 4.2. See Section 4.11. Such exact solution for steady-state $\left\langle X_n \right\rangle$ does not extend to the transient regime of pore filling, or to the individual reactant and product concentrations.

The fundamental challenge in solving the reaction-diffusion Equation (4.1) is to develop appropriate expressions for the diffusion fluxes, $J_C^{n>n+1}$. MF-type factorization approximations for probabilities of multi- cell configurations can fail dramatically. The *site approximation* neglects all spatial correlations and thus fails even to account for NN exclusion. Furthermore, it greatly overestimates diffusion fluxes for SFD, reactant penetration in the pore, and thus reactivity. The refined *pair approximation* accounts for NN correlations and thus excludes NN occupancy, but it still significantly overestimates diffusion fluxes and related quantities. See Section 4.10. Substantial additional insights into these shortcomings are provided below. An alternative *hydrodynamic treatment* applies for slowly varying concentration gradients, as mentioned previously. Thus, it is not geared to describe concentration oscillations occurring on the nanoscale near pore openings, but it is potentially relevant for description of longer mesoscale concentration variations deeper in the pore which do correspond to a classic counter-diffusion mode. The hydrodynamic diffusion fluxes satisfy $J_C^{n>n+1} = -D_{tr}\nabla \langle C_{n+1}\rangle$, where D_{tr} is the tracer diffusion coefficient for particles X [2,12,19]. However, for SFD, such D_{tr} are negligible, specifically decreasing to zero inversely with the pore length [25–28]. Consequently, this formulation greatly underestimates diffusion fluxes, reactant penetration, and thus reactivity for typical length pores.

Thus, another strategy is required to treat diffusive transport on the mesoscale, also accounting for concentration oscillations. A key ingredient which is motivated by generalized hydrodynamic (GH) treatments of fluids [22] is to replace hydrodynamic transport coefficients with ones appropriate for a shorter mesoscale. In our case, these reflect distinct behavior near the pore openings where fluctuations in adsorption-desorption processes are prominent. Specifically, we replace D_{tr} with a spatially varying $D_{tr}\left(n, n+1\right)$ for each NN pair of cells which is enhanced near the pore openings (see below) [13]. In addition, to ensure the diffusion flux vanishes in the steady-state, we define fractional coverages $\langle c_n\rangle = \langle C_n\rangle / \langle X_n\rangle$ for $C = A$ or B (and $c = a$ or b) and adopt a specific GH form

$$J_C^{n>n+1} = -\frac{1}{2}D_{tr}\left(n, n+1\right)\left(\langle X_n\rangle + \langle X_{n+1}\rangle\right)\nabla\langle c_{n+1}\rangle . \tag{4.5}$$

Note that Equation (4.5) automatically recovers the standard choice for conventional hydrodynamic counter-diffusion where $J_C = -D_{tr}\nabla\langle C\rangle$ in a continuum setting [2,12,19].

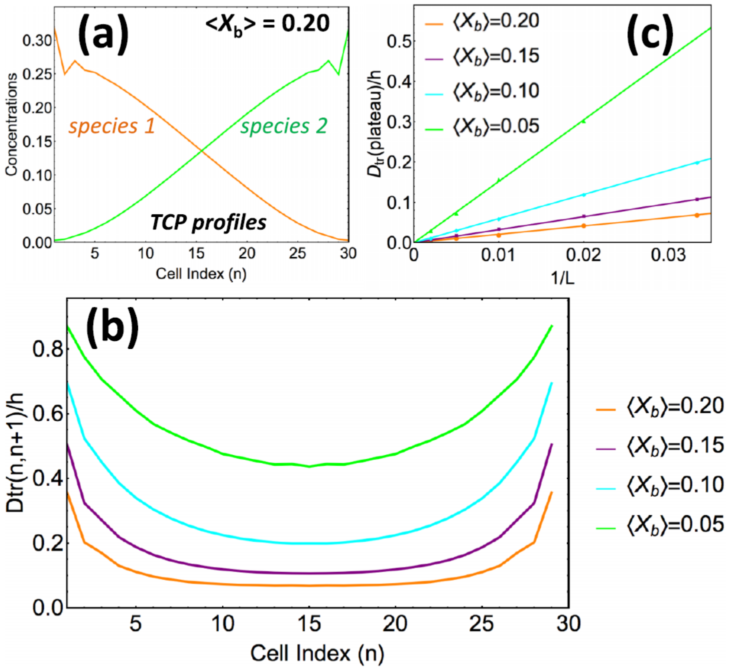

Figure 4.3: TCP concentration profiles for $L = 30$ and $\langle X_b \rangle = 0.20$; (b) GH $D_{tr}(n, n+1)$ versus n for $L = 30$ for various external fluid concentrations $\langle X_b \rangle$; (c) variation D_{tr} (plateau) $\sim \gamma h/L$ with increasing L, where $\gamma = 2.07, 3.23, 5.99, 15.3$ for $\langle X_b \rangle = 0.2, 0.15, 0.1, 0.05$, respectively.

Next, we outline the determination of the GH $D_{tr}(n, n+1)$ from analysis of the so-called tracer counter- permeation (TCP) [19]. Here, a species labeled 1 enters a pore only from the left, and differently labeled species 2 (which is identical in terms of interactions and diffusional dynamics) enters only from the right. Otherwise adsorption and desorption are treated as for the above simulations incorporating non-trivial boundary conditions at the pore opening. The TCP simulations reach a steady-state with equal and opposite fluxes of magnitude J_{TCP} of 1 from left to right, and 2 in the opposite direction through the pore. See Figure 4.3 (a).

Measuring the concentrations at different sites and equating the total flux with an expression of the type (4.5) allows extraction of the generalized tracer diffusion coefficients. Results are shown in Figure 4.3(b) for $L = 30$ (and for larger L in the supplementary material Figure S2). As expected, D_{tr} is naturally strongly reduced for higher total concentrations. Also, the GH $D_{tr}(n, n+1)$ decays to a non-zero plateau value, D_{tr} (plateau), in the pore center for sufficiently large L. Adapting previous studies which considered the overall tracer diffusivity for SFD in finite systems without NN exclusion [13, 19, 27, 28] to account for NN exclusion in our model, we anticipate that

$$D_{tr}\,(\text{plateau}) \sim \langle X_{\text{int}} \rangle^{-1} \left(1 - 2\,\langle X_{\text{int}} \rangle\right) h/L, \quad \text{for large } L. \tag{4.6}$$

Here, $\langle X_{\text{int}} \rangle$ is the plateau value of the total concentration $\langle X_n \rangle$ in the pore center. For $L = 30$, we find that $\langle X_{\text{int}} \rangle = 0.272, 0.210, 0.134$, and 0.059 for longer pores exceeds the external bulk fluid concentration $\langle X_b \rangle = 0.20, 0.15, 0.10, 0.05$, respectively. This relation for $D_{tr}\,(\text{plateau})$ reasonably estimates precise KMC values reported in Figure 4.3(c).

Finally, we remark that the above-mentioned overestimation of the diffusion fluxes by the site and pair approximations can be understood from the corresponding results for tracer diffusivity,

$$D_{tr}\,(\text{site}) = h\left(1 - \langle X_{\text{int}} \rangle\right)$$

and

$$D_{tr}\,(\text{pair}) = h\left(1 - 2\,\langle X_{\text{int}} \rangle\right) / \left(1 - \langle X_{\text{int}} \rangle\right), \tag{4.7}$$

which far exceed $D_{tr}\,(\text{plateau})$ for typical L. Derivation of these results is indicated in Section 4.10.

4.3.2 Predictions of analytic theory

Numerical solution of the GH reaction-diffusion Equation (4.1) is implemented incorporating the expression (4.2) for $J_C^{n>n+1}$ and our exact analytic solution for $\langle X_n \rangle$. The results almost exactly recover the individual reactant and product concentration profiles (including the concentration oscillations) obtained from KMC simulations shown in Figure 4.2 for $k/h = 0.001$, $L = 30$, and $\langle A_b \rangle = 0.2$. The degree of success of the GH theory for a range of k/h retaining $\langle A_b \rangle = 0.2$ is shown in Figure 4.4 focusing on the reactant profiles. Since $\langle X_n \rangle$ is recovered exactly, slight discrepancy in predicting reactant profiles is counterbalanced by a discrepancy of the same magnitude in prediction product profiles. To contrast the success of the GH theory, Figure 4.4 also shows shortcomings of the pair approximation which predicts far too great a reactant penetration into the pore due to overestimation of the diffusion flux in the presence of SFD. See the supplementary material Figure S3 for additional results. Since the total reaction rate, R_{tot}, for conversion of A to B simply reflects the total amount of reactant in the pore,

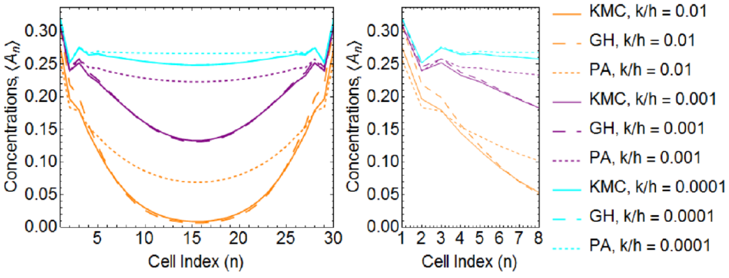

(a) (b)

Figure 4.4: (a) Comparison of GH solutions (long dashed curves) and pair approximation PA (short-dashed curves) predictions with precise KMC results (solid curves) for reactant concentration $\langle A_n \rangle$ for a pore of length $L = 30$ for $\langle A_b \rangle = 0.20$ and varying k/h. (b). Expanded view of behavior near the left end of the pore. GH and KMC results are indistinguishable for $k/h = 0.0001$, and very close for $k/h = 0.001$.

success in predicting the reactant concentration profile automatically translates into success in predicting R_{tot}.

The above results indicate that our GH theory is well-suited to describe the regime of small $k/h \leq 0.001$ where the reactant concentration exhibits slower mesoscale decay into the pore. For larger k/h where the reactant concentration decays more quickly on the nanoscale, the mesoscale GH treatment becomes somewhat less precise (although still reasonably accurate and certainly qualitatively correct). Actually for $k/h \sim 0.1$, higher-order MF type approximations achieve comparable accuracy to the GH formulation. See the supplementary material Figure S4.

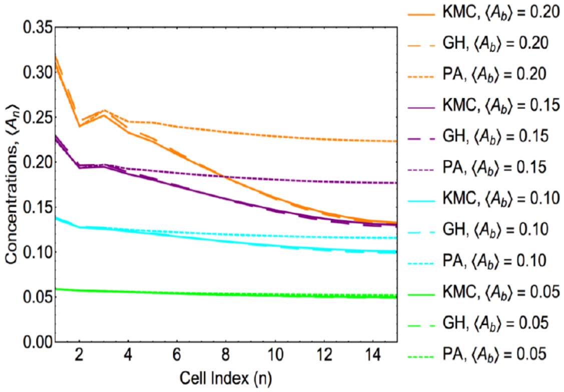

Figure 4.5: Reactant concentration $\langle A_n \rangle$ near the left end of a pore of length $L = 30$ with $k/h = 0.001$ and varying $\langle A_b \rangle$. Comparison of accurate GH solutions (long dashed curves), and pair approximation (PA) predictions, with KMC simulation results (solid curves).

To further illustrate the effectiveness of our GH formulation, one can also consider behavior for fixed $k/h = 0.001$, say, but varying the external fluid concentration $\langle A_b \rangle$. Naturally, this analysis necessarily incorporates the appropriate generalized tracer diffusion coefficients which depend strongly on $\langle A_b \rangle$, as shown in Figure 4.3. Comparison of successful GH predictions with precise KMC results (and also generally inadequate pair approximation predictions) is shown in Figure 4.5. Naturally, for lower concentrations, oscillations become significantly less prominent. Even the pair approximation becomes reliable for low enough concentrations where SFD constraints become less significant.

4.3.3 Characterization of strong non-equilibrium spatial correlations

We have already provided one perspective on why MF-type approximations overestimate reactant penetration into the pore (and thus reactivity), specifically tying this feature to their overestimation of tracer diffusivity. Next, we provide an alternative perspective, and also a deeper understanding of the failure of the conventional MF type approximations. We emphasize that SFD in the presence of a reaction and also NN exclusion generates strong non-equilibrium spatial correlations. A direct consequence of these strong spatial correlations is the feature that the exact diffusion flux,

$$J_A^{n>n+1} = h \left[\langle A_n E_{n+1} E_{n+2} \rangle - \langle E_{n-1} E_n A_{n+1} \rangle \right], \tag{4.8}$$

from 4.2 is *far smaller* than site or pair approximation predictions, and similarly for $J_B^{n>n+1}$. To restate this observation, these strong correlations imply that the triplet probabilities, $\langle A_n E_{n+1} E_{n+2} \rangle$ and $\langle E_{n-1} E_n A_{n+1} \rangle$ are *far closer to each other* than the site or pair approximation predictions.

In the site and pair approximations, neglecting oscillations in the total concentration, one has that

$$\langle A_n E_{n+1} E_{n+2} \rangle \approx G \left(\langle X_{\text{int}} \rangle \right) \langle A_n \rangle$$

and

$$\langle E_{n-1} E_n A_{n+1} \rangle \approx G \left(\langle X_{\text{int}} \rangle \right) \langle A_{n+1} \rangle, \tag{4.9}$$

where $G(x) = (1-x)^2$ in the site approximation and $G(x) = (1-2x)/(1-x)$ in the pair approximation. Thus, the large values of $J_A^{n>n+1}$ derive from the significant difference in the estimates of these triplet probabilities. This difference in turn derives from the significant difference between $\langle A_n \rangle$ and $\langle A_{n+1} \rangle$ near the pore openings given strong concentration variations in that region.

On the other hand, to understand exact behavior, it is useful to first note the exact identities

$$\langle A_n E_{n+1} E_{n+2} \rangle = \langle E_{n-1} A_n E_{n+1} E_{n+2} \rangle$$

and

$$\langle E_{n-1} E_n A_{n+1} \rangle = \langle E_{n-1} E_n A_{n+1} E_{n+2} \rangle \,. \tag{4.10}$$

Here, we have used the feature that the site to the left (right) of A in the configuration $A_n E_{n+1} E_{n+2}$ ($E_{n-1} E_n A_{n+1}$) must be empty due to NN exclusion. Next, considering the central pair of cells n and $n+1$ in the quartet configurations $E_{n-1} A_n E_{n+1} E_{n+2}$ and $E_{n-1} E_n A_{n+1} E_{n+2}$, we recognize that A is likely to hop back and forth between these two cells. This follows as the cells on each end of the quartet are specified empty ensuring that such motion is compatible with NN exclusion. This facile motion naturally tends to equalize these two probabilities. Precise results from KMC simulation analysis shown in Figure 4.6 confirm this picture choosing a longer pore with $L = 100$ to clearly show behavior.

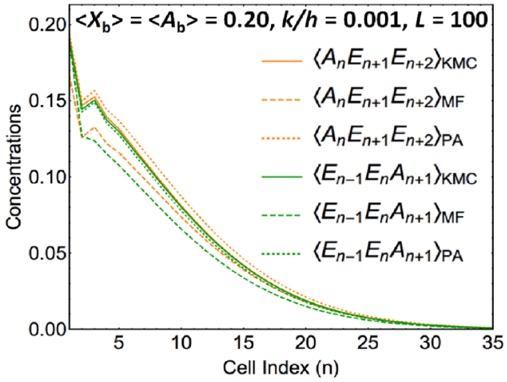

Figure 4.6: Comparison of KMC estimates of key triplet probabilities controlling the diffusion flux of A with site (SA) and pair (PA) approximation estimates for $L = 100$, $k/h = 0.001$, and $\langle A_b \rangle = 0.2$. In 4.9, one has that the prefactor $G \approx 0.530(0.626)$ in the site (pair) approximation, explaining why the latter predictions are slightly larger in magnitude.

4.4 Summary

In summary, catalytic conversion subject to SFD produces strong non-equilibrium spatial correlations which occur in addition to correlations of thermodynamic origin due to intermolecular interactions (NN exclusion in our model). After accounting for equilibrium correlations and concentration oscillations in the total concentration, we show that a suitably refined GH treatment can capture both non-equilibrium and thermodynamic correlations. As a consequence, this formulation can reliably predict the mesoscale variation of the reactant concentration profile (as well as the concentration oscillations), and thus also predict the reaction yield. Our analytic formulation also provides deeper insight into the origin and nature of these correlations than is provided just from KMC simulation studies.

It should also be emphasized that our model is readily amenable to refinement and extension. One can relax the SFD constraint by allowing the exchange of A and B on second NN sites in the pore with rate $p_{\mathrm{ex}}h$, where p_{ex} reflects the passing propensity (and $p_{\mathrm{ex}} = 0$ for SFD) [2]. Passing reduces the strength on the non-equilibrium correlations that develop during reaction, so the GH formulation becomes even more accurate. Also, beyond treatment of just the initial stages of reaction, one can analyze the reaction yield for various specified fractions, f, of reactant converted to product in the external fluid, so now product can renter the pore. (Note that we assume a separation of time scales where the steady-state for a specific f is achieved on a short time scale compared to the overall reaction.) The overall reaction kinetics can be pieced together from a sequence of such simulations for increasing f [2].

4.5 Supplementary Material

See the supplementary material for a more comprehensive set of simulation results for both generalized tracer diffusivity and steady-state concentration profiles. Figure S1: Steady state concentration profiles for increasing pore lengths. Figure S2: Generalized tracer diffusion coefficients, $D_{tr}\left(n, n+1\right)$, versus n for various pore lengths. Table SI gives values for D_{tr} (plateau).

Figure S3. Comparison of KMC, GH, and PA predictions for reactant profiles for various pore lengths. Figure S4. Comparison of predictions from MF-type site, pair, and triplet approximations.

4.6 Acknowledgements

We acknowledge discussions with Igor Slowing and Marek Pruski motivating this study. We thank Tiago Oliveira for discussions on the theoretical formulation. This work was supported by the U.S. Department of Energy (USDOE), Office of Basic Energy Sciences, Division of Chemical Sciences, Geosciences, and Biosciences through the Ames Laboratory Chemical Physics program. The work was performed at Ames Laboratory which is operated for the USDOE by Iowa State University under Contract No. DE-AC02 − 07CH11358.

4.7 Appendix A: Concentration Oscillations in a Semi-Infinite Fluid

Determination of the adsorption rate for reactants into the pore in our model with NN exclusion requires analysis of the concentration variation approaching a planar wall in a semi-infinite lattice-gas model on a simple-cubic lattice with NN exclusion. Consistent with the notation of Section 4.2, we let $\langle X_0 \rangle$ denote the concentration in cells in the layer adjacent to the wall, $\langle X_{-1} \rangle$ the concentration in cells in the next layer away from the wall, $\langle X_{-2} \rangle$ the concentration in the next layer further away, etc., and $\langle X_b \rangle$ denotes the bulk concentration far from the wall.

Simple analytic estimation of this variation, and specifically of the (weakly) enhanced concentration adjacent to the wall, is possible utilizing a pair approximation. To this end, it is convenient to consider the semi-infinite equilibrated fluid as having arbitrary-range exchange dynamics described by a rate r, where exchange events are consistent with NN exclusion. In equilibrium, the corresponding flux of atoms from a cell adjacent to the wall to the bulk, $J_{w \to b}$, and the reverse flux from the bulk to the wall, $J_{b \to w}$, must balance. If P_7 is the probability of an empty cell in the bulk with all six NN cells also empty, then one has that

$$J_{w \to b} = r \langle X_0 \rangle P_7,$$

where

$$P_7 \approx (1 - 2\langle X_b\rangle)^6 / (1 - \langle X_b\rangle)^5 \tag{4.11}$$

in the pair approximation. Let P_6 denote the probability that a cell against the wall, as well as all 5 of the NN cells, are empty. Then, one has that

$$J_{b\to w} = r\langle X_b\rangle P_6,$$

where

$$P_6 \approx (1 - 2\langle X_0\rangle)^4 (1 - \langle X_0\rangle - \langle X_{-1}\rangle) / (1 - \langle X_0\rangle)^4 \tag{4.12}$$

in the pair approximation. Let us first assume that $\langle X_{-1}\rangle \approx \langle X_b\rangle$, i.e., that concentration oscillations die out quickly away from the wall. Then, from the equality $J_{w\to b} = J_{b\to w}$, one obtains that $\langle X_0\rangle \approx 0.2189$ (versus the Monte Carlo simulation value 0.211) for $\langle X_b\rangle = 0.20$. We also obtain $\langle X_0\rangle \approx 0.1071$ (versus the simulation value 0.106) for $\langle X_b\rangle = 0.10$, etc. Thus, the pair approximation gives a quite reliable estimate of the (weak) concentration enhancement near the wall.

The above analysis can be refined to provide additional assessment of concentration oscillations away from the wall. The next level of analysis retains $\langle X_{-1}\rangle$ as an independent variable, but assumes that $\langle X_{-2}\rangle \approx \langle X_b\rangle$. Then, in addition to the equality $J_{w\to b} = J_{b\to w}$, one also balances fluxes between the layer of cells with concentration $\langle X_{-1}\rangle$ and the bulk. Using the pair approximation, this yields two coupled equations for two unknowns, $\langle X_0\rangle$ and $\langle X_{-1}\rangle$ in terms of $\langle X_b\rangle$. Their solution yields $\langle X_0\rangle \approx 0.2192$ and $\langle X_{-1}\rangle \approx 0.1979$ for $\langle X_b\rangle = 0.20$. Thus, one predicts that $\langle X_0\rangle$ and $\langle X_{-1}\rangle$ are 9% above and 1% below $\langle X_b\rangle$, respectively, versus simulation results which give values 6% above and 0.5% below $\langle X_b\rangle$, respectively. This pair approximation analysis also yields $\langle X_0\rangle \approx 0.1072$ and $\langle X_{-1}\rangle = 0.0995$ for $\langle X_b\rangle = 0.10$, also mimicking the rapid decay seen in simulation studies. These results support the assumption in the simplest analysis that concentration oscillations decay quickly away from the wall.

The analytic treatment is readily further refined for an even more complete assessment of concentration oscillations. We have also performed a more complete Monte Carlo simulation analysis of the semi-infinite system with NN exclusion. However, $\langle X_{-2}\rangle$, $\langle X_{-3}\rangle$, etc., are very close to $\langle X_b\rangle$, so the above more limited analysis provides an essentially complete picture.

4.8 Appendix B: Concentration Variations in the External Fluid

Our tailored simulations to extract adsorption and desorption parameters (described in Section 4.2.2) produce nontrivial and distinct concentration variations in the external fluid which might be regarded as a semi-infinite system. For the former, the concentration just depends on distance from the wall. For the latter there is a complicated three-dimensional variation with the strongest deviation from the bulk fluid concentration occurring around the cell specified empty just outside the pore. We argue that information from these tailored simulations provides boundary conditions at pore openings which allow simulation of the reaction model just in the pore region (which in turn recovers reaction behavior in the entire pore + external fluid system). From this perspective, one would also expect that information from the tailored simulations should allow recovery of the equilibrium concentration variations in the external fluid under steady-state conditions. We note that these equilibrium variations are distinct from those in tailored simulations for either adsorption or desorption parameters.

The tailored simulations for adsorption correspond to the situation where the end cell of the pore is empty, which occurs a fraction $\langle E_1 \rangle = 1 - \langle X_1 \rangle$ of the time. Those corresponding to desorption correspond to the situation where this end cell in the pore is occupied, which occurs a fraction $\langle X_1 \rangle$ of the time. Thus, we claim that the equilibrium distribution for the model is simply given by a corresponding weighted average of the distributions in the tailored simulations. This feature is illustrated schematically in Figure 4.7 where we just show concentration variation along a 1D line of cells in the fluid which extend out from the pore opening. The ability to reconstruct the equilibrium distribution from the tailored simulations also reflects a spatial Markov field property of lattice-gas models with NN interactions [29] which applies not just for infinite systems, but also in more complex (e.g., pore + external fluid) geometries. We will elaborate on this feature in a separate paper dealing with more general models.

4.9 Appendix C: Internal Pore Versus External Fluid Concentrations

It is appropriate to provide further insight into the strong enhancement of total concentration in the center of the pore, $\langle X_{\text{int}} \rangle$, relative to that in the external bulk fluid, $\langle X_b \rangle$. The

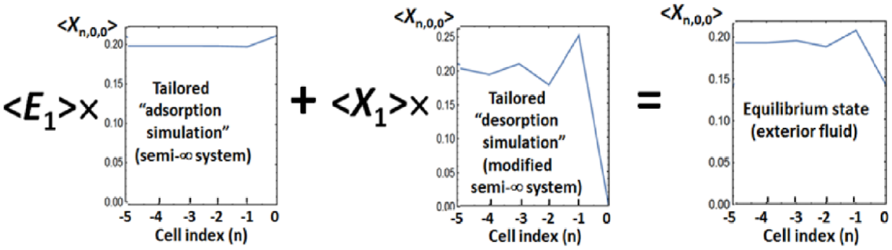

Figure 4.7: Relationship of concentration in external fluid in tailored simulations for adsorption and desorption parameters to the equilibrium concentration distribution for the model. Shown is a 1D cut of the concentration for a line of cells extending from the left end of the pore (where $n = 0$ is just outside the pore, $n = -1$ is further out, etc.). Behavior is shown for $L = 30$ and $\langle X_b \rangle = 0.2$ where $\langle X_1 \rangle = 0.321$ and $\langle E_1 \rangle = 0.679$.

concentration in the center of long pores can be determined directly in terms of $\langle X_b \rangle$ by considering an infinite 3D lattice-gas model with NN exclusion suitably coupled to a 1D lattice-gas model with NN exclusion. Analogous to Section 4.7, this coupling is realized by direct exchange between the systems described by rate r, where exchange events are consistent with NN exclusion. In equilibrium, the corresponding flux of atoms from the 3D to the 1D system, $J_{\text{3D}\to\text{1D}}$, and the reverse flux from the 1D to the 3D system, $J_{\text{1D}\to\text{3D}}$, must balance. If P_7 denotes the probability of an empty cell in the 3D system with all neighbors empty as in (4.11), then one has that

$$J_{\text{1D}\to\text{3D}} = r \langle X_{\text{int}} \rangle P_7, \tag{4.13}$$

where a pair approximation estimate of P_7 is given in (4.11). If P_3 denotes the probability of an empty cell in the 1D system with both neighbors empty, then one has that

$$J_{\text{3D}\to\text{1D}} = r \langle X_b \rangle P_3,$$

where

$$P_3 = (1 - \langle X_{\text{int}} \rangle)^2 / (1 - \langle X_{\text{int}} \rangle) . \tag{4.14}$$

For this 1D model, a pair approximation factorization is in fact exact, so the only approximation is in the factorization of P_7 in (4.13). Then, from the equality $J_{\text{1D}\to\text{3D}} = J_{\text{3D}\to\text{1D}}$, one obtains $\langle X_{\text{int}} \rangle \approx 0.3057$ (versus the precise KMC value of 0.273) for $\langle X_b \rangle = 0.20$. One also obtains $\langle X_{\text{int}} \rangle \approx 0.1374$ (versus the precise KMC value of 0.134) for $\langle X_b \rangle = 0.10$, etc. Not surprisingly, one finds that the pair approximation is somewhat less accurate in predicting the strong enhancement of concentration in the pore interior relative to the bulk (at least for higher $\langle X_b \rangle$) compared to its success in predicting the weak enhancement near infinite walls in Section 4.7. There are other analytic strategies which could be employed, e.g., matching chemical potentials for the 1D and 3D systems, where the latter might be determined, e.g., from virial expansion. However, the pair approximation clearly captures the key feature of concentration enhancement inside the pore.

Precise direct assessment of concentration enhancement inside the pore can naturally also be achieved by Monte Carlo simulation of the coupled 3D and 1D systems. We have implemented such simulations and recover the previously reported values of $\langle X_{\rm int} \rangle$ from KMC simulations of the reaction model.

4.10 Appendix D: Further Analysis of Reaction-Diffusion Equations

In Section 4.3.1 we have described just the lowest-order equations in the coupled hierarchy of exact evolution equations for the stochastic reaction model, e.g.,

$$\mathrm{d}/\mathrm{d}t \, \langle A_n \rangle = -k \, \langle A_n \rangle - \nabla J_A^{n>n+1},$$

where

$$J_A^{n>n+1} = h \left[\langle A_n E_{n+1} E_{n+2} \rangle - \langle E_{n-1} E_n A_{n+1} \rangle \right] \tag{4.15}$$

for $3 \leq n \leq L-2$. As indicated in Section 4.3.1, separate equations are needed for cells at the end of the pore. For example, for $n = 1$, one has

$$\begin{aligned} \mathrm{d}/\mathrm{d}t \, \langle A_1 \rangle = & - k \, \langle A_1 \rangle - h \left[\langle A_1 E_2 E_3 \rangle - \langle E_0 \rangle \langle E_1 A_2 E_3 \rangle \right] \\ & - h \left[P_5 \, \langle A_1 \rangle - \langle A_0 \rangle \langle E_1 E_2 \rangle \right] \end{aligned} \tag{4.16}$$

and

$$\begin{aligned} \mathrm{d}/\mathrm{d}t \, \langle A_2 \rangle = & - k \, \langle A_2 \rangle - h \left[\langle A_2 E_3 E_4 \rangle - \langle E_1 E_2 A_3 E_4 \rangle \right] \\ & - h \left[\langle E_0 \rangle \langle E_1 A_2 \rangle - \langle A_1 E_2 E_3 \rangle \right], \end{aligned} \tag{4.17}$$

where $\langle E_0 \rangle = 1 - \langle A_0 \rangle$, $\langle E_1 A_2 E_3 \rangle = \langle E_1 A_2 \rangle = \langle A_2 \rangle$ and appropriate factorizations are implemented for probabilities of hopping involving the state of cells both inside and just outside the pore. An example of a next-highest-order equation in the hierarchy is

$$\begin{aligned}\mathrm{d}/\mathrm{d}t\,\langle A_n E_{n+1} E_{n+2}\rangle = &-k\,\langle A_n E_{n+1} E_{n+2}\rangle - h\,[\langle A_n E_{n+1} E_{n+2}\rangle - \langle E_{n-1} E_n A_{n+1} E_{n+2}\rangle] \\ &- h\,[\langle E_{n-2} E_{n-1} A_n E_{n+1} E_{n+2}\rangle - \langle A_{n-1} E_n E_{n+1} E_{n+2}\rangle] \\ &- h\,[\langle A_n E_{n+1} E_{n+2} A_{n+3}\rangle - \langle A_n E_{n+1} A_{n+2} E_{n+3} E_{n+4}\rangle] \\ &- h\,[\langle A_n E_{n+1} E_{n+2} B_{n+3}\rangle - \langle A_n E_{n+1} B_{n+2} E_{n+3} E_{n+4}\rangle]\,. \end{aligned} \tag{4.18}$$

We have grouped terms for forward and reverse hopping events between pairs of sites corresponding to loss and gain of the configuration of interest. Since cells adjacent to A or B must be empty, including this feature means that grouped hopping terms include the same set of cells. For example, $\langle A_n E_{n+1} E_{n+2}\rangle = \langle E_{n-1} A_n E_{n+1} E_{n+2}\rangle$ specifies the state of cells $n-1$, n, $n+1$, and $n+2$, as does $\langle E_{n-1} E_n A_{n+1} E_{n+2}\rangle$.

Next, we comment further on MF-type factorization approximations which facilitate truncation of the hierarchy to yield a closed set of evolution equations. The *site approximation* ignoring all correlations sets

$$\langle C_n D_{n+1} F_{n+2}\rangle \approx \langle C_n\rangle\,\langle D_{n+1}\rangle\,\langle F_{n+2}\rangle\,, \tag{4.19}$$

so, e.g., $\langle A_n E_{n+1} E_{n+2}\rangle \approx \langle A_n\rangle\,\langle E_{n+1}\rangle\,\langle E_{n+2}\rangle$, leading immediately to a closed set of equations for $\langle A_n\rangle$ and $\langle B_n\rangle$. However, as noted previously, this approximation does not impose the basic constraint for models with NN exclusion that the concentration in any cell should be no higher than 1/2. The *pair approximation* sets

$$\langle C_n D_{n+1} F_{n+2}\rangle \approx \langle C_n D_{n+1}\rangle\,\langle D_{n+1} F_{n+2}\rangle\,/\,\langle D_{n+1}\rangle\,, \tag{4.20}$$

so, e.g., $\langle A_n E_{n+1} E_{n+2}\rangle \approx \langle A_n E_{n+1}\rangle\,\langle E_{n+1} E_{n+2}\rangle\,/\,\langle E_{n+1}\rangle = \langle A_n\rangle\,(1-\langle X_{n+1}\rangle-\langle X_{n+2}\rangle)\,/\,(1-\langle X_{n+1}\rangle)$. This again leads to a closed set of equations for $\langle A_n\rangle$ and $\langle B_n\rangle$. Results from numerical analysis of these equations are shown in Figs 4.4-4.6, and in the supplementary material. The *triplet approximation* sets

$$\langle C_n D_{n+1} F_{n+2} G_{n+3}\rangle \approx \langle C_n D_{n+1} F_{n+2}\rangle\,\langle D_{n+1} F_{n+2} G_{n+3}\rangle\,/\,\langle D_{n+1} F_{n+2}\rangle\,, \tag{4.21}$$

Thus, this approximation does not directly approximate any quantities (in the flux terms) in the lowest-order equations. However, in higher-order equations such as (4.18), one must implement factorization, e.g., $\langle A_{n-1} E_n E_{n+1} E_{n+2}\rangle \approx \langle A_{n-1} E_n E_{n+1}\rangle\,\langle E_n E_{n+1} E_{n+2}\rangle\,/\,\langle E_n E_{n+1}\rangle$.

This expression can be recast noting that $\langle E_n E_{n+1} E_{n+2} \rangle = \langle E_{n+1} E_{n+2} \rangle - \langle A_n E_{n+1} E_{n+2} \rangle - \langle B_n E_{n+1} E_{n+2} \rangle$ and $\langle E_{n+1} E_{n+2} \rangle = 1 - \langle X_{n+1} \rangle - \langle X_{n+2} \rangle$. From numerical analysis of the equations for the triplet approximation, we find only minor improvement over the pair approximation. See the supplementary material Figure S4. This further demonstrates the challenge of capturing strong non-equilibrium spatial correlations with MF-type approximations, and also highlights the success of the GH approach.

Finally, we discuss the evaluation of tracer diffusivity within the site and pair approximations. To this end, consider the generic form of the reaction-diffusion equations, and specifically the diffusion flux, away from the pore openings where $\langle E_n \rangle \approx \langle E_{\text{int}} \rangle = 1 - \langle X_{\text{int}} \rangle$ is effectively constant. In the site approximation, factorizing $\langle A_n E_{n+1} E_{n+2} \rangle \approx \langle E_{\text{int}} \rangle^2 \langle A_n \rangle$ and $\langle E_{n-1} E_n A_{n+1} \rangle \approx \langle E_{\text{int}} \rangle^2 \langle A_{n+1} \rangle$ yields $J_X^{n>n+1} = -h \langle E_{\text{int}} \rangle^2 \nabla \langle A_{n+1} \rangle$. On the other hand, first utilizing exact identities and then factorizing corresponding to $\langle A_n E_{n+1} E_{n+2} \rangle = \langle A_n - E_{n+2} \rangle \approx \langle E_{\text{int}} \rangle \langle A_n \rangle$ and similarly for $\langle E_{n-1} E_n A_{n+1} \rangle$, yields

$$J_A^{n>n+1}(\text{site}) = -h \langle E_{\text{int}} \rangle \nabla \langle A_{n+1} \rangle . \tag{4.22}$$

We adopt the last analysis which to some extent accounts for NN exclusion. Noting that this analysis applies for a standard counter-diffusion mode, it follows that $D_{tr}(\text{site}) = h \langle E_{\text{int}} \rangle = h (1 - \langle X_{\text{int}} \rangle)$. In the pair approximation, factorizing $\langle A_n E_{n+1} E_{n+2} \rangle \approx \langle E_n E_{n+1} \rangle \langle A_n \rangle / \langle E_n \rangle \approx (1 - 2 \langle X_{\text{int}} \rangle) \langle A_n \rangle / (1 - \langle X_n \rangle)$ and similarly for $\langle E_{n-1} E_n A_{n+1} \rangle$ yields

$$J_A^{n>n+1}(\text{pair}) = -h (1 - 2 \langle X_{\text{int}} \rangle) / (1 - \langle X_{\text{int}} \rangle) \nabla \langle A_{n+1} \rangle . \tag{4.23}$$

Noting that this analysis applies for a standard counter-diffusion mode, it follows that $D_{tr}(\text{pair}) = h (1 - 2 \langle X_{\text{int}} \rangle) / (1 - \langle X_n \rangle)$. Hence, these analyses provide a derivation of (4.7).

4.11 Appendix E: Further Analysis of Reaction-Diffusion Equations for $\langle X_n \rangle$

The (pure) diffusion equations, $\mathrm{d}/\mathrm{d}t \langle X_n \rangle = -\nabla J_X^{n>n+1}$, for the total concentration profile $\langle X_n \rangle$ within the pore are non-trivial due to the NN exclusion constraint. The nontrivial feature is the appearance of triplet probabilities in the expression for the diffusion flux, $J_X^{n>n+1} =$

$h\left[\langle X_n E_{n+1} E_{n+2}\rangle - \langle E_{n-1} E_n X_{n+1}\rangle\right]$, for $3 \leq n \leq L-2$. As with reaction-diffusion equations, some modification is required for the end sites within the pore. For example, one has that

$$\mathrm{d}/\mathrm{d}t\,\langle X_1\rangle = -h\left[P_5\,\langle X_1\rangle - \langle X_0\rangle\,\langle E_1 E_2\rangle\right] - h\left[\langle X_1 E_2 E_3\rangle - \langle E_0\rangle\,\langle E_1 X_2\rangle\right] \tag{4.24}$$

and

$$\mathrm{d}/\mathrm{d}t\,\langle X_2\rangle = h\left[\langle E_0\rangle\,\langle E_1 X_2\rangle - \langle X_1 E_2 E_3\rangle\right] - h\left[\langle X_2 E_3 E_4\rangle - \langle E_1 E_2 X_3\rangle\right], \tag{4.25}$$

where $\langle E_0\rangle = 1 - \langle X_0\rangle$, and appropriate factorizations are implemented for probabilities of hopping involving the state of cells both inside and just outside the pore.

Our interest in these equations is the behavior of the solutions in the equilibrium steady-state. We have argued in (4.4) that in the equilibrium state (but not for time evolution), the factorization of the pair approximation, e.g., $\langle X_n E_{n+1} E_{n+2}\rangle = \langle X_n E_{n+1}\rangle\,\langle E_{n+1} E_{n+2}\rangle\,/\,\langle E_{n+1}\rangle$, becomes exact. This is a consequence of the Markov random field property of equilibrium lattice-gas models in any dimension with NN interactions [29]. It is applied here for the special case of a 1D lattice-gas model with NN exclusion. To clarify this issue, consider the conditional probabilities,

$$\langle C_n | D_{n+1} F_{n+2} \ldots\rangle \equiv \langle C_n D_{n+1} F_{n+2} \ldots\rangle\,/\,\langle D_{n+1} F_{n+2} \ldots\rangle\,, \tag{4.26}$$

for cell n to be in state C *given* that cell $n+1$ is in state D, cell $n+2$ is in state F, etc. Then the spatial Markov property implies that $\langle C_n | D_{n+1} F_{n+2} \ldots\rangle = \langle C_n | D_{n+1}\rangle$, and in particular that $\langle C_n | D_{n+1} F_{n+2}\rangle = \langle C_n | D_{n+1}\rangle$. The latter equality demonstrates that the factorization used in the pair approximation becomes exact.

Application of this factorization allows exact solution for steady-state $\langle X_n\rangle$ by solution of the resulting coupled set of equations given the values of $\langle X_0\rangle$ and P_5 in Section 4.2.2 recover exactly the oscillations in total concentration within the pore, i.e., the concentration oscillation which would be seen in the coupled 1D pore + 3D extended fluid system.

As a final aside, we offer a simple test case for the validity of our strategy of capturing behavior in the pore for a coupled system with analysis just of the pore. Consider a coupled 1D pore + 1D extended fluid again with NN interactions. This just corresponds to an infinite 1D lattice-gas model with NN exclusion so the concentration should be constant, $\langle X_b\rangle$, everywhere in equilibrium. Refining the above equations for this 1D case (where $\langle X_0\rangle$ is replaced by

$\langle X_b \rangle / (1 - \langle X_b \rangle)$ and P_5 is replaced by $(1 - 2\langle X_b \rangle) / (1 - \langle X_b \rangle)$, we find that the equations are consistent with a solution $\langle X_n \rangle = \langle X_b \rangle$ for all n.

Bibliography

[1] K. Lindenberg, G. Oshanin, and M. Tachiya. Chemical kinetics beyond the textbook: Fluctuations, many-particle effects and anomalous dynamics. *J. Phys.: Condens. Matter*, 19(6), 2007.

[2] D-J. Liu, A. García, J. Wang, D. M. Ackerman, C-J. Wang, and J. W. Evans. Kinetic Monte Carlo simulation of statistical mechanical models and coarse-grained mesoscale descriptions of catalytic reaction–diffusion processes: 1D nanoporous and 2D surface systems. *Chem. Rev.*, 115:pp. 5979–6050, 2015.

[3] G. E. Karniadakis, A. Beskok, and N. Aluru. *Microflows and nanoflows: Fundamentals and simulation, 2nd ed.* Springer, New York, 2005.

[4] S. Matera, H. Meskine, and K. Reuter. Adlayer inhomogeneity without lateral interactions: Rationalizing correlation effects in CO oxidation at $\mathrm{RuO_2}(110)$ with first-principles kinetic Monte Carlo. *J. Chem. Phys.*, 142:134703, 2015.

[5] D-J. Liu and J. W. Evans. Transitions between strongly correlated and random steady-states for catalytic CO-oxidation on surfaces at high-pressure. *J. Chem. Phys.*, 142:134703, 2015.

[6] J. Kärger. *Handbook on heterogenous catalysis*, page p. 1714. Wiley-VCH, 2008.

[7] J. G. Tsikoyiannis and J. E. Wei. Diffusion and reaction in high-occupancy zeolite catalysts−I. A stochastic theory. *Chem. Eng. Sci.*, 46:pp. 233–253, 1991.

[8] J. Kärger, M. Petzold, H. P. Pfeifer, S. Ernst, and J. Weitkamp. Single-file diffusion and reaction in zeolites. *J. Catal.*, 136:pp. 283–299, 1992.

[9] C. Rödenbeck, J. Kärger, and K. Hahn. Exact analytical description of tracer exchange and particle conversion in single-file systems. *Phys. Rev. E **55**, 5697 (1997).*, 55:pp. 5697–5712, 1997.

[10] M. S. Okino, R. Q. Snurr, H. H. Kung, J. E. Ochs, and M. L. Mavrovouniotis. A consistent correlation approach to single file diffusion with reaction. *J. Chem. Phys.*, 111:pp. 2210–2221, 1999.

[11] S. V. Nedea, A. P. J. Jansen, J. J. Lukkien, and P. A. J. Hilbers. Steady-state properties of single-file systems with conversion. *Phys. Rev. E*, 65:066701, 2002.

[12] D-J. Liu, J. Wang, D. M. Ackerman, I. I. Slowing, M. Pruski, H-T. Chen, V. S-Y. Lin, and J. W. Evans. Interplay between anomalous transport and catalytic reaction kinetics in single-file nanoporous systems. *ACS Catal.*, 1:pp. 751–763, 2011.

[13] D. M. Ackerman, J. Wang, and J. W. Evans. Generalized hydrodynamic treatment of the interplay between restricted transport and catalytic reactions in nanoporous materials. *Phys. Rev. E*, 108:228301, 2012.

[14] Z. Karpinski, S. N. Gandhi, and W. M. H. Sachtler. Neopentane conversion catalyzed by Pd in L-zeolite: Effects of protons, ions, and zeolite structure. *J. Catal.*, 141:pp. 337–346, 1993.

[15] F. J. M. M. de Gauw, J. van Grondelle, and R. A. van Santen. Effects of single-file diffusion on the kinetics of hydroisomerization catalyzed by Pt/H–mordenite. *J. Catal.*, 204:pp. 53–63, 2001.

[16] L. Heinke, D. Tzoulaki, C. Chmelik, F. Hibbe, J. M. van Baten, H. Lim, J. Li, R. Krishna, and J. Kärger. Assessing guest diffusivities in porous hosts from transient concentration profiles. *Phys. Rev. Lett.*, 102:065901, 2009.

[17] B. G. Trewyn, I. I. Slowing, S. Giri, H-T. Chen, and V. S-Y. Lin. Synthesis and functionalization of a mesoporous silica nanoparticle based on the Sol–Gel process and applications in controlled release. *Accounts Chem. Res.*, 40:pp. 846–853, 2007.

[18] K. Kandel, S. M. Althaus, C. Peraphatdit, B. G. Trewyn, M. Pruski, and I. I. Slowing. Substrate inhibition in the heterogeneous catalyzed aldol condensation: A mechanistic study of supported organocatalysts. *J. Catal.*, 291:pp. 63–68, 2012.

[19] P. H. Nelson and S. M. Auerbach. Modeling tracer counter-permeation through anisotropic zeolite membranes: from mean field theory to single-file diffusion. *Chem. Eng. J.*, 74:pp. 43–56, 1999.

[20] H. Spohn. *Large scale dynamics of interacting particles.* Springer, Berlin, 1991.

[21] A. Massi and E. Presutti. *Mathematical methods for hydrodynamic limits*, volume 1501. Springer Lectures in Mathematics, Berlin, 1991.

[22] B. J. Alder and W. E. Alley. Generalized hydrodynamics. *Phys. Today*, page p. 55, January 1984.

[23] A. Z. Panagiotopoulos. Thermodynamic properties of lattice hard-sphere models. *J. Chem. Phys.*, 123:104504, 2005.

[24] S. H. Payne and H. J. Kreuzer. Diffusion in a one-dimensional system with nearest and next-nearest neighbor interactions: Exact analysis based on the kinetic lattice gas model. *Phys. Rev. B*, 75:115403, 2007.

[25] E. J. A. Lea. Permeation through long narrow pores. *J. Theor. Biol.*, 5:pp. 102–107, 1963.

[26] D. G. Levitt and G. Subramanian. A new theory of transport for cell membrane pores. II. Exact results and computer simulation (molecular dynamics). *Biochim. Biophys. Acta*, 373:pp. 132–140, 1974.

[27] H. van Beijeren, K. W. Kehr, and R. Kutner. Diffusion in concentrated lattice gases. III. Tracer diffusion on a one-dimensional lattice. *Phys. Rev. B*, 28:pp. 5711–5723, 1983.

[28] H. Hahn and J. Kärger. Deviations from the normal time regime of single-file diffusion. *J. Phys. Chem. B*, 102:pp. 5766–5771, 1998.

[29] R. Kindermann and J. L. Snell. *Markov random fields and their applications.* American Mathematical Society, Providence, 1980.

CHAPTER 5. BOUNDARY CONDITIONS FOR DIFFUSION-MEDIATED PROCESSES WITHIN LINEAR NANOPORES: EXACT TREATMENT OF COUPLING TO AN EQUILIBRATED EXTERNAL FLUID

A paper published in the *Journal of Physical Chemistry - C*

Andrés García and James W. Evans[*]

Division of Chemical & Biological Sciences, Ames Laboratory– USDOE
and Department of Physics & Astronomy, Iowa State University, Ames, Iowa 50011, USA

Abstract

We consider a variety of diffusion-mediated processes occurring within linear nanopores, but which involve coupling to an equilibrated external fluid through adsorption and desorption. By determining adsorption and desorption rates through a set of tailored simulations, and by exploiting a spatial Markov property of the models, we develop a formulation for performing efficient pore-only simulations of these processes. Coupling to the external fluid is described exactly through appropriate non-trivial boundary conditions at the pore openings. This formalism is applied to analyze: (*i*) tracer counter permeation (TCP) where different labeled particles adsorb into opposite ends of the pore and establish a non-equilibrium steady state; (*ii*) tracer exchange (TE) with exchange of differently labeled particles within and outside the pore; and (*iii*) catalytic conversion reactions where a reactant in the external fluid adsorbs into the pore and converts to a product which may desorb. The TCP analysis also generates a

---

[*] Author to whom correspondence should be addressed. Electronic mail: evans@ameslab.gov

position-dependent generalized tracer diffusion coefficient, the form of which controls behavior in the TE and catalytic conversion processes. We focus on the regime of single-file diffusion within the pore which produces the strongest correlations and largest deviations from mean-field type behavior. Behavior is quantified precisely via kinetic Monte Carlo simulations, but also captured with appropriate analytic treatments.

5.1 Introduction

There is extensive interest in diffusion-mediated processes within arrays of linear nanopores as found in microporous and mesoporous materials including zeolites, metal organic frameworks, and classes of mesoporous carbon and silica nanoparticles [1–4]. Many related studies for both gas-phase and solution-phase systems are motivated by applications to separations and catalysis. Behavior of these diffusion-mediated processes is often strongly impacted by inhibited transport within narrow pores. The extreme case of single-file-diffusion (SFD), where the pores are so narrow that molecules cannot pass within the pore [5–8], is well-known to exhibit anomalous tracer diffusion [9].

In gas-phase systems, Knudsen diffusion generally applies within the narrow pores of interest here. Behavior can be quantified by Molecular Dynamics (MD) simulations, results of which are sometimes mapped onto one-dimensional (1D) lattice models for diffusion with lattice sites representing, e.g., distinct cages in zeolitic materials [1, 2, 4]. In the solution-phase systems of primary interest here, each pore has open ends and its interior is typically coupled through adsorption and desorption of particles to a well-stirred equilibrated external fluid. We will focus on the transport of larger molecular species with linear size comparable to the pore diameter, and thus which are subject to SFD, in a solvent of smaller molecules which will be treated implicitly in our modeling. One could thus regard the larger species as following Brownian or Langevin type dynamics due to random collisions with the solvent species [10,11]. Basic features of the diffusion coefficient for such species might be suggested by predictions of hydrodynamic formulations [12], including the effects of confinement [13, 14]. However, it is recognized that related Stokes-Einstein-Debye type formulations can breakdown on the molecular scale [15, 16]. Instead, a more precise characterization of diffusion behavior can in principle be provided by appropriate classical or Langevin MD simulations incorporating a complete specification of relevant interactions in the system.

We argue that the detailed form of interactions between diffusing particles (other than steric blocking which imposes SFD), and of any variation of diffusivity across the pore, will not impact the basic features of transport subject to SFD which will be characterized in this study. Indeed, for this reason, the majority of previous studies of SFD have used simplified models to better elucidate the fundamental origins and nature of transport behavior.

There are in fact a variety of diffusion-mediated processes in finite-length nanopores for which theoretical analyses, and where possible also experimental investigation, are of particular interest. These include the following:

(i) Assessment of the mean-squared displacement (MSD) of a tagged particle within a pore [17, 18]. Recently, the dependence of MSD behavior on initial location of the tagged particle was used to define a location-dependent generalized tracer diffusion coefficient [19, 20].

(ii) Tracer exchange (TE) where tagged particles from the external fluid enter a pore initially filled with untagged particles [21–23], and tracer zero-length column (TZLC) experiments which can track the desorption of tagged particles initially within a pore to an external fluid populated by untagged particles [18]. Behavior in both cases reflects the location-specific and mean values of the intra-crystalline residence time [14]. These residence times can also be determined directly by simulation.

(iii) Tracer counter permeation (TCP) analysis of transport within finite length nanopores where different ends of each pore are connected to decoupled reservoirs with differently labeled but otherwise identical particles [24, 25]. Assessment of steady-state fluxes of labeled particles through the pore then quantifies the intra-pore diffusivity. Characterization of the concentration profiles for labeled particles, together with the above-mentioned flux, provides another route for determination of a generalized tracer diffusion coefficient [20, 24, 25].

(iv) Catalytic conversion reactions where a reactant diffuses into the pore from the external fluid, converts to product at interior catalytic sites, and then possibly exits the pore [19–21,26–29]. Catalytic yield is reduced by inhibited transport within the pore, especially SFD, which greatly limits efficient removal of product from the pore.

To describe these processes, we will consider spatially-discrete stochastic lattice-gas (LG) models where both the pore region and external fluid are tessellated into a simple-cubic array of cells, and where discrete molecular positions correspond to the centers of the cells [20]. Adsorption to and desorption from a pore, and also diffusion within a pore, involve hopping between adjacent cells. This modeling framework enables Kinetic Monte Carlo simulation of the overall diffusion or reaction-diffusion process on the appropriate time- and length-scales. Furthermore, by considering increasingly finer arrays of cells (relative to molecular sizes and the pore dimensions), one can approach a more realistic stochastic continuum model. This strategy is familiar for equilibrium studies of fluids [30]. For our application, the discrete models approach a continuum multi-particle Langevin diffusion-type model (for which direct Langevin simulation is generally not computationally viable).

However, even simulation of the spatially-discrete models would be prohibitive if it was necessary simulate explicitly diffusive dynamics in the external fluid as well as in the pore interior. Thus, our goal here is to show that this is not necessary. Specifically, one can perform "standalone" simulations of the pore region provided that one determines appropriate non-trivial boundary conditions (BC's) describing the coupling to the external fluid through adsorption-desorption processes. We will show that determination of these BC's can be achieved with a special set of *tailored simulations* to characterize adsorption and desorption propensities (and sometimes other features), as will be described in detail in the following Sections. We emphasize that the possibility of exact pore-only simulations utilizing just a finite number of boundary conditions derives from the imposed equilibrium condition on the external fluid.

For simplicity, we focus attention on models with a single type of particle with regard to both inter-particle interactions and pore-particle interactions, and also with regard to particle hopping dynamics. However, these particles can be colored, labelled, or tagged differently as is appropriate for various applications or analyses [17–22, 24–29], as will be described in Section 5.2.2. For these classes of models, in a "color-blind" characterization of the system which does not distinguish between differently labeled particles, steady-states correspond to a classic single-component equilibrium system. We shall see that the complex pore + exterior fluid geometry of the system induces a non-trivial heterogeneity in the total concentration for models with non-trivial inter-particle interactions. Nonetheless, despite the complex model geometry, one can exploit a spatial Markov "shielding" property of such equilibrium lattice-gas models [31]. This property allows, e.g., exact analytical determination of the behavior of the total particle concentration within the pore given the above boundary conditions. In contrast, properties involving labeled particles cannot generally be determined exactly by analytical methods. However, they can be obtained efficiently from pore-only simulations using appropriate BC's.

In Section 5.2 we describe in more detail the basic stochastic LG models with just steric interactions and uniform diffusivity on which we focus here, and introduce appropriate notation. In Section 5.3, we develop an exact formulation and determination of adsorption-desorption rates and boundary conditions for these models. KMC simulation results for TCP, TE, and catalytic conversion are presented in Section 5.4. In Section 5.5, additional analytic results are provided which provide deeper insight into observed behavior. Model refinements including the introduction of finite strength interactions between particles, and variability in diffusion across the pore, are described in Section 5.6. Finally, conclusions are presented in Section 5.7.

5.2 Basic Models and Notation

5.2.1 Stochastic LG models

In our LG models, the pore is represented by a cubic array of $N \times M \times L$ cells, with cross-section size of $n_x = N \times M$ and pore length L, and where typically $L \approx 25 - 200$. For our applications, the lattice constant, a, is regarded as comparable to or smaller than the typical molecular size of $\sim 1\,\mathrm{nm}$, so these pore lengths are of the order of $aL \sim 100\,\mathrm{nm}$. Below, for convenience we set $a = 1$. The pore is connected at either end to reservoirs which are represented by semi-infinite cubic lattices of cells. As noted in Section 5.1, particles have discrete locations corresponding to cell centers. For the models considered in this study, these particles are subject to finite-range R exclusion interactions. $R = 0$ corresponds to exclusion of multiple occupancy of cells, but otherwise there are no interactions between particles; $R = 1$ corresponds to nearest-neighbor (NN) exclusion, so there are no occupied NN pairs of cells; $R = \sqrt{2}$ corresponds to NN and second NN exclusion, etc. Regarding particles as non-overlapping spheres centered on cells, $R = 0$ corresponds to sphere diameter $0 < d \leq 1$, $R = 1$ to $1 < d \leq \sqrt{2}$, $R = \sqrt{2}$ to $\sqrt{2} < d \leq \sqrt{3}$, $R = \sqrt{3}$ to $\sqrt{3} < d \leq 2$, $R = 2$ to $2 < d \leq \sqrt{5}$, etc. Particles hop at rate h (per direction) between adjacent cells within the pore, and also between adjacent cells near the pore opening with one cell just inside and one just outside the pore. In all cases, hopping is subject to the exclusion interactions. Thus, a hop occurs only if the selected NN cell is empty and also if hopping to that cell creates no pairs of particles within the exclusion range (e.g., no NN pairs of particles for $R = 1$). Previous studies have considered these models extensively for $1 \times 1 \times L$ cell pores with $R = 0$ [17, 19–22, 25–29] and in one case with $R = 1$ [32].

Particles within semi-infinite reservoirs coupled to each end of the pore are regarded as equilibrated. In this respect, the hopping or exchange dynamics for such particles between cells in the external fluid is irrelevant. However, one could regard this equilibration as being due to very rapid hopping between adjacent cells, again subject to the range R exclusion interactions.

For applications to TE, TCP, or catalytic conversion, particles will be appropriately assigned one of two labels, A or B, or colors, blue or red, respectively, as described in detail below. However, they retain the same hopping dynamics and interactions. Thus, as noted in Section 5.1, if one is color blind and just considers the distribution of particles of either color, $X = A + B$, this distribution in the steady-state corresponds to a classic equilibrium distribution for a single-component lattice-gas subject to range R exclusion. Even for the complex pore + exterior fluid geometry, these models satisfy a *spatial Markov property* [31]. This property implies that a wall of cells with specified state of suitably defined thickness, R, dividing the system into two disconnected regions shields cells on one side from the influence of those on the other. This feature is most useful considering walls composed of $N \times M \times R$ linear segments of cells within the pore, as will be illustrated below. Another significant feature of these hard-core type models for the equilibrated external fluid on the 3D cubic lattice is that they exhibit non-trivial *phase transitions* which correspond to order-disorder transitions for smaller R, and first-order transitions for larger R [30]. For example, for $R = 1$ (NN exclusion), the interacting particle model has a non-trivial equilibrium state exhibiting an order-disorder transition at a critical concentration of $\langle X_c \rangle \approx 0.209$ [30]. For $R = \sqrt{2}$, the model exhibits an order-disorder transition at critical concentration $\langle X_c \rangle \approx 0.104$ [30], etc.

Also of particular significance, we note that consideration of limiting behavior of these equilibrium LG models for increasing R is well-known to provide an effective tool to elucidate behavior of the continuum hard-sphere model [30]. Returning to the non-equilibrium TE, TCP and catalytic conversion models, as noted in Section 5.1, our discrete LG models will approach continuum Langevin diffusion or reaction-diffusion models upon simultaneously increasing the exclusion range, R, and pore dimensions, so that R remains a fixed fraction of the pore diameter.

5.2.2 Particle labeling for various applications

Next, we describe the labelling or coloring of particles appropriate for various analyses or applications. First, we discuss analysis of *tracer diffusion* of tagged particle(s) for studies of MSD or TE. Extending basic studies of *mean-square displacement* (MSD) [17] for $R = 0$ to $R > 0$, one would first equilibrate a distribution of unlabeled particles in the entire external fluid + pore system at a prescribed external fluid concentration, $\langle X_b \rangle$. Then, a single particle at a specified initial position inside the pore would be tagged or colored, with the rest of the particles inside and outside the pore being untagged or uncolored. One must also specify how the evaluation of MSD accounts for those trajectories where the tagged particle exits the pore [13]. For analysis of *tracer exchange* (TE) [22], again one would first equilibrate unlabeled particles for a prescribed $\langle X_b \rangle$. Then, particles initially outside the pore would be colored blue and labeled A , and those initially inside the pore would be colored red and labeled B. Thus, A diffuses into the pore, and B diffuses out of the pore irreversibly as it becomes instantaneously diluted in the well-stirred external fluid of A and does not reenter. These studies track the evolution of the concentration profiles and thus the total number of A and B in the pore. The tracer exchange curve, $\gamma(t)$, is defined as the fraction of A particles in the pore, so that

$\gamma(0) = 0$ and $\gamma(t) \to 1$ as $t \to \infty$ [21]. The mean intercrystalline residence time can be obtained from [21]

$$\tau_{\text{intra}} = \int_{0<t<\infty} \mathrm{d}t \left[1 - \gamma(t)\right].$$

For *tracer counter permeation* (TCP) studies [24], particles in the reservoir coupled to the left end of the pore are colored blue and labeled A, and those in the reservoir coupled to the right end are colored red and labeled B, say. Both reservoirs have the same bulk concentration, $\langle X_b \rangle$. After adsorption, there is a finite probability that A (B) particles diffuse through the pore and exit the opposite right (left) end, where they are immediately infinitely diluted in the equilibrated reservoir of B (A) particles. Thus, particles after completely traversing the pore do not re-enter. After a transient period depending on the initial conditions [25], the system reaches a non-equilibrium steady state. In this steady-state, one can monitor the equal and opposite but non-trivial fluxes of colored particles through the pore to assess diffusivity within the pore. From the ratio of these fluxes and the local steady-state concentration gradients, one can determine a generalized tracer diffusion coefficient [24, 25].

In our treatment of simple first-order *catalytic conversion reactions* [19, 26–29], reservoirs connected to both ends of the pore are exclusively populated by reactant particles which are colored blue and labeled A, say. Once reactant particles have diffused into the pore, they convert to product particles colored red or labeled B, say, at specified catalytic cells at rate r. This reaction rate, r, is an additional parameter in the reaction model, behavior of which depends strongly on the ratio r/h. Product particles have the same interactions and diffusion dynamics as reactant particles, and can in principle exit the pore (although a SFD constraint greatly inhibits this process). When product exits the pore, it is immediately infinitely diluted in the reactant reservoirs and does not re-enter the pore. After a transient period reflecting the initial conditions, the system reaches a non-equilibrium steady state with reactant (product) concentration decaying (growing) into the pore with the center of long pores exclusively populated by product. For systems subject to SFD, reactant penetration to the pore, and thus catalytic yield, is greatly inhibited.

We could (but do not) consider other more complex catalytic conversion processes within this framework of a single type of particle (with regard to interactions and hopping dynamics) but with different labels. For example, one could consider sequential multi-step conversion reactions, $A \to B \to C$ occurring at specified cells within the pore [33]. Alternatively, one could consider different reactants A in the left and B in the right reservoirs which diffuse into the pore and when on adjacent sites undergo a bimolecular reaction $A + B \to C + D$ (with C replacing A, and D replacing B).

Finally, our primary interest here is in analyzing TCP, TE, and catalytic conversion subject to a SFD constraint which induces the strongest non-equilibrium correlations and most non-trivial behavior [20]. This SFD condition is simply imposed by selecting the range of the exclusion interaction so that particles cannot pass within the pore.

5.2.3 Notation

Cells are labeled by (i, j, k) where k corresponds to the direction of the pore axis, and layers or planes of cells within the pore correspond to $k = 1$ to L. Layers just outside the pore correspond to $k = 0$ and $k = L + 1$. For all k, (i, j) labels the position of cells in planes orthogonal to the direction of the pore axis. Again, the lattice constant is set as $a = 1$ below. For particles of type $C = A$, B, or X, we let $\langle C_{i,j,k} \rangle$ denote the probability that cell (i, j, k) is occupied by (the center of) a particle of type C. If $\langle E_{i,j,k} \rangle$ denotes the probability that cell (i, j, k) is empty, then $\langle A_{i,j,k} \rangle + \langle B_{i,j,k} \rangle = \langle X_{i,j,k} \rangle$ and $\langle E_{i,j,k} \rangle + \langle X_{i,j,k} \rangle = 1$. We also define the average concentration in a layer k within the pore as $\langle C_k \rangle = \sum_{i,j} \langle C_{i,j,k} \rangle / \sum_{i,j} 1$, where $\sum_{i,j} 1 = n_x = N \times M$. We will also need to consider probabilities of various multi-cell configurations, e.g., $\langle C_{i,j,k} E_{i,j,k+1} \rangle$ denotes the probability that cell (i, j, k) is occupied by C, and cell $(i, j, k + 1)$ is empty. It will also be instructive to consider associated conditional probabilities, $\langle \Omega | \Xi \rangle = \langle \Omega \Xi \rangle / \langle \Xi \rangle$, which denotes the probability of Ω *given* Ξ, where Ω and Ξ denote the configurations of non-intersecting subsets of cells. For example $\langle C_{i,j,k} | E_{i,j,k+1} \rangle = \langle C_{i,j,k} E_{i,j,k+1} \rangle / \langle E_{i,j,k+1} \rangle$ denotes the probability that cell (i, j, k) is occupied by C *given* that cell $(i, j, k + 1)$ is empty. Again, $\langle X_b \rangle$ denotes the particle concentration in the bulk external fluid far from the pore openings, and $\langle E_b \rangle = 1 - \langle X_b \rangle$.

5.3 Adsorption-Desorption Boundary Conditions for Basic Models

Below, we describe the development of adsorption-desorption boundary conditions for various pore cross-sections and interaction ranges, R. First, we consider the simplest and most coarse-grained model of a $1 \times 1 \times L$ cell pore. Next, we consider the more complex cases of a $2 \times 1 \times L$ and more general $N \times 1 \times L$ cell pores. Finally, we treat cases of $2 \times 2 \times L$ and more general $N \times N \times L$ cell pores.

5.3.1 $1 \times 1 \times L$ cell pore (the coarsest model)

Cells in the pore correspond to $(i, j, k) = (0, 0, 0)$ with $k = 1$ to L, and for these cells we just use a single label k. The left (right) reservoir corresponds to cells (i, j, k) with $k \leq 0$ ($k \geq L + 1$). We consider LG models for various exclusion ranges, R. As indicated in Section 5.2.1, we will utilize a spatial Markovian shielding property for the equilibrium steady-state of these models [31]. One manifestation of this property is that strings of R contiguous cells within the pore with specified state shield cells on one side of the string from the effect of cells on the other side. Below we focus on determining adsorption and desorption rates for various R. Schematics of these processes are provided in Figure 5.1(a)-(e) where the actual 3D cubic lattice of cells in the semi-infinite external fluid reservoirs is for convenience represented by 2D square lattice of cells. The discussion below however refers to the actual 3D reservoirs. Specifically, we develop expressions for the rates of adsorption and desorption of particles of type $C = A$, B, or X, where adsorption, we assume that the relevant reservoir is exclusively populated by C with a fixed bulk concentration $\langle C_b \rangle = \langle X_b \rangle$.

Exclusion range $R = 0$, i.e., no interactions between particles on adjacent cells, but exclusion of multiple occupancy of a single cell. See Figure 5.1(a)-(b). The maximum concentration is $\langle X_{\max} \rangle = 1$. This classic non-interacting model has been considered in most previous studies of TE, TCP, and conversion reactions [17–22, 24–29]. The model thermodynamics is trivial, the equilibrium state corresponding to a random distribution of particles with the prescribed concentration $\langle X_b \rangle$. Thus, the rate of adsorption, R_{ads}, to an end site within the pore, and the

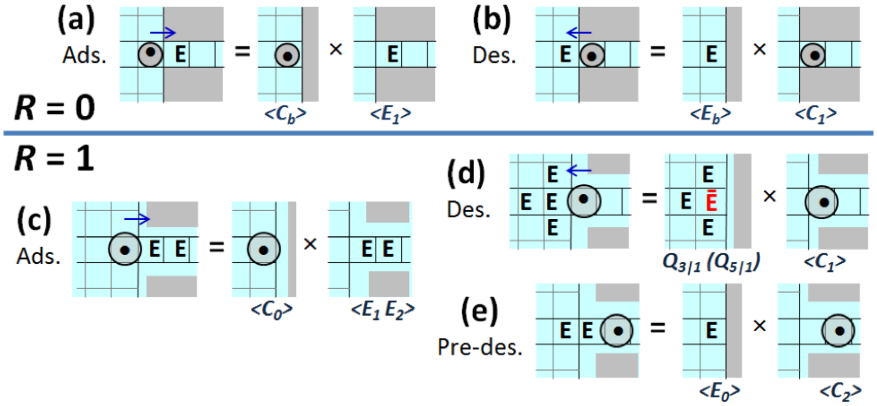

Figure 5.1: 2D schematic of configurations relevant for adsorption, desorption, and pre-desorption in $1 \times 1 \times L$ cell models for $R = 0$ and $R = 1$. E denotes empty cells; $\bar{E}$ in red denotes cells prescribed to be empty. Conditional probabilities, $Q_{n|m}$, indicating the number of sites required (n) and given (m) empty for a 2D (3D) exterior fluid lattice.

rate of desorption, R_{des}, from an end site within the pore to the exterior fluid, are trivially

$$R_{\mathrm{ads}} = h \langle C_{0,0,0} E_1 \rangle = h \langle C_b \rangle \langle E_1 \rangle , \quad \text{and} \quad R_{\mathrm{des}} = h \langle C_{0,0,0} C_1 \rangle = h \langle E_b \rangle \langle C_1 \rangle . \tag{5.1}$$

Here, we use that $\langle C_{0,0,0} \rangle = \langle C_b \rangle = \langle X_b \rangle$, since the external fluid concentration is uniform, and we use that cell occupancies inside and outside the pore are uncorrelated.

Exclusion range $R = 1$, i.e., no nearest-neighbor (NN) pairs of particles. The maximum concentration is now $\langle X_{\max} \rangle = 1/2$ both within the pore and in the exterior fluid. Recall that this $R = 1$ model exhibits an order-disorder transition in the external fluid at $\langle X_c \rangle \approx 0.209$ [30]. Treatment of adsorption and desorption in this model is now non-trivial [32]. Noting that both cell 1 and cell 2 must be empty for adsorption to a left end cell 1 within the pore (see Figure 5.1(c)), the corresponding rate is given by

$$R_{\mathrm{ads}} = h \langle C_{0,0,0} E_1 E_2 \rangle = h \langle C_{0,0,0} | E_1 E_2 \rangle \langle E_1 E_2 \rangle \equiv h \langle C_0 \rangle \langle E_1 \rangle \langle E_2 \rangle . \tag{5.2}$$

Using the spatial Markov property that a single cell shields for $R = 1$, one has that $\langle C_0 \rangle = \langle C_{0,0,0} | E_1 E_2 \rangle = \langle C_{0,0,0} | E_1 \rangle$ is the conditional concentration at cells just outside the pore opening *given* that the end cell within the pore is empty. In fact, $\langle C_0 \rangle$ corresponds to the concentration in the layer against the wall for a semi-infinite system with $R = 1$, and thus can be determined from a tailored simulation for such a semi-infinite system. Its value is slightly enhanced relative to $\langle C_b \rangle$ since such cells against the wall in 3D have only 5 NN which could be occupied (versus 6 in the bulk).

Desorption from an end site within the pore to the exterior fluid requires the target site just outside the pore be empty as well as the additional five cells NN to that cell in the 3D external fluid [32]. See Figure 5.1(d). The associated rate of desorption from the left end of the pore is given by

$$\begin{aligned} R_{\text{des}} &= h \langle E_{0,0,-1} E_{1,0,0} E_{-1,0,0} E_{0,1,0} E_{0,-1,0} E_{0,0,0} C_1 \rangle \\ &= h \langle E_{0,0,-1} E_{1,0,0} E_{-1,0,0} E_{0,1,0} E_{0,-1,0} | E_{0,0,0} C_1 \rangle \langle E_{0,0,0} C_1 \rangle = h Q_{5|1} \langle C_1 \rangle . \end{aligned} \tag{5.3}$$

We use that $\langle E_{0,0,0} C_1 \rangle = \langle C_1 \rangle$ and also use the spatial Markov property

$$Q_{5|1} = \langle E_{0,0,-1} E_{1,0,0} E_{-1,0,0} E_{0,1,0} E_{0,-1,0} | E_{0,0,0} \rangle .$$

The conditional probability, $Q_{5|1}$ is determined from a separate tailored simulation for a semi-infinite system with $R = 1$ and one cell against the wall specified empty, where one determines the conditional probability that 5 NN cells are empty in 3D.

Stand-alone simulations must also treat the pre-desorption step of hopping from cell 2 to cell 1 at the end of the pore which requires the cell just outside the pore to be empty. This probability is just $\langle E_{\text{pre}} \rangle = \langle E_0 \rangle = 1 - \langle X_0 \rangle$, as indicated in Figure 5.1(e).

Exclusion range $R > 1$. The rate of adsorption to an end site within the pore can again be expressed as the product of the concentration, $\langle C_0 \rangle$, of particles against the wall in a semi-infinite fluid times the probability of a suitable string of empty sites within the pore. Desorption from and end site within the pore now requires a larger set of cells just outside the pore to be empty, and the associated rate of desorption factors as the product of $\langle C_1 \rangle$ times a suitable conditional probability. Multiple non-trivial pre-desorption rates must also be determined. See Section 5.10 for $R = 2$.

5.3.2 $2 \times 1 \times L$ cell pore

This case presents new features not seen for the $1 \times 1 \times L$ cell models, which are readily illustrated schematically given the 2D pore geometry. Cells in the pore correspond to $(i, j, k) =$

$(0,0,k)$ and $(0,1,k)$ with $k = 1$ to L, and for these cells we just use a label $k_-\,(k_+)$ for $j = 0\,(j = 1)$. Note that $\langle C_{k_-}\rangle = \langle C_{k_+}\rangle$, i.e., there is just a single independent concentration for each layer k within the pore. Again, we will prescribe the treatment of adsorption, desorption, and pre-desorption processes, but we must also now prescribe the treatment of diffusion within the end layer in the pore. Exclusion range $R = 0$ again has a maximum concentration of $\langle X_{\max}\rangle = 1$ and allows a simple treatment of adsorption-desorption since the exterior fluid is random. However, $R = 0$ does not impose SFD and thus leads to greatly enhanced diffusion within the pore relative to cases with SFD. We do not comment further on this case. We will instead focus on the case $R = 1$ below, and provide extensive simulation results for this case in Section 5.4.

Exclusion range $R = 1$, i.e., no nearest-neighbor (NN) pairs of particles. In this case, there is at most a single particle in each layer k within the pore, and SFD is imposed. The maximum concentration is $\langle X_{\max}\rangle = 1/2$ both inside the pore and in the exterior fluid. An order-disorder transition occurs in the external fluid at $\langle X_c\rangle \approx 0.209$ [30]. Appropriate treatment of adsorption-desorption is non- trivial in this model in contrast to $R = 0$. In fact, the two required parameters for adsorption and desorption correspond to those in the $1 \times 1 \times L$ cell model with $R = 1$. However, we should note that for this $2 \times 1 \times L$ cell model with $R = 1$, the spatial Markovian shielding property for the equilibrium steady-state is somewhat more complicated than for $1 \times 1 \times L$. Specifically, it implies that a layer of two vertical cells within the pore with specified state shields cells on one side from the effect of cells on the other side. This feature is utilized below.

For the *adsorption rate*, the relevant multisite probability factors as the concentration, $\langle C_0\rangle$, of particles against the wall in a semi-infinite system with $R = 1$ (as determined for the $1 \times 1 \times L$ cell model) times the probability of a triple of empty cells at the pore opening. See Figure 5.2(a). This factorization follows rigorously from the Markov shielding property of the pair of empty cells $E_{1_+}E_{1_-}$. For *desorption*, a particle at $k = 1_+$ or $(0,1,1)$ ensures that cell $(0,1,0)$ just outside the pore is empty, and five additional cells are required to be empty. Thus, the configuration of the external fluid corresponds to that in a semi-infinite system with a single cell against the wall specified empty, and is identical to that in the tailored simulation for desorption in the $1 \times 1 \times L$ cell model with $R = 1$. In this case, again we determine the conditional probability, $Q_{5|1}$, of five empty cells NN to this specified empty cell. See Figure 5.2(b). Pre-desorption where the particle hops from cell $k = 2_{\pm}$ to cell $k = 1_{\pm}$ must also be treated appropriately, noting that this requires a cell just outside the pore to be empty. However, the situation is analogous to the $1 \times 1 \times L$ cell model with $R = 1$. The relevant conditional probability that a cell just outside the pore is empty given both cells in layer $k = 1$ are empty is given by $\langle E_{\text{pre}} \rangle = \langle E_0 \rangle = 1 - \langle X_0 \rangle$, so it is determined without additional tailored simulations. See Figure 5.2(c).

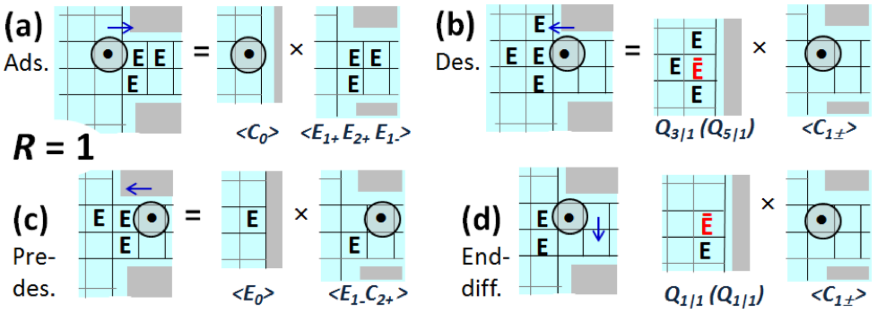

Figure 5.2: 2D schematic of configurations relevant for adsorption, desorption, and pre-desorption, and end layer hopping in the $2 \times 1 \times L$ cell model with $R = 1$. Q's with (without) parenthesis correspond to 3D (2D) exterior fluid. All NN cells to particles are empty.

However, unlike the $1 \times 1 \times L$ cell model with $R = 1$, additional non-trivial information is needed to treat lateral hopping within the pore in the end layer $k = 1$. See Figure 5.2(d). For a particle at $k = 1_+$ or $(0, 1, 1)$ hopping to $k = 1_-$ or $(0, 0, 1)$, both cells just outside the pore must be empty as well as additional sites within the pore. This probability can be factorized exactly using the Markov shielding property of the pair of cells $C_{1_+}E_{1_-}$ as indicated in Figure 5.2(d). The additional information needed to prescribe lateral hopping is the conditional probability, $Q_{1|1}$, to find an additional empty cell just above or below the cell specified empty. This is obtained from the same tailored simulation used to assess desorption where one site against a wall in a semi-infinite system is specified empty. Key parameters for this model ($\langle C_0 \rangle$, $Q_{5|1}$, $\langle E_{\text{pre}} \rangle$, and $Q_{1|1}$) are listed in Table 5.1.

5.3.3 $N \times 1 \times L$ cell pore for $N \geq 3$

While the 3D pore geometries of $N \times N \times L$ cell models are of more physical relevance, the $N \times 1 \times L$ cell models with 2D pore geometries present analogous features and complications. These features are more readily illustrated schematically in the 2D pore geometry. Cells in the pore correspond to $(i, j, k) = (0, j, k)$ for $j = 0$ to $N - 1$ and $k = 1$ to L. Unlike the above cases for $N \leq 2$, all these models exhibit lateral concentration variation within pore. Note that $\langle C_{0,j,k} \rangle = \langle C_{0,N-1-j,k} \rangle$, etc., by reflection symmetry about the longitudinal pore center. In fact, one can provide an exact analysis of this variation for the total concentration for the equilibrium steady state in the center of a long pore. See Section 5.5.1 and Section 5.9. For $R = 0$, adsorption-desorption is again trivial, so we do not discuss this case further. For $R > 0$, we divide the discussion into two cases. For $R < N - 1$, SFD is not imposed, and these models are characterized by multiple independent and non-trivial adsorption and desorption rates. For $R \geq N - 1$, SFD is imposed. There is a single adsorption and desorption rate for smaller $N \leq 3$, but not necessarily for larger $N \geq 4$.

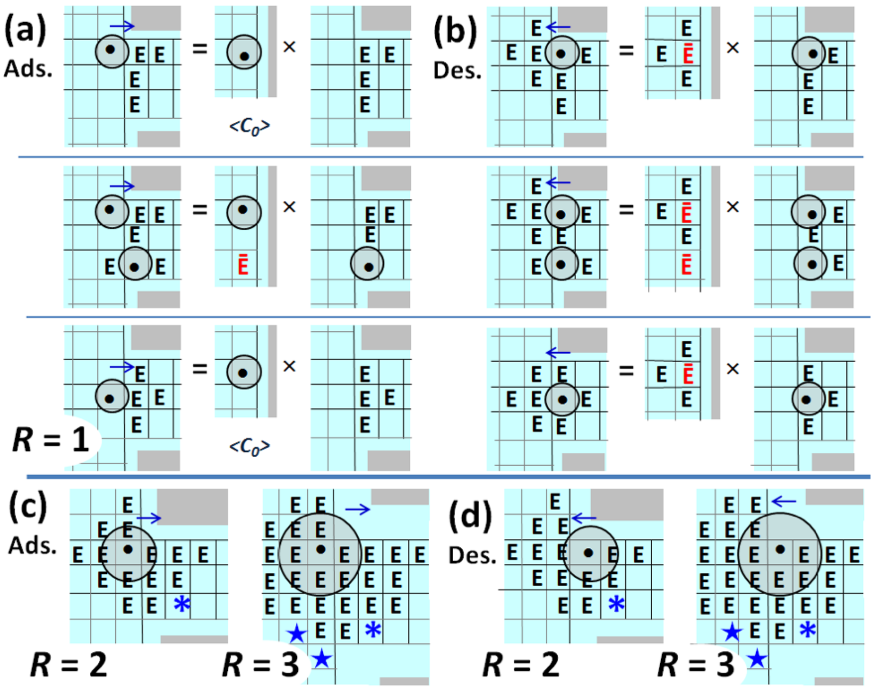

Figure 5.3: 2D schematic of configurations relevant for determination of adsorption and desorption rates for particles of type $C = A$, B, or X. (a,b) $3 \times 1 \times L$ cell model with $R = 1$ (no SFD). (c,d) $3 \times 1 \times L$ cell model with $R = 2$ (SFD), and $4 \times 1 \times L$ cell mode with $R = 3$ (SFD).

First, we illustrate behavior for $R < N - 1$ in the simple case $N = 3$ and $R = 1$. Here, particles diffusing on the top and bottom row within the pore can pass each other. Also, significantly, there are multiple populated configurations of the end row which complicates the description of adsorption and desorption. Figure 5.3(a) illustrates three distinct situations in which adsorption must be described. The rates for two of these involve the concentration of particles against the wall in a semi-infinite system which comes from one tailored simulation. The other requires a separate tailored simulation in a semi-infinite system where one cell against the wall is specified empty. Figure 5.3(b) illustrates three distinct situations for desorption. Two of these require the same tailored simulation as in the adsorption case with one cell against the wall in a semi-infinite system specified empty. The third requires a separate tailored simulation with two cells against the wall specified empty. Pre-desorption must also be described for this model. There are three distinct configurations to be considered (not shown), and diffusion within the end layer requires consideration of two cases (not shown), but the associated tailored simulations are included in the treatment of adsorption and desorption.

Second, we briefly comment on cases with exclusion range $R \geq N - 1$ (for $N \geq 3$) which imposes SFD. Schematics of adsorption and desorption processes are shown in Figure 5.2(c) and Figure 5.2(d), respectively, where E labels cells required to be empty for the processes to occur. For $N = 3$ and $R = 2$, a single adsorption and desorption rate apply. This follows since the occupancy of the site indicated by the asterisk does not influence sites not already labeled as E (empty) in the external fluid. On the other hand, for $N = 4$ and $R = 3$ (corresponding to spheres with diameter $3 < d \leq \sqrt{10}$), the occupancy of the site indicated by the asterisk does influence the occupancy of two sites not already labeled by E in the external fluid. These two sites are indicated by stars. Thus, one must determine two distinct adsorption rates and two distinct desorption rates depending on whether the site labeled by the asterisk is occupied or not. The TOC figure illustrates multi-particle configurations for $N = 4$ and $R = 3$ where cells required to be empty due to exclusion are labeled by black E, and additional cells required to be empty for implementation of the indicated adsorption and desorption processes are labeled by blue E. For $N = 4$ with larger $R = \sqrt{10}$, there are still two distinct rates. However, for $N = 4$ with still larger $R \geq \sqrt{13}$, a single adsorption and desorption rate apply.

5.3.4 $2 \times 2 \times L$ cell pore

Cells in the pore correspond to (i, j, k) for $i = 0$ or 1, and $j = 0$ or 1, and for $k = 1$ to L. Again, by symmetry, there is just a single concentration, $\langle C_{0,0,k}\rangle = \langle C_{0,1,k}\rangle = \langle C_{1,0,k}\rangle = \langle C_{1,1,k}\rangle$, in each layer k. Exclusion ranges $R = 0$ and $R = 1$ do not enforce SFD. Description of adsorption-desorption is again trivial for $R = 0$, but not for $R = 1$. Now, $R = \sqrt{2}$ which is the smallest $R-$value which imposes SFD. We describe the treatment of adsorption, desorption, and pre-desorption processes for $R = 1$ and $R = \sqrt{2}$, but must also now consider diffusion within the end layer in the pore. Extensive results for $R = \sqrt{2}$ are presented in Section 5.4.

<u>*Exclusion range* $R = 1$</u>, i.e., no NN pairs of particles, so there can be up to two particles in each layer k within the pore, and SFD is not imposed. As for the $3 \times 1 \times L$ cell model with $R = 1$, there are multiple adsorption and desorption rates to be determined, as we now briefly describe. Adsorption can occur either into a completely empty end layer, or into a cell in the end layer where the diagonally opposite corner cell is populated. Two separate tailored simulations are required to determine these rates, one for a semi-infinite system, and the other for such a system with a single cell against the wall specified empty. Desorption can occur either from an end layer with a single particle, or from an end layer with two particle in diagonally opposite corner cells. Two appropriate tailored simulations are required to determine the associated rates.

<u>*Exclusion range* $R = \sqrt{2}$</u>, i.e., no NN or second NN pairs of particles, so there is at most a single particle in each layer k within the pore, and SFD is imposed. The maximum concentration is $\langle X_{\max}\rangle = 1/4$ both in the pore and in the exterior fluid. The latter corresponds to layers of skewed 2×2 ordering. As noted above, an order-disorder transition occurs in the external fluid at critical concentration $\langle X_c\rangle = 0.104$ [30]. Appropriate treatment of adsorption-desorption is of course non-trivial in this model, somewhat akin to the $2 \times 1 \times L$ cell model with $R = 1$. For this $2 \times 2 \times L$ cell model with $R = \sqrt{2}$ (or with $R = 1$), the spatial Markovian shielding property for the equilibrium steady-state has the following form: a complete layer

of four cells within the pore, i.e., $(i, j) = (0, 0)$, $(1, 0)$, $(0, 1)$, $(1, 1)$ with fixed k, which have specified state shields cells on one side from the effect of cells on the other side. This feature is utilized below.

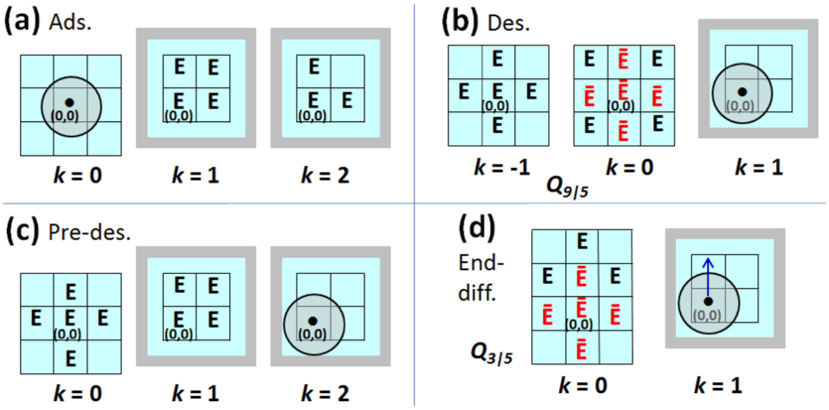

Figure 5.4: Schematic for the $2 \times 2 \times L$ cell model with $R = \sqrt{2}$ or configurations relevant for determination of: (a) adsorption; (b) desorption; (c) pre-desorption; (d) hopping in the end layer, for particles of type $C = A$, B, or X.

For the *adsorption rate*, the relevant multisite probability factors as the concentration, $\langle C_0 \rangle$, of particles against the wall in a semi-infinite system times the probability of a configuration of seven empty cells at the pore opening. See Figure 5.4(a). This factorization follows rigorously from the Markov shielding property of the quartet of empty cells $E_{(0,0,1)}E_{(1,0,1)}E_{(0,1,1)}E_{(1,1,1)}$. For *desorption*, a particle at $(0, 0, 1)$ ensures five cells $(0, 0, 0)$, $(1, 0, 0)$, $(-1, 0, 0)$, $(0, 1, 0)$, and $(0, -1, 0)$ just outside the pore are empty, and an additional nine cells are required to be empty. Thus, the configuration of the external fluid corresponds to that in a semi-infinite system with five cells against the wall specified empty. A tailored simulation is performed to determine the conditional probability, $Q_{9|5}$, that the additional nine cells are empty. See Figure 5.4(b). Pre-desorption where the particle hops from cell $(0, 0, 2)$ to cell $(0, 0, 1)$ must also be treated appropriately. The particle at $(0, 0, 2)$ ensures three cells with $k = 1$ are empty. Pre-desorption requires the forth cell for $k = 1$ be empty, and an additional five cells just outside the pore with $k = 0$ are also empty. See Figure 5.4(c). We exactly factorize the probability for pre-desorption. One factor is the conditional probability that five sites outside the pore are empty given the state of the sites inside the pore. The other is the probability of the configuration of sites inside the pore. The first conditional probability corresponds to the probability of finding the five empty cells against the wall in a semi-infinite system, $\langle E_{5\text{pre}} \rangle$, and can be obtained from a tailored simulation.

As for the $2 \times 1 \times L$ cell model, additional non-trivial information to treat lateral hopping within the pore in the end layer $k = 1$. See Figure 5.4(d). Consider a particle at $(0, 0, 1)$ hopping to $(1, 0, 1)$. The presence of the particle implies that five cells just outside the pore are empty. For hopping, an additional three cells just outside the pore must be empty (as well as additional sites within the pore). This probability can be factorized exactly. One factor is the conditional probability, $Q_{3|5}$, for three empty cells outside the pore given the five empty cells outside the pore and the specified configuration of cells inside the pore. The other factor is the probability of the configuration of cells inside the pore. Using the Markov shielding property, this conditional probability equals the conditional probability for a semi-infinite system with five cells specified empty that an additional three cells are empty. See again Figure 5.4(d). $Q_{3|5}$ can be obtained from the same tailored simulation as used to assess desorption. Key parameters for this model ($\langle C_0 \rangle$, $Q_{9|5}$, $Q_{5\text{pre}}$, and $Q_{3|5}$) are given in Table 5.1.

5.3.5 $N \times N \times L$ cell pore for $N \geq 3$

Cells in the pore correspond to (i, j, k) for $i = 0$ to $N - 1$, $j = 0$ to $N - 1$ and $k = 1$ to L. Unlike the above cases for $N \leq 2$, all these models exhibit lateral concentration variation within pore. Note that some $\langle C_{i,j,k} \rangle$ for fixed k are equal by rotational symmetry, and by reflection symmetry about the longitudinal pore center. In fact, one can provide an exact analysis of this variation for the total concentration for the equilibrium steady state in the center of a long pore. See Section 5.9. For $R = 0$, adsorption-desorption is again trivial. For $1 \leq R < (N - 1)\sqrt{2}$, SFD is not imposed, and these models are characterized by multiple independent and non-trivial adsorption and desorption rates. For $R \geq (N - 1)\sqrt{2}$, SFD is imposed. For smaller R in this range, there can be multiple distinct adsorption and desorption rates.

Table 5.1: Parameters from tailored simulations determining adsorption, desorption, pre-desorption, and end-layer diffusion rates for the three SFD models. See Section 5.10 for analytic estimates of these parameters.

$\langle C_b \rangle$	Adsorption	Desorption	Pre-desorption	End Diffusion
$\mathbf{1 \times 1 \times L,\ R = 0}$	$\langle \mathbf{C_0} \rangle$	$\langle \mathbf{E_0} \rangle = \mathbf{1} - \langle \mathbf{C_0} \rangle$	–	–
$\langle C_b \rangle$	$\langle C_b \rangle$	$1 - \langle C_b \rangle$	–	–
$\mathbf{2 \times 1 \times L,\ R = 1}$	$\langle \mathbf{C_0} \rangle$	$\mathbf{Q_{5\|1}}$	$\langle \mathbf{E}_{\mathrm{pre}} \rangle = \mathbf{1} - \langle \mathbf{C_0} \rangle$	$\mathbf{Q_{1\|1}}$
0.20	0.2106	0.2792	0.7894	0.7331
0.10	0.1055	0.5466	0.8945	0.8821
$\mathbf{2 \times 2 \times L,\ R = \sqrt{2}}$	$\langle \mathbf{C_0} \rangle$	$\mathbf{Q_{9\|5}}$	$\langle \mathbf{E_{5\mathrm{pre}}} \rangle$	$\mathbf{Q_{3\|5}}$
0.10	0.1232	0.1936	0.4421	0.5190
0.05	0.0589	0.5326	0.7143	0.8003

5.4 KMC Simulation Results for TCP, TE and Catalytic Conversion

In the analysis below, we focus on comparison of behavior for *three* SFD models which are all subject to the SFD constraint: a $1 \times 1 \times L$ cell pore with $R = 0$ and $\langle X_b \rangle = 0.4$; a $2 \times 1 \times L$ cell pore with $R = 1$ and $\langle X_b \rangle = 0.2$; and a $2 \times 2 \times L$ cell pore $R = \sqrt{2}$ and $\langle X_b \rangle = 0.1$. The exterior fluid concentration consistently is selected to be 40% of the maximum possible value for all models, so comparison of these cases is natural.

5.4.1 Characterization of TCP

Figure 5.5(a)-(c) shows steady-state TCP concentration profiles for the above three SFD models for a pore with $L = 25$ obtained from pore-only simulations utilizing the non-trivial boundary conditions for $R > 0$ described in Section 5.3. For the $1 \times 1 \times L$ cell model with $R = 0$, we note stronger deviations from linearity persisting deeper into the pore, as will be elucidated below. For the other models with $R > 0$, the concentration is strongly enhanced in the pore interior due to the lower cell coordination number relative to the external fluid. Profiles are more linear in the pore interior, but display oscillations near the pore openings reflecting the change in coordination number of cells transiting from the external fluid to the pore interior.

Figure 5.5(d) shows a schematic of steady-state TCP configurations for general systems subject to SFD. These have the special feature that particles are strictly ordered with A on

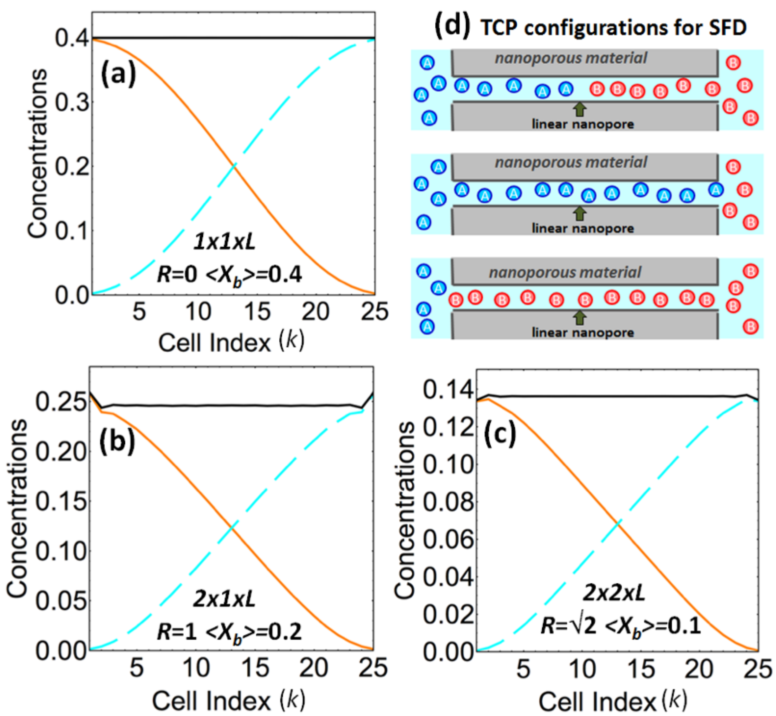

Figure 5.5: TCP profiles for: (a) $1 \times 1 \times L$ cell pore with $R = 0$ and $\langle X_b \rangle = 0.4$; (b) $2 \times 1 \times L$ cell pore with $R = 1$ and $\langle X_b \rangle = 0.2$; and (c) $2 \times 2 \times L$ cell pore with $R = \sqrt{2}$ and $\langle X_b \rangle = 0.1$. In all cases, SFD applies, $L = 25$, and $\langle X_b \rangle / \langle X_{\max} \rangle = 0.4$. (d) Schematic of possible TCP steady-state configurations for SFD.

the left, and B on the right [18, 25]. A "typical" configuration has an interface between the A- and B-populated regions somewhere in the middle of the pore (top image). A non-zero flux of A (B) from left to right (right to left) through the pore corresponds to situations where the pore is completely populated by A (B). In these cases, the interface has reached the right (left) end of the pore, as shown in the middle (bottom) image. This latter observation motivates characterization of the distribution of interface locations [25]. However, first a more precise definition of interface location is needed. A simple asymmetric choice identifies the interface location with the right-most A (or left-most B). In this case, the location takes only integer values. A symmetric definition identifies the interface location as midway between the right-most A and the left-most B, which implies that the location can take both integer and half-integer values. In either case, we set the location to $k = 0$ ($k = L + 1$) if the pore is devoid of A (B).

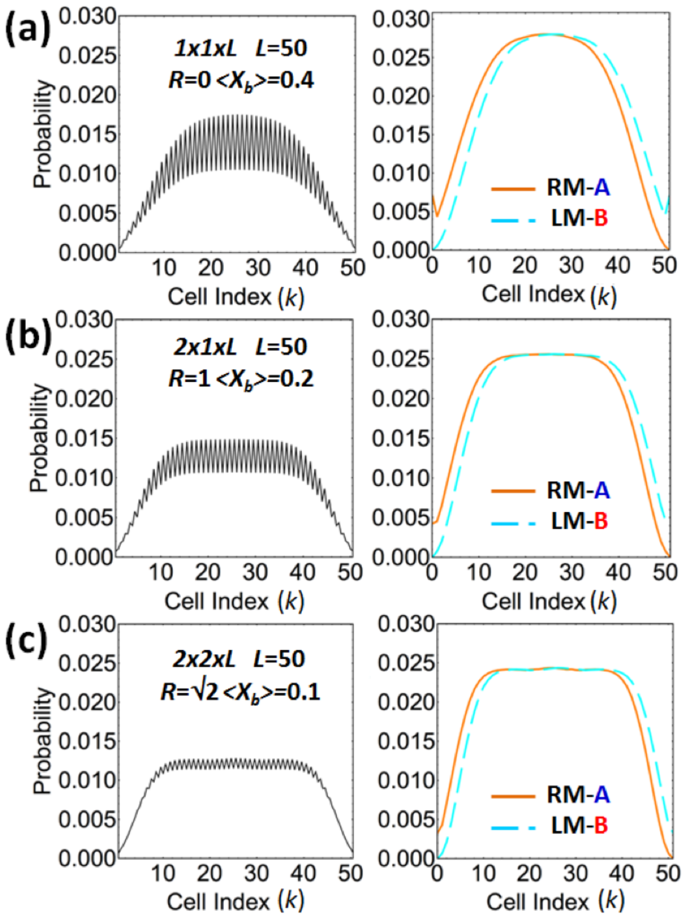

Figure 5.6: Interface location distribution for TCP profiles with SFD in pores with $L = 50$ for: (a) $1 \times 1 \times L$ cell model with $R = 0$ and $\langle X_b \rangle = 0.4$; (b) $2 \times 1 \times L$ cell model with $R = 1$ and $\langle X_b \rangle = 0.2$; (c) $2 \times 2 \times L$ cell model with $R = \sqrt{2}$ and $\langle X_b \rangle = 0.1$. Left row: symmetric definition. Right row: right-most (RM) A (solid orange) and left-most (LM) B (dashed blue).

Interface location distributions are shown for the three SFD models in Figure 5.6(a)-(c). In the most simple picture, one might anticipate a uniform distribution of interface locations within the entire pore. This behavior would correspond to exactly linear TCP profiles. In fact, for long enough pores, the distribution does have a plateau in the pore interior, i.e., the interface location is uniformly distributed apart from pore end effects. Indeed, this depletion of the distribution near the pore ends corresponds to the flattening of the TCP profiles in that region, which in turn has significant consequences for the generalized tracer diffusivity discussed below. Note that for maximal concentrations in the three models which we consider with one particle for each layer k, the interface location using the symmetric definition is restricted to half-integers. From Figure 5.6(a)-(c) we see that this preference for half-integer locations is weakened but maintained at lower concentrations.

5.4.2 Determination of generalized tracer diffusivity

Next, we utilize the above results for TCP concentration profiles, together with an assessment of the flux, J_A ($J_B = -J_A$) of A (B) through the pore, to determine the generalized tracer diffusion coefficient, $D_{tr}(k, k+1)$, for each adjacent pair of layers in the pore [19,20,24]. Our treatment is motivated by hydrodynamic transport theory for continuum systems with a single type of particle carrying one of two labels, A or B, with slowly varying concentration gradients [20, 24, 34, 35]. In a counter-diffusion mode with constant total concentration, $\langle X \rangle = \langle A \rangle + \langle B \rangle$, so that $\nabla \langle A \rangle = -\nabla \langle B \rangle$, one has $J_A = -D_{tr} \nabla \langle A \rangle$ and $J_B = -D_{tr} \nabla \langle B \rangle$ which are equal and opposite, and where D_{tr} is the tracer diffusion coefficient. As an aside, we note that for more general diffusion modes, the diffusion fluxes also depend on the chemical or collective diffusion coefficient, D_c, which is concentration-independent for $R = 0$ [20, 36], but which has a non-trivial dependence on concentration for our models with $R > 0$ [37].

We generalize these considerations to our discrete system where the total concentration in each layer $\langle X_k \rangle = \langle X_k^{\mathrm{eq}} \rangle$ is equilibrated, but not constant for $R > 0$ [32]. We first introduce fractional concentrations via $\langle c_k \rangle = \langle C_k \rangle / \langle X_k^{\mathrm{eq}} \rangle$ for $C = A$ or B. If $J_C^{k>k+1}$ denotes the net flux of C from cell k to $k+1$ (which is independent of k for steady-state TCP). Then, $D_{tr}(k, k+1)$ is defined via

$$J_C^{k>k+1} = -\frac{1}{2} \left(\langle X_k^{\mathrm{eq}} \rangle + \langle X_{k+1}^{\mathrm{eq}} \rangle \right) D_{tr}(k, k+1) \nabla \langle c_{k+1} \rangle , \tag{5.4}$$

where $\nabla G_k = G_k - G_{k-1}$ is a discrete derivative. Note that this definition correctly ensures equal and opposite fluxes for A and B, and recovers the hydrodynamic expressions. The form of $J_C^{k>k+1}$ for general $\langle X_k \rangle$ is more complex [38], but is not needed here.

Results for $D_{tr}(k, k+1)$ based on (5.6) are shown for the three SFD models in Figure 5.7(a)-(b). Concentrations and their gradients are obtained from profiles of the type shown in Figure 5.5(a)-(c). Flux values can be obtained either from counting the number of A's and B's transiting the pore during the simulation, or from end layer concentrations. For example, one has $J_A = hQ \langle A_L \rangle$ where Q is the appropriate conditional probability that a particle on the end site within the pore can desorb, e.g., $Q = \langle E_b \rangle$ for the $1 \times 1 \times L$ cell model with $R = 0$, $Q = Q_{5|1}$ for a $2 \times 1 \times L$ cell model with $R = 1$, and $Q = Q_{9|5}$ for a $2 \times 2 \times L$ cell model with $R = \sqrt{2}$.

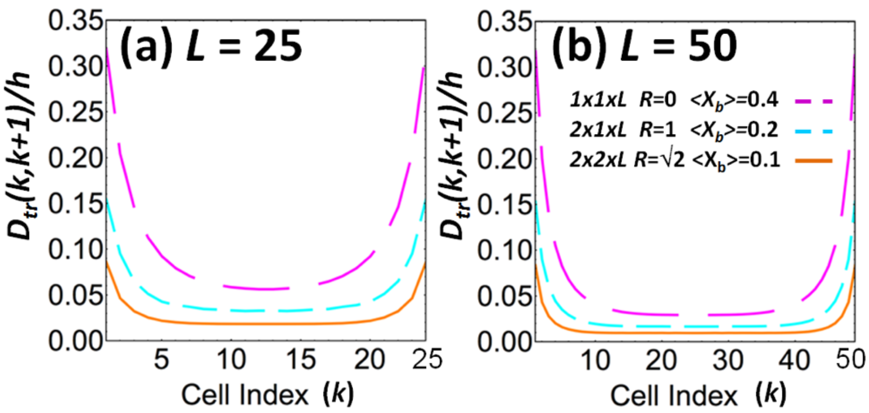

Figure 5.7: Comparison of $D_{tr}\,(k, k+1)$ for three models for: (a) $L = 25$ where $D_{tr}\,(\max)\,/h = 0.3188$, 0.1545, and 0.0861 for $1 \times 1 \times L$, $2 \times 1 \times L$, and $2 \times 2 \times L$. (b) $L = 50$ where $D_{tr}\,(\max)\,/h = 0.3174$, 0.1532, and 0.0835 for $1 \times 1 \times L$, $2 \times 1 \times L$, and $2 \times 2 \times L$.

We emphasize two key features of these results. First, there is a well-defined minimum plateau, $D_{tr}\,(\min)$, in the values of $D_{tr}\,(k, k+1)$ in the pore interior, especially for longer pores. The plateau value decreases with increasing L as discussed further below. Second, near pore openings, there is a strong enhancement in $D_{tr}\,(k, k+1)$-values. This enhancement is most substantial in $1 \times 1 \times L$ cell model with $R = 0$, a feature corresponding to the strong deviations in linearity of the TCP profiles for this case. It has been suggested [25] that an upper bound on the maximum value, $D_{tr}\,(\max) = D_{tr}\,(1, 2) = D_{tr}\,(L-1, L)$ of $D_{tr}\,(k, k+1)$ might be obtained from appropriate mean-field type estimates of D_{tr}. The MF site approximation for the $1 \times 1 \times L$ cell model yields [20] $D_{tr}\,(1 \times 1 \times L, \text{site}) = h\,(1 - \langle X_{\text{int}} \rangle) = 0.6h$ for $\langle X_{\text{int}} \rangle = 0.4$, and appropriate MF pair approximations for the $2 \times 1 \times L$ and $2 \times 2 \times L$ cell models also yield estimates well above $D_{tr}\,(\max)$. See Section 5.10.

Previous treatments for the classic $1 \times 1 \times L$ cell model with $R = 0$ have considered an overall diffusivity, $D_{tr}\,(\text{pore})$, for finite pores of length L. The dependence of $D_{tr}\,(\text{pore})$ on concentration and pore length was assessed by simulations and also analytic treatments for systems both with periodic boundary conditions [17, 39, 40], and for a TCP setup with a near-jammed pore [18]. We will associate the minimum plateau value, $D_{tr}\,(\mathrm{min})$, with $D_{tr}\,(\mathrm{pore})$ not just for the $1\times1\times L$ cell model with $R=0$ but for all models. Adapting previously derived expressions for $D_{tr}\,(\mathrm{pore})$ for $1\times1\times L$ cell models with $R=0$ [17, 18, 39, 40] to more general models, one might anticipate that

$$D_{tr}\,(\mathrm{min}) \approx \langle X_{\mathrm{eff}}\rangle^{-1}\,(1-\langle X_{\mathrm{eff}}\rangle)\,h/L_{\mathrm{eff}}\ ? \tag{5.5}$$

Here, $\langle X_{\mathrm{eff}}\rangle = \langle X_{\mathrm{int}}\rangle\,/\,\langle X_{\mathrm{max}}\rangle$ denotes a scaled effective concentration, and $L_{\mathrm{eff}} \propto L$ is an appropriate measure of pore length. Indeed, results shown in Figure 5.8 reveal an almost perfect inverse proportionality to pore length, L for all models consistent with (5.5).

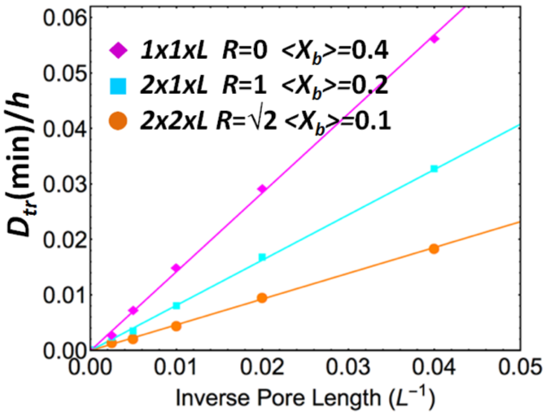

Figure 5.8: Linear variation of $D_{tr}\,(\mathrm{min})$ with $1/L$ where $D_{tr}\,(\mathrm{min}) \approx 1.42h/L$, $0.82h/L$, and $0.46h/L$ for the $1\times1\times L$, $2\times1\times L$, and $2\times2\times L$ cell model, respectively.

For the $1\times1\times L$ cell model with $R=0$, the $2\times1\times L$ cell model with $R=1$, and also the $2\times2\times L$ cell model with $R=\sqrt{2}$, a maximally populated or jammed pore has one particle per layer k, and we set $L_{\mathrm{eff}}=L$ [41]. If one makes the crude approximation that $\langle X_{\mathrm{int}}\rangle \approx \langle X_b\rangle$ for the $2\times1\times L$ and $2\times2\times L$ cell models, then the three models considered in this section all have the same $\langle X_{\mathrm{eff}}\rangle \approx 0.4$ yielding $D_{tr}\,(\mathrm{min}) \approx 1.5h/L$ for all models. This estimate is quite effective for the classic $1\times1\times L$ cell model with $R=0$, but not for the other models. Correcting this estimate by using the simulation value of $\langle X_{\mathrm{int}}\rangle$ yields slightly improved $D_{tr}\,(\mathrm{min}) \approx 1.03h/L$ with $\langle X_{\mathrm{int}}\rangle = 0.246$ for the $2\times1\times L$ cell model and $D_{tr}\,(\mathrm{min}) \approx 0.83h/L$ with $\langle X_{\mathrm{int}}\rangle = 0.136$ for the $2\times2\times L$ cell model. However, these values are still significantly above the precise simulation values. Thus, we conclude that tracer diffusivity is intrinsically lower in the $2 \times 1 \times L$ and $2 \times 2 \times L$ cell models relative to the $1 \times 1 \times L$ cell model, and that the traditional treatments must be modified.

This behavior presumably reflects the feature that diffusional dynamics is intrinsically more inhibited due to special features of superlattice ordering in the $2 \times 1 \times L$ and $2 \times 2 \times L$ cell models. To illustrate this feature, we note that unlike $1 \times 1 \times L$ cell models, there are frozen or jammed configurations (where no hopping is possible) with concentrations below the maximum value. Such configurations can be constructed, e.g., by removing every third particle along the pore from a configuration with maximum coverage. The consequences of such ordering have not been considered in previous analyses.

5.4.3 Characterization of tracer exchange

Figure 5.9(a)-(c) show KMC simulation results for the three SFD models for tracer exchange concentration profiles of particles of type A entering a pore initially filled with particles of type B. We emphasize that in contrast to previous studies of TE for the classic $1 \times 1 \times L$ model with $R = 0$, in our studies for models with $R > 0$, the equilibrated total concentration is not uniform inside the pore (both initially and subsequently). As time $t \to \infty$, the concentration of A-type particles inside the pore converges to this total equilibrium concentration. Profiles are shown for a sequence of quickly growing times $ht = 5^n$ with $n = 1, 2, \ldots$. Results reflect slow pore filling which is a consequence of inhibited transport due to SFD. Predictions of behavior assuming a position-independent mean-field tracer diffusion coefficient would produce much faster pore filling. Discussion of an effective beyond-mean-field analytic treatment of TE is presented in Section 5.5.4. Associated results are also shown in Figure 5.9(a)-(c).

5.4.4 Characterization of catalytic conversion

We consider reaction models where all sites within the pore are catalytic and convert reactant A to product B at rate r. Figure 5.10(a)-(c) shows KMC simulation results for the three SFD models for steady- state concentration profiles for both reactant, A, and product, B, in a first-order catalytic conversion reaction. Specifically, we show the variation of these profiles with decreasing ratio of reaction rate, r, to hopping rate, h, for $r/h = 0.1$, 0.01, 0.001 and

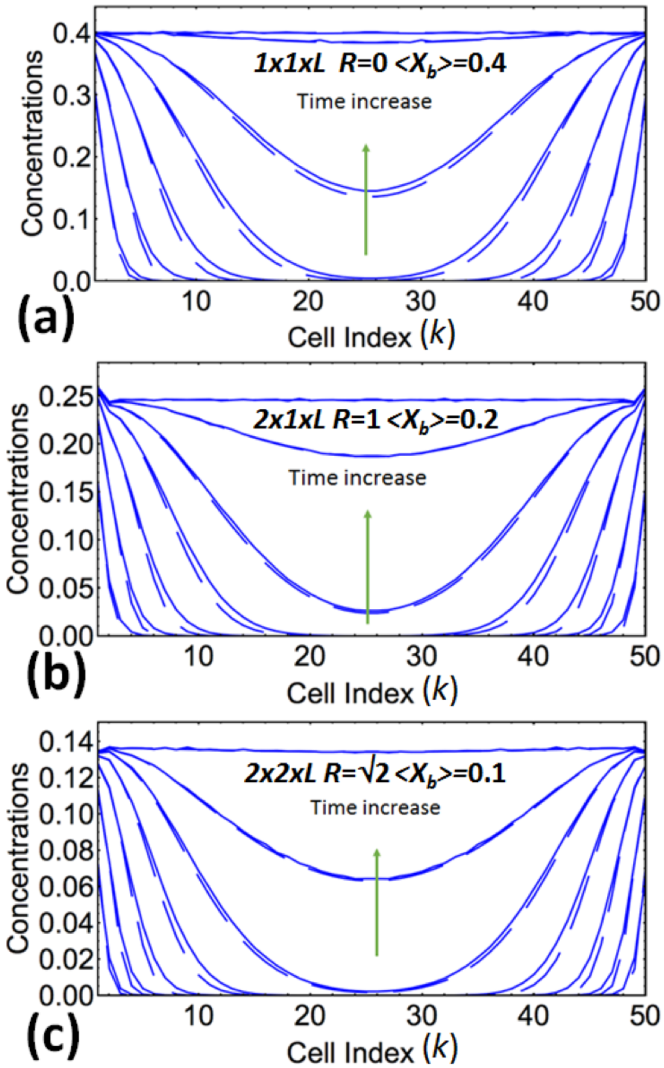

Figure 5.9: Profile evolution for tracer exchange for the three models. Time: 0, 5, 5^2,. . . , 5^7. Solid curves: KMC simulation. Dashed curves: generalized hydrodynamic theory.

0.0001. The key feature is that reduced r/h allows deeper penetration of reactant into the pore before reaction. However, it should be emphasized that the reactant penetration depth does not scale like $(h/r)^{1/2}$ which would be expected (and is found) in mean-field treatments. Instead-reactant penetration is greatly reduced and described by distinct scaling behavior reflecting the special features of reaction in the presence of SFD [19, 20]. Discussion of an effective beyond-mean-field analytic treatment of catalytic conversion is presented in Section 5.5.4. Associated results are also shown in Figure 5.10(a)-(c).

5.5 Further Insights From Analytic Treatments

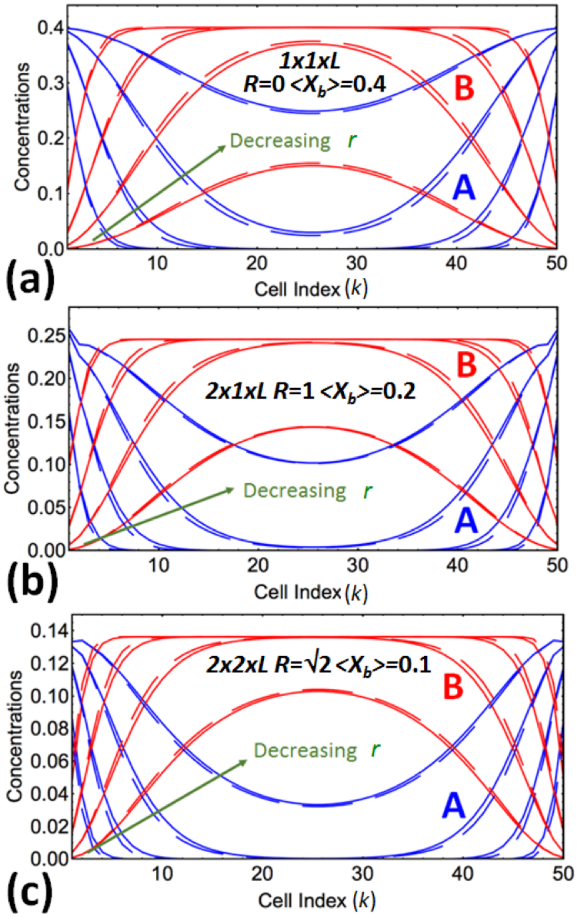

Figure 5.10: Steady-state concentration profiles for catalytic conversion of the three models for a range of $r/h = 0.1$, 0.01, 0.001, and 0.0001 for $L = 50$. Solid curves: KMC simulation. Dashed curves: generalized hydrodynamic theory.

The above KMC simulation based studies provide a self-contained comprehensive characterization of diffusion and reaction-diffusion behavior. However, deeper insight into some features of behavior can be obtained from the following analytic treatments.

5.5.1 Pore Interior versus external fluid concentrations

A key feature for models with exclusion range $R > 0$ is the enhancement of the total particle concentration within the pore interior, $\langle X_{\text{int}} \rangle$, relative to that in the external fluid, $\langle X_b \rangle$. This behavior can be understood since cells in the pore region can have a smaller number of nearby cells within the interaction range (which could potentially be occupied by particles) relative to cells in the external fluid. This tends to boost the concentration. To quantify this behavior, we consider an equilibrium pore + external fluid system with long-range exchange dynamics between pairs of sites in the bulk external fluid and in the center of a long pore at rate f. We exploit the feature that fluxes for exchange into and out of the pore must balance in equilibrium [32].

First, consider the $2 \times 1 \times L$ cell model with $R = 1$. Let P_7 denote the probability that a cell in the external fluid together with all its six NN cells are empty. Since P_7 includes 6 NN pairs, a MF-type pair approximation implies that $P_7 \approx (1 - 2\langle X_b \rangle)^6 / (1 - \langle X_b \rangle)^5$. Also, let P_4 denote the probability that a cell in the middle of a long pore together with all its three NN cells are empty. Since P_4 includes 3 NN pairs, in a pair approximation, one has that $P_4 \approx (1 - 2\langle X_{\text{int}} \rangle)^3 / (1 - \langle X_{\text{int}} \rangle)^2$. Then, the exchange flux of atoms from a cell in the middle of a long pore to the cell in the bulk external fluid, $J_{2\times1\to3\text{D}}$, and for the reverse process, $J_{3\text{D}\to2\times1}$, are given by

$$J_{2\times1\to3\text{D}} = fP_7 \langle X_{\text{int}} \rangle \quad \text{and} \quad J_{3\text{D}\to2\times1} = fP_4 \langle X_b \rangle . \tag{5.6}$$

Finally, equating $J_{2\times1\to3\text{D}} = J_{3\text{D}\to2\times1}$ yields $\langle X_{\text{int}} \rangle = 0.2663$ (0.1245) versus the simulation values of 0.246 (0.122) for $\langle X_b \rangle = 0.20$ (0.10).

For the $2 \times 2 \times L$ cell model with $R = \sqrt{2}$, let P_{19} denote the probability that a cell in the bulk external fluid together with all its 6 NN cells and 12 second NN cells are empty. Since P_{19} includes 30 NN pairs and 32 second NN pairs, a pair approximation implies that $P_{19} \approx (1 - 2\langle X_b \rangle)^{62} / (1 - \langle X_b \rangle)^{105}$. Also, let P_{10} denote the probability that a cell in the middle of a long pore together with all its 4 NN cells and 5 second NN cells are empty. Since P_{10} includes 14 NN pairs and 16 second NN pairs, a pair approximation implies that $P_{10} \approx (1 - 2\langle X_b \rangle)^{30} / (1 - \langle X_b \rangle)^{50}$. Then the exchange flux out of the pore, $J_{2\times2\to3\text{D}}$, and into the pore, $J_{3\text{D}\to2\times2}$, satisfy

$$J_{2\times2\to3\text{D}} = fP_{19} \langle X_{\text{int}} \rangle \quad \text{and} \quad J_{3\text{D}\to2\times2} = fP_4 \langle X_b \rangle . \tag{5.7}$$

Finally equating $J_{2\times2\to3\text{D}} = J_{3\text{D}\to2\times2}$ yields $\langle X_{\text{int}} \rangle = 0.1437$ (0.0672) versus the simulation values of 0.136 (0.066) for $\langle X_b \rangle = 0.10$ (0.05).

5.5.2 Determination of the total concentration profile in the pore interior

For the $1 \times 1 \times L$ cell model with $R = 0$, the total concentration is uniform within and outside the pore with value $\langle X_b \rangle$. However, for the $2 \times 1 \times L$ cell model with $R = 1$, and the $2 \times 2 \times L$ cell model with $R = \sqrt{2}$, KMC simulation results reveal oscillatory behavior of the total concentration, $\langle X_k \rangle$, near the pore ends. See Figure 5.5(b)-(c). We show that the complete profile, $\langle X_k \rangle$, not just $\langle X_{\text{int}} \rangle = \left\langle X_{L/2} \right\rangle$, can be recovered with an analytic treatment incorporating the appropriate non-trivial boundary conditions.

For either of these models with $R > 0$, we start by developing a set of diffusive evolution equations for the $\langle X_k \rangle$ which will ultimately be solved in the steady-state. However, these equations couple through the diffusive flux terms to probabilities of various multisite probabilities. Using the spatial Markov property [31], these multisite probabilities can be factorized and expressed in terms of $\langle X_j \rangle$ and $\langle X_{j,j+1} \rangle$ where the latter gives the probability for one of the configurations with a pair of particles in layers j and $j + 1$. These closed coupled sets of equations for $\langle X_k \rangle$ and $\langle X_{k,k+1} \rangle$ have a generic form for $k = 2$ to $L = 2$. Those for the end layers $k = 1$, 2, $L - 1$, and $L - 2$ have a special form reflecting the non-trivial boundary conditions and involving the quantities described in Section 5.3. See Section 5.9 for a more detailed discussion.

5.5.3 Reconstruction of the external fluid concentration distribution

The tailored simulations for $R > 0$ which determine adsorption and desorption parameters produce non-trivial and distinct concentration variations in the semi-infinite external fluid. In the simplest case for determination of $\langle C_0 \rangle$, the concentration just depends on distance from the wall. In cases where sites against the wall are specified empty, there is a complicated three-dimensional variation. Since these tailored simulations provide boundary conditions at pore openings which allow exact analysis of behavior within the pore region, one might anticipate that information from them should also allow recovery of equilibrium concentration variations in the external fluid under steady-state conditions [32]. Indeed, this is the case. Various tailored simulations correspond to different configurations of the end of the pore. A suitable weighted average of the external fluid concentrations in these recovers that in the steady-state of the reaction model. The ability to reconstruct the equilibrium distribution from the tailored simulations also reflects the spatial Markov field property [31] of these lattice-gas models.

For the $2 \times 1 \times L$ cell model with $R = 1$, or the $2 \times 2 \times L$ cell model with $R = \sqrt{2}$, the two required tailored simulations have the end layer in the pore either completely empty or populated by one particle. The former occurs with probability, $\langle E_1 \rangle$, and the latter involves $n_x = N \times M = 2$ or 4 equivalent configurations each occurring with probability $\langle X_1 \rangle$, so that $\langle E_1 \rangle + n_x \langle X_1 \rangle = 1$. Then the external fluid concentration is obtained by weighting that for the semi-infinite fluid by $\langle E_1 \rangle$ and that for each of the n_x positions of the particle in the end layer by $\langle X_1 \rangle$ [32]. The reconstruction is more complicated for models where multiple tailored simulations are required to account for all possible configurations of the layer(s) at the end of the pore influencing the external fluid (e.g., $1 \times 1 \times L$ for $R \geq 2$, and $N \times 1 \times L$ with $N \geq 3$, or $N \times N \times L$ with $N \geq 2$ for $R = 1$).

5.5.4 Labeled particle concentration profiles in non-equilibrium states

Given the definition of our generalized tracer diffusion coefficient, $D_{tr}(k, k+1)$, it is clear that one could reconstruct the TCP profiles by solving the appropriate discrete diffusion equations incorporating this $D_{tr}(k, k+1)$. However, we claim that knowledge of $D_{tr}(k, k+1)$, together with the non-trivial boundary conditions at the pore opening, also enables characterization of other non-trivial behavior including the form of the labelled particle concentration profiles in TE and in catalytic conversion reactions. This characterization is achieved through analysis of appropriate discrete generalized hydrodynamic equations for the relevant diffusion or reaction-diffusion processes [19, 20].

With regard to TE, there exist previous analytic studies for the $1 \times 1 \times L$ cell model with $R = 0$ [21, 22], but our approach is different. We solve the discrete time-dependent diffusion equation,

$$\mathrm{d}/\mathrm{d}t \, \langle C_k \rangle = -\nabla J_C^{k>k+1} \quad \text{with } J_C^{k>k+1} \text{ from (5.4) and } \nabla G_k = G_k - G_{k-1}, \tag{5.8}$$

together with the appropriate initial conditions for labeled particles and with time invariant $\langle X_k \rangle = \langle X_k^{\mathrm{eq}} \rangle$. We find that this analytic prediction recovers the evolution of the concentration profiles determined precisely from KMC simulation in Section 5.4 for all three models considered. See Figure 5.9(a)-(c).

For description of the non-trivial reactant and product concentration profiles in catalytic conversion reactions, we use the discrete reaction-diffusion equations

$$\mathrm{d/dt}\,\langle A_k \rangle = -r\,\langle A_k \rangle - \nabla J_A^{k>k+1} \quad \text{and} \quad \mathrm{d/dt}\,\langle B_k \rangle = +r\,\langle A_k \rangle - \nabla J_B^{k>k+1}. \tag{5.9}$$

The form of $J_C^{k>k+1}$ must be generalized from (5.4) to treat cases with evolving total concentration [38], but here we focus on analysis of behavior in the reactive steady state where $\mathrm{d/dt}\,\langle C_k \rangle = 0$ and $J_C^{k>k+1}$ reduces to (5.4). Extending previous success with this approach for the $1 \times 1 \times L$ cell model with $R = 0$ [19, 20] and with $R = 1$ [32], we find that the analytic treatment recovers steady-state concentration profiles given in Section 5.4 for the $2 \times 1 \times L$ cell model with $R = 1$ and the $2 \times 2 \times L$ cell model with $R = \sqrt{2}$. See Figure 5.11(a)-(c).

There is one caveat in the analysis of these equations which does not arise in the KMC simulations. This relates to determination of the rate at which particles adsorb into the pore. For the $2 \times 1 \times L$ cell model with $R = 1$, from Figure 5.2(a), the adsorption rate is given by $R_{\mathrm{ads}} = \langle C_0 \rangle \langle E_{1_+} E_{2_+} E_{1_-} \rangle$. The concentration $\langle C_0 \rangle$ was determined from tailored simulations.

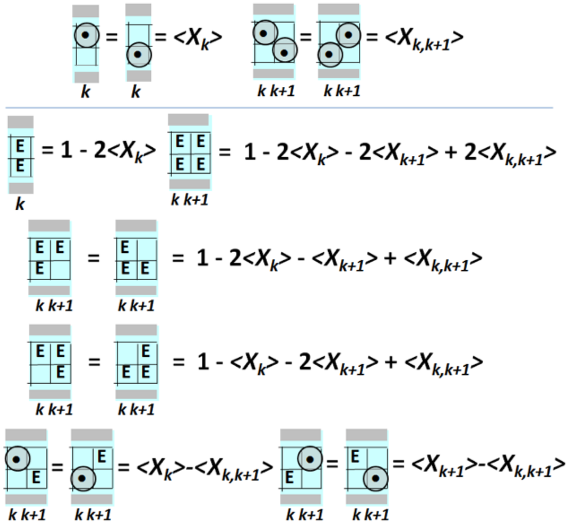

Figure 5.11: Key single- and multi-cell probabilities and exact relations between them.

The quantity $\langle E_{1_+}E_{2_+}E_{1_-}\rangle$ was determined "in-situ" in the pore-only KMC simulations. For the above analytic treatment, an estimate of $\langle E_{1_+}E_{2_+}E_{1_-}\rangle$ is needed which we obtain directly from simulations of an equilibrated single-component system (although analytic determination is also possible). For example, we find that $\langle E_{1_+}E_{2_+}E_{1_-}\rangle = 0.3433$ (0.6482) for $\langle X_b\rangle = 0.2$ (0.1). The situation is analogous for the $2 \times 2 \times L$ cell model with $R = \sqrt{2}$ where the adsorption rate is given by $R_{\text{ads}} = \langle C_0\rangle \langle E_{0,0,1}E_{1,0,1}E_{0,1,1}E_{1,1,1}E_{0,0,2}E_{1,0,2}E_{0,1,2}\rangle$. Appropriate simulations to determine the probability of these seven empty cells give values 0.2112 (0.5688) for $\langle X_b\rangle = 0.1\,(0.05)$.

5.6 Refined Models: Finite Interactions, Diffusion Variability, etc.

5.6.1 Finite-strength interactions

First, we consider the inclusion of finite-strength interactions beyond possible short-range steric blocking for the three SFD models for which detailed analysis was presented in Section 5.4. In the simplest case, we modify the $1 \times 1 \times L$ cell model with $R = 0$ to include finite NN interactions between particles [21]. This model satisfies a spatial Markov property wherein, e.g., single cells within the pore shield cells on one side from the influence of those on the other [31]. Now hopping rates must be selected to be consistent with detailed-balance. In a so-called initial-value approximation (IVA), these depend only on the state of cell(s) NN to the initial cell before hopping, but in general choices they depend on state of cells NN to both initial and final cells [42]. The adsorption rate is determined from simulations in a semi-infinite system assessing the probability for various configurations of NN sites for a particle against the wall. For IVA, one simply multiplies these probabilities by the appropriate hopping rates. For more general choices, one also needs to account for the state of site $k = 2$. Determination of the desorption rate requires a separate simulation to assess for the IVA choice the probability of an empty cell just outside the pore with a populated end site. For general choices, one must also determine the probabilities of all possible configurations of NN external fluid sites to this empty cell.

For the $2 \times 1 \times L$ cell model with $R = 1$, one might naturally include finite-strength interactions of range $\sqrt{2}$. It is still the case that a vertical wall of two cells within the pore shields cells on one side from the influence of those on the other. A more extensive set of analysis is now required to determine the probabilities of various configurations impacting adsorption and desorption rates, analogous to the above $1 \times 1 \times L$ cell example. For the $2 \times 2 \times L$ cell model with $R = \sqrt{2}$, one might naturally include finite strength-interactions of range 2. Now a vertical wall of eight cells of thickness two (rather than thickness one) within the pore is required to shield cells on one side from the influence of those on the other. Thus, for example in determining rates for the adsorption process shown in Figure 5.4(a), one needs to perform tailored simulations for two separate cases with cell $(1, 1, 2)$ for $k = 2$ occupied and empty as this impacts the state of the external fluid. Again, extensive analysis is required to determine probabilities of various configurations impacting adsorption and desorption rates.

Certainly, the presence of these finite-strength interactions will impact the concentration in the pore interior relative to that in the external fluid. Analytic assessment can again come from the type of flux balance described in Section 5.5.1. One could also include finite-strength interactions between particles and the pore walls which would also impact the concentration in the pore interior. It is also well-recognized that finite strength interactions impact the collective diffusion coefficient for the system [37,42]. However, the presence of finite-strength interactions should not alter the basic features of transport for SFD which reflect the (generalized) tracer diffusion behavior and are dominated by the stronger no-passing constraint.

5.6.2 Diffusion variability

Next, consider incorporation of spatial variability in diffusivity across the pore for $N \times 1 \times L$ or $N \times N \times L$ cell pores with $N \geq 3$. (For $N \leq 2$, all rows of cells in the direction of the pore axis are equivalent by symmetry, and thus are characterized by the same hop rates for diffusion.) In the absence of finite inter-particle interactions, all cells which are not blocked by steric interactions are energetically equivalent. Thus hopping rates between NN pairs of cells must be the same in both directions according to detailed-balance. However, one can specify different rates for hopping between NN cells in different symmetry-inequivalent rows of cells along the pore, e.g., a different rate for the central row in a $3 \times 1 \times L$ cell model compared to the outer rows. Different rates can also be specified for the cross-channel direction. Clearly these alternative prescriptions of diffusive kinetics will not impact the spatial Markov properties of the model (an equilibrium property) or our basic formulation and determination of exact boundary conditions for adsorption and desorption.

With regard to the basic features of transport for SFD, the main impact of the more general prescription of diffusivity is that the generalized tracer diffusion coefficient will scale with the average hop rate in the direction of the pore axis (which replaces the single hop rate in the simpler models).

5.6.3 Distinct particle types

For the catalytic conversion reaction models, in general the product species will have different diffusivity (and interactions) than the reactant species. Now in a “color-blind” analysis, where one cannot distinguish between reactant and product species, steady-states do not correspond to a single-component equilibrium model [20]. Consequently, a spatial Markov property does not apply for the non-equilibrium steady-state within the pore, although it does still apply for the external fluid as we retain a well-stirred equilibrium assumption. This condition suffices to still allow exact determination of adsorption and desorption rates from tailored simulations. Thus, one can still implement stand-alone pore simulations with exact boundary conditions.

5.7 Conclusions

We have successfully developed an approach which allows efficient pore-only simulation for various intra-pore diffusion and reaction-diffusion processes in linear nanopores where we exactly account for coupling to an equilibrated external fluid. This is achieved by formulating exact adsorption-desorption boundary conditions (BC’s) describing the coupling to an external fluid. Parameters in these BC’s are obtained from suitably tailored simulations. We describe these processes by spatially discrete lattice-gas models with finite-range exclusion, and our formulation exploits an exact spatial Markov shielding property of these models. These models converge to continuum hard-sphere Langevin type models upon taking increasingly fine lattices (i.e., reducing the lattice constant relative to molecule and pore dimensions).

Our formulation is tested for various models where transport within the pore is subject to single-file diffusion. Specifically, we assess behavior for tracer counter permeation (TCP), tracer exchange (TE), and catalytic conversion reactions within the linear nanopore. Furthermore, after extracting a generalized tracer diffusion coefficient from the TCP analysis, we show how simulation results for TE and catalytic conversion can be recovered from an analytic generalized hydrodynamic formulation incorporating the generalized tracer diffusion coefficient.

5.8 Acknowledgements

We acknowledge discussions with Igor Slowing and Marek Pruski motivating this study. This work was supported by the U.S. Department of Energy (USDOE), Office of Basic Energy Sciences, Division of Chemical Sciences, Geosciences, and Biosciences through the Ames Laboratory Chemical Physics program. The work was performed at Ames Laboratory which is operated for the USDOE by Iowa State University under Contract No. DE-AC02- 07CH11358.

5.9 Appendix A: Derivation of Governing Equations for $\langle x_k \rangle$

Utilizing the non-trivial boundary conditions at the pore openings together with the spatial Markov property of the lattice-gas models, it is possible to determine analytically the entire profile for the total concentration, $\langle X_k \rangle$, inside the pore. As noted in Section 5.5.2 we start by developing a set of diffusive evolution equations for $\langle X_k \rangle$. For the simplest $1 \times 1 \times L$ cell models with $R = 0$ or $R = 1$, one can obtain a closed set of equations for the $\langle X_k \rangle$ [20, 32]. However, for other more complex models, these equations couple through the diffusive flux terms to probabilities of various multisite probabilities.

$2 \times 1 \times L$ model with $R = 1$. This case, while being relatively simple, illustrates the key features of the more complicated models. Thus, it is instructive to provide a detailed presentation. First, in Figure 5.11, we provide some examples of relevant single- and multi-cell

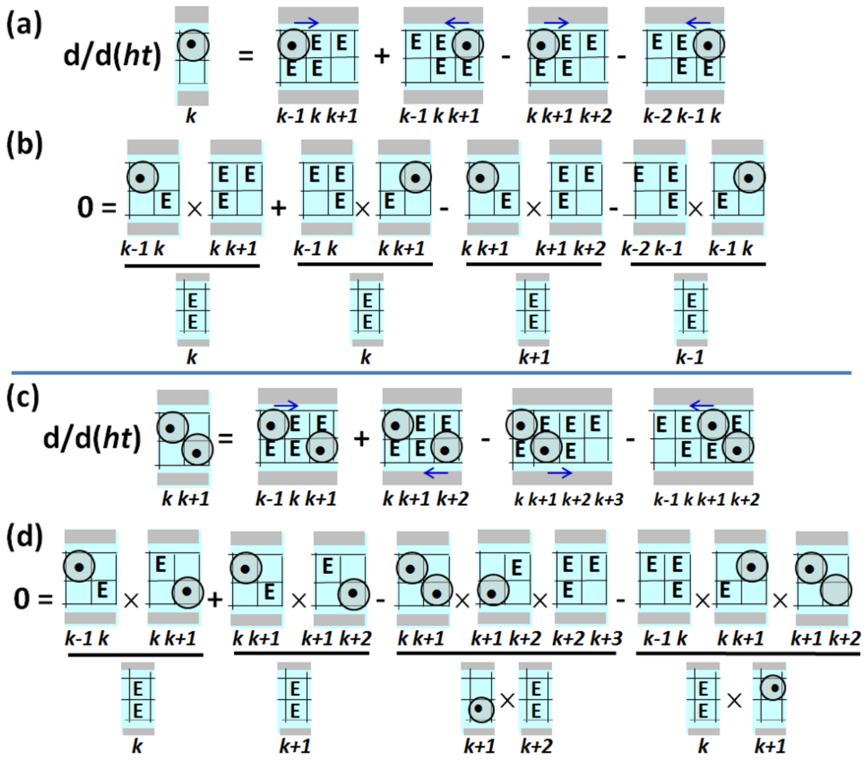

Figure 5.12: Evolution equations for: (a) $\langle X_k \rangle$ and (c) $\langle X_{k,k+1} \rangle$ for the $2 \times 1 \times L$ cell model with $R = 1$. Steady-state factorized forms of these equations are shown in (b) and (d).

probabilities and of the exact relationships between them based on conservation of probability. Of particular significance will be the pair probability $\langle X_{k,k+1} \rangle$ for one of the two configurations with a pair of particles in layers k and $k+1$. Next, in Figure 5.12(a),(c) we show the generic form of the evolution equations for $\langle X_k \rangle$ in the pore interior, as well as those for $\langle X_{k,k+1} \rangle$. Note that cross-pore hopping terms cancel in the equation for $\langle X_k \rangle$. In the steady-state where the total concentration is equilibrated, we can factor these multi-site probabilities using the Markov property for this model which implies that a vertical pair of cells of any specified state shields cells on one side from the influence of those on the other. The steady-state factorized form of these equations is shown in Figure 5.12(b),(d). Using the relations in Figure 5.11, all of the quantities can be rewritten in terms of $\langle X_k \rangle$ and $\langle X_{k,k+1} \rangle$. These coupled sets of equations for $\langle X_k \rangle$ and $\langle X_{k,k+1} \rangle$ have a generic form for $k = 2$ to $k = L - 2$. To provide a closed set of equations for these quantities we must add appropriate equations for the end layers $k = 1, 2, L-1$, and L. These are illustrated in Figure 5.13(a)-(d) and have a special form reflecting the non-trivial boundary conditions and involving the quantities described in Section 5.3.

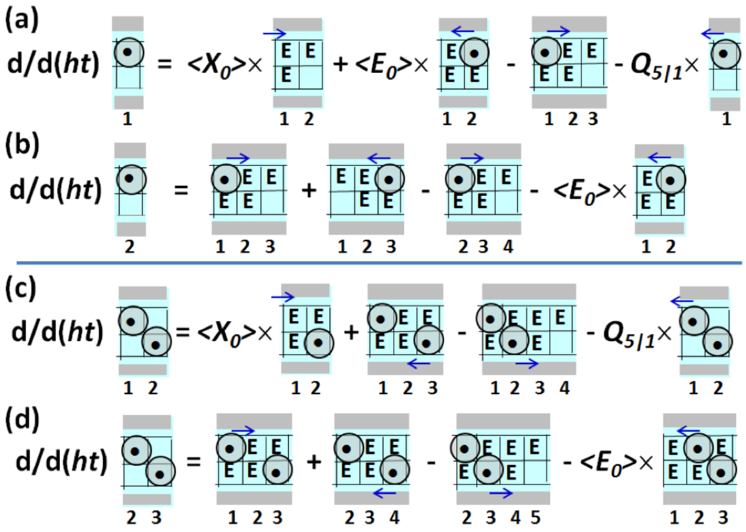

Figure 5.13: Evolution equations for: (a) $\langle X_1 \rangle$; (b) $\langle X_2 \rangle$; (c) $\langle X_{1,2} \rangle$; and (d) $\langle X_{2,3} \rangle$ for the $2 \times 1 \times L$ cell model with $R = 1$. Steady-state factorized forms of these equations can be obtained analogous to Figure 5.12(b),(d).

In the interior of a very long pore, it is clear that $\langle X_k \rangle = \langle X_{\text{int}} \rangle$ and $\langle X_{k,k+1} \rangle = \langle X_{2_{\text{int}}} \rangle$ are independent of k and are intimately related. This relationship follows from the factorized equation in Figure 5.12(d), together with the relations in Figure 5.11, imply that

$$\langle X_{\text{int}} \rangle \left(\langle X_{\text{int}} \rangle - \langle X_{2_{\text{int}}} \rangle \right) = \langle X_{2_{\text{int}}} \rangle \left(1 - 3 \langle X_{\text{int}} \rangle + \langle X_{2_{\text{int}}} \rangle \right), \tag{5.10}$$

which determines $\langle X_{2_{\text{int}}} \rangle$ in terms of $\langle X_{\text{int}} \rangle$. One finds the expected behavior that $\langle X_{2_{\text{int}}} \rangle \sim \langle X_{\text{int}} \rangle^2$ for $\langle X_{\text{int}} \rangle << 1$, and $\langle X_{2_{\text{int}}} \rangle \sim \langle X_{\text{int}} \rangle \sim 1/2$ for a jammed pore.

$3 \times 1 \times L$ cell model with $R = 1$. We first note that an alternative treatment of the above $2 \times 1 \times L$ cell model with $R = 1$ could use as two independent variables the probabilities of the possible configurations of an adjacent pair of columns (i.e., of 4 cells) with one particle and three empty cells, and with two particles and two empty cells. (The latter is the variable $\langle X_{k,k+1} \rangle$ selected above.) In this spirit, for the $3 \times 1 \times L$ cell model, one might naturally choose as independent variables the probability of configurations of an adjacent pair of columns (i.e., of 6 cells) with one, two, and three particles (and other cells specified empty). The Markov property for this model implies that columns of three cells shield. This allows factorization of

the configuration probabilities appearing in the steady state version of these equations so that they can ultimately be written as a closed set in terms of the selected variables. This analysis for a long pore determines the distinct concentration for the central row versus the upper and lower rows.

$2 \times 2 \times L$ cell model with $R = \sqrt{2}$. The treatment of this case is quite analogous to that of the $2 \times 1 \times L$ cell model with $R = 1$. Again, the evolution equations for $\langle X_k \rangle$ for the concentrations in each layer couple to the pair probability, $\langle X_{k,k+1} \rangle$, for one of the four configurations with a pair of particles in layers k and $k+1$. Again, cross-pore hopping terms cancel in the equation for $\langle X_k \rangle$. In the steady-state where the total concentration is equilibrated, we can factor these multi-site probabilities using the Markov property for this model which implies that a layer of four cells of any specified state shields cells on one side from the influence of those on the other.

5.10 Appendix B: Supplementary Material

5.10.1 Boundary conditions for a $1 \times 1 \times L$ cell pore with $R = 2$

To illustrate the additional complications in treating models with longer interaction range $R \geq 2$, we consider the simplest case: the $1 \times 1 \times L$ cell model for $R = 2$, i.e., no pairs of particles with separations 2 or less. In this case, there are no pairs of particles in the 3D fluid with separations 1, $\sqrt{2}$, $\sqrt{3}$, or 2. The maximum concentration in this model is $\langle X_{\max} \rangle = 1/3$ within the pore. The rate of adsorption to an end site within the pore is given by

$$R_{\text{ads}} = h \langle C_{0,0,0} E_1 E_2 E_3 \rangle = h \langle C_{0,0,0} | E_1 E_2 E_3 \rangle \langle E_1 E_2 E_3 \rangle = h \langle C_0 \rangle \langle E_1 E_2 E_3 \rangle . \tag{5.11}$$

Using the spatial Markov property that a pair of cells shields for $R = 2$, one has $\langle C_0 \rangle = \langle C_{0,0,0} | E_1 E_2 E_3 \rangle = \langle C_{0,0,0} | E_1 E_2 \rangle$ is the conditional concentration, $\langle C_0 \rangle$, at cells just outside the pore opening *given* that the end pair of sites within the pore are empty. Again, $\langle C_0 \rangle$ corresponds to the concentration in the layer against the wall for a semi-infinite system, and can be determined from a tailored simulation. See Figure 5.14(a).

Desorption from an end site within the pore to the exterior fluid requires 23 sites just outside the pore to be empty in 3D. Using the spatial Markov property, the associated rate of

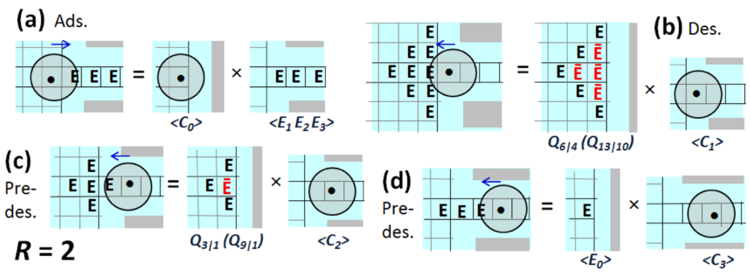

Figure 5.14: 2D schematic of configurations relevant for adsorption, desorption, and pre-desorption in $1 \times 1 \times L$ cell model for $R = 2$. E denotes empty cells; $\bar{E}$ in red text denotes cells prescribed to be empty. Conditional probabilities, $Q_{n|m}$ indicating the number of sites required (n) and given (m) empty for a 2D (3D) exterior fluid lattice.

desorption is given by

$$R_{\text{des}} = hQ_{13|10} \langle C_1 \rangle \,. \tag{5.12}$$

Here $Q_{13|10}$ is the conditional probability for 13 cells to be empty *given* 10 cells closest to the pore opening are empty in 3D. $Q_{13|10}$ is determined from a *second tailored simulation* for a semi-infinite system with 10 cells against the wall specified empty. See Figure 5.14(b).

Stand-alone simulations must also treat the pre-desorption step of hopping from cell 2 to cell 1 at the end of the pore which requires 10 cells just outside the pore to be empty in 3D. Analysis of the associated conditional probability, $Q_{9|1}$, requires a *third tailored simulation given* one cell against the wall in a semi-infinite system is specified empty. See Figure 5.14(c). One must also treat hopping from cell 3 to cell 2 which requires a single cell just outside the opening of the pore to be empty. See again Figure 5.14(d).

5.10.2 Mean-field type treatments of tracer diffusivity

Below, $J_C^{k>k+1}$ denotes the net flux of $C = A$ or B from cell layer k to $k + 1$. We consider behavior in a counter diffusion mode where the pore is occupied by just A and B such that the total concentration of particles $X = A + B$ or either type is constant (at least in the pore interior). Thus $\langle X_{\text{int}} \rangle$ and $\langle E_{\text{int}} \rangle = 1 - \langle X_{\text{int}} \rangle$ are independent of k. Schematics of the multi-cell probabilities associated with this diffusion flux are given in Figure 5.15 for the $1 \times 1 \times L$ cell model with $R = 0$, the $2 \times 1 \times L$ cell model with $R = 1$, and $2 \times 2 \times L$ cell model with $R = \sqrt{2}$.

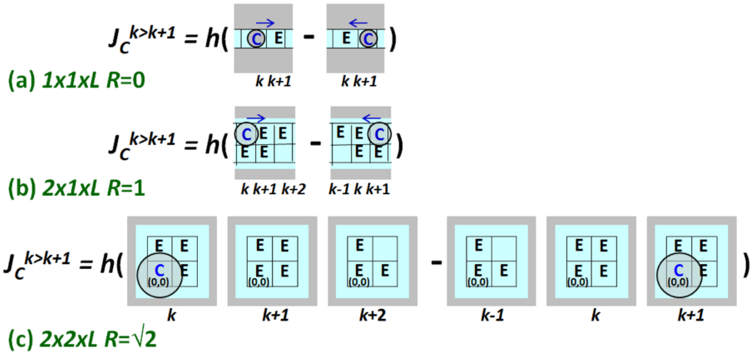

Figure 5.15: Schematic of multi-cell configurations probabilities defining $J_C^{k>k+1}$ for the: (a) $1 \times 1 \times L$ cell model with $R = 0$; (b) $2 \times 1 \times L$ cell model with $R = 1$; and (c) $2 \times 2 \times L$ cell model with $R = \sqrt{2}$.

First, we consider behavior for the 1x1xL cell model with R = 0 where it is natural to apply a standard mean-field (MF) site approximation to obtain 5.15(a)

$$\begin{aligned} J_C^{k>k+1} &= h\left(\langle C_k E_{k+1}\rangle - \langle E_k C_{k+1}\rangle\right) \\ &\approx \left(\langle C_k\rangle \langle E_{k+1}\rangle - \langle E_k\rangle \langle C_{k+1}\rangle\right) = -h\,\langle E_{\text{int}}\rangle\, \nabla \langle C_{k+1}\rangle\,, \end{aligned} \tag{5.13}$$

where $\nabla \langle C_k\rangle = \langle C_k\rangle - \langle C_{k-1}\rangle$. We thus conclude that

$$D_{tr}\left(1 \times 1 \times L, R = 0, \text{MF site}\right) = h\,\langle E_{\text{int}}\rangle = h\left(1 - \langle X_{\text{int}}\rangle\right). \tag{5.14}$$

This result implies that $D_{tr}\left(1 \times 1 \times L, \text{MF site}\right) = 0.6h$ for $\langle X_{\text{int}}\rangle = 0.4$ which is significantly above $D_{tr}\,(\max) \approx 0.32h$ for this model with $L \geq 25$.

For any model with $R > 0$, the site approximation is inadequate as it does not account for the exclusion of nearby pairs of particles. However, the pair approximation is reasonable for the $2 \times 1 \times L$ cell model with NN exclusion. We now consider the $2 \times 1 \times L$ cell model with $R = 1$. Here, we use the simplified notation $\langle C_{0,j,k}\rangle = \langle C_{j,k}\rangle$ for cells within the pore where $j = 0$ or 1 and $1 \leq k \leq L$. After applying the standard pair approximation to factorize the probabilities of multi-cell configurations appearing in Figure 5.15(b) for $J_C^{k>k+1}$, one obtains

$$\begin{aligned} J_C^{k>k+1} \approx{}& h\frac{\langle C_{1,k}E_{0,k}\rangle \langle C_{1,k}E_{1,k+1}\rangle \langle E_{0,k}E_{0,k+1}\rangle \langle E_{1,k+1}E_{0,k+1}\rangle \langle E_{1,k+1}E_{1,k+2}\rangle}{\langle C_{1,k}\rangle \langle E_{0,k}\rangle \langle E_{0,k+1}\rangle \langle E_{1,k+1}\rangle^2} \\ &- h\frac{\langle C_{1,k+1}E_{0,k+1}\rangle \langle C_{1,k+1}E_{1,k}\rangle \langle E_{0,k}E_{0,k+1}\rangle \langle E_{1,k+1}E_{0,k+1}\rangle \langle E_{1,k-1}E_{1,k}\rangle}{\langle C_{1,k+1}\rangle \langle E_{0,k+1}\rangle \langle E_{0,k}\rangle \langle E_{1,k}\rangle^2}. \end{aligned} \tag{5.15}$$

Using that exact relations including $\langle C_{1,k}E_{0,k}\rangle = \langle C_k\rangle$, $\langle E_{0,k}\rangle = \langle E_{\text{int}}\rangle$, $\langle E_{0,k}E_{0,k+1}\rangle = 2\langle E_{\text{int}}\rangle - 1$, etc., it follows that

$$J_C^{k>k+1} \approx h\left(2\langle E_{\text{int}}\rangle - 1\right)^3 \langle E_{\text{int}}\rangle^{-4} \nabla \langle C_{k+1}\rangle . \tag{5.16}$$

From (5.16), we conclude that

$$\begin{aligned} D_{tr}\left(2\times 1\times L, R=1, \text{pair}\right) =& h\left(2\langle E_{\text{int}}\rangle - 1\right)^3 / \langle E_{\text{int}}\rangle^4 \\ =& h\left(1 - 2\langle X_{\text{int}}\rangle\right)^3 / \left(1 - \langle X_{\text{int}}\rangle\right)^4 . \end{aligned} \tag{5.17}$$

This result implies that, e.g., $D_{tr}\left(2\times 1\times L, R=1, \text{pair}\right) = 0.406h$ for $\langle X_{\text{int}}\rangle = 0.246$ which is significantly above $D_{tr}\,(\text{max}) \approx 0.15h$ for this model with $L \geq 25$.

For the $2\times 2\times L$ cell model with $R = \sqrt{2}$, it is reasonable to implement a pair approximation which accounts for the feature that both NN and second NN pairs of cells cannot be occupied. Each of the multi-site configurations shown in 5.15(c) determining the particle flux include: 3 NN CE pairs, 14 NN EE pairs, 3 second NN CE pairs, and 16 second NN EE pairs. Either the NN or second NN EE pairs produce a factor $2\langle E_{\text{int}}\rangle - 1$. Also accounting for cells shared between multiple NN and second NN pairs, we obtain

$$\begin{aligned} D_{tr}\left(2\times 2\times L, R=\sqrt{2}, \text{pair}\right) =& h\left(2\langle E_{\text{int}}\rangle - 1\right)^{30} / \langle E_{\text{int}}\rangle^{56} \\ =& h\left(1 - 2\langle X_{\text{int}}\rangle\right)^{30} / \left(1 - \langle X_{\text{int}}\rangle\right)^{56} . \end{aligned} \tag{5.18}$$

This result implies that $D_{tr}\left(2\times 2\times L, R=\sqrt{2}, \text{pair}\right) = 0.263h$ for $\langle X_{\text{int}}\rangle = 0.136$ which is significantly above $D_{\text{tr}}\,(\text{max}) \approx 0.08h$ for this model with $L \geq 25$.

5.10.3 Analytic estimates of adsorption parameters

Determination of the adsorption rate for reactants into the pore in our $2\times 1\times L$ cell model with $R = 1$ and the $2\times 2\times L$ cell model with $R = \sqrt{2}$ requires analysis of the concentration variation approaching a planar wall in a semi-infinite lattice-gas model on a simple-cubic lattice with $R = 1$ and $R = \sqrt{2}$, respectively. We let $\langle X_0\rangle$ denote the concentration in cells in the layer adjacent to the wall, $\langle X_{-1}\rangle$ the concentration in cells in the next layer away from the wall, etc., and $\langle X_b\rangle$ denotes the bulk concentration far from the wall. Analytic estimation of this concentration variation, and importantly of $\langle X_0 \rangle$, is possible utilizing appropriate pair approximations. In this analysis, we consider the semi-infinite equilibrated fluid as having arbitrary-range exchange dynamics described by a rate f, where exchange events are consistent with range R exclusion. In equilibrium, the corresponding flux of atoms from a cell adjacent to the wall to the bulk, $J_{w \to b}$, and the reverse flux from the bulk to the wall, $J_{b \to w}$, must balance.

First, we estimate $\langle X_0 \rangle$ for models with $R = 1$. The probability, P_7, of an empty cell in the bulk with all six NN cells also empty is estimated in a standard pair approximation as $P_7 \approx (1 - 2\langle X_b \rangle)^6 / (1 - \langle X_b \rangle)^5$. The probability, P_6, of an empty cell against the wall with all five NN cells also empty is estimated as $P_6 \approx (1 - 2\langle X_0 \rangle)^4 (1 - \langle X_0 \rangle - \langle X_{-1} \rangle) / (1 - \langle X_0 \rangle)^4$. Then it follows that

$$J_{w \to b} = r \langle X_0 \rangle P_7 \quad \text{and} \quad J_{b \to w} = r \langle X_b \rangle P_6. \tag{5.19}$$

Assuming that $\langle X_{-1} \rangle \approx \langle X_b \rangle$, i.e., rapid decay of concentration oscillations, the equality $J_{w \to b} = J_{b \to w}$, yields $\langle X_0 \rangle \approx 0.2189\,(0.1071)$ versus the Monte Carlo simulation values of $0.211\,(0.106)$ for $\langle X_b \rangle = 0.20\,(0.10)$. The above analysis can be refined to provide additional assessment of concentration oscillations away from the wall.

For models with $R = \sqrt{2}$, we implement a pair approximation which accounts for the feature that both NN and second NN pairs of cells cannot be occupied. The probability, P_{19}, of an empty cell in the bulk with all six NN cells and all additional twelve second NN cells also empty is estimated as $P_{19} \approx (1 - 2\langle X_b \rangle)^{18} / (1 - \langle X_b \rangle)^{17}$. The probability, P_{14}, of an empty cell against the wall with all five NN cells and all additional eight second NN cells also empty is estimated as $P_{14} \approx (1 - 2\langle X_0 \rangle)^8 (1 - \langle X_0 \rangle - \langle X_{-1} \rangle)^5 / (1 - \langle X_0 \rangle)^{12}$. Then, it follows that

$$J_{w \to b} = r \langle X_0 \rangle P_{19} \quad \text{and} \quad J_{b \to w} = r \langle X_b \rangle P_{14}. \tag{5.20}$$

Assuming again that $\langle X_{-1} \rangle = \langle X_b \rangle$, the equality $J_{w \to b} = J_{b \to w}$, yields $\langle X_0 \rangle \approx 0.187\,(0.081)$ versus the Monte Carlo simulation values of $0.123\,(0.059)$ for $\langle X_b \rangle = 0.10\,(0.05)$. The above analysis can be refined to assess concentration oscillations [32].

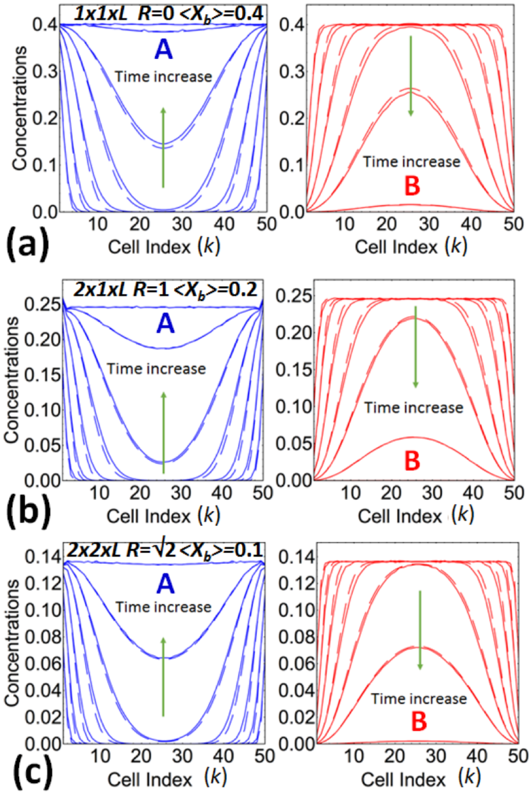

Figure 5.16: Profile evolution for tracer exchange for the three models. Time: 0, 5, 5^2,...,5^7. Solid curves: KMC simulation. Dashed curves: generalized hydrodynamic theory.

5.10.4 Analytic estimates of desorption parameters

To treat desorption, one needs to assess the conditional probability $Q_{5|1}$ ($Q_{9|5}$) in the $2\times1\times L$ ($2\times2\times L$) cell model with $R=1$ ($R=\sqrt{2}$). Recall that $Q_{5|1}=P_6/P_1$ denotes the conditional probability in a semi-infinite system to five empty cells NN to a specified empty cell against the wall in the semi-infinite system for $R=1$. Here P_6 (P_1) is the probability of all 6 cells (just one cell against the wall) being empty. See Figure 5.3(b). $Q_{9|5}$ is the conditional probability to find nine empty cells NN to a set of five empty cells against the wall for $R=\sqrt{2}$. Here P_{14} (P_5) is the probability of all 14 cells (just 5 cells against the wall) being empty. See Figure 5.4(b).

For the $1\times1\times L$ cell model with $R=1$, a standard pair approximation leads to the estimate

$$P_6 \approx \langle E_{0,0,-1}E_{0,0,0}\rangle \langle E_{0,0,0}E_{1,0,0}\rangle \langle E_{0,0,0}E_{0,1,0}\rangle \langle E_{0,0,0}E_{-1,0,0}\rangle \langle E_{0,0,0}E_{0,-1,0}\rangle / \langle E_0\rangle^4 .$$

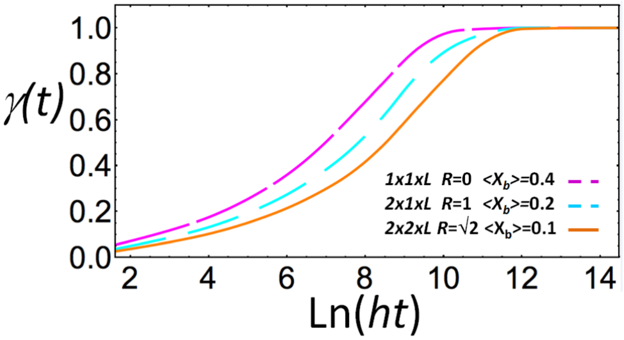

Figure 5.17: Simulated tracer exchange curves for the three models in Figure 5.16.

Since $\langle E_{0,0,-1}E_{0,0,0}\rangle = 1 - \langle X_0\rangle - \langle X_{-1}\rangle$, $\langle E_{0,0,0}E_{1,0,0}\rangle = 1 - 2\langle X_0\rangle$, etc., and $\langle E_0\rangle = 1 - \langle X_0\rangle = P_1$, it follows that

$$Q_{5|1}\,(\text{pair}) = P_6/P_1 = (1 - \langle X_0\rangle - \langle X_{-1}\rangle)\,(1 - 2\langle X_0\rangle)^4 \,/\, (1 - \langle X_0\rangle)^5\,. \tag{5.21}$$

For $\langle X_b\rangle = 0.2$, we conclude that $Q_{5|1}\,(\text{pair}) = 0.237$ (0.213) just using $\langle X_0\rangle \approx \langle X_{-1}\rangle \approx \langle X_b\rangle = 0.2$ (using simulation values of $\langle X_0\rangle = 0.212$ and $\langle X_{-1}\rangle = 0.199$). These compare with the simulation value of $Q_{5|1} = 0.279$ for $\langle X_b\rangle = 0.2$. For $\langle X_b\rangle = 0.1$, we conclude that $Q_{5|1}\,(\text{pair}) = 0.555$ just using $\langle X_0\rangle \approx \langle X_{-1}\rangle \approx \langle X_b\rangle = 0.1$, compared to the simulation value of $Q_{5|1} = 0.547$.

For the $2 \times 2 \times L$ cell model with $R = \sqrt{2}$, we implement a pair approximation which accounts for the feature that both NN and second NN pairs of cells cannot be occupied. P_{14} is factorized into 4 NN pairs and 4 second NN pairs in layer $k = -1$, 12 NN pairs and 8 second NN pairs in layer $k = 0$, and 5 NN pairs and 16 second NN pairs with one empty cell in layer $k = 0$ and the other in layer $k = -1$. Likewise, P_5 factorizes into 4 NN pairs and 4 second NN pairs in layer $k = 0$. One concludes that

$$Q_{9|5}\,(\text{pair}) = P_{14}/P_5$$

$$= (1 - \langle X_0\rangle - \langle X_{-1}\rangle)^{21}\,(1 - 2\langle X_{-1}\rangle)^8\,(1 - 2\langle X_0\rangle)^{12} \,/\, \left[(1 - \langle X_{-1}\rangle)^{32}\,(1 - \langle X_0\rangle)^{41}\right]. \tag{5.22}$$

For $\langle X_b\rangle = 0.1\,(0.05)$, we conclude that $Q_{5|1}\,(\text{pair}) = 0.233\,(0.562)$ just using $\langle X_0\rangle \approx \langle X_{-1}\rangle \approx \langle X_b\rangle = 0.1\,(0.05)$, compared to the simulation value of $Q_{5|1} = 0.194\,(0.533)$.

5.10.5 Additional analysis of tracer exchange

Here, we provide a more complete presentation of results than in Section 5.4.3 for TE where the pore is initially populated by B and the exterior reservoir by A (and the total concentration is equilibrated). Figure 5.16 shows the evolution of concentration profiles both for A entering the pore and for B exiting the pore. In Figure 5.17, we show the corresponding tracer exchange curve, $\gamma(t)$, versus t, where $\gamma(t)$ simply gives the fraction of particles inside the pore which are of type A at time t.

Bibliography

[1] N. Y. Chen, J. F. T. Degnan, and C. M. Smith. *Molecular transport and reaction in zeolites.* VCH, New York, 1994.

[2] D. S. Sholl. Understanding macroscopic diffusion of adsorbed molecules in crystalline nanoporous materials via atomistic simulations. *Acc. Chem. Res.*, 39:pp. 403–411, 2006.

[3] J. Kärger. *Handbook on heterogenous catalysis*, page p. 1714. Wiley-VCH, 2008.

[4] M. K. F. Abouelnasr and B. Smit. Diffusion in confinement: Kinetic simulations of self- and collective diffusion behavior of adsorbed gases. *Phys. Chem. Chem. Phys.*, 14:pp. 11600–11609, 2012.

[5] V. Gupta, S. S. Nivarthi, A. V. McCormick, and H. T. Davis. Evidence for single file diffusion of ethane in the molecular sieve AlPO4−5. *Chem. Phys. Lett.*, 247:pp. 596–600, 1995.

[6] V. Kukla, J. Kornatowski, D. Demuth, I. Girnus, H. P. Pfeifer, L. V. C. Ress, S. Schunk, K. K. Unger, and J. Kärger. NMR studies of single-file diffusion in unidimensional channel zeolites. *Science*, 272:pp. 702–704, 1996.

[7] T. Meersmann, J. W. Logan, R. Simonutti, S. Caldarelli, A. Comotti, P. Sozzani, L. G. Kaiser, and A. Pines. Exploring single-file diffusion in one-dimensional nanochannels by laser-polarized 129Xe NMR spectroscopy. *J. Phys. Chem. A*, 104:pp. 11665–11670, 2000.

[8] M. Dvoyashkin, H. Bhase, N. Mirnazari, S. Vasenkov, and C. R. Bowers. Single-file nanochannel persistence lengths from NMR. *Anal. Chem.*, 86:pp. 2200–2204, 2014.

[9] T. E. Harris. Diffusion with “collisions” between particles. *J. Appl. Prob.*, 2:pp. 323–338, 1965.

[10] B. Cichocki, M. L. Eikiel Jeżewska, and E. Wajnryb. Brownian motion of a particle with arbitrary shape. *J. Chem. Phys.*, 142:214902, 2015.

[11] S. Delong, F. B. Usabiaga, and A. Donev. Brownian dynamics of confined rigid bodies. *J. Chem. Phys.*, 143:144107, 2015.

[12] B. Carrasco and J. García de la Torre. Hydrodynamic properties of rigid particles: Comparison of different modeling and computational procedures. *Biophysical J.*, 75:pp. 3044–3057, 1999.

[13] M. De Corato, F. Greco, G. D’Avino, and P. L. Maffettone. Hydrodynamics and brownian motions of a spheroid near a rigid wall. *J. Chem. Phys.*, 142:194901, 2015.

[14] H. B. Eral, J. M. Oh, D. van den Ende, F. Mugele, and M. G. H. Duits. Anisotropic and hindered diffusion of colloidal particles in a closed cylinder. *Langmuir*, 26:pp. 16722–16729, 2010.

[15] F. Fernandez-Alonso, F. J. Bermejo, S. E. McLain, J. F. Turner, J. J. Molaison, and K. W. Herwig. Observation of fractional Stokes-Einstein behavior in the simplest hydrogen-bonded liquid. *Phys. Rev. Lett.*, 98:077801, 2007.

[16] D. A. Turton and K. Wynne. Stokes–Einstein–Debye failure in molecular orientational diffusion: Exception or rule? *J. Phys. Chem. B*, 118:pp. 4600–4604, 2014.

[17] H. Hahn and J. Kärger. Deviations from the normal time regime of single-file diffusion. *J. Phys. Chem. B*, 102:pp. 5766–5771, 1998.

[18] P. H. Nelson and S. M. Auerbach. Self-diffusion in single-file zeolite membranes is Fickian at long times. *J. Chem. Phys.*, 110:pp. 9235–9243, 1999.

[19] D. M. Ackerman, J. Wang, and J. W. Evans. Generalized hydrodynamic treatment of the interplay between restricted transport and catalytic reactions in nanoporous materials. *Phys. Rev. Lett.*, 108:228301, 2012.

[20] D-J. Liu, A. García, J. Wang, D. M. Ackerman, C-J. Wang, and J. W. Evans. Kinetic Monte Carlo simulation of statistical mechanical models and coarse-grained mesoscale descriptions of catalytic reaction–diffusion processes: 1D nanoporous and 2D surface systems. *Chem. Rev.*, 115:pp. 5979–6050, 2015.

[21] C. Rödenbeck, J. Kärger, and K. Hahn. Exact analytical description of tracer exchange and particle conversion in single-file systems. *Phys. Rev. E*, 55:pp. 5697–5712, 1997.

[22] S. Vasenkov and J. Kärger. Different time regimes of tracer exchange in single-file systems. *Phys. Rev. E*, 66:052601, 2002.

[23] L. Heinke, D. Tzoulaki, C. Chmelik, F. Hibbe, J. M. van Baten, H. Lim, J. Li, R. Krishna, and J. Kärger. Assessing guest diffusivities in porous hosts from transient concentration profiles. *Phys. Rev. Lett.*, 102:065901, 2009.

[24] P. H. Nelson and S. M. Auerbach. Modeling tracer counter-permeation through anisotropic zeolite membranes: From mean field theory to single-file diffusion. *Chem. Eng. J.*, 74:pp. 43–56, 1999.

[25] D. M. Ackerman and J. W. Evans. Tracer counter-permeation analysis of diffusivity in finite-length nanopores with and without single-file dynamics. *Phys. Rev. E*, 95:012132, 2017.

[26] J. G. Tsikoyiannis and J. E. Wei. Diffusion and reaction in high-occupancy zeolite catalysts-I. A stochastic theory. *J. Chem. Eng. Sci.*, 46:pp. 233–253, 1991.

[27] J. Kärger, M. Petzold, H. P. Pfeifer, S. Ernst, and J. Weitkamp. Single-file diffusion and reaction in zeolites. *J. Catal.*, 136:283 – 299, 1991.

[28] S. V. Nedea, A. P. J. Jansen, J. J. Lukkien, and P. A. J. Hilbers. Steady-state properties of single-file systems with conversion. *Phys. Rev. E*, 65:066701, 2002.

[29] D. M. Ackerman, J. Wang, J. H. Wendel, D-J. Liu, M. Prusky, and J. W. Evans. Catalytic conversion reactions mediated by single-file diffusion in linear nanopores: Hydrodynamic versus stochastic behavior. *J. Chem. Phys.*, 134:114107, 2011.

[30] A. Z. Panagiotopoulos. Thermodynamic properties of lattice hard-sphere models. *J. Chem. Phys.*, 123:104504, 2005.

[31] R. Kindermann and J. L. Snell. *Markov random fields and their applications.* American Mathematical Society, Providence, 1980.

[32] A. García and J. W. Evans. Catalytic conversion in nanoporous materials: Concentration oscillations and spatial correlations due to inhibited transport and intermolecular interactions. *J. Chem. Phys.*, 146:174705, 2016.

[33] D-J. Liu, J. Wang, D. M. Ackerman, I. I. Slowing, M. Prusky, H-T. Chen, V. S-Y. Lin, and J. W. Evans. Interplay between anomalous transport and catalytic reaction kinetics in single-file nanoporous systems. *ACS Catal.*, 1:pp. 751–763, 2011.

[34] H. Spohn. *Large scale dynamics of interacting particles.* Springer, Berlin, 1991.

[35] J. Quastel. Diffusion of color in the simple exclusion process. *Commun. Pure Appl. Math.*, 45:pp. 623–679, 1992.

[36] R. Kutner. Chemical diffusion in the lattice gas of non-interacting particles. *Phys. Lett. A*, 81:pp. 239–240, 1981.

[37] S. H. Payne and H. J. Kreuzer. Diffusion in a one-dimensional system with nearest and next-nearest neighbor interactions: Exact analysis based on the kinetic lattice gas model. *Phys. Rev. B*, 75:115403, 2007.

[38] Extending results from hydrodynamic transport theory [34, 35] to the discrete model, we would select $J_A = -\frac{1}{2} D_c\,(k, k+1)\,(\langle A_k \rangle + \langle A_{k+1} \rangle)\, \nabla \langle x_k \rangle - D_{tr}\,(k, k+1) \left[\frac{1}{2} (\langle B \rangle_k + \langle B_{k+1} \rangle)\, \nabla \langle a_k \rangle - \frac{1}{2} (\langle A \rangle_k + \langle A_{k+1} \rangle)\, \nabla \langle b_k \rangle \right]$, with $\langle c_k \rangle = \langle C_k \rangle / \langle X_k^{\mathrm{eq}} \rangle$. $D_c\,(k, k+1)$ is determined from D_c evaluated for concentration $\frac{1}{2} (\langle X_k + \langle X_{k+1} \rangle \rangle)$.

[39] D. G. Levitt and G. Subramanian. A new theory of transport for cell membrane pores. II. Exact results and computer simulation (molecular dynamics). *Biochimica et Biophysica Acta - Biomembranes*, 373:pp. 132–140, 1974.

[40] H. van Beijeren, K. W. Kehr, and R. Kutner. Diffusion in concentrated lattice gases. III. Tracer diffusion on a one-dimensional lattice. *Phys. Rev. B*, 28:pp. 5711–5723, 1983.

[41] A jammed pore in the $1 \times 1 \times L$ cell model with $R = 1$ has one particle in every second layer, and we set $L_{\text{eff}} = \frac{1}{2}L$ [32].

[42] T. Ala-Nissila, R. Ferrando, and S. C. Ying. Collective and single particle diffusion on surfaces. *Adv. Phys.*, 57:pp. 949–1078, 2002.

CHAPTER 6. MOLECULAR PASSING PROPENSITY IN NARROW PORES: 2D LANGEVIN ANALYSIS OF MONOMERS AND LINEAR OLIGOMERS IN A RECTANGULAR CHANNEL

Abstract

We consider a two dimensional monomer-oligomer system in an infinitely long rectangular channel of width W, where the monomers and oligomers diffuse undergoing Brownian motion. The oligomers are linear and are made out of non-intersecting circles. The interactions between the monomers, oligomers and the channel's walls are purely steric; meaning that the oligomers cannot intersect with each other or the pore walls. Based on this, we measure the passing propensity of the monomers and the oligomers in the small gap regime, where we expect the passing propensity as a function of gap size to follow a power law $P \sim (g/r)^{\sigma}$. Using the scaling law, we determine σ for the monomer-dimer system and the monomer-trimer system. We compare the results for the monomer-dimer and monomer-trimer case using Langevin molecular dynamics simulations to those obtained by solving the corresponding Fokker-Planck equation. For wider gaps, the asymptotic behavior of the passing propensity for longer monomer-oligomer systems is examined.

6.1 Introduction

Solution-phase transport and reaction processes in nanoporous materials are strongly impacted when the diameter of the pores become comparable to a suitable defined linear size of the relevant molecular species [1]. There is broad recognition that inhibited passing within the pores, and in particular the extreme case of single-file-diffusion (SFD) which corresponds to no passing, produces anomalous diffusion behavior. In the case of SFD, the mean-square displacement of a tagged particle increases sub-linearly with time contrasting the standard linear increase [2]. It is also clear that such inhibited passing should impact behavior in more complicated reaction-diffusion processes such as catalytic polymerization. In such solution-phase polymerization processes, monomers diffuse in the presence of a solvent into catalytically functionalized nanoporous material and the polymerization reaction occurs when monomers meet other monomers or previously formed oligomers in the vicinity of catalytic sites [3–5].

Despite the evident importance of assessing suitably-defined passing propensities, P, for various species within pores, there has been relatively little analysis of such quantities [6, 7]. A reasonable strategy to assess solvent-mediated passing of species of interest is to implement Langevin molecular dynamics simulations for this process where the solvent is treated implicitly. It is also appropriate to note that an alternative but mathematically equivalent treatment of such passing processes can instead analyze boundary-value problem for the Fokker-Planck equations (FPE) which correspond to the Langevin dynamics [6]. Given the lack of previous systematic studies of this phenomena, here we implement simple modeling for the passing on monomers and linear oligomers as a function of oligomer length. Furthermore, given the lack of basic insight into such behavior, we consider just a $2D$ version of this process where the monomers are chosen as circles of radius r, and the oligomers as linear strings of circles also of radius r, where both species diffuse within a rectangular pore of width W. The only interactions are the pore walls. One advantage of this system is that one can more readily compare the results of Langevin simulations with those of an equivalent Fokker-Planck analysis, where the latter has greater potential to provide deeper insight into behavior.

For the above system, it is clear that passing is sterically blocked for pore width smaller than a critical value of $W_c = 4r$. Thus, if one defines a gap size as $g = W - 4r$, the passing propensity P must vanish as g decreases to $g_c = W_c - 4r = 0$. Furthermore, it is natural to explore possible scaling behavior $P \sim (g/r)^{\sigma}$, where σ denotes a non-trivial exponent [6]. Such a scaling analysis will be the one component of the current study.

6.2 Description of the System

Consider a mesoporous material that is immersed in a continuous fluid in which two kind of molecules are dissolved in it. The molecules in the fluid are monomers and oligomers, as described in Section 6.1, that can diffuse into and within the pores. These oligomers randomly diffuse within the pore following a Wiener process, i.e. Brownian motion; see Figure 6.1. In a somewhat coarse grained model, the oligomers are regarded as spheres and the pores as cylindrical channels. Further simplifications of the system requires: (*i*) The system to be two-dimensional, (*ii*) the oligomers, instead of being composed of spheres, to be composed of circles, and (*iii*) instead of a cylindrical channel of radius R, a rectangular channel of width W; that will be referred to as the "pore" from here on, see Figure 6.2.

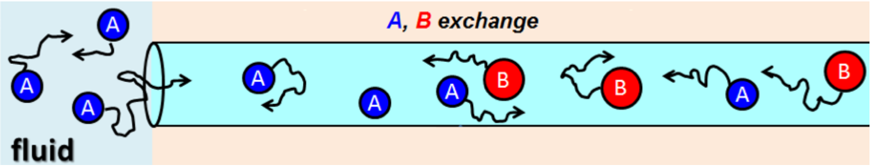

Figure 6.1: Schematic of the diffusion model. Particles of different species undergo Brownian motion and diffuse into the pore. Within the pore they can pass each other.

In the case of a two-dimensional and less coarse grained model, the oligomers can be composed of circles of not necessarily the same radius, and in different arrangements. It is the case that we shall focus on linear oligomers; that is, monomers, dimers, trimers, tetramers, and pentamers, all made of non-intersecting circles of equal radius, that is set to unity; see Figure 6.3.

To determine the passing propensity, we shall consider a monomer-oligomer system. Specifically, the five types of setups that are going to be considered are monomer-monomer (m-m), monomer-dimer (m-d), monomer-trimer (m-tr), monomer-tetramer (m-te), and monomer-pentamer (m-p). To describe the system thoroughly, the following assumptions are made: (*i*) The oligomers move in a viscous isotropic and homogenous fluid, meaning that if a *rigid* set of axis is set and fixed on an oligomer, no matter where the oligomer is placed, or how the oligomer is rotated, the diffusion tensor remains the same when calculated with respect to the fixed axis. (*ii*) The pore in an infinite length rectangle along the main axis and it has a cross

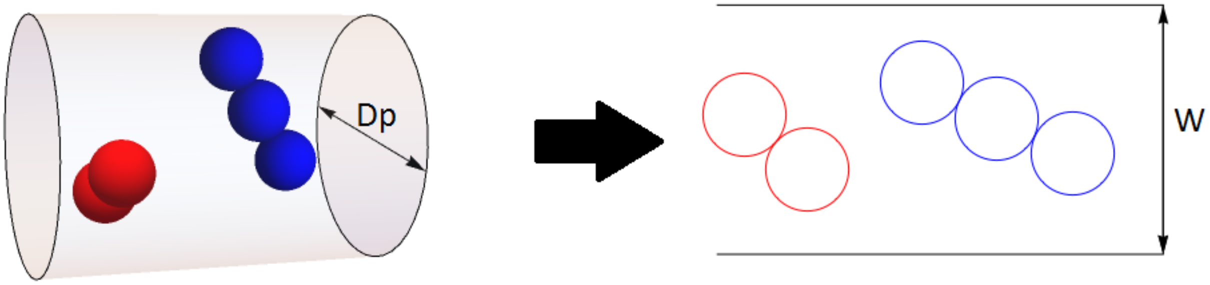

Figure 6.2: Mapping of the 3D problem to 2D. The case depicted above would be that of a dimer and trimer. The oligomers that are made of spheres and move in an infinitely long cylinder with cross-section diameter D_p are mapped into an infinite rectangular pore of width W.

section width W, see Figure 6.1. (iii) The solvent is an ideal fluid, where no-slip boundary conditions are used. (iv) There is no hydrodynamic interaction of the oligomers with the walls. (v) The oligomers only have steric interactions with each other and the pore walls; other type of long and short range interactions are suppressed. (vi) The oligomers are made of circles, all of equal radii. (vii) The oligomers are rigid, meaning that the relative angles and distances of the atoms within an oligomer are constant.

With these assumptions, the equations of motion are obtained and two methods are presented to obtain the scaling exponent σ, for a m-d and m-tr system.

6.3 The Equations of Motion

To get the translational equations of motion, one uses Newton's second law

$$\vec{F}_{i_{\rm net}} = m_i \ddot{\vec{r}}_i, \tag{6.1}$$

with $\dot{\vec{r}} = \frac{\mathrm{d}\vec{r}}{\mathrm{d}t}$, $\ddot{\vec{r}} = \frac{\mathrm{d}^2\vec{r}}{\mathrm{d}t^2}$, etc. The net force exerted on the $i^{\rm th}$ oligomer, $\vec{F}_{i_{\rm net}}$, is just the sum of *all* forces on all the atoms in the oligomer. The forces that are applied on the oligomers, in this case, are the frictional forces, that are proportional to the velocity and a force described by random Wiener process, so that the equations read

$$m\ddot{\vec{r}} = -\tilde{\zeta}_t \dot{\vec{r}} + \vec{F}(t)\,; \tag{6.2}$$

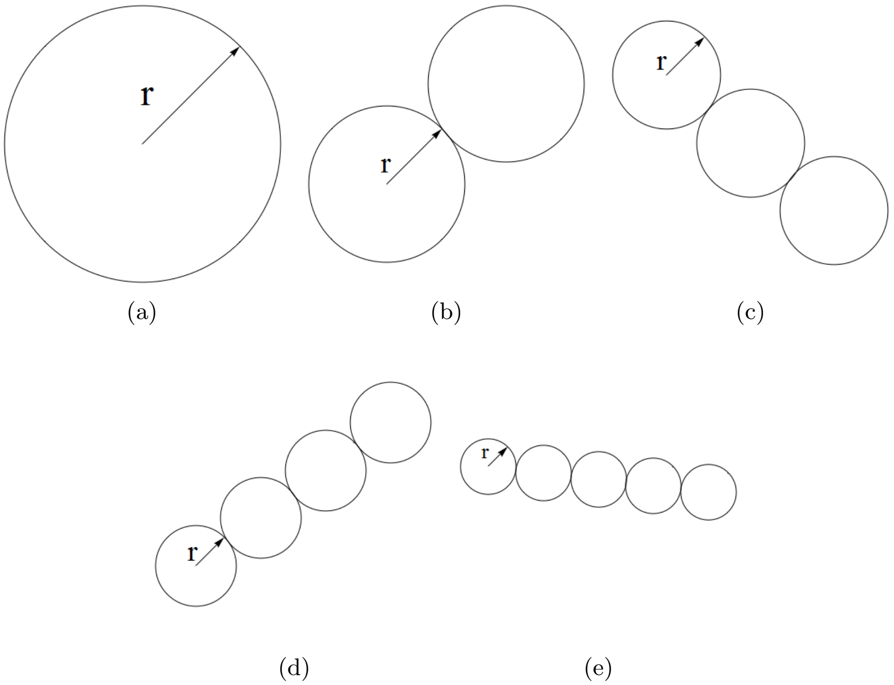

(a) (b) (c) (d) (e)

Figure 6.3: 2D oligomers to be examined. The shapes of the oligomers to be used, not to scale, are (a) monomer, (b) dimer, (c) trimer, (d) tetramer and (e) pentamer. The radius of each circle is $r = 1$ and the mass of each circle is taken as $m = 1$, such that, for each oligomer, the center of mass of coincides with the geometrical center.

where $\tilde{\zeta}_t$ is the *mass independent translational* friction tensor. Assumptions on $\tilde{\zeta}_t$ are given further ahead. The last term in Equation 6.2, $\vec{F}(t)$, is a random *normal* distributed force, such that the time average of the force is zero and the forces are spatially uncorrelated

$$\left\langle \vec{F}(t) \right\rangle = 0, \tag{6.3a}$$

$$\left\langle F_i(t) F_j\left(t'\right) \right\rangle = 2k_B T \zeta_{t_i} \delta_{ij} \delta\left(t - t'\right). \tag{6.3b}$$

This equation is now not a deterministic differential equation, but a stochastic differential equation. Thus, we are forced to use different methods to solve this equation. We shall consider the overdamped equations of motion, $\ddot{\vec{r}} = 0$, thus, Equation 6.2 becomes

$$\tilde{\zeta}_t \vec{r} = \vec{F}(t) \quad \text{with} \quad \vec{F}(t) = \sqrt{2k_B T} \tilde{\zeta}_t^{1/2} \tilde{\mathcal{W}} \quad \text{and} \quad \tilde{D}_t = k_B T \tilde{\zeta}_t^{-1}; \tag{6.4}$$

where $\tilde{D}_t$ is the positive definite translation diffusion tensor and $\tilde{\mathcal{W}}$ is a 2×1 vector of normally distributed random numbers. From Equation 6.4, the stochastic differential equation to be solved is

$$\dot{\vec{r}} = \sqrt{2}\tilde{\mu}_t \vec{\mathcal{W}}, \tag{6.5}$$

where $\tilde{\mu}_t$ is a tensor such that $\tilde{\mu}_t \tilde{\mu}_t^T = \tilde{D}_t$. Physically, $\tilde{D}_t$ is required to be a symmetric positive definite tensor, thus, $\tilde{\mu}_t$ is obtained from a Cholesky decomposition and is symmetric.

For oligomers that are composed of two or more circles, besides the oligomers translating, the oligomers can rotate. Since the system is analyzed in two dimensions, the oligomer can only rotate about the plane, that is simpler than that of the formulation of the problem in three dimensions. The rotational equation of motion is simple and given by

$$\tau_{i_{\text{net}}} = I_i \ddot{\theta}_i. \tag{6.6}$$

The net torque exerted on the i^{th} oligomer, $\vec{\tau}_{i_{\text{net}}}$, is just the sum of *all* torques on all the atoms in the oligomer. The torques that are applied on the oligomers, in this case, are the frictional torques applied to the oligomer with respect to center of mass of the oligomer. The torques that are applied are proportional to the angular velocity with respect to the plane and a random Wiener process, i.e., a torque due to Brownian motion, so that the equation reads

$$I\ddot{\theta} = -\zeta_r \dot{\theta} + \tau\left(t\right); \tag{6.7}$$

where ζ_r is the *inertia independent rotational* friction coefficient, $\zeta_r > 0$. The term $\tau\left(t\right)$ is the random *normal* distributed torque, such that the time average of the torque is zero and obeys

$$\langle \tau \rangle = 0, \tag{6.8a}$$

$$\left\langle \tau\left(t\right)\tau\left(t'\right)\right\rangle = 2k_B T \zeta_r \delta(t - t'). \tag{6.8b}$$

Since we are working in the overdamped regime, $\ddot{\theta} = 0$, thus, the equation to be solved is

$$\zeta_r \dot{\theta} = \tau\left(t\right). \tag{6.9}$$

To solve the equations, there is the possibility of solving the differential equations using a FPE approach, since for every Langevin equation there exists a FPE [6,8,9]. In this context,

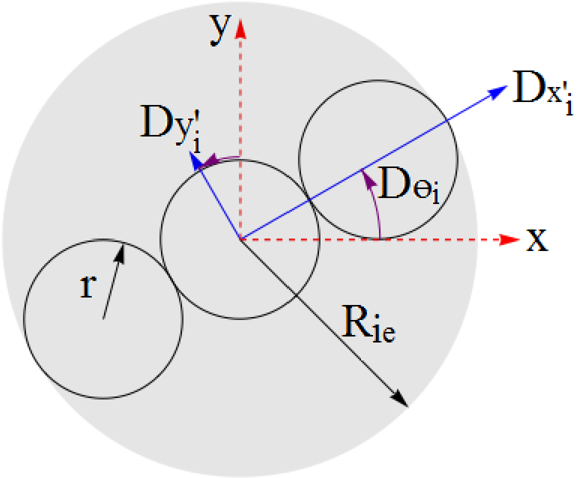

Figure 6.4: Conventions for translation and rotation of an oligomer. The oligomers are made of circles, in this example a trimer, of the same radius, that is set to unity, $r = 1$. For translation, the i^{th} oligomer translates along the x'_i and y'_i body-fixed axes, represented by the solid arrows. If the oligomer is not a monomer, it rotates about its geometrical center. The diffusion coefficients $D_{x'_i}$, $D_{y'_i}$ and D_{θ_i}, are all set to unity. The surrounding disk is defined as the disk of radius R_{i_e} that encloses the oligomer, and is centered at the geometrical center. The pore-fixed axes are represented by the dashed lines.

a FPE has already been used to analyze the system for the m-m and the m-d case [6]; where Langevin MD simulations were also used to validate the results. The small gap limit for a trimer and wider gaps for longer linear oligomers are going to be examined.

6.4 Using an Algorithmic Process to Solve the Equations

To obtain the passing probabilities, a FPE method can be used. In particular, the limit of small gaps has already been examined for the m-m and higher dimensional cases such as sphere-sphere and sphere-dimer case [6, 10]. To solve Equation 6.9 and Equation 6.5, a stochastic simulation method is used. We make the assumptions: (*i*) The oligomers are made of circles of the same radii, that we label as r. For simplicity, we use $r = 1$. (*ii*) A body-fixed frame for each oligomer is used to calculate the diffusion tensor and calculate the displacements. The rotations are calculated about the center of mass of the oligomer, that in this case coincides with the geometrical center, e.g., see Figure 6.4. (*iii*) The oligomers are chosen so that they are linear, and the circles of which they are composed do not intersect each other. (*iv*) Choose the translational diffusion tensor and the rotational diffusion coefficient of the oligomers to be independent of the oligomer length and width. Also the forces and torques are uncorrelated, so that in the body-fixed frame

$$\tilde{D}_t = \begin{pmatrix} D_{x'} & 0 \\ 0 & D_{y'} \end{pmatrix} \quad \text{and} \quad D_r = D_\theta; \tag{6.10}$$

in the appropriate units. The dimensions of the diffusion tensor, $\tilde{D}_t$, are units of length squared divided by time, $\left[\tilde{D}_t\right] = L^2/T$. In the rotational case, the dimensions of the diffusion tensor, D_r, are 1 divided by units of time, $[D_r] = 1/T$. This choice simplifies the FPE, and makes it suitable to compare the translational and rotational scales by setting $[L] = 1$. This will be useful to compare the results with the ones in [6].

It is worth mentioning that there is currently no theory to choose the diffusion coefficients for complicated shaped oligomers in two dimensions, whereas for the three dimensional case the coefficients can be approximately obtained using several assumptions [11–14].

The discrete version of Equation 6.8b is obtained from the relation

$$\langle G_i\left(t\right) G_j\left(t\right)\rangle = \frac{1}{\Delta t_n} \int_{t_n}^{t_{n+1}} G_i\left(t\right) G_j\left(t\right) \mathrm{d}t = \frac{2 k_B T \tilde{\zeta}_i \delta_{ij}}{\Delta t_n}; \tag{6.11}$$

where G can represent either the components of the force F or the torque τ. To solve the equations, an Euler-Maruyama scheme is used

$$\frac{\vec{r}_{i+1} - \vec{r}_i}{\Delta t} = \sqrt{\frac{2}{\Delta t}} \tilde{\mu}_{t_i} \vec{\mathcal{W}}_i, \quad \frac{\theta_{i+1} - \theta_i}{\Delta t} = \sqrt{\frac{2}{\Delta t}} \tilde{\mu}_{r_i} \vec{\mathcal{W}}_i; \tag{6.12}$$

with $\tilde{\mu}_{t_i} = \sqrt{D_{t_i}} = 1$ and $\tilde{\mu}_r = \sqrt{D_r} = 1$, that results in the simplification in the equations

$$\frac{\vec{r}_{i+1} - \vec{r}_i}{\Delta t} = \sqrt{\frac{2}{\Delta t}} \vec{\mathcal{W}}_i, \quad \frac{\theta_{i+1} - \theta_i}{\Delta t} = \sqrt{\frac{2}{\Delta t}} \vec{\mathcal{W}}_i. \tag{6.13}$$

The form of Equation 6.13 provides an algorithm to solve the equations at each time step.

6.4.1 The simulation algorithm

Define the following quantities: (i) The *position of the* i^{th} *oligomer* as the position of the center of mass of the i^{th} oligomer, $\vec{x}_i = (x_i, y_i)$. (ii) The *orientation of an oligomer* as the direction of the unit vectors fixed in the oligomer with respect to a fixed frame in the pore. (iii) The *separation of the oligomers* as the difference in position of the first and the second oligomer $\Delta\vec{x} = \vec{x}_1 - \vec{x}_2 = (x_1 - x_2, y_1 - y_2)$. (iv) A *move* is the change in position and/or orientation of the oligomers. (v) The *initial separation* in the x axis of the oligomers as Δx_0. (vi) A *pass* as the separation of the oligomers such that $\Delta x \leq -\Delta x_0$. (vii) A *fail* as the separation of the oligomers such that $\Delta x \geq 2\Delta x_0$. $(viii)$ A *trial* as a series of valid movements from a starting position that end in a pass or a fail. (ix) A *run* as a defined number of trials. (x) The *passing propensity* as the number of trials in a run that result in a pass, divided by the total number of trials (passes + fails).

Using these definitions, the algorithm used follows the steps:

Step 1 Setup the width of the pore so that there is a possibility of oligomers passing each other; if there is not such a pore width, terminate the program. Set the pass and fail counters to zero, and the number of maximum trials, $N_{\max}$, to some integer number greater than zero.

Step 2 Setup the oligomers in a valid initial configuration and set the initial separation of the oligomers in the x axis as Δx_0.

Step 3 Save the information of the current configuration of the oligomers.

Step 4 Make a move for oligomer 1 and oligomer 2:

(a) Stochastically change the position and orientation of oligomer 1 and oligomer 2. The orientation of an oligomer only has to be changed if it is *not* a monomer.

(b) If the oligomers intersect the wall or each other, reset the oligomers to the configuration before making the moves and go to **Step 4(a)**; otherwise, continue to **Step 5**.

Step 5 Check the separation of the oligomers:

(a) If the separation of the oligomers in the x axis is less than or equal to $-\Delta x_0$, add one to the pass counter and continue to **Step 6**.

(b) If the separation of the oligomers in the x axis is greater than or equal to $2\Delta x_0$, add one to the fail counter and continue to **Step 6**.

(c) If the separation of the oligomers in the x axis is such that $-\Delta x_0 < \Delta x < 2\Delta x_0$, go to **Step 3**.

Step 6 Check if the simulation is done:

(a) If the number of trials is less than N_{max}, go to **Step 2**; otherwise continue to **Step 7**.

Step 7 Get the passing propensity as $P = \#$ of passes$/N_{\text{max}}$ and finish the program.

To exactly determine the minimum pore width of the linear oligomers used here, it is trivial to see that the minimum vertical phase space that the oligomer has available is $ps_{\text{min}} = W - 2r$, that is when the oligomer's longest axis is aligned with the main axis of the pore. Discussion for general shaped configurations is discussed in Section 6.8.

6.4.2 Setting up the initial configuration

The initial configuration of the oligomers is important since it influences the passing propensity. The physical condition that we choose for the starting position is when the oligomers are separated by a distance along the x axis of the pore $\Delta x_0 = r_c = R_{1_e} + R_{2_e}$, where r_c is the sum of the radius of the *surrounding disks* of the oligomers, see Figure 6.4. The surrounding disk of an oligomer is defined as the minimum disk with radius R_{i_e} from the center of mass of the oligomer that encloses all the atoms in the oligomer. Even if the surrounding disk gives an idea of the typical oligomer size, it often provides no information about the shortest or longest axis of the oligomer.

The fixed choice of the initial separation of the oligomers along the x axis leaves two free parameters, that are the y position and orientation of the oligomers within the pore. The initial y position of the oligomers are randomly determined from the available phase space for the oligomer to move in. The procedure to determine the initial y position of each oligomer is to: (i) Set the center of mass of the oligomer in the $y = 0$ coordinate, see Figure 6.5a) (ii) Randomly rotate the oligomer about the center of mass, such that the oligomer does not intersect the pore walls, and fix the orientation of the oligomer; the oligomers will not intersect each other because of the initial Δx_0 position, see Figure 6.5b) (*iii*) For the i^{th} oligomer, get the available space in the y axis and call it $L_{ps_i} = L_{t_i} + L_{b_i}$, as defined in Figure 6.5b) . (*iv*) Include the physical constraint that the oligomers will always have a tendency to be in an initial orientation such that the phase space for them to move is maximum, i.e., get the ratio $P = L_{ps}/(W - 4r)$ and choose a random number in the range $n = (0, 1)$. If n is less than or equal to P, accept the orientation of the oligomer and choose a random position for the oligomer in the y direction, such that the oligomer does not intersect the pore walls.

As it is important to keep track of the position of the atoms in the oligomers, it is important to keep track of the position of the center of mass, and the orientation of the axis of the oligomers, since the moves will always be performed with respect to this body-fixed frame. An example of a valid initial configuration of the oligomers is shown in Figure 6.5c).

6.4.3 Moving the Oligomers: Translation and Rotation

To get the translational and rotational quantities, it is convenient to refer to Equation 6.13, that clearly gives an algorithm to choose the displacements. Since we are working in a body-fixed frame and the fluid in which the oligomers are moving in is isotropic and homogeneous, the diffusion tensor and coefficient will remain constant. To get the displacements, the procedure is to: (*i*) Get 3 normal distributed random numbers. (*ii*) With the diffusion tensor for each component, calculate the displacement. Following Equation 6.13

$$d_i = \sqrt{2\Delta t}\mathcal{W}_i, \tag{6.14}$$

where $i \in \{1, 2, 3\}$. (*iii*) The translational quantities are associated with the first two indices, $i \in \{1, 2\}$, and the rotational with the last, $i = 3$. To implement the translational algorithm, a transformation to the pore-fixed frame is needed. If the body-fixed frame vector basis of the i^{th} oligomer is defined by $\{\hat{e}_{i_1}, \hat{e}_{i_2}\}$, where the vectors are expressed in the pore-fixed frame, the displacement vector of the oligomers in the pore-fixed frame is

$$\Delta\vec{x}_i = d_1\hat{e}_{i_1} + d_2\hat{e}_{i_2}. \tag{6.15}$$

(*iv*) Translate the center of mass by $\Delta\vec{x}_i$ and all the atoms by $\Delta\vec{x}_i$.

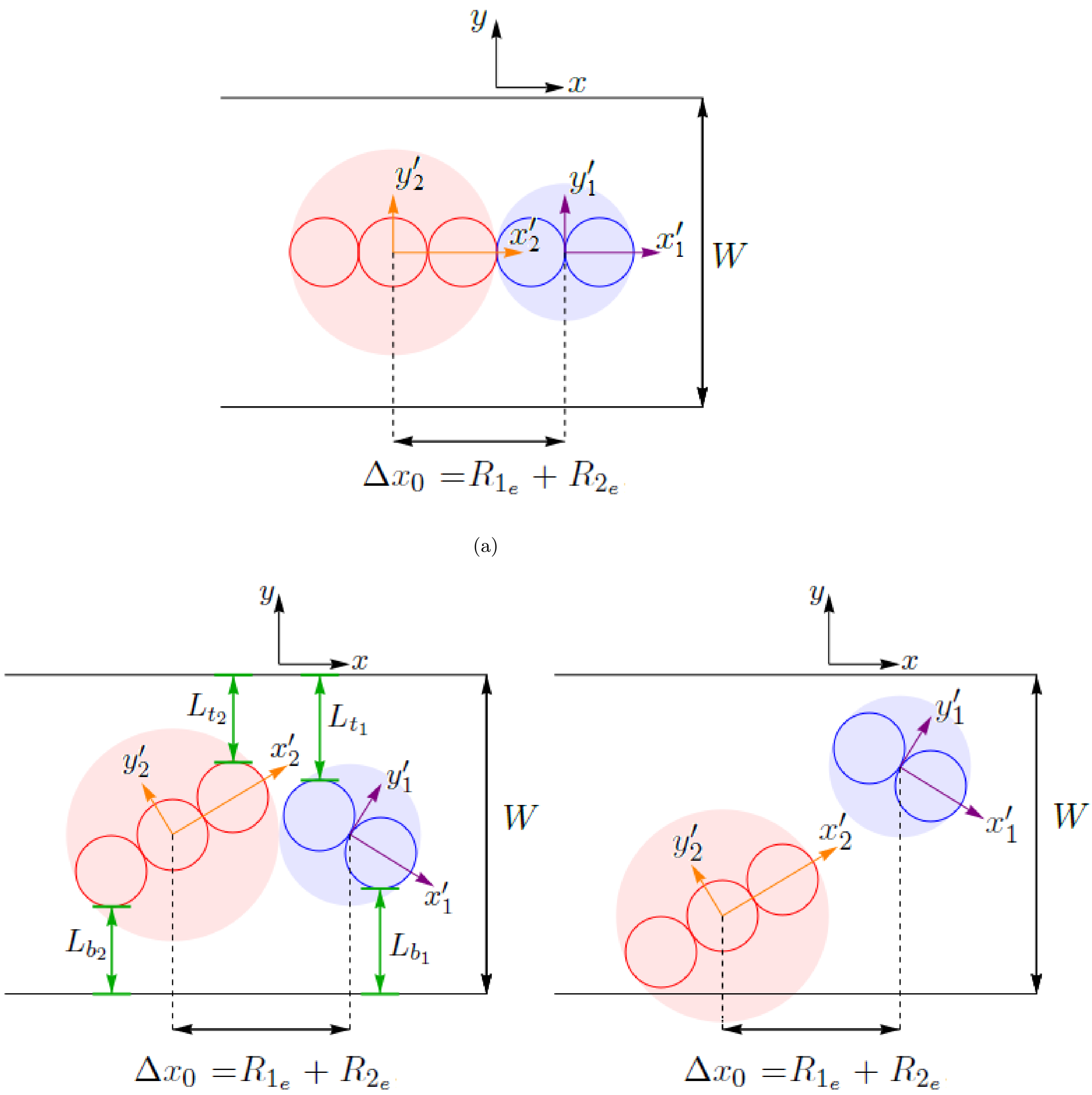

(a)

(b)

(c)

Figure 6.5: 2D oligomers initial trial setup. The procedure to set up a trial, initially, is to (a) setup the oligomers separated by a distance of $\Delta x_0 = R_{1_e} + R_{2_e}$, as shown. (b) Rotate each oligomer by an arbitrary angle about its geometrical center and get the available phase space. Determine if the configuration is valid. (c) If the configuration is valid, set the y position of each oligomer randomly, according with the available y phase space; otherwise, repeat the process until a valid configuration is reached.

To rotate the oligomer: (*i*) Translate the oligomer such that the center of mass of the oligomer lies at the $(x, y) = (0, 0)$ coordinate. (*ii*) Rotate the atoms of the oligomer, along with $\hat{e}_{i_1}$, $\hat{e}_{i_2}$, about the plane of the oligomer. (*ii*) Move the atoms and the center of mass such that the position of the center of mass matches with the original position of where it was.

Once the oligomers are moved, it has to be checked whether the oligomers obey the steric constraints, i.e., the oligomers do not intersect each other or the pore walls; the two cases are evaluated separately. To check if the oligomers intersect the pore walls, it is useful to first check if the surrounding disks (defined in Section 6.4.2) intersect the pore wall. If the surrounding disk of an oligomer does not intersect the pore walls, the oligomer does not intersect the pore walls. Otherwise, intersection of every circle in the oligomer with the pore walls has to be checked. To check the intersection of the oligomers, it suffices to check if the surrounding disks do not intersect each other. If this does not happen the oligomers cannot intersect. Otherwise, the intersection of the oligomers has to be checked for each of the circles the oligomers are composed of.

To evaluate the intersection criteria of the oligomers within the pore, define three logical variables Ac_{w_1}, Ac_{w_2} and Ac_{12}; where Ac_{w_1} and Ac_{w_2} are the binary logical variables (true/-false) that denote the intersection of the oligomers with the wall and Ac_{12} the binary logical variable that denotes if the oligomers intersect each other. To accept a move of the oligomers $Am\left(Ac_{w_1}, Ac_{w_2}, Ac_{12}\right)$ must be *true*, where

$$Am\left(U_1, U_2, \ldots, U_N\right) = U_1 \wedge U_2 \wedge \ldots \wedge U_N; \tag{6.16}$$

the "$\wedge$" operator makes reference to the logical "and" operator and "$\vee$" to the logical "or" operator.

To evaluate Ac_{w_i}, the intersection of the oligomers' circles with the pore walls have to be tested. Define $y_t = +W/2$ and $y_b = -W/2$ as the equations of the lines where the pore has its walls. For the oligomer *not* to intersect the pore walls, then either two of the conditions have to be met: (*i*) That the surrounding disk, $R_{i_{\text{surr}}}$, does not intersect the pore walls; a condition that is enough for the oligomer to not intersect the pore walls; or (*ii*) the individual circles, of which the oligomer is composed of, should not intersect the pore walls. Thus,

$$Ac_{w_i} = \{[(y_{i_{\rm cm}} + R_{i_{\rm surr}}) \leq y_t] \wedge [(y_{i_{\rm cm}} - R_{i_{\rm surr}}) \geq y_b]\} \vee \bigwedge_{j=1}^{N_i} \left\{ \left[\left(y_{i_j} + r_{i_j}\right) \leq y_t\right] \wedge \left[\left(y_{i_j} - r_{i_j}\right) \geq y_b\right] \right\} \tag{6.17}$$

must be true. To determine if the oligomers *do not* intersect each other, Ac_{12}, then either two of the conditions have to be met: (i) That the surrounding disks of the oligomers do not intersect each other; a condition that is enough for the oligomers to not intersect each other; or (ii) the individual circles of both oligomers should not intersect each other. Thus,

$$Ac_{12} = \left\{ \left[(x_{1_{\rm cm}} - x_{2_{\rm cm}})^2 + (y_{1_{\rm cm}} - y_{2_{\rm cm}})^2 \right] \geq (R_{1_{\rm surr}} + R_{2_{\rm surr}})^2 \right\} \vee \bigwedge_{i=1}^{N_1} \bigwedge_{j=1}^{N_2} \left\{ \left[\left(x_{1_i} - x_{2_j}\right)^2 + \left(y_{1_i} - y_{2_j}\right)^2 \right] \geq \left(r_{1_i} + r_{2_j}\right)^2 \right\} \tag{6.18}$$

must be true. See Figure 6.6.

To determine the outcome of a trial, the following criteria is used: (i) If the molecules have passed each other, the separation of the centers of mass of the oligomers along the x axis of the pore has to be less than or equal to $-\Delta x_0$, or (ii) if the molecules have failed to pass each other, the separation of the centers of mass of the oligomers along the x axis of the pore has to be greater than or equal to $2\Delta x_0$, see Figure 6.7. If the separation of the centers of mass of the oligomers along the x axis of the pore does not meet the pass or fail criteria, the trial continues until one of the two conditions is met.

It is important to notice that if the problem is to be solved computationally, for relatively narrow pores and when oligomers are in the passing positions, the number of conditions to be evaluated are $N_1 \cdot N_2$, a quantity that must be evaluated *at least once* for each move. The evaluation of these conditions, the translation and rotation of the oligomers, and the generation of the normal distributed random numbers are the main sources to determine the speed at which the program runs. Thus, it is of the highest importance to determine an appropriate time step Δt, so that the oligomers appropriately explore the possible phase space and make no unphysical moves (e.g., pass through each other), but is fast enough to output results in an acceptable amount of time.

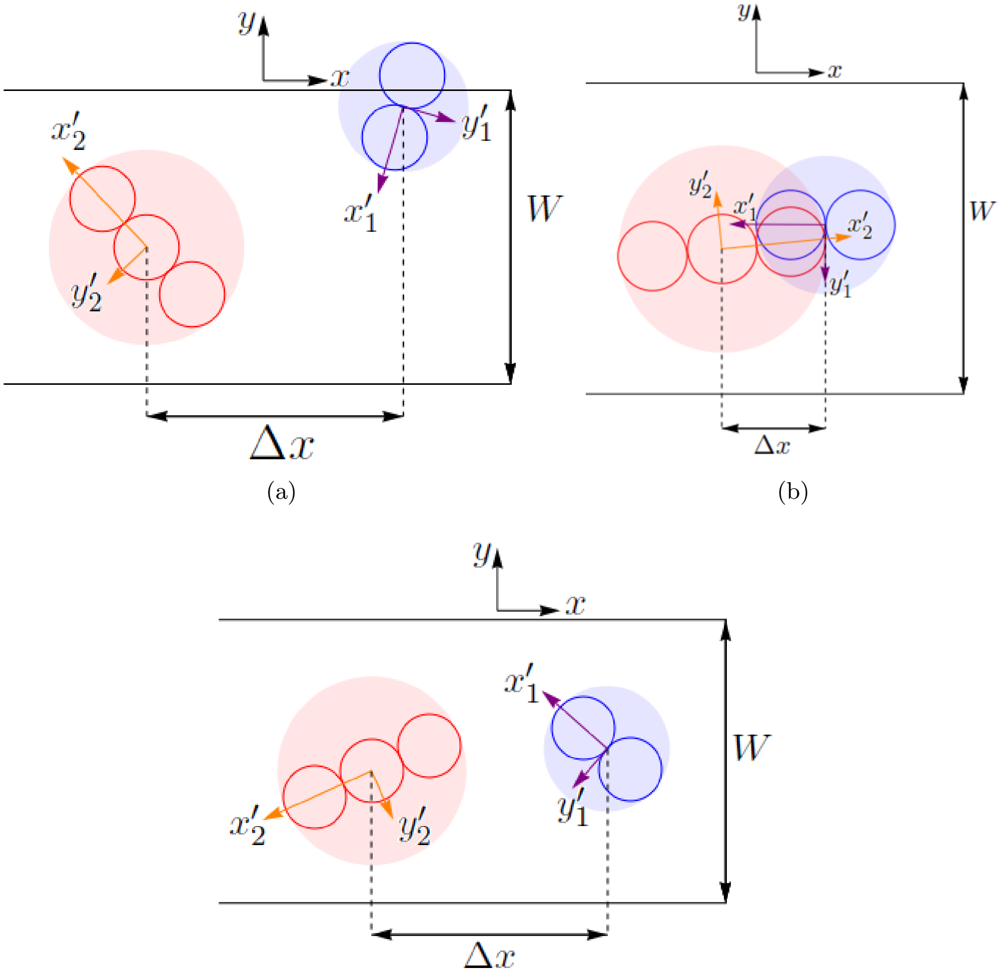

(a) (b)

(c)

Figure 6.6: 2D oligomers, examples of valid and invalid configurations. The configuration is not valid when (a) one or both oligomers intersect the pore, or (b) the oligomers intersect each other. An example of a valid configuration is when both oligomers (c) do not intersect each other or the pore.

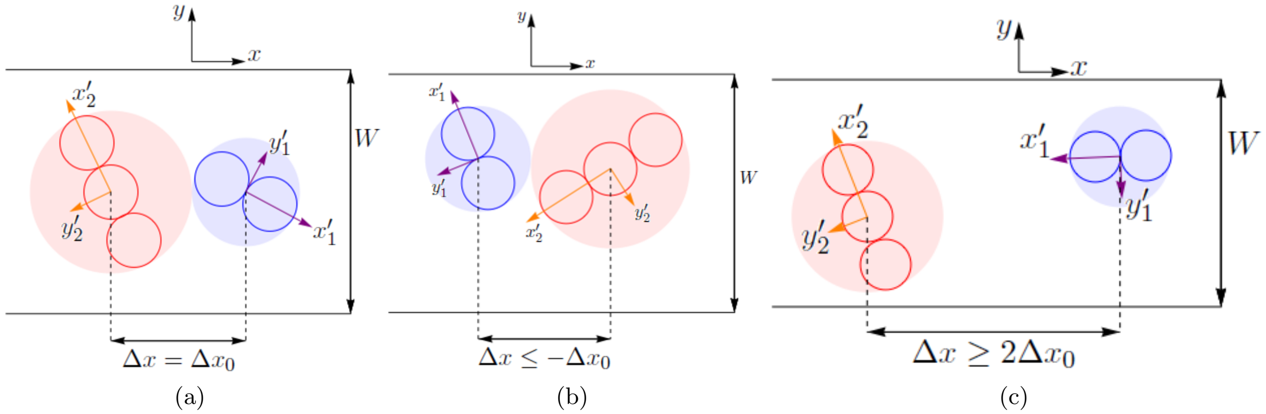

Figure 6.7: 2D oligomers, examples of a passing and failing criteria. Define Δx_0 from (a) a valid initial condition. The oligomers have (b) passed each other if the separation of the centers of mass of the oligomers along the x axis of the pore is greater than or equal to $-\Delta x_0$. The oligomers have (c) failed to pass each other if the separation of the centers of mass of the oligomers along the x axis of the pore is greater than or equal to $2\Delta x_0$.

6.5 Results

To determine the passing propensity of the oligomers, the diffusion tensor for each oligomer in the body-fixed axis and in dimensionless units is given by

$$D_{x_i'} = D_{y_i'} = D_{\theta_i} = 1; \tag{6.19}$$

see Figure 6.4. To obtain the passing propensity in the wide pore limit, the oligomer systems that are chosen are (see Figure 6.8): (i) m-m, (ii)m-d, (iii) m-tr, (iv) m-te, and (iv) m-p. Using dimensionless quantities, *all* the circles have unit radius $r = 1$, the pore widths to be explored are in the range $W/r \in [4.4, 10.8]$. Define the gap as the vertical phase space available for oligomers to pass each other, when in the transition state, see Figure 6.9; for this particular case the gap is simply given by $g = W - 4r$, that clearly implies $(g/r) = (W/r) - 4$. Thus, gaps in the range of $(g/r) = [0.4 - 6.8]$ are examined. The remaining parameter that needs to be chosen is the time step Δt. To get physical results, a time step that is small enough for the oligomer to properly explore the phase space is needed. However, the smaller the time step, the longer it will take for the simulations to run. Thus, it is convenient to probe several time steps, and determine which is the biggest time step at which the results start converging. The passing propensity is obtained as a function of the gap divided by the unit radius.

Following the algorithm in Section 6.4.1, the results for the different monomer-oligomer systems are obtained. The number of trials needed to get the simulations to converge to a stable result is $N = 2.5 \times 10^5$. To determine the number of trials needed to get accurate results, the passing propensity $P = \#$ of passes$/n$ is calculated each $n = 100$ trials, until $n = N$, and a visual estimate of how many trials are needed to get a constant probability, i.e., a small fluctuation of results about a fixed value; examples are shown in Figure 6.11.

The passing propensity as a function of the gap for the different systems are presented in Figure 6.11. From the results in Figure 6.11, the optimal time step for the simulations is determined to be $\Delta t = 10^{-4}$. The results for $\Delta t = 10^{-4}$ for all the systems are compared in Figure 6.12.

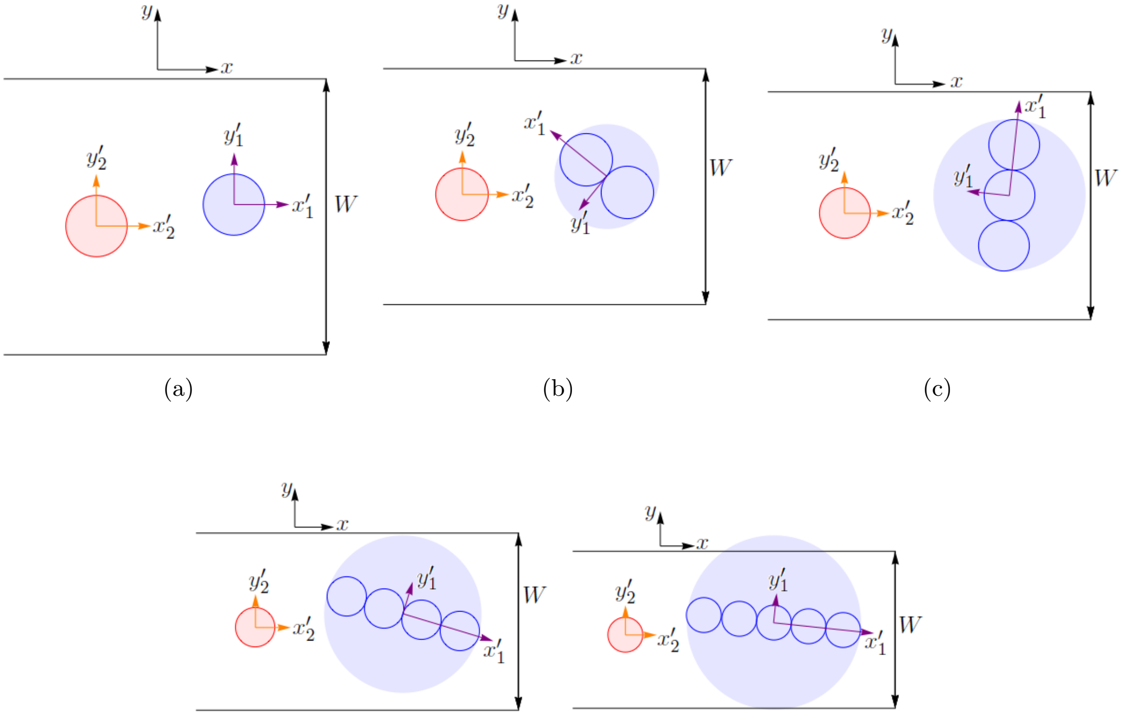

(a) (b) (c)

(d) (e)

Figure 6.8: 2D oligomers systems to be examined, (a) m-m, (b) m-d, (c) m-tr, (d) m-te and (e) m-p. All the circles have the same radius $r = 1$ and the same diffusion coefficients along the body-fixed axis. Diagrams not to scale.

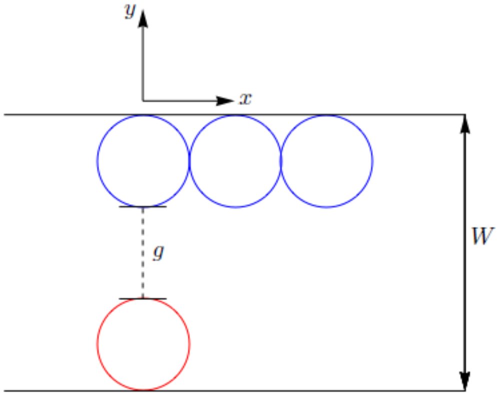

Figure 6.9: Gap definition for a 2D system of oligomers. The gap is defined as the minimum amount of phase space available for the oligomers to pass each other in the transition state.

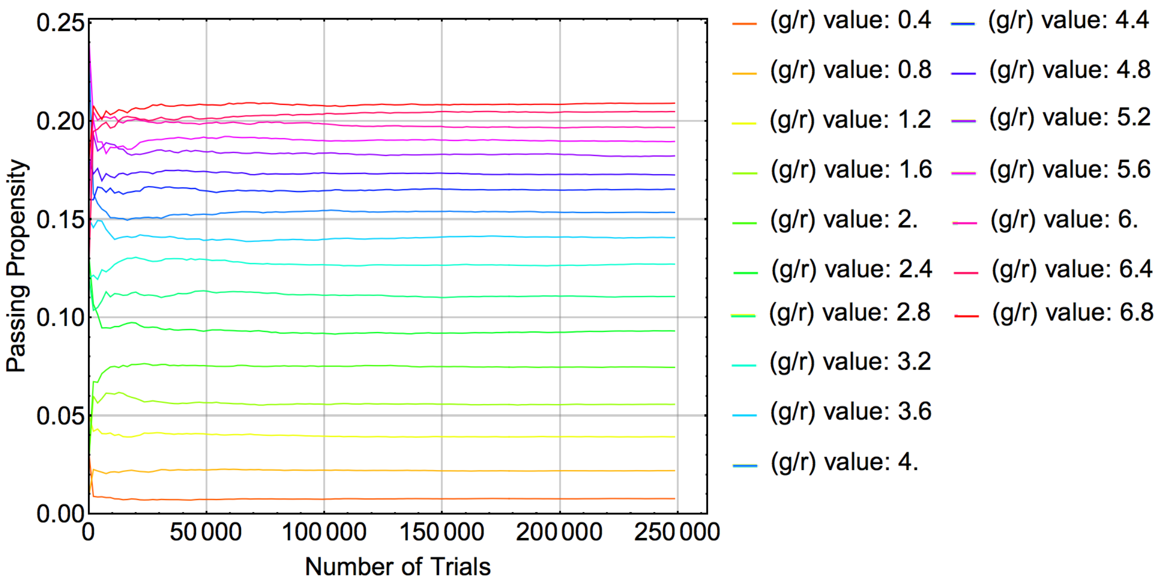

Figure 6.10: 2D passing propensity evolution with number of trials, the m-d case. A time step of $\Delta t = 10^{-4}$ is used. The passing propensity for several gap sizes is shown; fluctuations after $n = 120\,000$ trials are small and can be considered as the minimum number of trials to get a reliable estimate.

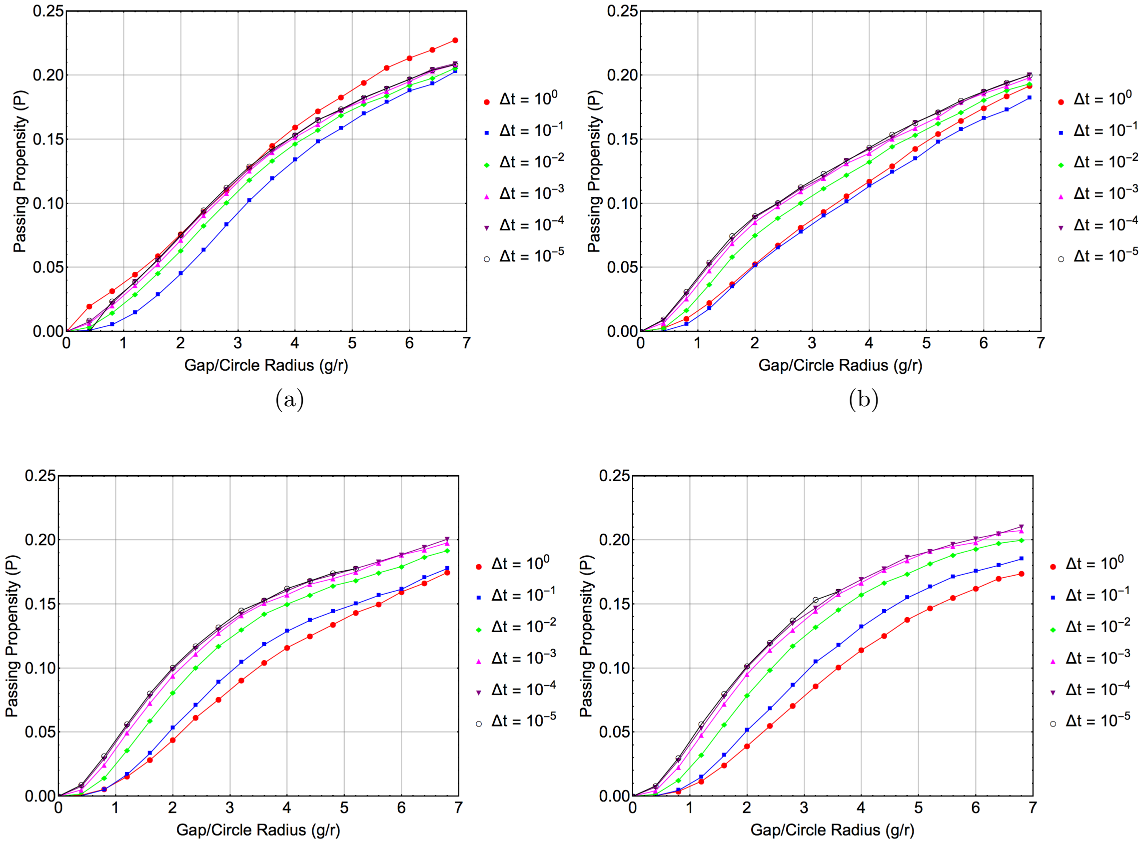

(a) (b)

(c) (d)

Figure 6.11: Passing propensity for different monomer-oligomer systems. Time steps of $\Delta t = \{10^0, 10^{-1}, 10^{-2}, 10^{-3}, 10^{-4}, 10^{-5}\}$ are used to determine the optimal time step for the (a) m-d, (b) m-tr, (c) m-te and (d) m-p systems. The optimal time step is determined to be $\Delta t = 10^{-4}$.

For specific gap sizes, the passing propensity for longer monomer-oligomer system is bigger than that for shorter oligomers. This can be explained by the available phase space for the oligomers to move in. Assume a linear oligomer made out of N barely touching but non-intersecting circles, as the oligomers that were used as the models, see Figure 6.8. If a gap is fixed, as the oligomer becomes longer, the less phase space available the oligomer will have to move and rotate in it. With the additional constraint that the long axis of the oligomer is more likely to be initially aligned with the x-axis of the pore, the longer the oligomer, the more likely it will remain aligned with the pore with increasing oligomer length, whereas for shorter oligomers, as the gap grows wider, the longest axis of the oligomer will be more likely to be perpendicular to the x-axis of the pore (see Figure 6.5). If the results are examined for $(g/r) = 0.4$ and $(g/r) = 0.8$, the results are consistent in that the smallest passing propensity is for the m-p system, and gradually increases as the number of circles of the oligomer decrease down to two, i.e., the m-d system; see Figure 6.12. It can also be inferred that the magnitude of the passing propensity, for larger gaps than the ones shown, will eventually assume the order $P_{\text{monomer}} \geq P_{\text{dimer}} \geq P_{\text{trimer}} \geq P_{\text{tetramer}} \geq P_{\text{pentamer}}$; as one would expect.

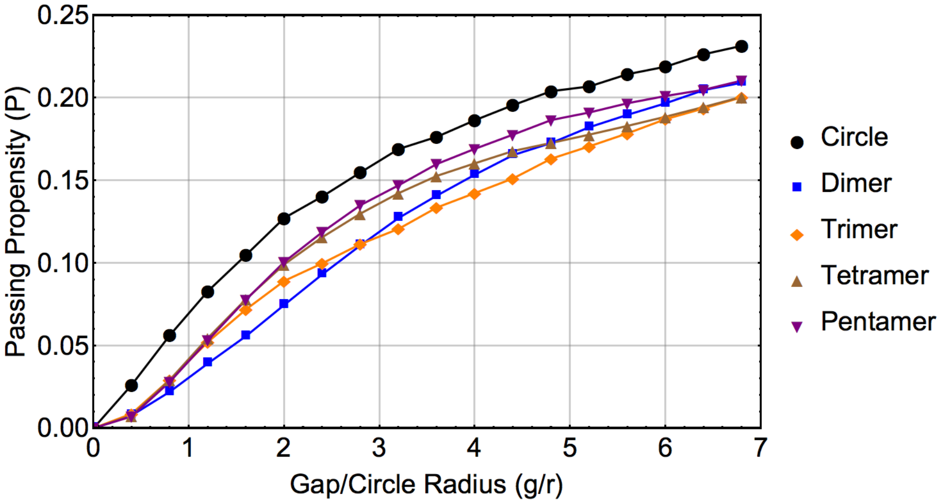

Figure 6.12: Passing propensity for different monomer-oligomer systems as function of (g/r). A time step of $\Delta t = 10^{-4}$ is used. To determine the passing propensity for each (g/r) data point, $N = 250\,000$ trials are used.

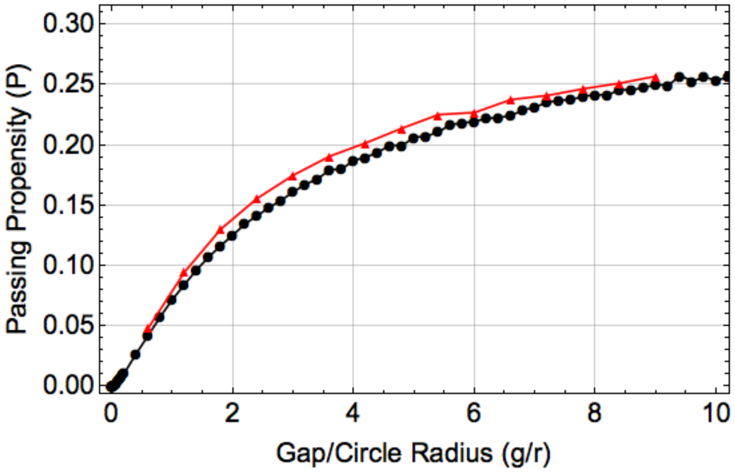

Figure 6.13: Results for the m-m system. The results obtained for this work match (red markers/triangles), to within the uncertainty, with those reported in [6, 10] (black markers/circles), specially when going to the small gap regime.

To validate the results, the m-m system is compared with the Langevin MD simulation results of [6, 10]. The results are further validated for the small gap regime, see Section 6.5.1. The results for m-m obtained in this work are compared to those in [6, 10] in Figure 6.13 and Figure 6.16(a), and the numerical results are compared in Table 6.1.

Of special interest are the results obtained for the m-d and m-tr systems. Using the results for the m-d and m-tr systems implementing the FPE [15] are obtained and compared to those obtained in this work, see Figure 6.14. It must be noted that when using the FPE, the same technique from [6] is implemented for the longer monomer-oligomer system, i.e., the flux of “injected” probability is kept constant, so that the boundary valued problem can be solved; the reader is referred to [6] for details. The results using the FPE approach do not really match the Langevin MD simulation results as the gap starts to get bigger, however, for smaller gaps the methods start to converge, see Section 6.5.1; consistent with the assumption that the probability for small gaps should converge. However, for scaling purposes, if the results are plotted in a log-log scale, when using the FPE approach, the general trend is that the results converge with those of the Langevin approach, in particular for the m-tr system.

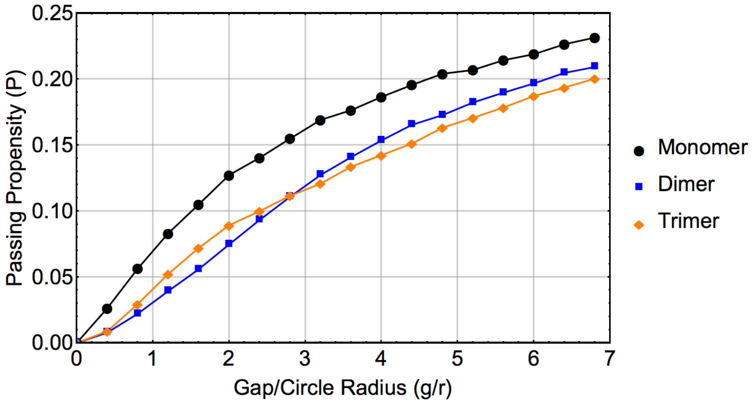

(a)

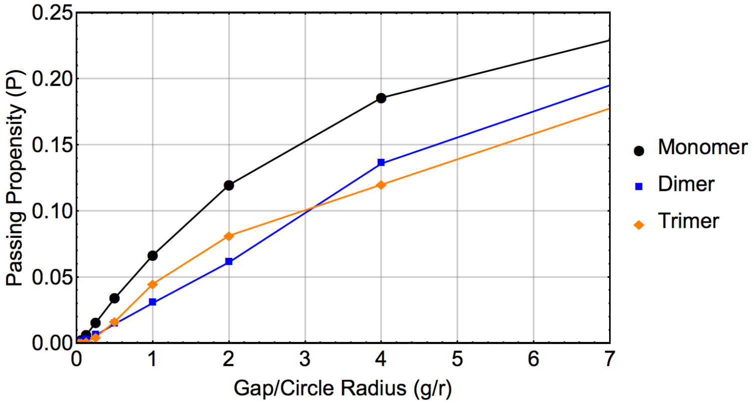

(b)

Figure 6.14: Comparing results for the monomer-oligomer system with the FPE. Comparing the results from (a) this work compared to the (b) results using the Fokker-Planck equation [15] for m-m (black circles), m-d (blue squares) and m-tr (orange diamonds). The results are qualitatively similar.

Table 6.1: Results for the m-m system. The results obtained for (a,c) this work match, to within the uncertainty, with (b,d) those reported in [6,10] , specially when going to the small gap regime.

Comparing M-M Results

	P			$\mathrm{Log}_{10}(P)$	
(g/r)	(a)	(b)	$\mathrm{Log}_{10}(g/r)$	(c)	(d)
0.6	0.0486	0.04262	-0.221849	-1.31336	-1.37039
1.2	0.09506	0.08473	0.0791812	-1.022	-1.07196
1.8	0.13052	0.11699	0.255273	-0.884323	-0.931851
2.4	0.15593	0.14161	0.380211	-0.80707	-0.848906
3.	0.17521	0.16145	0.477121	-0.756441	-0.791962
3.6	0.19083	0.1795	0.556303	-0.719353	-0.745936
4.2	0.20193	0.19004	0.623249	-0.694799	-0.721155
4.8	0.21411	0.19979	0.681241	-0.669363	-0.699426
5.4	0.22531	0.21108	0.732394	-0.64722	-0.675553
6.	0.22707	0.21962	0.778151	-0.64384	-0.658328
6.6	0.23779	0.22472	0.819544	-0.623806	-0.648358
7.2	0.24114	0.23552	0.857332	-0.617731	-0.627972
7.8	0.24672	0.24058	0.892095	-0.607796	-0.61874
8.4	0.25136	0.24594	0.924279	-0.599704	-0.609171
9.	0.25716	0.24999	0.954243	-0.589797	-0.602077

6.5.1 Small Gap Results

In the small gap limit, the passing propensity is believed to behave as a power law, $P \sim (g/r)^{\sigma}$. From results in [6], in a m-m system the σ parameter is determined to be $\sigma = 1.4$ using Langevin MD simulations that matches well when solving the FPE. For this case, the scaling coefficient σ for the m-d and m-tr system is determined, both using the Langevin method. As for the previous Section, all the radii of the circles in the i^{th} oligomer are set to $r = 1$ and the diffusion coefficients in the body-fixed frames axes are chosen to be $D_{x'_i} = D_{y'_i} = D_{\theta_i} = 1$; see Figure 6.4. Since for smaller gaps the probability is significantly lower, a larger number of trials have to be run. We choose this number to be $N = 5\,000\,000$ for gaps that are smaller than $(g/r) = 0.2$, otherwise, the number of simulations remains the same, $N = 250\,000$. As noted before, the time step is of crucial importance to optimize the data acquisition process. Thus, we choose a time step of $\Delta t = 10^{-5}$, that is the time step for which the results barely change if the time step is decreased, as noted in [10].

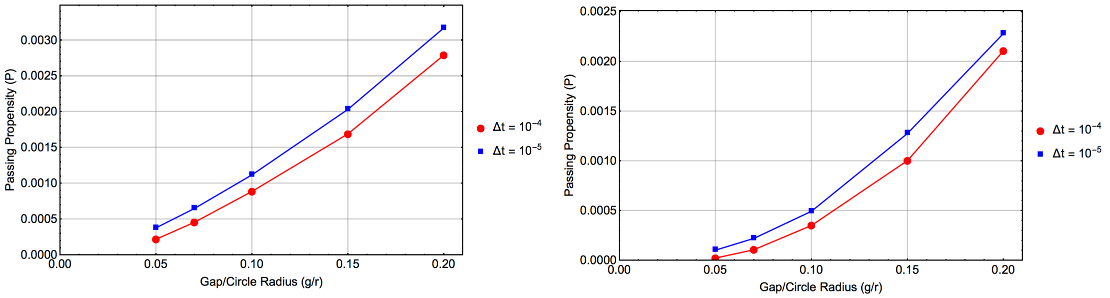

(a) (b)

Figure 6.15: Passing propensity as a function of gap size for small gaps. Results for (a) m-d and (b) m-tr are shown. Since the difference in the results for the two time steps is significant, we choose $\Delta t = 10^{-5}$ for subsequent analysis.

The first feature to be explored is how well the passing propensity converges by changing the time step, in the small gap regime. For bigger time steps than $\Delta t = 10^{-4}$, it is clear that the simulations will not produce acceptable results, so we mainly focus on the time steps $\Delta t = \left\{10^{-4}, 10^{-5}\right\}$. Since for small gaps the passing propensity is small, a subtle change in results will change the scaling σ in a significant way. Since the results for $\Delta t = 10^{-4}$ differ significantly from the results for $\Delta t = 10^{-5}$, we choose to use the time step $\Delta t = 10^{-5}$ for the subsequent analysis; see Figure 6.15.

For wider gaps, the FPE analysis yields results that do not agree with the Langevin analysis. However, for smaller gaps, the results should converge. To see how well the results converge, a log-log plot of the passing propensity against the full range of gaps examined is presented in Figure 6.16; the data for the m-m case corresponds to that in [6]. It is the case that for the m-m and the m-tr case, the results for both the Langevin simulations and the FPE agree for small gaps, whereas the results for the m-d do not. However, it is seen that in the last few data points for the m-d case, the results begin to be closer together and possibly converge at smaller gap sizes.

To determine the scaling exponent σ, the results from the Langevin simulations are going to be used. It is worthwhile to mention again that the definition of "small gap" refers to the regime where $P \sim (g/r)^{\sigma}$. As can be seen from Figure 6.16, the small gap regime for the m-m system starts at gap sizes smaller than that for m-d and m-tr systems. Thus, it is important

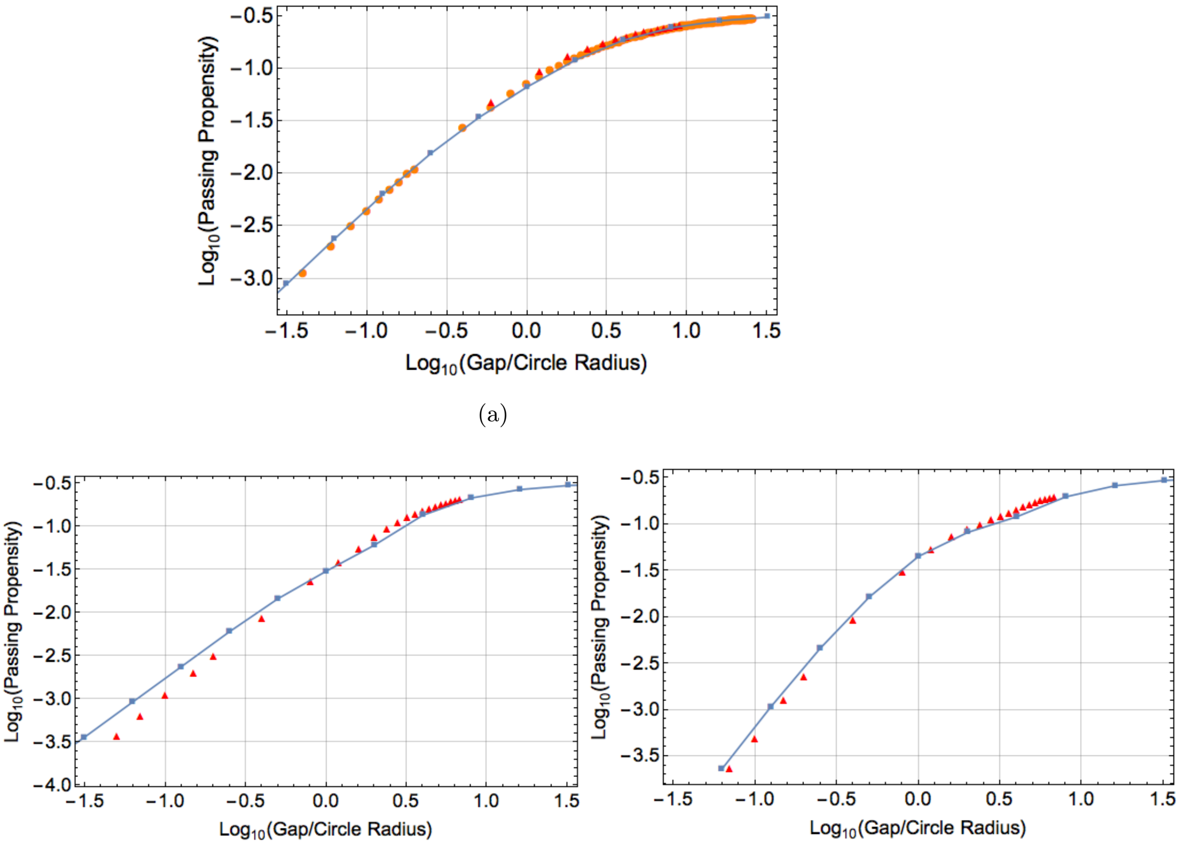

(a)

(b)

(c)

Figure 6.16: Passing propensity as a function of gap size for small gaps with $\Delta t = 10^{-5}$, log-log scale. Results for (a) m-m, (b) m-d and (c) m-tr are shown. Triangles are used to represent the results obtained in this work, circles for the results in [6] and squares for the FPE results.

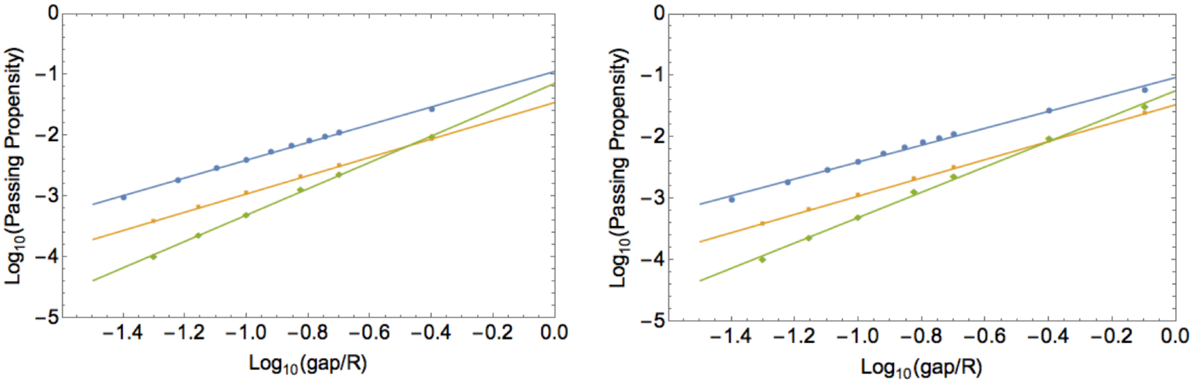

(a)

(b)

Figure 6.17: Small gap scaling for the different systems. Results for parameter (a) fitting using gaps up to $(g/r) = 0.4$, and parameter (b) fitting using gaps up to $(g/r) = 0.8$. The data points for the m-m system are represented by the blue circles, for the m-d system by the tan squares and for the m-tr system by the green diamonds.

to determine what gap sizes are adequate to determine σ for each system. The systems to be examined are m-d and m-tr; the m-te and m-p systems are not examined. The small gaps range for both the m-d and the m-tr systems range from $(g/r) = 0.05$ to $(g/r) = 0.2$. Of particular interest is the point where the m-d and the m-tr curves intersect, and the ordering of the magnitude of the passing propensity becomes natural, i.e., for longer monomer-oligomer systems the passing propensity should be smaller than for shorter monomer-oligomer systems. The methodology to determine the scaling exponent σ exploits the properties of logarithms

$$P = \alpha(g/r)^{\sigma} \quad \Rightarrow \quad \mathrm{Log}_b\left(P\right) = \sigma \mathrm{Log}_b\left(g/r\right) + \mathrm{Log}_b\left(\alpha\right). \tag{6.20}$$

Thus, we use the logarithm of the gaps and with the respective passing propensity of the system under consideration, and then make a linear fit $y = ax + c$ of the data; with $y = \mathrm{Log}_{10}\left(P\right)$, $x = \mathrm{Log}_{10}\left(g/r\right)$, and $a = \sigma$. Results are presented in Figure 6.17. The results for the fits are presented in Table 6.2.

From Figure 6.17, it can be inferred that the points used to fit the data changes significantly, and it is not clear if the point with $(g/r) = 0.8$ lies within the small gap regime. Statements about the validity of the linear fits can be made from Table 6.2. The R^2 values for the linear fits indicate that for the m-m system, the gap value $(g/r) = 0.8$ might be too big, this from a

Table 6.2: Linear fits to determine the small gap scaling exponent σ. Refer to Figure 6.17 for the definition of (a) and (b); (c) corresponds to the fits from the data obtained by solving the FPE [15]. The R^2 values, or how close the values are to the regression line, are given below each data set.

	Fits for monomer-oligomer small gap results		
Oligomer	monomer	dimer	trimer
(a)	$y = 1.46x - 0.944$	$y = 1.50x - 1.45$	$y = 2.17x - 1.14$
R^2	0.9974	0.9998	0.9990
σ	1.46 ± 0.1	1.50 ± 0.1	2.17 ± 0.1
(b)	$y = 1.37x - 1.03$	$y = 1.49x - 1.47$	$y = 2.06x - 1.24$
R^2	0.9943	0.9998	0.9971
σ	1.37 ± 0.1	1.49 ± 0.1	2.06 ± 0.1
(c)	$y = 1.41x - 0.92$	$y = 1.36x - 0.60$	$y = 1.96x + 1.77$
R^2	0.9998	0.9999	0.9987
σ	1.41	1.36	1.96

slight decrease in the R^2 value for data set (b); thus, to two significant figures, the value for the scaling exponent of the m-m system can be considered to be $\sigma = 1.4$, as the results in [6] suggest. For the m-d system, the R^2 value remains the same when adding the $(g/r) = 0.8$ gap to the fitting data. Thus, it can be inferred that the scaling exponent for the m-d system, to two significant figures, is $\sigma = 1.5$, slightly above the $\sigma = 1.4$ predicted by solving the FPE, and the gap $(g/r) = 0.8$ correspond to the small gap regime. For the m-tr system, the R^2 value slightly changes when adding the $(g/r) = 0.8$ gap to the fitting data, and the scaling exponent σ is slightly different for both cases. Thus, it can be inferred, that the scaling exponent will lie somewhere between 2.17 and 2.06, that can be taken as $\sigma \approx 2.1$; a value slightly above the one proposed by solving the FPE for the m-tr system [15].

It is worth noticing that the intersection point of the curves for the m-d and the m-tr intersect twice; the intersection point for the wider gap regime can be easily obtained. In Figure 6.17(b), the monomer- dimer and m-tr fitted curves intersect closer at the location where the data points are, so that the most likely values for scaling exponent are closer to those in data set (b) of Table 6.2(b).

6.6 Summary and Conclusion

The passing propensity within infinite rectangular pores of width W for monomer-oligomer systems has been elucidated by using a Langevin simulation approach, and the results have been compared to those obtained by solving the FPE [6, 15]; both in the small gap regime, where $P \sim (g/r)^{\sigma}$, and for wider gaps. For the small gap regime, m-m, m-d and m-tr systems were examined; for the wider gap the former, including m-te and m-p systems, were examined.

The scaling exponents for the small gap regime are determined to be $\sigma_{\text{m-m}} = 1.4 \pm 0.1$, $\sigma_{\text{m-d}} = 1.5 \pm 0.1$ and $\sigma_{\text{m-tr}} \approx 2.1 \pm 0.1$, that are consistent with the idea that the longer the oligomer is, the passing propensity should get smaller faster, and are consistent with those obtained by solving the FPE in the small gap regime, however, they exhibit a slightly higher value than those predicted in [6, 15].

For wider gaps, the passing propensity for some of the oligomers, in general, do not follow the order $P_{\text{m-d}} \geq P_{\text{m-tr}} \geq P_{\text{m-te}} \geq P_{\text{m-p}}$, however it is natural to expect it, since the physical condition that initially the shortest axis of the oligomer tends to be perpendicular to the longest axis of the pore, favors passing for longer oligomers in a specific gap regime. Asymptotically, it is expected that the natural order of the passing propensity becomes $P_{\text{m-d}} \geq P_{\text{m-tr}} \geq P_{\text{m-te}} \geq P_{\text{m-p}}$.

The systems examined here have given insight in the scaling limit of small gaps for the monomer-oligomer system. Further work can be devoted to elucidating the scaling exponent for more complex systems such as dimer-oligomer systems. Further work can be directed towards the determination and scaling of more realistic three-dimensional systems such as sphere-oligomer, or even oligomer-oligomer, using more detailed modeling, as the exact diffusion coefficients can be exactly obtained from the procedure in [13].

6.7 Acknowledgements

We acknowledge discussions with Chi-Jen Wang; we also thank him for providing us with the FPE results for the monomer-monomer, monomer-dimer and monomer-trimer systems. This work was supported by the U.S. Department of Energy (USDOE), Office of Basic Energy Sciences, Division of Chemical Sciences, Geosciences, and Biosciences through the Ames

Laboratory Chemical Physics program. The work was performed at Ames Laboratory which is operated for the USDOE by Iowa State University under Contract No. DE-AC02-07CH11358.

6.8 Appendix A: Determining the Initial Orientation for a General Shaped Oligomer.

To approximately, but accurately, get the minimum pore width for oligomers to be able to fit the pore is to algorithmically get the shortest distance that transverses the oligomers, that will be defined as the *shortest axis* of the oligomer; in an analogous way, the longest distance that transverses the oligomers will be defined as the *long axis* of the oligomer.

To get the shortest oligomer axis and length, project each atom position vector onto a selected unit vector $\hat{r} = (\cos(\theta), \sin(\theta))$; with $\theta \in [0, \pi)$; and add and subtract the corresponding atom radius from this value, make a set of values out of the maximum values and a second list out of minimum values. From the set of these maximum values get the maximum value; for the list of the minimum values, get the minimum value. Subtract the minimum value from the maximum value and take the absolute value, this will be the length of the oligomer along $\hat{r}$, given a fixed angles θ. Do this for the complete range of θ and obtain the maximum length $l_{\max}$ and the minimum length $l_{\min}$. The minimum width of the pore for the oligomer to fit is $l_{\min}$. In Figure [add references] the shortest axis of the oligomers are shown.

In the particular case of two dimensions, the value of the shortest axis determines the minimum pore width for a single oligomer to fit in the pore, even if the oligomer does not have a symmetry axis. The minimum passing space will be useful to determine the initial setup of each trial.

Bibliography

[1] D-J. Liu, A. García, J. Wang, D. M. Ackerman, C-J. Wang, and J. W. Evans. Kinetic Monte Carlo simulation of statistical mechanical models and coarse-grained mesoscale descriptions of catalytic reaction-diffusion processes: 1D nanoporous and 2D surface systems. *Chem. Rev.*, 115:pp. 5979–6050, 2015.

[2] T. E. Harris. Diffusion with "collisions" between particles. *J. Appl. Prob.*, 2:pp. 323–338, 1965.

[3] V. S-Y. Lin, D. R. Radu, M-K. Han, W. Deng, S. Kuroki, B. H. Shanks, and M. Pruski. Oxidative polymerization of $1,4$-diethynylbenzene into highly conjugated poly(phenyle butadiynylene) within the channels of surface-functionalized mesoporous silica and alumina materials. *J. Am. Chem. Soc. (Commun.)*, 124:pp. 9040–9041, 2002.

[4] D-J. Liu, H-T. Chen, V. S-Y. Lin, and J. W. Evans. Statistical mechanical modeling of catalytic polymerization within surface functionalized materials. *Phys. Rev. E*, 80:011801, 2009.

[5] D-J. Liu, H-T. Chen, V. S-Y. Lin, and J. W. Evans. Polymer length distributions for catalytic polymerization in mesoporous materials: Non-Markovian behavior associated with partial extrusion. *J. Chem. Phys.*, 132:154102, 2010.

[6] C-J. Wang, D. M. Ackerman, I. I. Slowing, and J. W. Evans. Langevin and Fokker-Plank analyses of inhibitted molecular passing processes controlling transport and reactivity in nanoporous materials. *Phys. Rev. Lett.*, 113:038301, 2014.

[7] D. S. Scholl. Characterizing adsorbate passage in molecular sieve pores. *Chem. Eng. J.*, 74:pp. 25–32, 1999.

[8] N. G. Van Kampen. *Stochastic processes in physics and chemistry. Third edition.* Elsevier, 2007.

[9] W. T. Coffey, Y. P. Kalmykov, and J. T. Waldron. *The Langevin equation.* World Scientific, 2004.

[10] D. M. Ackerman. *Interplay between inhibited transport and reaction in nanoporous materials.* PhD thesis, Iowa State University, 2013.

[11] J. García de la Torre and V. A. Bloomfield. Hydrodynamic properties of complex, rigid, biological macromolecules: Theory and applications. *Quaterly Reviews of Biophysics*, 14:pp. 81–139, 1981.

[12] S. E. Harding. A general method for modeling macromolecular shape in solution: A graphical (II-G) intersection procedure for triaxial ellipsoids. *Biophys. J.*, 51:pp. 673–680, 1987.

[13] B. Carrasco and J. García de la Torre. Hydrodynamic properties of rigid particles: Comparison of different modeling and computational procedures. *Biophyscial Journal*, 75:pp. 3044–3057, 1999.

[14] S. Hansen. Translation friction coefficients for cylinders of arbitrary axial ratios estimated by monte carlo simulation. *J. Chem. Phys.*, 121:pp. 9111–9115, 2004.

[15] C-J. Wang, A. García, and J. W. Evans. Using the 2D Fokker-Planck equation to elucidate the passing propensity of a circle-dimer and circle-trimer system (unpublished). Passing propensity of oligomers using a Fokker-Planck equation approach, 2017.

CHAPTER 7. LANGEVIN ANALYSIS OF THE MOLECULAR PASSING PROPENSITY IN CYLINDRICAL PORES: APPLICATION TO PNB CONVERSION INTO AN ALDOL PRODUCT

Abstract

Langevin molecular dynamic simulations are used to determine the passing propensity of 4-nitrobenzaldehyde and 4-(4-nitrophenyl)-2-butanone in a cylindrical channel. The molecules are coarse-grained to molecules made out of spheres. By imposing non-overlapping steric constraints on the molecules with the pore walls and between themselves, the passing propensity of the molecules in the channel is determined. Then, the passing propensities, along with other parameters, are then mapped into a further coarse-grained kinetic Monte Carlo model, where the whole reaction-diffusion system is modeled. The results for the product yield in the Monte Carlo simulation are then compared with the experimental results. All length units are given in angstroms (Å) and mass units in atomic mass units (*au*), unless otherwise stated.

7.1 Introduction

Solution-phase catalytic conversion processes in nanoporous materials involve diffusion of reactant from the exterior fluid into the pores, conversion to product in the vicinity of catalytic sites, and ideally efficient diffusion product out of the pores. The latter is necessary to free up space for additional reactant to enter the pores. Thus, there is some recognition that inhibited passing of reactants and products within the pores, and in particular the extreme case of single-file-diffusion (SFD) corresponding to no passing, strongly inhibits reaction yield [1–4].

A detailed molecular-level description of this process could in principle be provided by many-particle Molecular Dynamics (MD) simulations, or many-particle Langevin simulations (where the solvent is treated implicitly). However these approaches are not particularly useful due to the large number of particles and/or the fundamental difficulty in accessing experimentally relevant time scales. Thus, instead typically coarse-grained stochastic lattice-gas modeling is implemented where the pore is divided into a linear array of cells with size comparable to the reactant and product species . Adsorption and desorption from the pore, and diffusion with the pore, are treated by movement of reactants and products between the cells with appropriately selected rates. Just allowing hopping to adjacent unoccupied cells corresponds to imposing a SFD constraint. Thus, in general one allows exchange of reactant and product on adjacent sites at a rate controlled by an exchange probability, P_{ex}, [2,4] defined precisely in subsequent sections. From the comments above, it is clear that reaction yield should depend strongly on this parameter P_{ex}.

For modeling of specific reaction processes, it is clear that reliable systems specific parameters are needed for input into the coarse-grained modeling. In particular, it is important to obtain a reliable estimate of some measure of passing propensity, P, for reactants and products (defined in subsequent sections), which directly determines the exchange probability, P_{ex}, introduced above. While the above mentioned many-particle MD or Langevin simulations of the overall process are not viable, we suggest that targeted Langevin simulations of a single pair of reactant and product molecules is viable, and can provide effective quantification and insight into the behavior of P. There is a lack of such analysis for specific systems in the literature. However, such simulations will be the main focus of this Chapter. Our modeling will be simplified assuming that the major factor controlling P is steric effects (i.e., non-overlap of reactant and product molecules treated as rigid with hard-core interactions, and no overlap of these species with the pore walls).

In Section 7.2, the general strategy to model the molecules and the Langevin equations of motion are presented. In Section 7.3, the implementation of the Langevin simulations is discussed and algorithm to determine the passing propensity P is given. In Section 7.4, details on how to get the numerical quantities needed as input for the Langevin simulations are examined. In Section 7.5, the results for the Langevin simulations are analyzed and a brief discussion of how to get parameters for the kinetic Monte Carlo (KMC) simulations is presented. Finally, in

Section 7.6, the results for the KMC simulations are presented, ending with a brief summary and conclusion in Section 7.7.

7.2 General Strategy to Model the Molecules and the Langevin Equations of Motion

To determine passing propensity of the molecules, P, and the product yield for the reaction described in Section 7.1, the parameters of the system must be determined. To determine these parameters, a thorough description of the system under study is necessary. The system under consideration consists of amine functionalized mesoporous silica nanoparticles. These nanoparticles are characterized by the structure of its nanopores, i.e., the nanopores are linear, cylindrical, transverse the particle and do not intersect with each other [5–7], see Figure 7.1. The nanoparticles are immersed in an acetone and 4-nitrobenzaldehyde solution. Inside the pore, the 4-nitrobenzaldehyde molecules diffuse near the pore walls, where the 4-nitrobenzaldehyde molecules catalytically and irreversibly react with the acetone in the presence of catalytic amine groups, and forms 4-(4-nitrophenyl)-2-butanone [8]. The width of the pores in the silica nanoparticles we consider range from $\sim 2\,\mathrm{nm} - 5\,\mathrm{nm}$, pores that are wide enough for the 4-nitrobenzaldehyde and 4-(4- nitrophenyl)-2-butanone molecules to be able to pass each other. When the molecules are close to the pore ends, the product molecules can diffuse out of the pore, thus populating the outside of the pore with product, that can eventually diffuse into the pore again, when the outside concentration is high enough.

7.2.1 The equations of motion

To describe how bodies move in a three-dimensional environment, the way the bodies translate and rotate are needed. For an isotropic body, i.e., a sphere, the equations of motion take a simple and straight forward form. Spheres are often used in modeling complicated shaped bodies [9–11]. The main strategy will be to coarse grain the molecules as a set of spheres whose radii corresponds to the van der Waals radius of the atoms which they are composed of.

Before writing the equations of motion for the molecules, we shall make some approximations: (i) The molecules move in a viscous isotropic and homogeneous liquid, meaning that if a

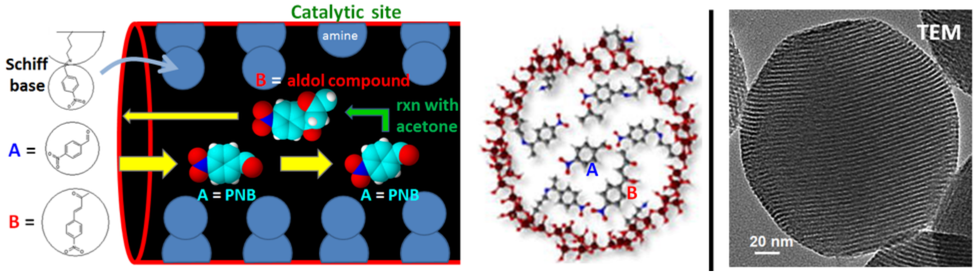

Figure 7.1: Schematic of the process and silica nanoparticles. To the left Schematic of the conversion of PNB to an aldol compound by reaction with acetone in amine-functionalized MSN. The attachment of PNB to the amine functionalized groups form a Schiff base, reducing the effective pore diameter. In the middle, pore cross-sectional schematic. To the right, TEM image of mesoporous silica nanoparticle (MSN) with visible pores oriented from left to right.

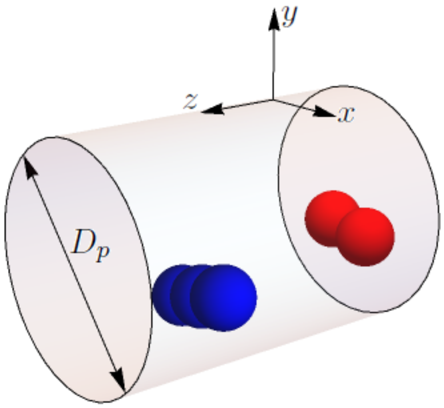

Figure 7.2: Pore model for the 3D Langevin simulations. The molecules, that are modeled as a collection of spheres, undergo Brownian motion within an infinite length cylindrical pore of cross-sectional diameter D_p.

rigid set of axis is set and fixed on a molecule, no matter where the molecule is placed, or how the molecule is rotated within the fluid, the diffusion tensor remains the same when calculated with respect to the fixed axis. (*ii*) The pore is an infinite length cylinder along the main axis and it has cross section diameter D_p, see Figure 7.2. (*iii*) The solvent is an ideal fluid, where no-slip boundary conditions are used. (*iv*) The molecules only have steric interaction with each other and the pore walls; other type of long and short distance interactions are suppressed.

To get the translation equations of motion, one uses Newton's second law

$$\vec{F}_{i_{\text{net}}} = m_i \ddot{\vec{r}}_i, \tag{7.1}$$

with $\dot{\vec{r}} = \frac{\mathrm{d}\vec{r}}{\mathrm{d}t}$, $\ddot{\vec{r}} = \frac{\mathrm{d}^2\vec{r}}{\mathrm{d}t^2}$, etc. The net force on the i^{th} molecule, $\vec{F}_{i_{\text{net}}}$, is just the sum of *all* forces on all the atoms in the molecule. The forces that are applied on the molecules, in this case, are the frictional forces, that are proportional to the velocity, and a random Wiener process, reflecting the thermal fluctuations in the solvent environment, so that the equations read

$$m\ddot{\vec{r}} = -\tilde{\zeta}_t\dot{\vec{r}} + \vec{F}\,(t)\,; \tag{7.2}$$

where $\tilde{\zeta}_t$ is the *mass independent translational* friction tensor, further details are given in Section 7.2.2. The last term in Equation 7.2, $\vec{F}\,(t)$, is a random *normal* distributed force, such that the time average of the force is zero and the forces are spatially correlated [12]

$$\left\langle \vec{F}\,(t) \right\rangle = 0, \tag{7.3a}$$

$$\left\langle F_i\,(t)\,F_j\,(t')\right\rangle = 2k_BT\zeta_{t_{ij}}\,\delta\left(t - t'\right); \qquad i, j \in \{x, y, z\}\,. \tag{7.3b}$$

The equation is now not a deterministic differential equation, but a stochastic differential equation. Thus, we are forced to use a numerical or computational method to solve this equation. We consider exclusively the overdamped regime, where $\ddot{\vec{r}} = 0$, so that Equation 7.2 becomes [13, 14]

$$\tilde{\zeta}_t\dot{\vec{r}} = \vec{F}\,(t) \quad \text{with} \quad \vec{F}\,(t) = \sqrt{2k_BT}\,\tilde{\zeta}_t^{1/2}\vec{\mathcal{W}} \quad \text{and} \quad \tilde{D}_t = k_BT\,\zeta_t^{-1}; \tag{7.4}$$

where $\tilde{D}_t$ is the positive definite symmetric translation diffusion tensor and $\vec{\mathcal{W}}$ is a 3×1 vector of normally distributed random numbers. From Equation 7.4, the stochastic differential equation to be solved is

$$\dot{\vec{r}} = \sqrt{2}\,\tilde{\mu}_t\vec{\mathcal{W}}, \tag{7.5}$$

where $\tilde{\mu}_t$ is a symmetric tensor such that $\tilde{\mu}_t\tilde{\mu}_t^T = \tilde{D}_t$. Physically, $\tilde{D}_t$ is required to be a symmetric positive definite tensor, thus, $\tilde{\mu}_t$ is obtained from $\tilde{D}_t$ by a Cholesky decomposition. To solve the equations, an Euler-Maruyama scheme is used so that the discrete correlation of $\vec{F}\,(t)$ is [15]

$$\left\langle F_i\,(t_n)\,F_j\,(t_n)\right\rangle = \frac{1}{\Delta t_n}\int_{t_n}^{t_{n+1}} F_i\,(t)\,F_j\,(t)\,\mathrm{d}t = \frac{2k_BT\,\zeta_{t_{ij}}}{\Delta t_n}. \tag{7.6}$$

The solution of the equation, at each time step, is given by

$$\frac{\vec{r}_{i+1} - \vec{r}_i}{\Delta t} = \sqrt{\frac{2}{\Delta t}}\,\tilde{\mu}_{t_i}\vec{\mathcal{W}}_i \quad \rightarrow \quad \vec{r}_{i+1} = \vec{r}_i + \sqrt{2\Delta t_i}\,\tilde{\mu}_{t_i}\vec{\mathcal{W}}_i; \quad f_i = f(t_i)\,. \tag{7.7}$$

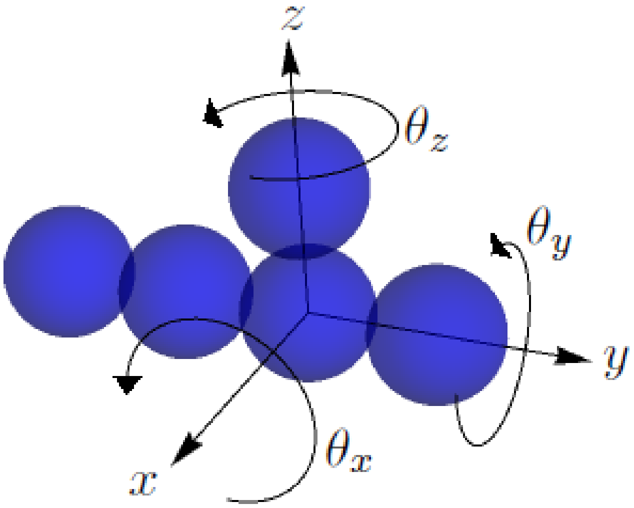

Figure 7.3: Rotations of asymmetric molecules. In general the molecules are asymmetric and rotations about the different axes have to be distinguished. The translational coordinates and rotation angles are shown; the x, y, z coordinates correspond to the translational coordinates and θ_x, θ_y and θ_z to the rotation angles.

For rotations, the equations of motion to be solved are similar to those of Newton's equations for translation

$$\vec{\tau}_{i_{\text{net}}} = \tilde{I}_i \ddot{\vec{\theta}}_i; \tag{7.8}$$

where $\tilde{I}_i$ is the moment of inertia tensor and $\vec{\theta}_i$ represents the angles of rotation around the different axis of the i^{th} molecule , see Figure 7.9 and Figure 7.10. As for the translational equations, the net torque on the i^{th} molecule, $\vec{\tau}_{i_{\text{net}}}$, is the sum of *all* torques on all the atoms in the molecule.

As for the translational part, the rotational equations of motion include a random Wiener process, that represent the torques induced by the thermal fluctuations in the solvent, and a frictional force that is proportional to the angular velocity of the body. The equations of motion are given by

$$\tilde{I}\ddot{\vec{\theta}} = -\tilde{\zeta}_r \dot{\vec{\theta}} + \vec{\tau}\,(t)\,; \tag{7.9}$$

where $\tilde{\zeta}_r$ is now the rotational friction tensor. In an analogous way to translations, the random torque obeys

$$\langle \vec{\tau}\,(t) \rangle = 0, \tag{7.10a}$$

$$\left\langle \tau_i\,(t)\,\tau_j\,\left(t'\right) \right\rangle = 2k_B T \zeta_{r_{ij}}\,\delta\left(t - t'\right); \qquad i, j \in \{x, y, z\}\,. \tag{7.10b}$$

Since we are working in the over-damped regime, $\ddot{\vec{\theta}} = 0$, the equations of motion are simplified to

$$0 = -\tilde{\zeta}_r \dot{\vec{\theta}} + \vec{\tau}\,(t)\,; \tag{7.11}$$

for which the solution is

$$\dot{\vec{\theta}} = \sqrt{2}\,\tilde{\mu}_r \vec{\mathcal{W}}, \tag{7.12}$$

where $\tilde{\mu}_t$ is a symmetric tensor such that $\tilde{\mu}_r \tilde{\mu}_r^T = \tilde{D}_r$, and is the rotational analogous of $\tilde{D}_t$. To solve the equations, an Euler-Maruyama scheme is used so that the discrete correlation of $\vec{\tau}\,(t)$ is [15]

$$\langle \tau_i\,(t_n)\,\tau_j\,(t_n) \rangle = \frac{1}{\Delta t_n} \int_{t_n}^{t_{n+1}} \tau_i\,(t)\,\tau_j\,(t)\,\mathrm{d}t = \frac{2k_B T\,\zeta_{r_{ij}}}{\Delta t_n}. \tag{7.13}$$

The solution of the equation, at each time step, is given by

$$\frac{\vec{\theta}_{i+1} - \vec{\theta}_i}{\Delta t} = \sqrt{\frac{2}{\Delta t}}\,\tilde{\mu}_{r_i} \vec{\mathcal{W}}_i \quad \rightarrow \quad \vec{\theta}_{i+1} = \vec{\theta}_i + \sqrt{2\Delta t_i}\,\tilde{\mu}_{r_i} \vec{\mathcal{W}}_i. \tag{7.14}$$

In principle, the equations of motion could be considered separately, however, it is well known that, in general, there is coupling between the translation and rotation of bodies [16]. It is a good strategy to merge Equations 7.2 and 7.9 into a single set of equations [14], that will be the topic of the next section.

7.2.2 Coupled translational and rotational equations of motion

To get the coupled equations of motion, define a 6 × 1 vector that contains the force and torque. The vector is defined as

$$\vec{\mathcal{F}}_{\text{net}} = \begin{pmatrix} \vec{F}_{\text{net}} \\ \vec{\tau}_{\text{net}} \end{pmatrix}. \tag{7.15}$$

with an adjustment of units for either one of the quantities $\vec{F}_{\text{net}}$ or $\vec{\tau}_{\text{net}}$, so that the units in Equation 7.15 match. We now proceed to write the equations of motion for the coupled system in terms of the friction tensor and the Wiener process in a body-fixed frame, where there is only fluid resistance

$$\vec{\mathcal{F}}_{\text{net}} = -\tilde{\zeta}\vec{\mathcal{V}} + \vec{\mathcal{F}}\left(t\right); \tag{7.16}$$

with $\tilde{\zeta}$ the grand resistance tensor, that contains all the information of the rotation, translation, and translation-rotation coupling friction terms. $\vec{\mathcal{V}}$ is a 6×1 vector that contains the time derivatives of the linear displacements, $\vec{x}$, and angular displacements, $\vec{\theta}$; with one of the quantities multiplied by the appropriate units so they can be merged into a single vector. $\tilde{\zeta}$ is the friction tensor, that is independent of the masses of the particles of which the molecule is composed of. The random force $\vec{\mathcal{F}}\left(t\right)$ is chosen in an analogous way to Equation 7.3, so that the properties of $\vec{\mathcal{F}}\left(t\right)$ are

$$\left\langle \vec{\mathcal{F}}\left(t\right) \right\rangle = 0, \tag{7.17a}$$

$$\left\langle \mathcal{F}_i\left(t\right)\mathcal{F}_j\left(t'\right) \right\rangle = 2k_BT\tilde{\zeta}_{ij}\,\delta\left(t-t'\right); \qquad i,j \in \{1,2,3,4,5,6\}\,. \tag{7.17b}$$

Thus, following the procedure in Section 7.2.1, the equations of motion to be solved in the overdamped regime $\vec{\mathcal{F}}_{\text{net}} = 0$ are

$$\tilde{\zeta}\frac{\mathrm{d}\vec{\mathcal{R}}}{\mathrm{d}t} = \sqrt{2k_BT}\tilde{\zeta}^{1/2}\vec{\mathcal{W}} \quad \rightarrow \quad \frac{\mathrm{d}\vec{\mathcal{R}}}{\mathrm{d}t} = \sqrt{2}\tilde{\mu}\vec{\mathcal{W}}; \tag{7.18}$$

with $\tilde{\mu}\tilde{\mu}^T = \tilde{D}$. The form of $\tilde{D}$ is a 6×6 positive definite symmetric tensor that is naturally decomposed into four 3×3 blocks, each of which contains the diffusion coefficients for translation ($\mathbf{D}_{tt}$), rotation ($\mathbf{D}_{rr}$), and translation-rotation ($\mathbf{D}_{tr}$) coupling

$$\tilde{D} = \begin{pmatrix} \mathbf{D}_{tt} & \mathbf{D}_{tr}^T \\ \mathbf{D}_{tr} & \mathbf{D}_{rr} \end{pmatrix}, \text{ where } T \text{ denotes the transposition operation.} \tag{7.19}$$

This tensor is a quantity that depends on the choice of the origin of the set of axis, the orientation of these with respect to the molecule, and the viscosity of the fluid in which the molecule is immersed. The diffusion tensor can be calculated by following the procedure in [9]; the procedure is outlined in Section 7.10. The vector $\vec{\mathcal{R}}$ is a 6×1 vector that contains the translational displacements $\vec{x} = (x, y, z)$ and the rotational angles, $\vec{\theta} = (\theta_x, \theta_y, \theta_z)$, about the x, y, and z axis, respectively. The vector $\vec{\mathcal{W}}$ is a 6×1 vector of independent and uncorrelated random normal distributed numbers.

To solve the equations of motion, at each time step, an Euler-Maruyama scheme is used. Define the i^{th} component of a vector $\vec{v}$ as v_i, and the ij component of a two dimensional tensor $\tilde{\eta}$ by η_{ij}. The solution at each time step of Equation 7.18 is

$$\mathcal{R}_{i_{n+1}} = \mathcal{R}_{i_n} + \sqrt{2\Delta t_n}\, \mu_{ij} \mathcal{W}_{j_n}, \tag{7.20}$$

where Einstein summation over repeated indexes is used.

7.3 Simulation Algorithm

In Section 7.2.2 the solution for each time step to the equations using an Euler-Maruyama scheme were derived (Equation 7.20). This solution to the equations and the constraints provide an algorithm to determine the passing propensity, P, as defined in Section 7.1.

It is convenient to define terminology before proceeding. Define the following quantities: (i) The *position of the i^{th} molecule* as the position of the center of mass of the i^{th} molecule, $\vec{x}_i = (x_i, y_i, z_i)$. ($ii$) The *orientation of a molecule* as the direction of the unit vectors fixed in the molecule with respect to a fixed frame in the pore. (iii) The *separation of the molecules* as the difference in position of the first and the second molecule $\Delta\vec{x} = \vec{x}_1 - \vec{x}_2 = (x_1 - x_2, y_1 - y_2, z_1 - z_2)$. ($iv$) A *move* is the change in position and/or orientation of the molecules. (v) The *initial separation* in the z axis of the molecules as Δz_0. (vi) A *pass* as the separation of the molecules such that $\Delta z \leq -\Delta z_0$. ($vii$) A *fail* as the separation of the molecules such that $\Delta z \geq 2\Delta z_0$. ($viii$) A *trial* as a series of valid movements from a starting position that end in a pass or a fail. (ix) A *run* as a defined number of trials. (x) The *passing propensity* as the number of trials in a run that result in a pass, divided by the total number of trials (passes + fails).

Using these definitions, the algorithm used follows the steps:

Step 1 Setup the width of the pore so that there is a possibility of molecules passing each other; if there is not such a pore width, terminate the program. Set the pass and fail counters to zero, and the number of maximum trials, $N_{\max}$, to some integer number greater than zero.

Step 2 Setup the molecules with the center of mass in the coordinate $(x_1, y_1, z_1) = (0, 0, R_{1_e})$ and $(x_2, y_2, z_2) = (0, 0, -R_{2_e})$, such the body-fixed axes of the molecules are aligned with the pore-fixed axes.

(a) Setup the molecules in a random and valid and initial orientation, i.e., the molecules do not intersect the pore walls, and set the initial separation of the molecules in the z axis as $\Delta z_0 = R_{1_e} + R_{2_e}$.

Step 3 Save the information of the current configuration of the molecules.

Step 4 Make a move for molecule 1 and molecule 2:

(a) Stochastically change the position and orientation of molecule 1 and molecule 2.

(b) If the molecules intersect the wall or each other, reset to the molecules to the configuration before making the moves and go to **Step 4(a)**; otherwise, continue to **Step 5**.

Step 5 Check the separation of the molecules:

(a) If the separation of the molecules in the z axis is less than or equal to $-\Delta z_0$, add one to the pass counter and continue to **Step 6**.

(b) If the separation of the molecules in the z axis is greater than or equal to $2\Delta z_0$, add one to the fail counter and continue to **Step 6**.

(c) If the separation of the molecules in the z axis is such that $-\Delta z_0 < \Delta z < 2\Delta z_0$, go to **Step 3**.

Step 6 Check if the simulation is done:

(a) If the number of trials is less than $N_{\max}$, go to **Step 2**; otherwise continue to **Step 7**.

Step 7 Get the passing propensity as $P = \#$ of passes$/N_{\max}$ and finish the program.

Details on the procedure are given next.

7.3.1 Estimating the minimum pore width

To exactly get the minimum pore width for molecules to be able to fit the pore, there is not a procedure, in general. What can be done to get a good estimate of this minimum pore width, for each molecule, is to algorithmically get the shortest distance that transverses the molecules, that will be defined as the *shortest axis* of the molecule; in an analogous way, the longest distance that transverses the molecules will be defined as the *long axis* of the molecule.

To get the shortest molecule axis and length, project each atom position vector onto a selected unit vector, $\hat{r} = (\sin(\theta)\cos(\phi), \sin(\theta)\sin(\phi), \cos(\theta))$; with $\theta \in [0, \pi)$ and $\phi \in [0, \pi)$; and add and subtract the corresponding atom radius from this value, make a set of values out of the maximum values and a second list out of minimum values. From the set of these maximum values get the maximum value; for the list of the minimum values, get the minimum value. Subtract the minimum value from the maximum value and take the absolute value, this will be the length of the molecule along $\hat{r}$, given fixed angles θ and ϕ. Do this for the complete range of θ and ϕ and obtain the maximum length $l_{\max}$ and the minimum length $l_{\min}$. The minimum width of the pore for the molecule to fit is $l_{\min}$. In Figure 7.4 the shortest and longest axes of the molecules are shown; refer to Section 7.4 for a more detailed description of the molecule models used.

7.3.2 Setting up the initial configuration

The initial configuration of the molecules is important since it influences the passing propensity. The physical condition that we choose for the starting position is when the molecules are separated by a distance along the z axis of the pore $\Delta z_0 = r_c = R_{1_e} + R_{2_e}$, where r_c is the

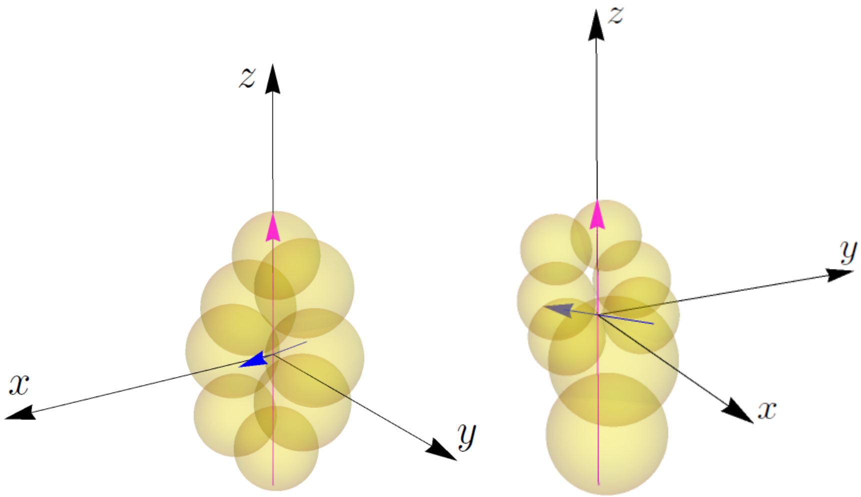

(a) (b)

Figure 7.4: 3D molecule models, longest and shortest axis of the molecules. The models for the molecules to be used for (a) 4-nitrobenzaldehyde and (b) 4-(4-nitrophenyl)-2-butanone; refer to Section 7.4 for a more detailed description of the molecule models used. The shortest axis of the molecule is represented by the shortest arrow (blue) and the longest by the longest (magenta) arrow. For the shortest axis for (a) is $l_{\min} = 3.40$ units and for (b) $l_{\min} = 5.92$ units.

sum of the radius of the *surrounding spheres* of the molecules, see Figure 7.5. The surrounding sphere of a molecule is defined as the minimum sphere with radius R_{i_e} from the center of mass of the molecule that encloses all the spheres in the molecule. Even if the surrounding sphere gives an idea of the typical molecule size, it often provides no information about the shortest or longest axis of the molecule.

The fixed choice of the initial separation of the molecules along the z axis leaves several free parameters, that are the x and y position of the molecules within the pore, and the orientations of the molecules. The initial x and y position of the molecules are randomly determined from the available phase space for the molecule to move in. The procedure to determine the initial x and y position of each molecule is to: (i) Set the center of mass of the molecule in the $(x, y) = (0, 0)$ coordinate. (ii) Randomly choose and *fix* the orientation of the body-fixed axis of the molecule, such that the molecule does not intersect the pore walls; the molecules will not intersect each other because of the initial Δz_0 position. This is to make sure the molecule can explore all the possible orientations uniformly. (iii) Get the projection of the molecule in

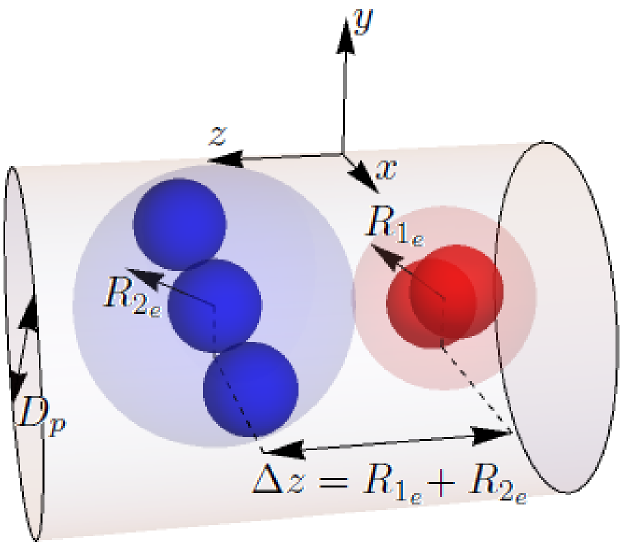

Figure 7.5: 3D molecule models, definition of the surrounding sphere; example with linear oligomers at a valid initial configuration. The figure shows a dimer and a trimer in the pore of diameter D_p. The surrounding spheres are located at the center of mass of the i^{th} oligomer, in this case the geometrical center of the molecules, and denoted as R_{i_e}.

the x and y plane of the molecule. (iv) Uniformly choose a unit vector in the xy-plane such that $\hat{r} = (\cos(\theta), \sin(\theta))$ with θ in the range $[0, 2\pi)$, so that the phase space available for the molecule to move in can be calculated and call it L_{ps}, for the selected orientation, see Figure 7.6. (v) Include the physical constraint that the molecules will always have a tendency to be in an initial orientation such that the phase space for them to move is maximum, i.e., get the ratio $P = L_{ps}/(D_p - l_{\min})$ and choose a random number in the range $n = (0, 1)$. If n is less than or equal to P, accept the orientation of the molecule and choose a random position for the molecule along the unit vector $\hat{r}$; that is, the molecule should not intersect the pore walls.

As it is important to keep track of the position of the spheres in the molecules, it is important to keep track of the position of the center of mass, the hydrodynamic center and the orientation of the axis of the molecules, since the moves will always be performed with respect to this body-fixed frame. An example of a valid initial configuration of the molecules is shown in Figure 7.7.

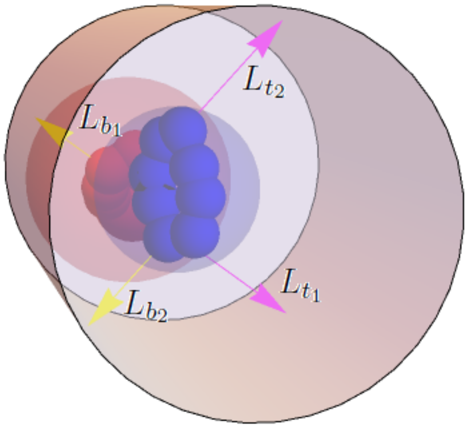

Figure 7.6: Setting up the initial orientation of the molecules in 3D. The phase space, for the molecules to move in a randomly chosen direction in the xy-plane, for the i^{th} molecule, is given by the sum of the lengths of the arrows, $L_{ps_i} = L_{t_i} + L_{b_i}$. The arrows start on the surface of the closest atom to the wall and end on the wall, in the previously chosen direction.

7.3.3 Moving the Molecules: Translation and Rotation

There are several methods to choose the rotation of the molecules, these include the use of quaternions and different schemes of Euler angles [17]. An important quantity that has not been introduced is the hydrodynamic center, that is the location where the overall force is imprinted on the molecule [9]. The hydrodynamic center is also the point about which the molecule rotates. For a free rotating particle the hydrodynamic center coincides with the center of mass, however this is not always the case. In Section 7.9, a procedure to calculate the position of the hydrodynamic center of a molecule made of spheres is given.

To get the translational and rotational quantities, it is convenient to refer to Equation 7.20, that clearly gives an algorithm to choose the displacements. Since we are working in a body-fixed frame and the fluid in which the molecules are moving in is isotropic and homogeneous, the diffusion tensors will remain constant. To get the displacements, the procedure is to: (i) Get a 6×1 vector made of normal distributed random numbers. (ii) With the diffusion tensor, calculate the displacement following Equation 7.20

$$d_i = \sqrt{2\Delta t}\mu_{ij}\mathcal{W}_j, \tag{7.21}$$

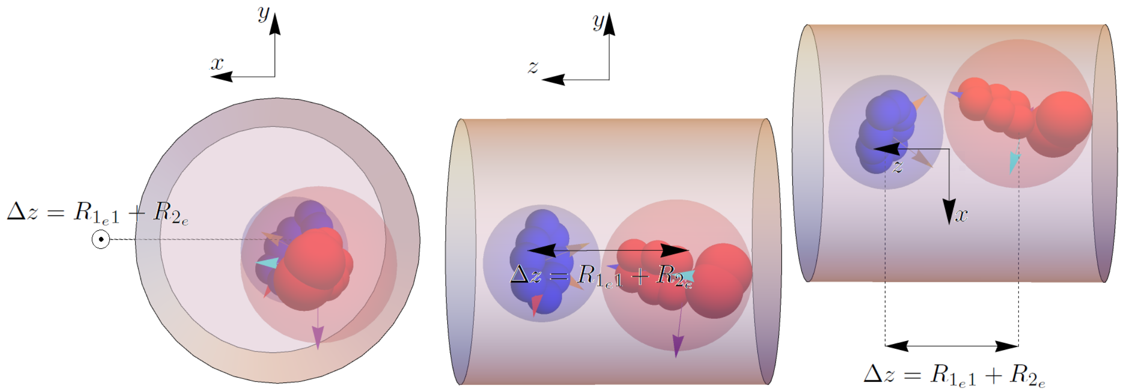

(a) (b) (c)

Figure 7.7: 3D valid initial configuration for the molecules, using the molecules for the simulation. View from the top of the (a) $z-$axis, (b) $x-$axis and (c) $y-$axis. The initial separation of the molecules in the $z-$axis is always the same, $\Delta z = \Delta z_0 = R_{1_e} + R_{2_e}$. The body-fixed axis of the molecules are represented by the arrows attached to the molecules; see Section 7.4 for details.

where Einstein summation convention over repeated indices is used and $i, j \in \{1, 2, 3, 4, 5, 6\}$. (iii) The translational quantities are associated with the first three indices, $i \in \{1, 2, 3\}$, and the rotational with the last three, $i \in \{4, 5, 6\}$. To implement the translational algorithm, a transformation to the pore-fixed frame is needed. If the body-fixed frame vector basis of the i^{th} molecule is defined by $\{\hat{e}_{i_1}, \hat{e}_{i_2}, \hat{e}_{i_3}\}$, where the vectors are written in the pore-fixed frame, the displacement vector of the molecules in the pore-fixed frame is

$$\Delta\vec{x}_i = d_1\hat{e}_{i_1} + d_2\hat{e}_{i_2} + d_3\hat{e}_{i_3}. \tag{7.22}$$

(iv) Translate the hydrodynamic center, center of mass, and all the spheres in the molecule by $\Delta\vec{x}_i$.

For the rotational part, several methods to rotate the molecules exist [17]. We choose an Euler-xyz rotation scheme, that is also known as the *Tait-Bryan angles rotation scheme*. The Tait-Bryan angle scheme consists on a sequence of rotations about the 3 different angles of rotation. In particular, we are interested in the scheme where the molecule is first rotated about the body-fixed frame along the x axis, then in the body-fixed frame about the y axis and then about the z axis. To rotate the molecule: (i) Translate the molecule such that the hydrodynamic center of the molecule lies at the $(x, y, z) = (0, 0, 0)$ coordinate. (ii) Rotate the spheres of the molecule, along with $\hat{e}_{i_2}$, $\hat{e}_{i_3}$ and the center of mass vector, about the $\hat{e}_{i_1}$ axis. (*iii*) Rotate the spheres of the molecule, along with $\hat{e}_{i_1}$, $\hat{e}_{i_3}$ and the center of mass vector, about the $\hat{e}_{i_2}$ axis. (*iv*) Rotate the spheres of the molecule, along with $\hat{e}_{i_1}$, $\hat{e}_{i_2}$ and the center of mass vector, about the $\hat{e}_{i_3}$ axis. (*v*) Move the spheres and the center of mass such that the position of the hydrodynamic center of matches with the original position of where it was.

The rotations are made using quaternions. The rotation of vector $\vec{x}$ about the unit vector $\hat{y}$ by an angle θ is given by $\vec{x}\,'$, using the formula

$$\vec{x}\,' = \cos(\theta)\,\vec{x} + (\vec{x}\cdot\hat{y})\,(1-\cos(\theta))\,\hat{y} + \cos(\theta)\,\vec{x}\times\hat{y}. \tag{7.23}$$

It is worth mentioning that it is tempting to try to find a *three* dimensional orthonormal set of axis where both the translational and rotational parts of the diffusion tensors are diagonal, with no coupling. This is, most of the time, not possible.

Once the molecules are moved, it has to be checked whether the molecules obey the steric constraints, i.e., the molecules do not intersect each other or the pore walls; the two cases are evaluated separately. To check if the molecules intersect the pore walls, it is useful to first check if the surrounding spheres (defined in Section 7.3.2) intersect the pore wall. If the surrounding spheres do not intersect the pore walls, the molecules do not intersect the pore walls. Otherwise, intersection of every sphere in the molecule with the pore walls has to be checked. To check the intersection of the molecules, it suffices to check if the surrounding spheres do not intersect each other. If this does not happen the molecules cannot intersect. Otherwise, the intersection of the molecules has to be checked for each of the spheres the molecules are made of.

To evaluate the intersection of the molecules with the pore and between each other, define three logical variables Ac_{w_1}, Ac_{w_2} and Ac_{12}; where Ac_{w_1} and Ac_{w_2} are the binary logical variables (true/ false) that denote the intersection of the molecules with the wall and Ac_{12} the binary logical variable that denotes if the molecules intersect each other. To accept a move of the molecules $Am\left(Ac_{w_1}, Ac_{w_2}, Ac_{12}\right)$ must be *true*, where

$$Am\left(U_1, U_2, \ldots, U_N\right) = U_1 \wedge U_2 \wedge \ldots \wedge U_N; \tag{7.24}$$

the "$\wedge$" operator makes reference to the logical "and" operator and "$\vee$" to the logical "or" operator.

To evaluate Ac_{w_i}, the intersection of the molecules' spheres with the pore walls have to be tested. If there are two circles, such that $R_1 > r_2$, and if the bigger circle is centered at $(x_1, y_1) = (0, 0)$ and the smaller one at (x_2, y_2), then circle 2 is inside circle 1, without any intersection, if $\left(\sqrt{x_2^2 + y_2^2} + r_2\right) \leq R_1$; that is equivalent to $\left(x_2^2 + y_2^2\right) \leq (R_1 - r_2)^2$. Define $R_p = D_p/2$ as the pore radius, r_{i_j} as the radius of the j^{th} sphere of the i^{th} molecule, and x_{i_j} and y_{i_j} as the x and y coordinates. For the molecule *not* to intersect the pore walls, then either two of the conditions have to be met: (i) That the surrounding sphere, $R_{i_{\text{surr}}}$, does not intersect the pore walls; a condition that is enough for the molecule to not intersect the pore walls; or (ii) the individual spheres, of which the molecule is composed of, should not intersect the pore walls. Thus,

$$Ac_{w_i} = \left[\left(x_{i_{\text{cm}}}^2 + y_{i_{\text{cm}}}^2\right) \leq \left(R_p - R_{i_{\text{surr}}}\right)^2\right] \vee \bigwedge_{j=1}^{N_i} \left[\left(x_{i_j}^2 + y_{i_j}^2\right) \leq \left(R_p - r_{i_j}\right)^2\right] \tag{7.25}$$

must be true.

To determine if the molecules *do not* intersect each other, Ac_{12}, then either two of the conditions have to be met: (i) That the surrounding spheres of the molecules do not intersect each other; a condition that is enough for the molecules to not intersect each other; or (ii) the individual spheres of both molecules, of which the molecules are composed of, should not intersect each other. Thus,

$$\begin{aligned} Ac_{12} = & \left\{\left[\left(x_{1_{\text{cm}}} - x_{2_{\text{cm}}}\right)^2 + \left(y_{1_{\text{cm}}} - y_{2_{\text{cm}}}\right)^2 + \left(z_{1_{\text{cm}}} - z_{2_{\text{cm}}}\right)^2\right] \geq \left(R_{1_{\text{surr}}} + R_{2_{\text{surr}}}\right)^2\right\} \vee \\ & \bigwedge_{i=1}^{N_1} \bigwedge_{j=1}^{N_2} \left\{\left[\left(x_{1_i} - x_{2_j}\right)^2 + \left(y_{1_i} - y_{2_j}\right)^2 + \left(z_{1_i} - z_{2_j}\right)^2\right] \geq \left(r_{1_i} + r_{2_j}\right)^2\right\} \end{aligned} \tag{7.26}$$

must be true. For a graphical representation, refer to Figure 7.8.

It is important to notice that if the problem is to be solved computationally, for relatively narrow pores and when molecules are in the passing positions, the number of conditions to be evaluated are $N1 \cdot N_2$, a quantity that must be evaluated *at least once* for each move. The evaluation of these conditions, rotating and translating the molecules, and the generation of the normal distributed random numbers are the main sources to determine the speed at which the program runs. Thus, it is convenient to model the system such that the molecules have the least number of spheres possible, as described in Section 7.4. It is also critical to determine an

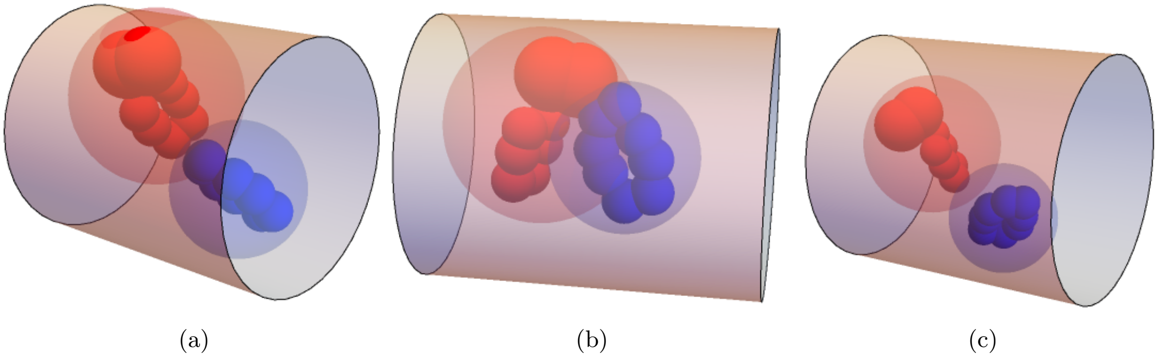
(a) (b) (c)

Figure 7.8: 3D molecule intersection validation conditions. If (a) one of the molecules, or both, intersect the pore wall, it is a forbidden configuration. (b) If the molecules intersect each other, it is a forbidden configuration. (c) The molecules do not intersect the pore walls or each other, thus, it is a valid configuration.

appropriate time step Δt, so that the molecules appropriately explore the possible phase space and not make unphysical moves (e.g., pass through each other), but is fast enough to provide results in an acceptable amount of time.

7.4 Coarse Graining the Molecules

As was mentioned in Section 7.2, the molecules to be used in the Langevin simulations are 4-nitrobenzaldehyde and 4-(4-nitrophenyl)-2-butanone. Since the length of the major axis of the molecules are comparable to that of the pore diameter, the shape of the molecules play a crucial role in determining the passing propensity, P, described in Section 7.1. The molecules are modeled using *solid spherical atoms*, where the radius of the spheres are determined to be the *van der Waals* radius of the atoms.

When modeling this system, the choice on the number of spheres with which to represent the molecules is of critical importance. As the number of spheres of which the molecule is composed of increases, the number of operations to move a molecule increases, thus, the required computational time to move a molecule increases. The molecules have to be chosen so that number of spheres is small, while retaining the essential geometrical features that will determine the allowed configurations of these inside the pore.

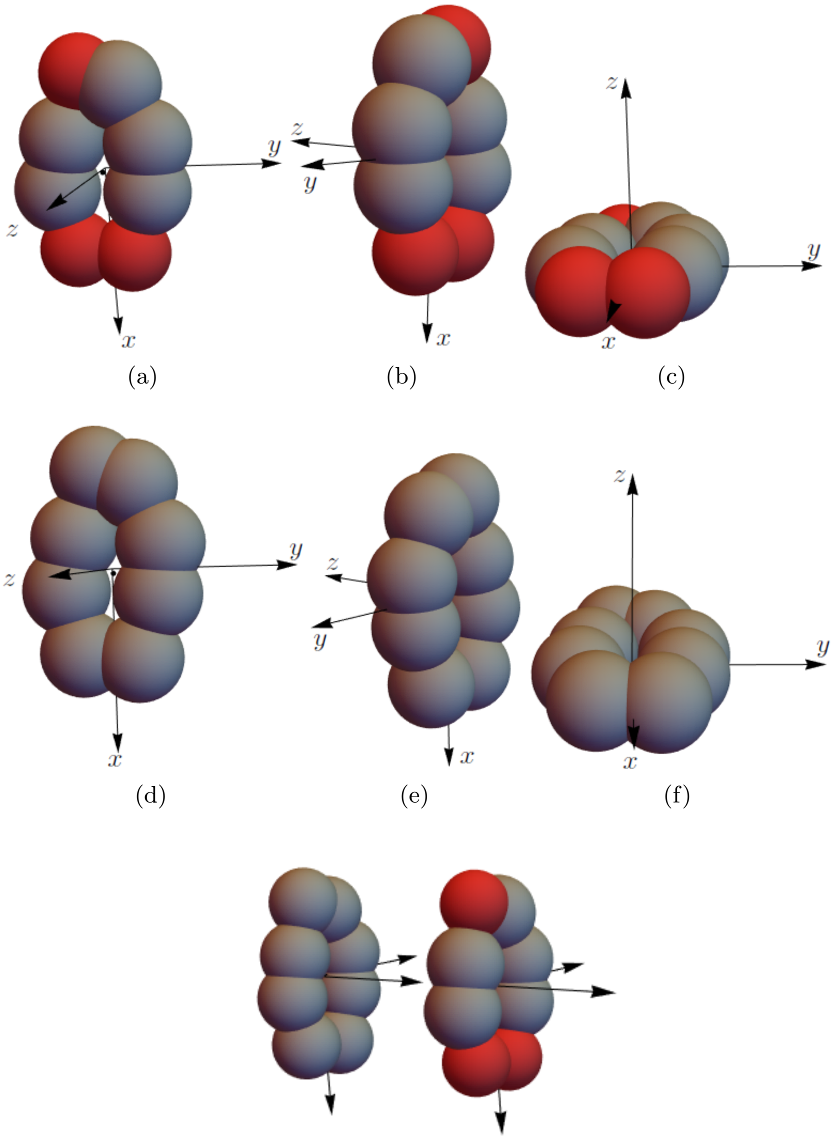

(a) (b) (c)

(d) (e) (f)

(g)

Figure 7.9: 3D 4-nitrobenzaldehyde molecule models. (a-c) The steric model used, different points of view, see Table 7.1; (d-f) The model used to calculate the hydrodynamic parameters, i.e., the diffusion tensor, see Table 7.3. (g) Comparing the two models.

Table 7.1: 4-nitrobenzaldehyde steric model, atoms and properties list with respect to the center of mass. All the length units are in angstroms (Å) and mass units in atomic mass units (u).

4-nitrobenzaldehyde steric model molecule						
Atom Number	Atom Type	Coordinate x	Coordinate y	Coordinate z	van der Walls Radius	Mass
1	O	3.2112	0.9307	-0.0019	1.52	15.9994
2	O	3.0311	-1.2571	-0.0002	1.52	15.9994
3	O	-3.8866	-0.6218	-0.0016	1.52	15.9994
4	C_H	0.7978	1.722	0.0008	1.7	12.0107
5	C_H	0.6277	-1.8921	0.0007	1.7	12.0107
6	C_H	-1.1109	1.8741	0.0008	1.7	12.0107
7	C_H	-1.3843	-1.4818	0.0005	1.7	12.0107
8	C_H	-3.3357	0.8647	-0.0012	1.7	12.0107

Although the exact shape of the molecules can be obtained (see Section 7.9), the molecules will be represented by an alternative set of spheres, that are given in Table 7.1 and Table 7.2 (see Figure 7.9(a-c) and Figure 7.10(a-c)).

The models for the molecule were chosen such that the most important geometrical details were retained. To determine the hydrodynamic properties of the molecules, i.e., the diffusion tensor, more constraints are set (see Section 7.10). Thus, a different model for the molecules has to be used. The models are chosen so that the constraints in Section 7.10 are met, and at the same time retaining the overall shape of the molecules in Table 7.1 and Table 7.2. The models of the molecules to be used to determine the hydrodynamic properties for the molecules are given in Table 7.3 and 7.4; in Figure 7.10 the molecules are shown. From the values in Table 7.3 and 7.4, and the axis shown in Figure 7.10, the diffusion tensor and its *square root* for the molecules in the hydrodynamic center are given by

$$\tilde{D} = \begin{pmatrix} \mathbf{D}_{tt} & \mathbf{D}_{tr}^T \\ \mathbf{D}_{tr} & \mathbf{D}_{rr} \end{pmatrix}, \quad \tilde{\mu} = \begin{pmatrix} \mu_{tt} & \mu_{tr}^T \\ \mu_{tr} & \mu_{rr} \end{pmatrix}; \tag{7.27}$$

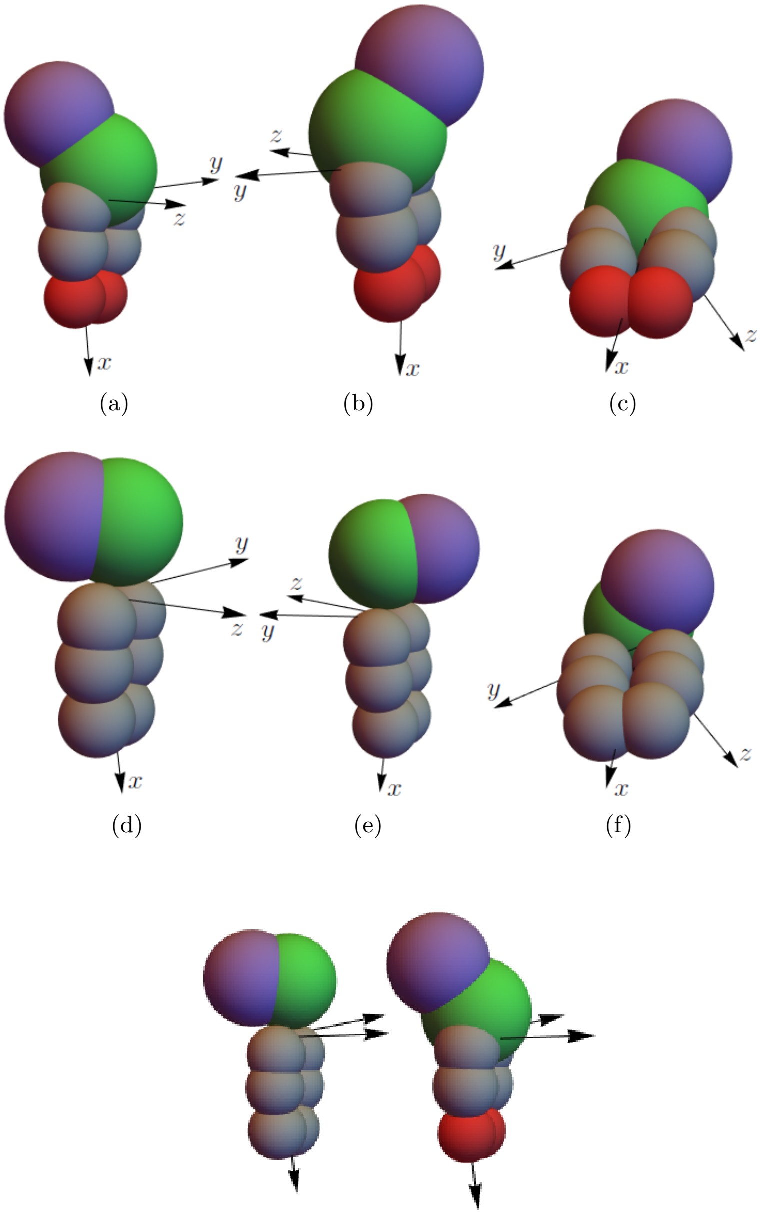

(a) (b) (c)

(d) (e) (f)

(g)

Figure 7.10: 3D 4-(4-nitrophenyl)-2-butanone molecule models. (a-c) The steric model used, different points of view, see Table 7.2; (d-e) The model used to calculate the hydrodynamic parameters, i.e., the diffusion tensor, different points of view, see Table 7.4. (f) Comparing the two models.

Table 7.2: 4-(4-nitrophenyl)-2-butanone steric model, atoms and properties list with respect to the center of mass. All the length units are in angstroms (Å) and mass units in atomic mass units (u).

4-(4-nitrophenyl)-2-butanone steric model molecule						
Atom Number	Atom Type	Coordinate x	Coordinate y	Coordinate z	van der Walls Radius	Mass
1	O	4.6229	0.6048	−0.6887	1.52	15.9994
2	O	4.3809	−1.3303	0.3192	1.52	15.9994
3	C	0.3655	1.8117	−0.6657	1.7	12.0107
4	C	−0.0008	−1.1512	0.8858	1.7	12.0107
5	C	2.2539	1.5148	−0.7967	1.7	12.0107
6	C	1.8818	−1.4603	0.7553	1.7	12.0107
7	C	−4.4445	−0.8195	−0.6628	2.7	12.0107
8	C	−1.7139	0.6337	0.2351	2.9	12.0107

with specific components for the 4-nitrobenzaldehyde molecule (A)

$$\mathbf{D}_{A_{tt}} = \begin{pmatrix} 1.7690 \times 10^{-2} & 5.7222 \times 10^{-5} & -1.1217 \times 10^{-7} \\ 5.7222 \times 10^{-5} & 1.5937 \times 10^{-2} & -5.4258 \times 10^{-8} \\ -1.1217 \times 10^{-7} & -5.4258 \times 10^{-8} & 1.4704 \times 10^{-2} \end{pmatrix}, \tag{7.28a}$$

$$\mathbf{D}^{T}_{A_{tr}} = \begin{pmatrix} 1.3156 \times 10^{-8} & 9.4785 \times 10^{-8} & -9.9911 \times 10^{-6} \\ -9.2178 \times 10^{-8} & -1.2536 \times 10^{-8} & -2.7047 \times 10^{-6} \\ -1.0049 \times 10^{-5} & 2.4085 \times 10^{-6} & -1.2819 \times 10^{-8} \end{pmatrix}, \tag{7.28b}$$

$$\mathbf{D}_{A_{rr}} = \begin{pmatrix} 6.4684 \times 10^{-4} & -1.1358 \times 10^{-6} & -9.9009 \times 10^{-9} \\ -1.1358 \times 10^{-6} & 4.7063 \times 10^{-4} & 1.0423 \times 10^{-8} \\ -9.9009 \times 10^{-9} & 1.0423 \times 10^{-8} & 4.2623 \times 10^{-4} \end{pmatrix}; \tag{7.28c}$$

Table 7.3: 4-nitrobenzaldehyde model for hydrodynamic quantity calculations, atoms and properties list with respect to the center of mass. All the length units are in angstroms (Å) and mass units in atomic mass units (u).

4-nitrobenzaldehyde hydrodynamic model molecule						
Atom Number	Atom Type	Coordinate x	Coordinate y	Coordinate z	van der Walls Radius	Mass
1	O	3.2112	0.9307	−0.0019	1.52	15.9994
2	O	3.0311	−1.2571	−0.0002	1.52	15.9994
3	O	−3.8866	−0.6218	−0.0016	1.52	15.9994
4	C	0.7978	1.722	0.0008	1.7	12.0107
5	C	0.6277	−1.8921	0.0007	1.7	12.0107
6	C	−1.1109	1.8741	0.0008	1.7	12.0107
7	C	−1.3843	−1.4818	0.0005	1.7	12.0107
8	C	−3.3357	0.8647	−0.0012	1.7	12.0107

and the 4-(4-nitrophenyl)-2-butanone molecule (B)

$$\mathbf{D}_{B_{tt}} = \begin{pmatrix} 1.3946 \times 10^{-2} & -5.7788 \times 10^{-6} & 2.4703 \times 10^{-6} \\ -5.7788 \times 10^{-6} & 1.2242 \times 10^{-2} & -1.0212 \times 10^{-4} \\ 2.4703 \times 10^{-6} & -1.0212 \times 10^{-4} & 1.1874 \times 10^{-2} \end{pmatrix}, \tag{7.29a}$$

$$\mathbf{D}^T_{B_{tr}} = \begin{pmatrix} -1.4641 \times 10^{-7} & 3.3012 \times 10^{-6} & 1.1200 \times 10^{-5} \\ -1.0059 \times 10^{-5} & -1.2793 \times 10^{-5} & 6.7952 \times 10^{-6} \\ -6.3523 \times 10^{-6} & 9.0551 \times 10^{-6} & 1.0817 \times 10^{-5} \end{pmatrix}, \tag{7.29b}$$

$$\mathbf{D}_{B_{rr}} = \begin{pmatrix} 3.5629 \times 10^{-4} & -3.2336 \times 10^{-6} & 2.0460 \times 10^{-6} \\ -3.2336 \times 10^{-6} & 2.2778 \times 10^{-4} & 5.2070 \times 10^{-6} \\ 2.0460 \times 10^{-6} & 5.2070 \times 10^{-6} & 2.1898 \times 10^{-4} \end{pmatrix}. \tag{7.29c}$$

Table 7.4: 4-(4-nitrophenyl)-2-butanone model for hydrodynamic quantity calculations, atoms and properties list with respect to the center of mass. All the length units are in angstroms (Å) and mass units in atomic mass units (u).

4-(4-nitrophenyl)-2-butanone hydrodynamic model molecule						
Atom Number	Atom Type	Coordinate x	Coordinate y	Coordinate z	van der Walls Radius	Mass
1	O	4.6229	0.6048	−0.6887	1.52	15.9994
2	O	4.3809	−1.3303	0.3192	1.52	15.9994
3	C	0.3655	1.8117	−0.6657	1.7	12.0107
4	C	−0.0008	−1.1512	0.8858	1.7	12.0107
5	C	2.2539	1.5148	−0.7967	1.7	12.0107
6	C	1.8818	−1.4603	0.7553	1.7	12.0107
7	C	−4.4445	−0.8195	−0.6628	2.7	12.0107
8	C	−1.7139	0.6337	0.2351	2.9	12.0107

As the $\tilde{D}$ tensor, the $\tilde{\mu}$ tensor is also calculated for the 4-nitrobenzaldehyde molecule (A)

$$\mu_{A_{tt}} = \begin{pmatrix} 1.3300\times10^{-1} & 2.2072\times10^{-4} & -4.4100\times10^{-7} \\ 2.2072\times10^{-4} & 1.2624\times10^{-1} & -2.1900\times10^{-7} \\ -4.4100\times10^{-7} & -2.1900\times10^{-7} & 1.2126\times10^{-1} \end{pmatrix}, \tag{7.30a}$$

$$\mu^T_{A_{tr}} = \begin{pmatrix} 8.3700\times10^{-8} & 6.1300\times10^{-7} & -6.4999\times10^{-5} \\ -6.0800\times10^{-7} & -8.5700\times10^{-8} & -1.8316\times10^{-5} \\ -6.8497\times10^{-5} & 1.6836\times10^{-5} & -9.0700\times10^{-8} \end{pmatrix}, \tag{7.30b}$$

$$\mu_{A_{rr}} = \begin{pmatrix} 2.5433\times10^{-2} & -2.4075\times10^{-5} & -2.1500\times10^{-7} \\ -2.4075\times10^{-5} & 2.1694\times10^{-2} & 2.4700\times10^{-7} \\ -2.1500\times10^{-7} & 2.4700\times10^{-7} & 2.0645\times10^{-2} \end{pmatrix}; \tag{7.30c}$$

and the 4-(4-nitrophenyl)-2-butanone molecule (B)

$$\mu_{B_{tt}} = \begin{pmatrix} 1.1809 \times 10^{-1} & -2.5251 \times 10^{-5} & 1.0787 \times 10^{-5} \\ -2.5251 \times 10^{-5} & 1.1064 \times 10^{-1} & -4.6501 \times 10^{-4} \\ 1.0787 \times 10^{-5} & -4.6501 \times 10^{-4} & 1.0897 \times 10^{-1} \end{pmatrix}, \tag{7.31a}$$

$$\mu_{B_{tr}}^{T} = \begin{pmatrix} -1.1000 \times 10^{-6} & 2.4650 \times 10^{-5} & 8.4253 \times 10^{-5} \\ -7.7946 \times 10^{-5} & -1.0161 \times 10^{-4} & 5.4692 \times 10^{-5} \\ -4.9960 \times 10^{-5} & 7.2447 \times 10^{-5} & 8.7521 \times 10^{-5} \end{pmatrix}, \tag{7.31b}$$

$$\mu_{B_{rr}} = \begin{pmatrix} 1.8875 \times 10^{-2} & -9.5644 \times 10^{-5} & 6.1519 \times 10^{-5} \\ -9.5644 \times 10^{-5} & 1.5091 \times 10^{-2} & 1.7432 \times 10^{-4} \\ 6.1519 \times 10^{-5} & 1.7432 \times 10^{-4} & 1.4796 \times 10^{-2} \end{pmatrix}. \tag{7.31c}$$

For more details on the molecules, refer to Section 7.9.

7.5 Langevin Results

To implement the Langevin simulation we use the molecule models described in Section 7.4. The components of the diffusion tensor used for the 4-nitrobenzaldehyde molecule are the ones obtained in Equations 7.28(a)-(c), with the components of the square root given by the quantities in Equations 7.30(a)-(c), and in a similar way for the 4-(4-nitrophenyl)-2-butanone molecule, the components of the diffusion tensor used are given by 7.29(a)-(c) and the components of its square root by 7.31(a)-(c); all calculated in the axis shown in Figure 7.10 and Figure 7.9. The set of pores diameters used is $D_p = \{15, 20, 25, 30\}$. The number of trials to determine the passing propensity is set to $N = 200\,000$. Examples of the convergence of the passing propensity with the number of trials is shown in Figure 7.11

Thus, to determine if the time step is adequate, the time steps explored are $\Delta t = \{1.0, 0.1, 0.01\}$, as initial guesses; the results are given in Figure 7.12. It can be seen that the results start converging when a time step as big as $\Delta t = 0.1$ is considered; thus, it is determined that reasonable results can be obtained by using a time step of $\Delta t = 0.1$, making it the optimum time step to determine the passing propensity. The values for the passing propensity as a function of pore width are given in Table 7.5.

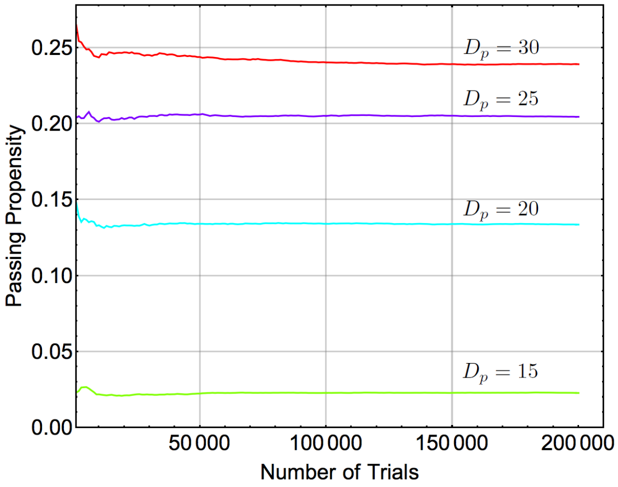

(a)

Figure 7.11: Passing propensity of molecules as a function of number of trials. A time step of $\Delta t = 1.0$ is implement, for pore diameters $D_p = \{15, 20, 25, 30\}$.

Table 7.5: Passing propensity as a function of pore width and time step. The passing propensity is determined using $N = 200\,000$ trials. Time steps of $\Delta t = \{1.0, 0.1, 0.01\}$ are examined. The results converge for times of the order $\Delta t = 0.1$. See Figure 7.12.

Time Step	Pore Diameter (Å)			
	15	20	25	30
1.0	0.02272	0.1336	0.2046	0.2392
0.1	0.02679	0.1362	0.2087	0.2409
0.01	0.02830	0.1377	0.2091	0.2421

It is worth mentioning that it can be inferred, by the magnitude of the probability, that the small gap regime has almost been reached. This, by noticing that the available passing space can be estimated using the shortest axes of the molecules. The shortest axes of the molecules are given by $l_{\text{min}} = 3.40$ units for the 4-nitrobenzaldehyde molecule and $l_{\text{min}} = 5.92$ units for the 4-(4-nitrophenyl)-2-butanone molecule, see Figure 7.4, so that the critical pore width for the system to undergo single-file diffusion is $D_{p_c} \approx l_{\text{min}_1} + l_{\text{min}_2} = 9.32$ units. Thus, the pore widths examined leave "gaps" of significant size, $g \geq 5.68$, for the molecules to pass each other; where the gap is defined as $g = D_p - l_{\text{min}_1} - l_{\text{min}_2}$. Figure 7.8 gives an idea of the scale, since the diagrams were made from data taken from the actual simulations.

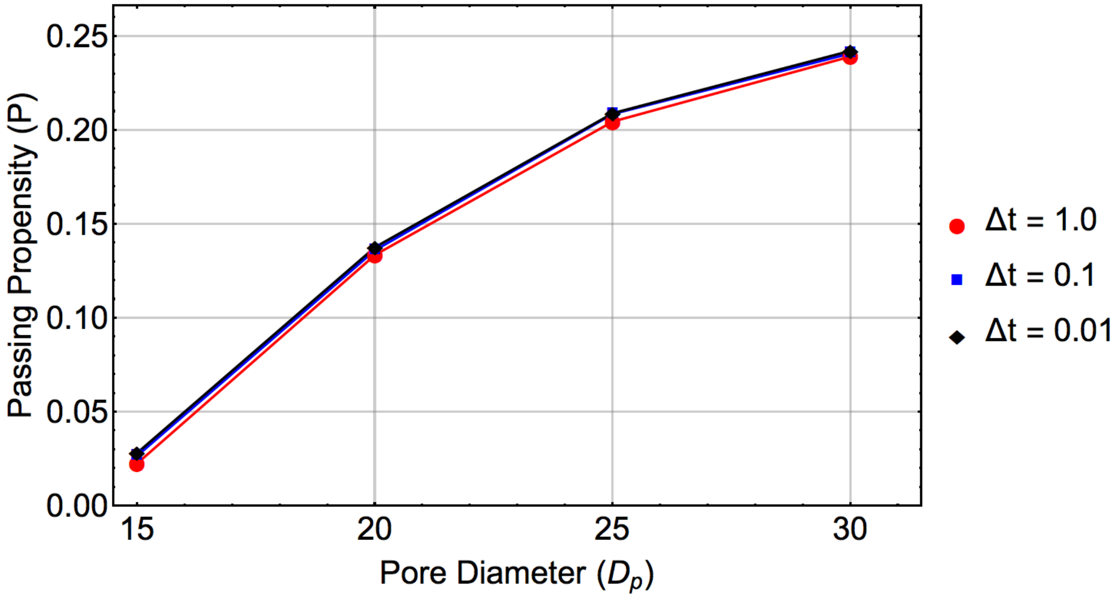

(a)

Figure 7.12: Passing propensity of molecules as a function of pore diameter. A time steps of $\Delta t = \{1.0, 0.1, 0.01\}$ are implemented, for pore diameters $D_p = \{15, 20, 25, 30\}$. The optimum time step is determined to be $\Delta t = 0.1$. The specific values are given in Table 7.5.

Having all the parameters from the Langevin simulations, these can be mapped onto parameters for a more coarse grained KMC model for validation with experimental data.

7.6 Kinetic Monte Carlo Results: Validation with Experimental Results

Using Langevin molecular dynamics simulations to model the system is prohibitive in this case, since the required time scales are not reachable, even for today's super-computers. Thus, we coarse-grain the continuous model to a 1 dimensional lattice-gas model, that has the characteristics: (i) The continuous pore of length L is tessellated into a linear array of L cells, where the width of each cell, a, matches the longest effective particle diameter. (ii) Instead of particles diffusing, the particles hop between adjacent neighboring cells. The hop rate of the 4-nitrobenzaldehyde particles and the 4-(4-nitrophenyl)-2-butanone molecules, that we shall call A and B respectively, can be different. (iii) The cells can have 3 states, with a particle A or B, or empty; with at most one particle per cell, that reflects the non-overlapping steric constraint. (*iv*) The particles can only hop to next neighbor cells. If the cell to which the particle is hopping is empty, the particles jump with hop rate h_A for A particles, or h_B for B particles. If the cell to which the particle is hopping is *not* empty and the particles are of different species, the particles can exchange with probability P_{ex} at a rate $h_{\text{ex}} = (h_A + h_B)/2$ [18]. (*v*) We shall be concerned with the initial phase of the reaction where there is only reactant in the well stirred fluid, and when the inside of the pore has reached a steady-state.

To determine the parameters for the KMC simulation from the Langevin MD simulation

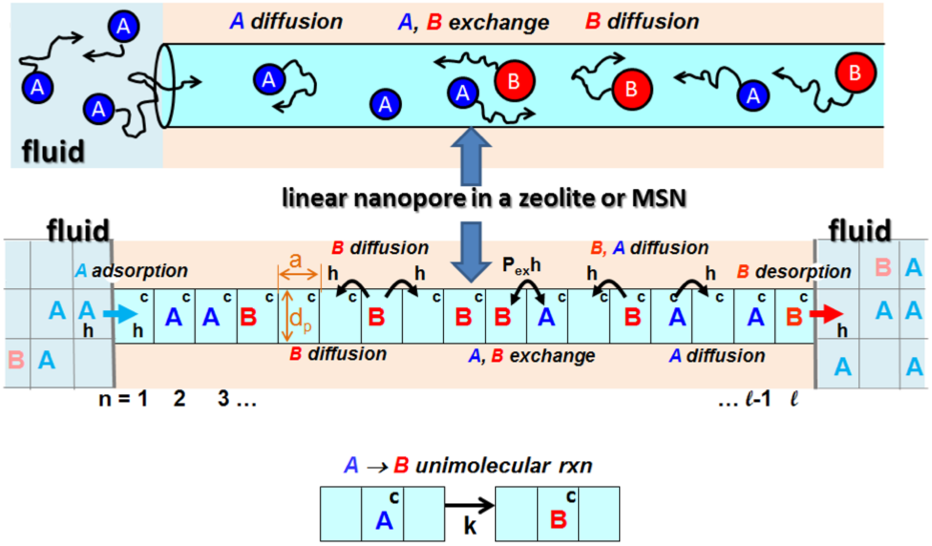

Figure 7.13: Coarse graining the continuum model to a discrete model. The continuous model is tessellated into an array of cells, where only one particle is allowed per cell, reflecting the steric interaction condition. The i^{th} particle specie hops to nearest neighbor empty cells with rate h_i, and if the particle hops to an adjacent occupied cell, it can exchange sites with a different species at a rate h_{ex}. Particles can adsorb/desorb from the pore, from both pore ends, from/into a well-stirred and equilibrated fluid. Irreversible conversion of A particles to B particles, at rate k, is only allowed within the pore.

parameters, the following relations are used [9, 18]

$$h = D_{\text{MD}} \text{a}^{-2}, \tag{7.32a}$$

$$P_{\text{ex}} = \frac{2P}{1-P}; \tag{7.32b}$$

where D_{MD} is the average translational diffusion tensor in the hydrodynamic center and is easily calculated as 1/3 of the trace of the translational diffusion 3 × 3 matrix

$$D_{\text{MD}} = \frac{1}{3}\text{tr}\left(\mathbf{D}_{tt}\right); \tag{7.33}$$

Table 7.6: Passing probability as a function of pore width. The passing probability, P_{ex}, is obtained from the passing passing propensity, P, using the Langevin results with a time step of $\Delta t = 0.01$.

	Pore Diameter (Å)			
	15	20	25	30
P	0.02830	0.1377	0.2091	0.2421
$P_{\text{ex}} = 2P/(1-P)$	0.05825	0.3195	0.5287	0.6395

and a is related to the typical particle size, see Figure 7.13. The passing probability between A and B particles for the KMC model, P_{ex}, is calculated from the passing propensity of the molecules, P defined in Section 7.1, for a specific pore width; that is determined from Langevin MD simulations.

The passing propensity for the molecules in Table 7.5, for a time step of $\Delta t = 0.1$, is mapped onto the KMC model, see Table 7.6. The average diffusion coefficients for each specie are given by one third of the trace of the matrices of Equation 7.28a and Equation 7.29a; thus, the values for the coefficients are $D_A = 1.6110 \times 10^{-2}$ and $D_B = 1.2687 \times 10^{-2}$. The hop rates are given by $h_A = 1.6110 \times 10^{-2}\text{a}^{-2}$ and $h_B = 1.2687 \times 10^{-2}\text{a}^{-2}$, where a^2 is a free parameter. Now that the parameters have been set, it remains to choose the reaction rate, that is not a trivial parameter to choose. Since there is *no* a priori knowledge of the reaction rate, the goal will be to get a family of curves and determine how the reactivity behaves as function of reaction rate divided by h_A; that will be related to the initial product yield for the results presented in [19].

To eliminate some of the system's parameters, it is instructive to write the master equations for the discrete system. The master equations are first order differential equations that determine the evolution of the system with time, so that, in this discrete model, the evolution equations will relate the concentration of reactant A and product B at time t, at each cell. To do this, relate the concentration of specie $C = \{A, B\}$ at site n at time t,

$\langle C_n \rangle (t) = \langle C_n \rangle$, with the coupled differential equations:

$$\begin{aligned}\frac{\mathrm{d}\langle A_n \rangle}{\mathrm{d}t} =& -k\langle A_n \rangle + h_A\left(\langle A_{n-1}E_n \rangle - \langle E_{n-1}A_n \rangle + \langle E_nA_{n+1} \rangle - \langle A_nE_{n+1} \rangle\right) + \\ & P_{\mathrm{ex}}h_{\mathrm{ex}}\left(\langle A_{n-1}B_n \rangle - \langle B_{n-1}A_n \rangle + \langle B_nA_{n+1} \rangle - \langle A_nB_{n+1} \rangle\right), \qquad (7.34a)\\ \frac{\mathrm{d}\langle B_n \rangle}{\mathrm{d}t} =& +k\langle A_n \rangle + h_B\left(\langle B_{n-1}E_n \rangle - \langle E_{n-1}B_n \rangle + \langle E_nB_{n+1} \rangle - \langle B_nE_{n+1} \rangle\right) + \\ & P_{\mathrm{ex}}h_{\mathrm{ex}}\left(\langle B_{n-1}A_n \rangle - \langle A_{n-1}B_n \rangle + \langle A_nB_{n+1} \rangle - \langle B_nA_{n+1} \rangle\right). \qquad (7.34b)\end{aligned}$$

such that the terms on the righthand side represent the gain/loss by reaction, diffusion to empty sites and exchange with different species. These equations are the lowest order differential equations in a hierarchy of coupled differential equations. We are interested in the steady state, so that $\mathrm{d}\langle A_n \rangle/\mathrm{d}t = \mathrm{d}\langle B_n \rangle/\mathrm{d}t = 0$, that makes it possible to re-write the master equations for the system in the form

$$\begin{aligned}0 =& -\frac{k}{h_A}\langle A_n \rangle + \left(\langle A_{n-1}E_n \rangle - \langle E_{n-1}A_n \rangle + \langle E_nA_{n+1} \rangle - \langle A_nE_{n+1} \rangle\right) + \\ & P_{\mathrm{ex}}\frac{h_{\mathrm{ex}}}{h_A}\left(\langle A_{n-1}B_n \rangle - \langle B_{n-1}A_n \rangle + \langle B_nA_{n+1} \rangle - \langle A_nB_{n+1} \rangle\right), \qquad (7.35a)\\ 0 =& +\frac{k}{h_A}\langle A_n \rangle + \frac{h_B}{h_A}\left(\langle B_{n-1}E_n \rangle - \langle E_{n-1}B_n \rangle + \langle E_nB_{n+1} \rangle - \langle B_nE_{n+1} \rangle\right) + \\ & P_{\mathrm{ex}}\frac{h_{\mathrm{ex}}}{h_A}\left(\langle B_{n-1}A_n \rangle - \langle A_{n-1}B_n \rangle + \langle A_nB_{n+1} \rangle - \langle B_nA_{n+1} \rangle\right). \qquad (7.35b)\end{aligned}$$

meaning that the only free parameter is k/h_A. With these considerations, the simulations are run and the initial reactivity of the system is determined for a family of values of $k_{\mathrm{ef}} = k/h_A$; where the reactivity η is defined as

$$\eta = k_{\mathrm{ef}}\sum_{i=1}^{L}\langle A_n \rangle. \qquad (7.36)$$

Since the typical length of the molecules is $\sim 1\,\mathrm{nm}$, see Figure 7.17 and Figure 7.18, and the typical length of the nanopores pores is $\sim 100\,\mathrm{nm}$ units, see Figure 7.2, the number of cells L that represent the pore is taken as $L = 100$. To determine the adsorption and desorption parameters, the details of the reaction are given: The catalytic reaction is performed for 2 hours at $60\,^{\circ}C$; this, with 3 mol% catalyst, 0.39 mmol 4-nitrobenzaldehyde, 1.5 mL acetone and 1.5 mL hexane [19]. This means that the percentage concentration of 4-nitrobenzaldehyde, by mass, is given by

$$\langle X_0 \rangle = 0.39\times 10^{-3}\,\mathrm{mol}\,M_{\mathrm{4NB}}/(0.39\times 10^{-3}\,\mathrm{mol}\,M_{\mathrm{4NB}} + 1.5\,\mathrm{mL}\rho_{\mathrm{ac}} + 1.5\,\mathrm{mL}\rho_{\mathrm{hex}}); \qquad (7.37)$$

with the values $M_{4\text{NB}} = 151.12 g/\text{mol}$, $\rho_{\text{ac}} = 0.786\, g/\text{mL}$ and $\rho_{\text{hex}} = 0.655\, g/\text{mL}$, this implies that the outside reactant concentration must be taken as $\langle X_0 \rangle = 0.03$. More details on how to determine the boundary conditions are given in [20]. The results for the simulations are presented in Figure 7.15.

The experimental results suggest that the percentage yield is not linearly correlated as the effective pore diameter increases, and could eventually plateau at values lower than 100%, both in the simulations and experimentally. By using a low concentration of $\langle X_0 \rangle$, the results do not match. However, we believe that the concentration $\langle X_0 \rangle$ by mass is not an appropriate measure of the actual concentration, due to the constraints imposed by the model. Thus, we explore a range of higher concentrations to determine if a higher concentration will yield similar results; the results are presented in Figure 7.15.

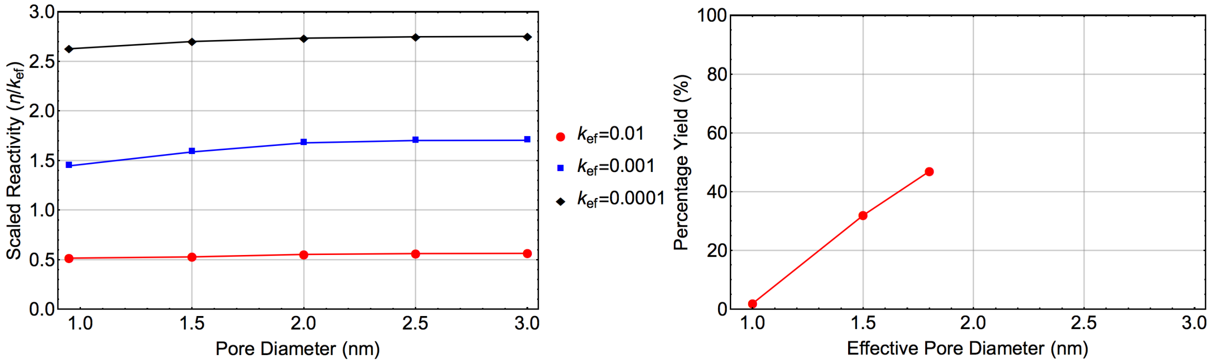

(a) (b)

Figure 7.14: (a) KMC results for several η/k_{ef} ratios against (b) experimental results for percentage yield in [19]. The parameters for the KMC simulation are taken as $h_A = 1$, $h_B = 0.788$, $h_{\text{ex}} = 0.894$ and $\langle X_0 \rangle = 0.03$. The catalytic reaction is performed for 2 hours at $60\,^{\circ}C$; this, with 3 mol% catalyst, 0.39 mmol 4-nitrobenzaldehyde, 1.5 mL acetone and 1.5 mL hexane [19].

With the KMC results for the higher concentrations, the trend gets closer to that of the experimental results, in particular for the $\langle X_0 \rangle = 0.8$ results with effective reaction rate $k_{\text{ef}} = 0.001$.

The KMC results indicate a similar trend for specific concentrations, however the small conversion; for small pore diameters the scaled reactivity grows at a faster rate than for wider pores, however, the plateau is reached for pore diameters lower than those for the experimental

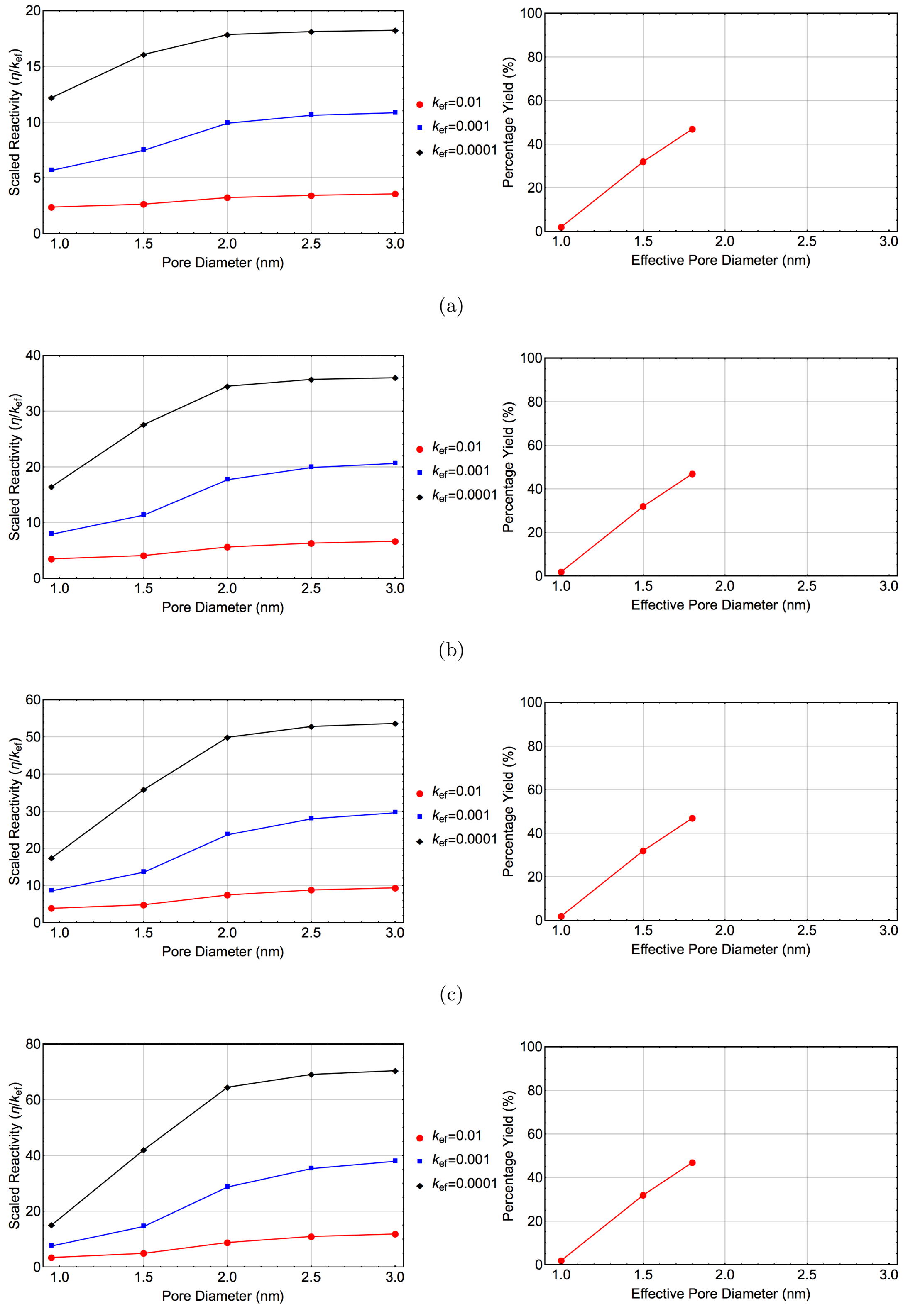

(a)

(b)

(c)

(d)

Figure 7.15: KMC results against experimental results, for outside concentrations of (a) $\langle X_0 \rangle = 0.2$, (b) $\langle X_0 \rangle = 0.4$, (c) $\langle X_0 \rangle = 0.6$, (c) $\langle X_0 \rangle = 0.8$. The parameters for the KMC simulation are taken as $h_A = 1$, $h_B = 0.788$, $h_{\text{ex}} = 0.894$. The catalytic reaction is performed for 2 hours at $60\,^{\circ}C$; this, with 3 mol% catalyst, 0.39 mmol 4-nitrobenzaldehyde, 1.5 mL acetone and 1.5 mL hexane [19].

results. It is worth mentioning that even if a trend exists, it is difficult to elucidate the true behavior with the limited amount of experimental data available.

7.7 Summary and Conclusion

Using molecular dynamics techniques, and molecular modeling techniques, we have determined the passing propensity of two molecules, 4-nitrobenzaldehyde and 4-(4-nitrophenyl)-2-butanone, made out of spheres, in an infinitely long cylindrical channel of diameter D_p, by only including steric constraints. Once the passing propensity of the two molecules was determined, the parameters were mapped into a further coarse grained KMC model to determine the reactivity of the system using several reaction rates. The results were then compared to experimental data.

It was found that the trend in the KMC results had some similarities with the experimental results. However, due to the lack of experimental results, a more thorough comparison with extended data sets should be conducted to verify the trend in the KMC results. Also, we believe that other important interactions between the molecules and the pore walls are missing from the model and will be the focus of future work.

7.8 Acknowledgements

We acknowledge useful discussion with Igor Slowing; we also thank him for providing the results for the product yield results of the reaction to compare them with the KMC data. This work was supported by the U.S. Department of Energy (USDOE), Office of Basic Energy Sciences, Division of Chemical Sciences, Geosciences, and Biosciences through the Ames Laboratory Chemical Physics program. The work was performed at Ames Laboratory which is operated for the USDOE by Iowa State University under Contract No. DE-AC02-07CH11358.

7.9 Appendix A: The Shape of the Molecules

The 4-nitrobenzaldehyde and 4-(4-nitrophenyl)-2-butanone molecule are modeled using spheres. The center of the spheres correspond to the location of the atoms of which these

Table 7.7: 4-nitrobenzaldehyde atom and properties list with respect to the center of mass, using a solid sphere model. All the length units are in angstroms (Å) and mass units in atomic mass units (u).

4-nitrobenzaldehyde						
Atom Number	Atom Type	Coordinate x	Coordinate y	Coordinate z	van der Walls Radius	Mass
1	O	3.2112	0.9307	-0.0019	1.52	15.9994
2	O	3.0311	-1.2571	-0.0002	1.52	15.9994
3	O	-3.8866	-0.6218	-0.0016	1.52	15.9994
4	N	2.5149	-0.1132	-0.0005	1.55	14.0067
5	C	1.1	0.0034	0.001	1.70	12.0107
6	C	-1.6803	0.2328	0.0007	1.70	12.0107
7	C	0.5042	1.2646	0.0009	1.70	12.0107
8	C	0.3056	-1.1431	0.0009	1.70	12.0107
9	C	-0.886	1.3793	0.0009	1.70	12.0107
10	C	-1.0846	-1.0285	0.0007	1.70	12.0107
11	C	-3.1296	0.353	-0.0009	1.70	12.0107
12	H	1.0914	2.1794	0.0007	1.20	1.00794
13	H	0.7351	-2.1417	0.0006	1.20	1.00794
14	H	-1.3357	2.3689	0.0006	1.20	1.00794
15	H	-1.684	-1.9351	0.0003	1.20	1.00794
16	H	-3.5417	1.3764	-0.0014	1.20	1.00794

are composed of. The radii of the spheres are the corresponding van der Waals radius of the atoms; see Table 7.7 and Table 7.8, along with Figure 7.16.

Comparing the typical dimensions of the molecules give insight on the validity of the models used. The molecules are compared in Figure 7.17 and Figure 7.18, revealing that the "real" molecules are similar to those used as the models.

7.10 Appendix B: Calculating the Diffusion Tensor and its Square Root

The procedure to get the diffusion tensor is the one developed in [9]. The general strategy is to calculate the 6×6 friction tensor $\tilde{\zeta}$ and use the simple relation

$$\tilde{D} = k_B T \tilde{\zeta}^{-1}. \tag{7.38}$$

Where the tensor $\tilde{D}$ is composed of 3×3 blocks, that correspond to the translational part $(\mathbf{D}_{tt})$, the rotational part $(\mathbf{D}_{rr})$, and the translational-rotational coupling $(\mathbf{D}_{tr})$, such that

$$\tilde{D} = \begin{pmatrix} \mathbf{D}_{tt} & \mathbf{D}_{tr}^T \\ \mathbf{D}_{tr} & \mathbf{D}_{rr} \end{pmatrix}. \tag{7.39}$$

The diffusion tensor is dependent of the reference frame used, and the hydrodynamic center can be calculated from this diffusion tensor. Once the hydrodynamic center is obtained, the diffusion tensor is calculated with respect to this point. The relative vector from the initially chosen reference frame to the hydrodynamic center is calculated as [9]

$$\begin{pmatrix} r_{\mathrm{DO}_x} \\ r_{\mathrm{DO}_y} \\ r_{\mathrm{DO}_z} \end{pmatrix} = \begin{pmatrix} \mathbf{D}_{rr}^{yy} + \mathbf{D}_{rr}^{zz} & -\mathbf{D}_{rr}^{xy} & -\mathbf{D}_{rr}^{xz} \\ -\mathbf{D}_{rr}^{xy} & \mathbf{D}_{rr}^{xx} + \mathbf{D}_{rr}^{zz} & -\mathbf{D}_{rr}^{yz} \\ -\mathbf{D}_{rr}^{xz} & -\mathbf{D}_{rr}^{yz} & \mathbf{D}_{rr}^{xx} + \mathbf{D}_{rr}^{yy} \end{pmatrix} \begin{pmatrix} \mathbf{D}_{tr}^{yz} - \mathbf{D}_{tr}^{zy} \\ \mathbf{D}_{tr}^{zx} - \mathbf{D}_{tr}^{xz} \\ \mathbf{D}_{tr}^{xy} - \mathbf{D}_{tr}^{yx} \end{pmatrix}. \tag{7.40}$$

For a molecule made of N particles, the strategy to calculate the 6×6 friction tensor, $\tilde{\zeta}$, is to get a $3N \times 3N$ matrix, $\mathcal{B}$, composed of N three times three blocks $\mathbf{B}$. Choose $\mathbf{T}_{ij}$ as the $3t \times 3$ tensor with the information of the hydrodynamic friction between the i^{th} and j^{th} sphere in the molecule. The entries of the matrix $\mathbf{B}$ match with the $\mathbf{T}_{ij}$ tensors, that is

$$\mathbf{B}_{ij} = \begin{cases} \mathbf{T}_{ij} & i \neq j \\ \frac{1}{\zeta_i}\mathbf{I} & i = j \end{cases}, \qquad \zeta_i = 6\pi\eta_0\sigma_i. \tag{7.41}$$

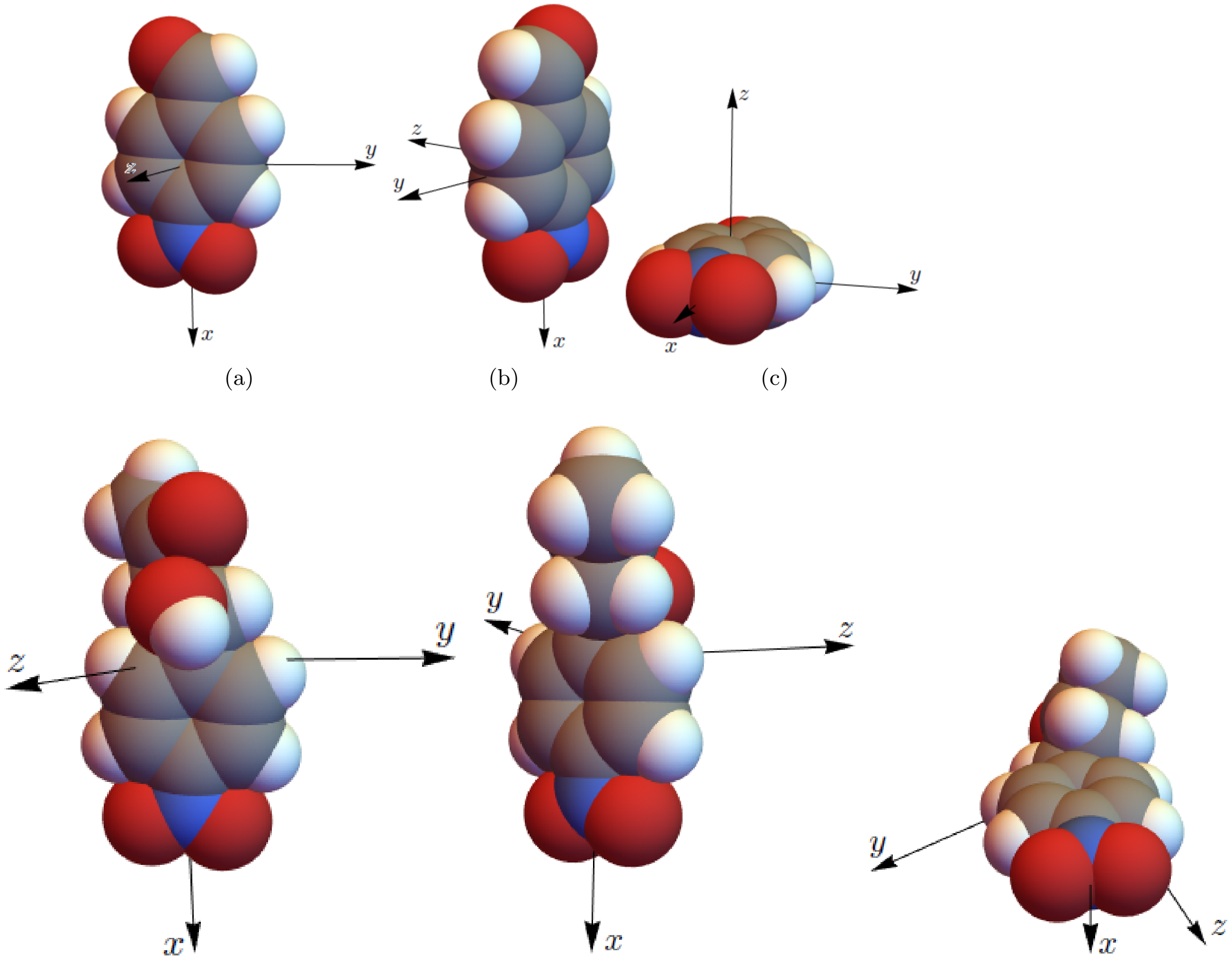

(a) (b) (c)

(d) (e) (f)

Figure 7.16: 3D real molecule models for (a-c) 4-nitrobenzaldehyde molecule model, see Table 7.7, and (d-f) 4-(4-nitrophenyl)-2-butanone, see Table 7.8; views from different perspectives.

Table 7.8: 4-(4-nitrophenyl)-2-butanone atom and properties list with respect to the center of mass. All the length units are in angstroms (Å) and mass units in atomic mass units (u).

4-(4-nitrophenyl)-2-butanone						
Atom Number	Atom Type	Coordinate x	Coordinate y	Coordinate z	van der Walls Radius	Mass
1	O	−2.0576	0.7186	1.6184	1.52	15.9994
2	O	−4.5294	0.7087	0.1689	1.52	15.9994
3	O	4.6229	0.6048	−0.6887	1.52	15.9994
4	O	4.3809	−1.3303	0.3192	1.52	15.9994
5	N	3.9027	−0.267	−0.1448	1.55	14.0067
6	C	−1.7139	0.6337	0.2351	1.70	12.0107
7	C	−0.2243	0.3946	0.1336	1.70	12.0107
8	C	−2.5134	−0.4907	−0.4331	1.70	12.0107
9	C	0.5755	1.3524	−0.4662	1.70	12.0107
10	C	0.309	−0.7771	0.6433	1.70	12.0107
11	C	−4.0182	−0.2778	−0.3586	1.70	12.0107
12	C	1.9497	1.1319	−0.5593	1.70	12.0107
13	C	1.6833	−0.9977	0.5503	1.70	12.0107
14	C	2.5037	−0.0431	−0.0509	1.70	12.0107
15	C	−4.8708	−1.3612	−0.967	1.70	12.0107
16	H	−1.9856	1.5935	−0.2207	1.20	1.00794
17	H	−2.2347	−0.5788	−1.4895	1.20	1.00794
18	H	−2.3256	−1.4512	0.0605	1.20	1.00794
19	H	0.1554	2.271	−0.8652	1.20	1.00794
20	H	−0.3106	−1.5252	1.1282	1.20	1.00794
21	H	2.558	1.8976	−1.034	1.20	1.00794
22	H	2.0803	−1.9228	0.9603	1.20	1.00794
23	H	−1.4492	1.3476	2.0429	1.20	1.00794
24	H	−4.6964	−2.3033	−0.4415	1.20	1.00794
25	H	−4.6256	−1.4685	−2.0265	1.20	1.00794
26	H	−5.9274	−1.0947	−0.8751	1.20	1.00794

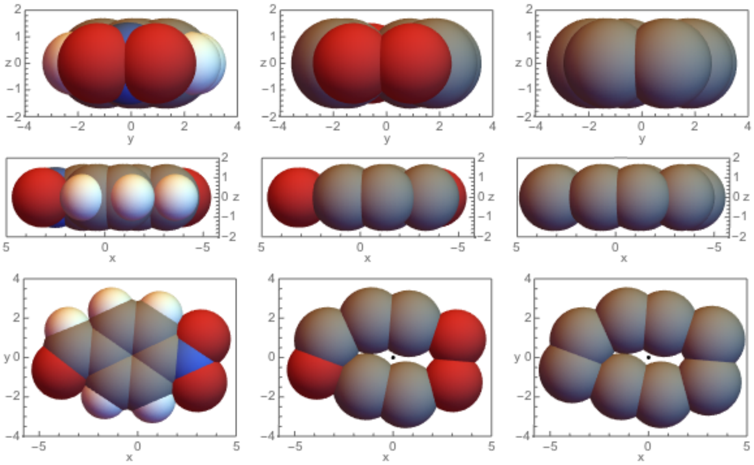

Figure 7.17: Comparing all the 3D models for the 4-nitrobenzaldehyde molecule from different perspectives. The left most images corresponds to the “real” molecule, see Table 7.7. The images in the middle correspond to the steric model, see Table 7.1. The images in the right correspond to the hydrodynamic model, see Table 7.3.

with $\mathbf{I}$ the 3×3 identity matrix. For spheres of different radii, σ_i and σ_j, and don't intersect, the expression for $\mathbf{T}_{ij}$ is given by [9]

$$\mathbf{T}_{ij} = (8\pi\eta_0 R_{ij})^{-1}\left(\mathbf{I} + \frac{\mathbf{R}_{ij}\mathbf{R}_{ij}}{R_{ij}^2} + \left[\frac{\sigma_i^2+\sigma_j^2}{R_{ij}^2}\right]\left[\frac{1}{3}\mathbf{I} - \frac{\mathbf{R}_{ij}\mathbf{R}_{ij}}{R_{ij}^2}\right]\right), \quad \mathbf{R}_{ij} = \vec{r}_i \otimes \vec{r}_j; \tag{7.42}$$

where $\vec{r}_i$ is the vector of the i^{th} particle with respect to the point where the friction tensor is being calculated, R_{ij}^2 is the distance between the particles squared, and η_0 is the viscosity of the fluid. For particles that intersect and have the *same radius* σ, the $\mathbf{T}_{ij}$ tensor is [9]

$$\mathbf{T}_{ij} = (6\pi\eta_0\sigma)^{-1}\left(\left[1 - \frac{9}{32}\frac{R_{ij}}{\sigma}\right]\mathbf{I} + \frac{3}{32}\frac{\mathbf{R}_{ij}\mathbf{R}_{ij}}{R_{ij}\sigma}\right). \tag{7.43}$$

Since the results are passing propensities and the particles are immersed in the same fluid, the viscosity of the fluid can be ignored, along with common factors, such as π.

Once the $\mathcal{B}$ tensor is calculated, define $\mathcal{C} = \mathcal{B}^{-1}$, such that $\mathcal{C}$ has the same dimensions as $\mathcal{B}$ does, i.e., a $3N \times 3N$ matrix. The different parts of the 6×6 friction tensor, that is made of four blocks of 3×3 tensors. If $\tilde{\zeta}$ is given by

$$\tilde{\zeta} = \begin{pmatrix} \zeta_{tt} & \zeta_{tr}^T \\ \zeta_{tr} & \zeta_{rr} \end{pmatrix}, \tag{7.44}$$

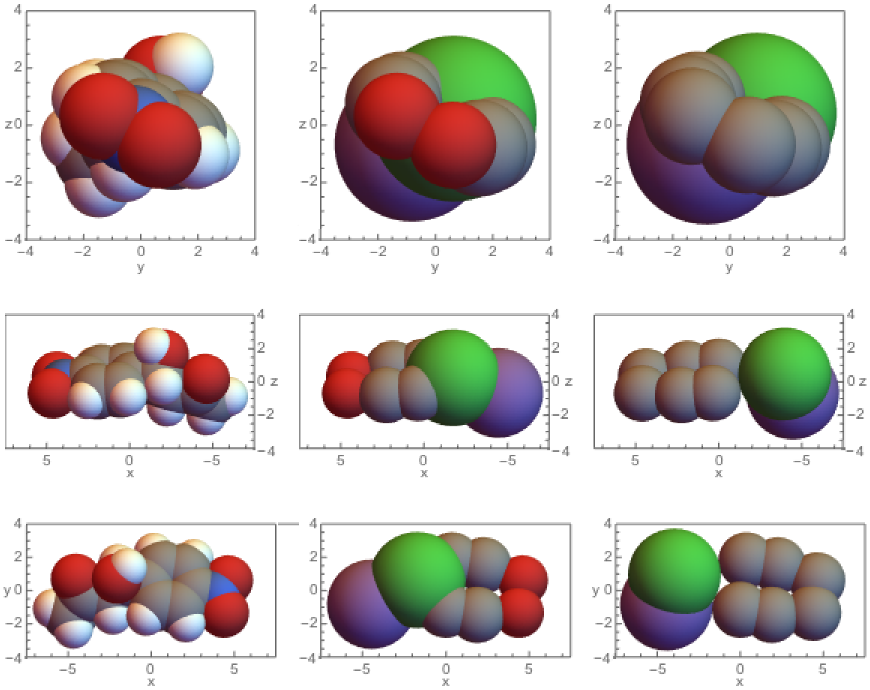

Figure 7.18: Comparing all the 3D models for the 4-(4-nitrophenyl)-2-butanone molecule from different perspectives. The left most images corresponds to the "real" molecule, see Table 7.8. The images in the middle correspond to the steric model, see Table 7.2. The images in the right correspond to the hydrodynamic model, see Table 7.4.

the 3×3 blocks ζ_{tt}, ζ_{tr} and ζ_{rr} are given by

$$\zeta_{tt} = \sum_{i=1}^{N} \sum_{i}^{N} \mathcal{C}_{ij}, \tag{7.45a}$$

$$\zeta_{tr} = \sum_{i=1}^{N} \sum_{i}^{N} \mathbf{U}_i \mathcal{C}_{ij}, \tag{7.45b}$$

$$\zeta_{rr}^{\text{uc}} = \sum_{i=1}^{N} \sum_{i}^{N} \mathbf{U}_i \mathcal{C}_{ij} \mathbf{U}_j^T; \tag{7.45c}$$

where $\mathcal{C}_{ij}$ are the 3×3 blocks from $\mathcal{C}$, and $\mathbf{U}_i$ is a 3×3 matrix related to the coordinates of the i^{th} particle

$$\mathbf{U}_i = \begin{pmatrix} 0 & -z_i & y_i \\ z_i & 0 & -x_i \\ -y_i & x_i & 0 \end{pmatrix}. \tag{7.46}$$

The rotational part of the tensor ζ_{rr} is related to ζ_{rr}^{uc} by [9]

$$\zeta_{rr} = \zeta_{rr}^{\text{uc}} + 6\eta_0 V \mathbf{I}, \qquad V = \frac{4}{3}\pi \sum_i \sigma_i^3. \tag{7.47}$$

Finally, the diffusion tensor $\tilde{D}$ is calculated using Equation 7.38 and is given by [9]

$$\tilde{D} = \begin{pmatrix} \mathbf{D}_{tt} & \mathbf{D}_{tr}^T \\ \mathbf{D}_{tr} & \mathbf{D}_{rr} \end{pmatrix} = k_B T \begin{pmatrix} \zeta_{tt} & \zeta_{tr}^T \\ \zeta_{tr} & \zeta_{rr} \end{pmatrix}^{-1}. \tag{7.48}$$

The diffusion tensor $\tilde{D}$ has to be a 6×6 positive definite and symmetric matrix, i.e., $\tilde{D}_{ij} = \tilde{D}_{ji}$, the matrix is invertible, diagonalizable, and the eigenvalues $\lambda > 0$.

Bibliography

[1] J. Kärger, M. Petzold, H. Pfeifer, S. Ernst, and J. Weitkamp. Single-file diffusion and reaction in zeolites. *J. Catal.*, 132:pp. 283–299, 1992.

[2] D. M. Ackerman, J. Wang, J. H. Wendel, D-J. Liu, M. Pruski, and J. W. Evans. Catalytic conversion reactions mediated by single-file diffusion in linear nanopores: Hydrodynamics vs stochastic behavior. *J. Chem. Phys.*, 134:114107, 2011.

[3] P. Bräuer, A. Brzank, and J. Kärger. Adsorption and reaction in single-file networks. *J. Phys. Chem. B*, 107:pp. 1824–1831, 2003.

[4] D-J. Liu, A. Garcia, J. Wang, D. M. Ackerman, C-J. Wang, and J. W. Evans. Kinetic Monte Carlo simulation of statistical mechanical models and coarse-grained mesoscale description of catalytic reaction-diffusion processes: 1D nanoporous and 2D surface systems. *Chem. Rev.*, 115:pp. 5979–6050, 2015.

[5] J. S. Beck, J. C. Vartuli, W. J. Roth, M. E. Leonowicz, C. T. Kresge, K. D. Schmitt, C. T-W. Chu, D. H. Olson, E. W. Sheppard, S. B. McCullen, J. B. Higgins, and J. L. Schlenker. A new family of mesoporous molecular sieves prepared with liquid crystal templates. *J. Am. Chem. Soc.*, 114:pp. 10834–10843, 1992.

[6] B. G. Trewyn, I. I. Slowing, S. Giri, H-T. Chen, and V. S-Y. Lin. Synthesis and functionalization of a mesoporous silica nanoparticle based on the Sol-Gel process and applications in controlled release. *Acc. Chem. Res.*, 40:pp. 846–853, 2007.

[7] D. Zhao, J. Feng, Q. Huo, N. Melosh, G. H. Fredrickson, B. F. Chmelka, and G. D. Stucky. Triblock copolymer syntheses of mesoporous silica with periodic 50 to 300 angstrom pores. *Science*, 279:pp. 548–552, 1998.

[8] K. Kandel, S. M. Althaus, C. Peeraphatdit, T. Kobayashi, B. G. Trewyn, M. Pruski, and I. I. Slowing. Solvent-induced reversal of activities between two closely related heterogeneous catalysis in the aldol reaction. *ACS Catal.*, 3:pp. 265–271, 2013.

[9] B. Carrasco and J. García de la Torre. Hydrodynamic properties of rigid particles: Comparison of different modeling and computational procedures. *Biophysical J.*, 75:pp. 3044–3057, 1999.

[10] J. García de la Torre and V. A. Bloomfield. Hydrodynamic properties of macromolecular complexes. I. Translation. *Biopolymers*, 16:pp. 1747–1763, 1977.

[11] S. E. Harding. A general method for modeling macromolecular shape in solution: A graphical (II-G) intersection procedure for triaxial ellipsoids. *Biophys. J.*, 51:pp. 673–680, 1987.

[12] M. Majka and P. F. Góra. Polymer unfolding and motion synchronization induced by spatially correlated noise. *Phys. Rev. E*, 86:051112, 2012.

[13] I. M. Ilie, W. J. Briels, and W. K. den Otter. An elementary singularity-free rotational Brownian dynamics algorithm for anisotropic particles. *J. Chem. Phys.*, 142:114103, 2015.

[14] S. Delong, F. B. Usabiaga, and A. Donev. Brownian dynamics of confined rigid bodies. *J. Chem. Phys.*, 143:144107, 2015.

[15] D. M. Ackerman. *Interplay between inhibited transport and reaction in nanoporous materials*. PhD thesis, Iowa State University, 2013.

[16] B. J. Berne and J. A. Montgomery. The coupling between translational and rotational motion. *Mol. Phys.*, 32:pp. 363–378, 1976.

[17] J. Diebel. Representing attitude: Euler angles, unit quaternions and rotation vectors. `https://www.astro.rug.nl/software/kapteyn/_downloads/attitude.pdf`, 2006.

[18] C-J. Wang, D. M. Ackerman, I. I. Slowing, and J. W. Evans. Langevin and Fokker-Plank analyses of inhibitted molecular passing processes controlling transport and reactivity in nanoporous materials. *Phys. Rev. Lett.*, 113:038301, 2014.

[19] I. I. Slowing. Conversion of 4-nitrobenzaldehyde to an aldol product. (unpublished).

[20] A. García and J. W. Evans. Boundary conditions for diffusion-mediated processes within linear nanopores: Exact treatment of coupling to an equilibrated external fluid. *J. Phys. Chem. C*, 121:pp. 8873–8888, 2017.

CHAPTER 8. GENERAL CONCLUSIONS

In this work, several reaction-diffusion systems in nanopores were analyzed *using lattice-gas* models. Kinetic Monte Carlo simulations were primarily used to determine the detailed concentration of the particles inside the pore, i.e., the pore's particle concentration profiles, when imposing the single-file diffusion (SFD) constraint in the systems. *All* the particles in the systems were assumed to have the same hop rates, unless otherwise stated.

The first system considered is an extension of the simple $A \to B$ reaction to an isomeric stereoselective reaction $A \to B^c + B^t$, where the local environment favors one of the isomers over the other depending on the local reaction conditions. It was found that this kind of reaction, at low reaction rates, allows an analytic treatment by making use of an extended generalized hydrodynamic method, that consists on individually assessing the pair quantities $\langle A_n E_{n+1} \rangle$ and $\langle E_n A_{n+1} \rangle$ rather than just the difference; mean-field theories fail completely in describing these reactions at low reaction rates. Also, it was found that at high reaction rates, where a mean field theory correctly describes the particle concentration profiles inside the pores, the extended generalized theory manages to describe it as well.

The next system considered was an extension of the simple $A \to B$ with $R = 0$ model, where more general steric interactions are used, i.e., a reaction-diffusion system with up to nearest-neighbor exclusion, $R = 1$, is considered. It was found that unlike the simple $A \to B$ model, the change from a 3D to a 1D environment induces non-trivial correlations in the adsorption and desorption processes; a feature that complicates the simulation of only the pore, instead of the fluid+pore, unlike for the simple $R = 0$ case where the adsorption and desorption parameters are trivially determined. These correlations in turn predict density oscillations near the pore walls and adsorption/desorption sites, that matches the prediction of fluid density oscillations near the pore walls in real fluids. Also, a methodology was developed to treat the fluid and the pore separately, instead of having to simulate the fluid and pore as a single system. Tailored simulations were implemented to determine adsorption and desorption parameters, that were used to simulate only the pore system. The single pore system, whose adsorption and desorption parameters were found by tailored simulations, particle concentration profiles matched that of the fluid coupled to the pore. An analytic theory to match the results from the KMC simulations, similar to that for the simple $A \to B$ model with $R = 0$, was developed and successfully implemented. This was also compared to *mean-field type of equations* that failed to predict the proper trend in the reaction-diffusion case. For the case of only diffusion, a *pair approximation* was sufficient to properly describe the concentration profile, confirming the Markovian property of the system.

Following the analysis of the two systems, we developed a framework that allows the implementation of simplified simulations for more general fluid+pore reaction-diffusion systems. Instead of a one-dimensional pore, we considered an $N \times M$ cross-sectional pore of length L coupled to a semi-infinite three-dimensional fluid, with a generalized exclusion range R. Tailored simulations to obtain the proper adsorption/desorption parameters to simulate only the pore are developed and are implemented for specific values of N, M and R; applications for these systems are shown and for each system an analytic theory is successfully developed. The pore concentration profiles are analytically reconstructed using the Markov property of the systems.

For systems in one-dimension, the SDF constraint is relaxed by including a passing probability between particles of different species. This passing probability was obtained by implementing Langevin MD simulations. The first case under consideration was motivated by polymerization reactions in narrow channels. Of particular interest is the simplification of the problem to two-dimensions. The molecules are initially coarse-grained to models where molecules made out of a collection of spheres diffusing in an infinitely long cylindrical channel of cross-section D_p. These molecules are mapped to molecules in two dimensions that are made of circles that diffuse in an infinitely long rectangular channel of width W; that is referred to as “the pore”. It is assumed that the oligomers have the same diffusion coefficients along their two main symmetry axes, as well as for the rotational diffusion coefficient. The interactions considered are steric, such that the molecules cannot intersect the pore walls or each other, otherwise the interactions are fluid-mediated. In this work, we were focused on elucidating the passing propensity for linear oligomers in monomer-oligomer systems. The small and large gap regimes were examined. It was concluded that for small gaps, the passing propensity of monomer-monomer, monomer-dimer and monomer-trimer systems scale as $P \sim (g/r)^{\sigma}$; where σ is the scaling exponent. This scaling exponent for different oligomers was determined to follow $\sigma_{\text{monomer}} \approx \sigma_{\text{dimer}} < \sigma_{\text{trimer}}$, that basically shows that for longer oligomers the passing propensity decreases faster with decreasing gap size. For wider gaps, it was found that the passing propensity for longer oligomers is higher than for shorter oligomers in a given range, this due to the initial constraint that the shortest axis molecules tend to be perpendicular to the longest axis of the pore. It can also be seen that as $g \rightarrow \infty$, the expected magnitude of the passing propensity P for different sized oligomers is restored, i.e., $P_{\text{circle}}(g) \geq P_{\text{dimer}}(g) \geq P_{\text{trimer}}(g) \geq P_{\text{tetramer}}(g) \geq \ldots$.

For the last part of this work, an application to the catalytic conversion of 4-nitrobenzaldehyde to 4-(4-nitrophenyl)-2-butanone is examined. The 4-nitrobenzaldehyde is dissolved in an acetone and hexane solution that contains mesoporous silica nanoparticles, that have amine functionalized nanopores. The aldolization reaction takes place in the nanopores. Based on the properties of the mesoporous silica, we implemented a KMC one-dimensional model with a constant concentration of reactant in the outside fluid with exclusion range $R = 0$. The particles do not have the same hop rate, and exchange is possible. To assess the exchange probability, a realistic model of the molecules was implemented. The exchange probability was determined by obtaining the passing propensity of the 4-nitrobenzaldehyde and 4-(4-nitrophenyl)-2-butanone molecules, that were coarse-grained as molecules made out of spheres, by Langevin MD simulations in three dimensions. The hydrodynamic properties such as the diffusion tensor were obtained by further approximation of the models. Once the passing propensities and diffusion tensors were obtained, these parameters were converted to the required parameters for the KMC simulations, where the reactivity for the molecules was obtained and compared with the experimental data; we believe that the effective fractional volume of the reactant is higher than the one calculated from the experimental data. We determine that the choice of outside concentration $\langle X_0 \rangle$ for the KMC model has to be higher than that described in the experiment, along with a low reaction rate. Even if the KMC results follow the experimental trend, we believe that other interactions and further modeling of the channel have to be included for effective modeling of the system.

8.1 Future Work

Prospective future work includes numerous possibilities. Currently, the analytic theories for the reaction-diffusion kinetic Monte Carlo models we have presented limit the hop rates of the particles to be the same; i.e, the hop rate for the i^{th} species is the same as the hop rate for the j^{th} species, $h_i = h_j$; and it is limited to the irreversible conversion of a single particle type. A future perspective would be to develop analytic theories for reaction-diffusion systems where particles of different species to have with unequal hop rates and/or where there is a bimolecular reaction $A + B \leftrightarrow C + D$. Further work can expand on obtaining an analytic theory for reaction-diffusion systems for wider pore lattices with higher exclusion range.

Future work for the Langevin MDs simulations would be directed towards refining the current model by including interactions that go beyond the steric interactions, or refine the steric interactions by modeling the interior of the pore in mode detail. Not only the modeling but the algorithm can be refined to include adaptative time steps and parallel processing capabilities.